Photophysical and Laser Studies on Perylenediimides and Nanographenes

Rafael Muñoz Mármol

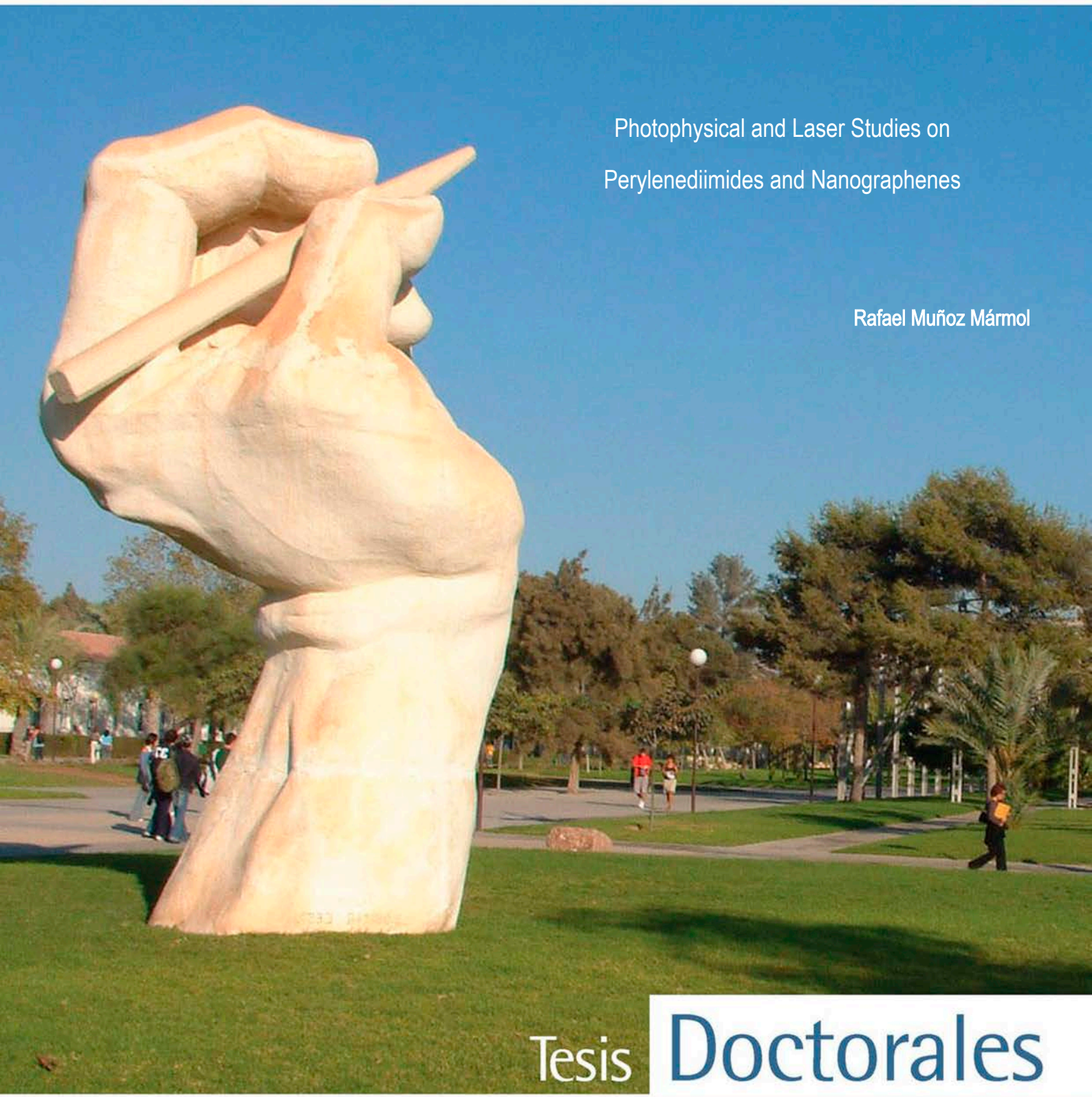

Universitat d'Alacant
Universidad de Alicante

Departamento de Física Aplicada
Instituto Universitario de Materiales de Alicante
Facultad de Ciencias

Photophysical and Laser Studies on Perylenediimides and Nanographenes

Rafael Muñoz Mármol

Tesis presentada para aspirar al grado de

DOCTOR POR LA UNIVERSIDAD DE ALICANTE
MENCIÓN DE DOCTOR INTERNACIONAL
DOCTORADO EN CIENCIA DE MATERIALES

Dirigida por:
Prof. María Ángeles Díaz García
Catedrática de la Universidad de Alicante

Financiada por:
Ministerio de Economía y Competitividad
y Fondo Social Europeo
(BES-2016-077681 y MAT2015-66586-R)

Alicante, octubre 2021

Abstract

Conjugated organic compounds have been extensively investigated, owing to their versatility for being integrated with other materials through cost-effective methods and their suitability for a wide range of optoelectronic applications; for instance, field-effect transistors, solar cells, LEDs and lasers among others. Particular interest exists nowadays in organic materials for lasing propelled by the development of biomedical and telecommunication applications. Indeed, the development of organic synthesis bottom-up techniques and quantum-chemical computation enable the intelligent design of organic compounds with tailored properties that can be beneficial for such applications. In this regard, understanding the relationship between the structural characteristics of the organic compounds and their optoelectronical properties is a mandatory step in the design process.

In the development of this thesis, the photophysical properties of two families of organic compounds –perylenediimides and nanographenes– dispersed in inert matrixes are evaluated with scope of improving their laser performance. Particularly, three actuations have been accomplished: *i*) systematic investigation of two commercial thermoplastic polymers –polystyrene and poly(methyl methacrylate)– as inert matrixes to disperse perylenediimide compounds with a mayor focus on optimizing the waveguide properties and reducing the operational energy requirements of the devices; *ii*) get insights on the photodegradation and concentration quenching mechanisms of perylenediimide compounds dispersed in polystyrene films with the aim of obtaining more lasting and efficient devices; and *iii*) studying the photophysical properties of novel nanographene compounds dispersed in inert matrixes with the purpose of elucidating the relationship between their structure –edge, heteroatoms, substituents– and their optical gain performance.

Sinopsis

Los compuestos orgánicos conjugados han sido investigado ampliamente debido a su versatilidad para integrarse con otros materiales a través de métodos de bajo coste y a su idoneidad para una amplia gama de aplicaciones optoelectrónicas; por ejemplo, transistores de efecto de campo, células solares, LEDs y láseres, entre otros. Actualmente existe un interés particular en los materiales orgánicos para láser promovido por el desarrollo de aplicaciones biomédicas y de telecomunicaciones. De hecho, el desarrollo de técnicas bottom-up en la síntesis orgánica y de métodos computacionales químico-cuánticos permiten el diseño inteligente de compuestos orgánicos con propiedades a medida que pueden ser beneficiosas para tales aplicaciones. En este sentido, comprender la relación entre las características estructurales de los compuestos orgánicos y sus propiedades optoelectrónicas es una etapa obligatoria en el proceso de diseño.

En el desarrollo de esta tesis se evalúan las propiedades fotofísicas de dos familias de compuestos orgánicos –perilenodiimidas y nanografenos– dispersos en matrices inertes con el objetivo de mejorar su funcionamiento como materiales activos para láseres. En particular, se han llevado a cabo tres actuaciones: *i*) la investigación sistemática de dos polímeros termoplásticos comerciales, poliestireno y polimetilmetacrilato, como matrices inertes para dispersar compuestos de perilenodiimida con el enfoque de optimizar las propiedades de la guía de ondas y reducir los requisitos de energéticos de los dispositivos; *ii*) conocer los mecanismos de fotodegradación y quenching de la fotoluminiscencia en derivados de perilenodiimida dispersos en películas de poliestireno con el objetivo de obtener dispositivos más duraderos y eficientes; y *iii*) estudiar las propiedades fotofísicas de compuestos novedosos de la familia de los nanografenos dispersos en matrices inertes con el fin de comprender la relación entre su estructura –borde, heteroátomos, sustituyentes– y su ganancia óptica.

A Julia Ortega Muñoz
que ha venido a este mundo
a traer alegría y felicidad

Agradecimientos

Seguramente la parte más dura de escribir de toda la tesis sea esta breve entrada. No por falta de gratitud, sino por el cierto sabor a despedida que deja. Por eso, no he sido capaz de escribir estas palabras hasta que ya todas las demás estaban escritas. Durante mi tiempo en Alicante, he conocido a mucha gente maravillosa que de una manera u otra forma parte de esta tesis y no quiero dejar de agradecérselo a todos.

En particular, le estoy tremendamente agradecido a mi tutora María Ángeles Díaz García por haberme dado la oportunidad de realizar mis estudios de doctorado bajo su tutela. Es gracias a su esfuerzo y valiosos consejos que esta tesis ha sido posible. Además, tengo que agradecerle tanto a ella como a José Moisés Villalvilla Soria, José Antonio Quintana Arévalo, Pedro Giménez Boj y Víctor Bonal Díaz que me hayan permitido formar parte del equipo de investigación durante estos cinco años. Con todos ellos he compartido innumerables horas de trabajo que me han permitido aprender de su dedicación y amor por la ciencia, ambos aspectos clave en mi desarrollo como investigador y persona.

También quiero mostrarles mi gratitud al Profesor Guglielmo Lanzani y los Doctores Giuseppe Paternò, Francesco Scotognella y Aaron Michael Ross que me dieron la oportunidad de pasar con ellos un tiempo en Milán que sin duda ha sido clave para mi formación y desarrollo. Así mismo, esta tesis no hubiese sido posible sin la colaboración de los Profesores Ángela Sastre Santos, Fernando Fernández Lázaro, Jishan Wu, Juan Casado Cordón, Juan Carlos Sancho García y Enrique Ortí Guillén y los Doctores Yanwei Gu, Nathalie Zink Lorre, Juan Aragó March, Fernando Gordillo Gámez y Paulius Baronas entre otros muchos. Gracias a todos por vuestro granito.

No quiero olvidarme de los muchos amigos que me llevo de Alicante con los que he compartido tantos momentos buenos y que siempre me han estado cercanos durante todo el proceso. No diré nombres para que no falte ninguno, pero a todos os estoy tremendamente agradecido por compartir vuestro tiempo conmigo y aguantarme.

Por supuesto todo esto no hubiese sido posible sin mi familia que me soporta en todo momento y a la que debo todo cuanto soy. Ellos son mi fuente de inspiración y mis fuerzas para continuar. A Marta Mazzarella en particular tengo que agradecerle todo su apoyo y compresión a lo largo de todo el proceso y muy especialmente en la parte final donde las fuerzas siempre faltan.

Index

List of Illustrations

List of Tables

List of Abbreviations

ASE	amplified spontaneous emission
BBO	barium borate
b-PDI	bay-substituted perylenediimide
COPV	carbon-bridged oligo(*p*-phenylene vinylene)
CT	charge transfer
DCG	dichromated gelatine
DCM	dichloromethane
DFB	distributed feedback
DFT	density functional theory
ESA	excited-state absorption
FWHM	full width at half maximum
HL	holographic lithography
HOMO	higher occupied molecular orbital
IC	internal conversion
ISC	intersystem crossing
LUMO	lower unoccupied molecular orbital
NG	nanographenes
NIR	near-infrared
OPA	optical parametric amplifier
OPO	optical parametric oscillator
OSL	organic solid-state laser
PB	photobleaching
PDI	perylenediimide
PL	photoluminescence
PLQY	photoluminescence quantum yield
PMMA	poly(methyl methacrylate)
PS	polystyrene
SC	single crystal
SE	stimulated emission
TA	transient absorption
TADF	thermally activated delayed fluorescence
TE	transversal electric
TFOL	thin-film organic laser

THF	tetrahydrofuran
TM	transversal magnetic
TRPL	time-resolved photoluminescence
UA	University of Alicante
u-PDI	bay-undoped perylenediimide
VPI	variable pump intensity
VSL	variable stripe length

List of Symbols

$\|i\rangle$	electronic state/level i
$\|i, \upsilon\rangle$	vibronic state of electronic level i and vibrational quantum number υ
A_{ji}	radiative decay rate for transition $\|j\rangle \rightarrow \|i\rangle$
d	resonator depth
E_i	energy of state/level $\|i\rangle$
E_{pump}	pump energy density
$E_{th\text{-}ASE}$	ASE threshold expressed as energy density
$E_{th\text{-}DFB}$	DFB laser threshold expressed as energy density
F	optical fluence
f	lens focal length
F_{pump}	pump optical fluence
g	optical gain
g_{net}	net gain
h	Planck' constant
h_f	film thickness
I	intensity
I_0	impinging intensity
I_{out}	output intensity
I_{pump}	pump intensity
k	wave vector
l	stripe length
n_c	refractive index of the cover
n_{eff}	effective refractive index
n_f	refractive index of the active film
Ni	population of state $\|i\rangle$
n_s	refractive index of the substrate
OD	optical density
T	transmittance
W_{ij}	stimulated rate of transition $\|i\rangle \rightarrow \|j\rangle$
W_{pump}	stimulated rate of the pumped transition
α	absorption coefficient
Γ	confinement factor

γ_i	spontaneous decay rate of state $\|i\rangle$
γ_{ji}	spontaneous decay rate of transition $\|j\rangle \rightarrow \|i\rangle$
$\Delta T/T$	optically induced change of transmittance
$-\Delta\alpha/\alpha$	optically induced change of absorption coefficient
θ_d	divergence angle
κ	propagation losses
Λ	grating period
λ	light wavelength
λ_{ASE}	ASE emission wavelength
λ_{DFB}	DFB laser emission wavelength
λ_{pump}	pump wavelength
ν	light frequency
σ_{ij}	absorption cross-section of transition $\|i\rangle \rightarrow \|j\rangle$
σ_{ji}	stimulated emission cross-section of transition $\|i\rangle \rightarrow \|j\rangle$
$\tau_{1/2}$	photostability half-life
τ_i	lifetime of state $\|i\rangle$
τ_{ji}	lifetime of transition $\|j\rangle \rightarrow \|i\rangle$
τ_{PL}	photoluminescence lifetime
τ_{rad}	radiative lifetime
ϕ_{PL}	photoluminescence quantum yield
ω	light angular frequency

Introduction

Since the first experimental demonstration of laser emission by Theodore H. Maiman in 1960,[1] this technology has undergone an unprecedented expansion, becoming part or our daily life. Indeed, the term LASER (Light Amplification by Stimulated Emission of Radiation) has become an everyday word with the pass of time and now lasers are used in a wide set of areas including telecommunications, industrial manufacturing, laser surgery or high-precision instrumentation, among others. The study of the laser and its applications is a multidisciplinary field, which relied originally on physics, chemistry and materials science; but nowadays, it is also part of photonics, nanotechnology, biomedical engineering, and much more. After so many years, laser research is still today a burgeoning research field with more than sixty thousand research articles published during the year 2020. Its relevance is such that discoveries or inventions to the laser has been awarded, among direct and indirect nominations, at least thirty-eight times with the Nobel Prize, though, paradoxically, T. H. Maiman never was awarded one.[2]

Lasers based on organic active media have attracted great attention for many years, mainly because they enable wavelength tuning across the visible spectrum, but recently because they offer the possibility for compactness, mechanical flexibility and low-cost production.[3,4] Particular, many efforts have been centred on thin-film organic lasers (TFOLs), arriving at the point in which these devices can be pumped with low-power optical sources and very recently even electrically.[5] With regards to applications, organic lasers have already demonstrated potential in various areas. For example, as tunable sources for Spectroscopy,[6,7] amplifiers for optical communications,[8] vapour explosive chemical sensors[9] and highly sensitive and possibly specific non-intrusive label-free sensors for drug discovery, biological research, diagnostic tests, food safety, etc.[10–14] Indeed, TFOLs present a great potential in the area of biomedicine, for the detection or monitoring of a wide range of diseases. The early identification of disease biomarker proteins is crucial to have a good diagnosis and to improve treatment success.

The development of these applications is propelled by the advances in materials science, particularly with the development of novel organic compounds. Interestingly, the properties of organic molecules depend not only on their composition, but also on how their atoms are arranged (i.e. on the size and shape of the molecule).[15] Therefore, the smart design of materials with tailored optoelectronic properties becomes possible through bottom-up synthesis techniques used in organic chemistry, which provide the means for obtaining the compounds with outstanding precision and reproducibility.[16,17] Additionally,

photophysical studies and computational models are needed for understanding the actual relationship between the different molecular characteristics and the optoelectronic properties. In this concern, the connection between many of the molecular physical characteristics (e.g. the molecular edge and shape or the core twist) and the optical gain properties remains still unknown,[18] which is limiting the further development of practical applications. Indeed, there are still important aspects from the point of view of the organic materials that need to be assessed in order to bring TFOL applications at a level of commercialization.

At first sight, the desirable material should be simultaneously processable by low-cost solution-based methods, photostable and energetically efficient, at least as to enable pumping with compact sources. In this sense, organic compounds dispersed in thermoplastic matrixes, prepared as thin-film waveguides, are among the more photostable materials used for this purpose and have demonstrated to be efficient materials. However, there is still plenty of room for improving the energetic requirements by optimizing the waveguide performance. Additionally, the understanding of the photodegradation mechanisms might lead to an improvement of the already high stability.

Furthermore, there is a growing interest in materials operating in the near-infrared (NIR) region[19] fuelled by the development of biomedical[20] and telecommunication applications.[21] Up to date, only a few organic lasers have been demonstrated in the range beyond 700 nm,[4,19] mainly a consequence of the detrimental effect of fast non-radiative decay following the energy gap law,[22,23] concentration quenching mechanisms[24] and intra-gap absorption of charge-transfer (CT) and triplet states.[8,25] Hence, a proper understanding of such mechanisms and how to prevent them might lead to a new generation of NIR organic emitters. In this regard, there are emerging materials which offer a great promise for light-emitting devices and integration with other technologies, whose knowledge is at an infant level. That is the case of nanographenes (NGs).

The main objective of this thesis is to study the photophysical properties of organic molecules dispersed in inert matrixes with the scope of improving their performance as laser materials. In this regard, several actuations have been performed: *i*) systematic investigation of two commercial thermoplastic polymers (polystyrene, PS; and poly(methyl methacrylate), PMMA) as inert matrixes to disperse perylenediimide (PDI) compounds with a mayor focus on optimizing the waveguide properties and reducing the operational energy requirements of the devices; *ii*) get insights on the photodegradation and concentration quenching mechanisms of PDI compounds dispersed in PS films with the aim of obtaining more lasting and efficient devices; and *iii*) studying the photophysical properties of novel NG compounds dispersed in inert matrixes with the purpose of elucidating the relationship between their structure (edge, heteroatoms, substituents) and their optical gain performance.

This thesis dissertation is organized around three main blocks plus some concluding remark:

First, an introduction divided in two chapters. The fundamental photophysics principles for light amplification in organic molecules are presented in chapter 1, including also the operational working principles of the devices used for the materials'

characterization, i.e. planar waveguides and distributed feedback (DFB) lasers. The second chapter provides an updated bibliographic compendium of the organic compounds used as gain media, to establish the frame to set the motivation and objectives of this thesis.

Next, the procedures adopted for the samples' manufacture and characterization are fully explained in chapter 3. Practically, all the samples analysed in the development of this thesis are planar waveguides used for the materials' characterization, although there are also some DFB lasers used to demonstrate the convenience of these materials for practical applications. The characterization techniques have been divided in three categories, namely, steady-state optical properties, transient photophysical properties and lasing studies. The standard optical characterization and the amplified spontaneous emission (ASE) and lasing experiments were performed at the University of Alicante (UA), whereas the transient absorption (TA) and time-resolved photoluminescence (TRPL) experiments were performed during the three-moths stay at the Politecnico di Milano or in collaboration with the University of Vilnius.

In third place, results are presented in two separated parts according to the organic materials analysed in them. Chapter 4 gathers all the studies performed with PDI compounds, whilst those performed with NGs are presented in chapter 5.

Finally, the thesis dissertation concludes with a summary of the main results and a prospective for the further development of the treated topics.

Chapter 1
Photophysics Fundamentals

Laser radiation consists of photons oscillating in phase that propagate with high directionality forming a beam, i.e. with a high degree of temporal and spatial coherence. To achieve this kind of light, laser devices are built following a scheme of three fundamental elements (see Figure 1.1): *i*) an active medium, in which the electromagnetic radiation can be amplified; *ii*) a pumping source that supply the active medium with the energy needed for the amplification; and *iii*) an optical cavity or resonator that provides the optical feedback to optimize the amplification and determine the temporal and spatial coherences.

The theoretical bases for the development of the thesis are laid through this chapter, which articulates in five sections. In first place, the basic radiation-matter interactions that give rise to laser radiation are described in Section 1.1. Section 1.2 deals with the characteristics of the medium needed to generate the light amplification, the principal models and the basic method to study the amplification properties of active media. Next, organic molecules are introduced in Section 1.3, as suitable candidates for lasing, and the working principles of the planar waveguides used for the materials characterization in Section 1.4. Finally, the role of the laser resonator is presented in Section 1.5 with particular emphasis in DFB resonators.

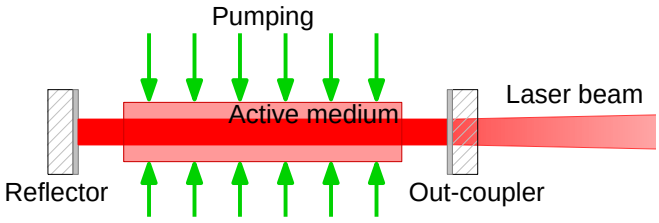

Figure 1.1 Basic laser architecture.

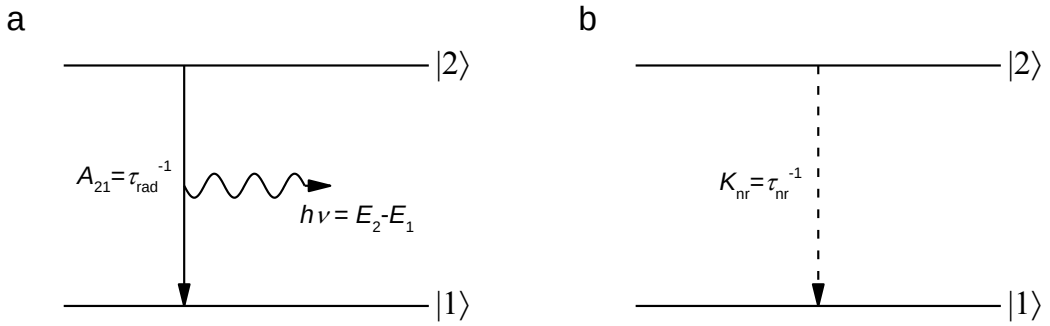

Figure 1.2 Two-level system spontaneous transitions. (a) Radiative decay or spontaneous emission and (b) non-radiative decay.

1.1 Basic Light-Matter Interactions

In 1900, Max Planck derived the expression for the intensity spectral distribution of the black-body emission, using for the first time, the concept of quanta (photon). In the same line, Albert Einstein postulated in 1905 the quantization of the electromagnetic energy to explain the photo-electric effect. Niels Bohr was inspired by both works when he presented in 1913 his atomic model, in which electrons could only stay in fixed energy levels and exchange quanta of energy with the outside world. Let us consider a two-level system formed by two electronic levels or states, with energies E_1 and E_2. According to Bohr, two phenomena could happen: *i*) the absorption of one photon with energy $h\nu = E_2 - E_1$ and subsequent promotion of an electron from the state $|1\rangle$ to state $|2\rangle$; and *ii*) the decay of an electron in the exited state $|2\rangle$ to the state $|1\rangle$ by emitting a photon with the same energy as before. Complementary, Albert Einstein presented its quantum theory of radiation in 1917, where he postulated the existence of an alternative de-excitation channel, the so-called stimulated emission (SE). This process requires the existence of an external electromagnetic field resonant with the electronic transition ($h\nu$) that would interact with the excited system, thus provoking its decay by emitting a photon ($h\nu$). Although, these three are the more elementary phenomena describing light-matter interaction, they are also at the base of the laser emission, as it is described next.

1.1.1 Spontaneous Emission

According to statistical physics, a two-level system in its excited state is out of equilibrium and, eventually, decays back to its ground state by emitting a photon ($h\nu = E_2 - E_1$), see Figure 1.2a. Then, the emission of such photon is a spontaneous process called spontaneous emission. Typically, this process gives rise to luminescence in materials, termed as photoluminescence (PL) whenever the electrons have been excited optically. Now, let us suppose a material made up of N atoms, each one modelled by a two-level

system. If the number of atoms (population) in the upper state $|2\rangle$ at time t is $N_2(t)$, the rate equation for the decay can be written[26]

$$\frac{dN_2(t)}{dt} = -A_{21}N_2(t) \tag{1.1}$$

where A_{21} is the Einstein coefficient accounting for the probability per unit time that the electron decays from level $|2\rangle$ to level $|1\rangle$, which depends exclusively on the transition. Equation 1.1 can be solved to obtain

$$\begin{aligned} N_2(t) &= N_2(0)\exp(-A_{21}t) \\ &= N_2(0)\exp(-t/\tau_{\text{rad}}) \end{aligned} \tag{1.2}$$

where

$$\tau_{\text{rad}} = \frac{1}{A_{21}} \tag{1.3}$$

and τ_{rad} is the radiative lifetime of the transition $|2\rangle \rightarrow |1\rangle$. Thus, the excited state population decays exponentially with a time constant τ_{rad}. In real systems, other non-radiative mechanisms that depend on the medium surrounding the system might contribute to the electron decay with a probability per unit time $K_{\text{nr}} = \tau_{\text{nr}}^{-1}$ (see Figure 1.2b), in which case the combined probability of the transition ($A_{21} + K_{\text{nr}}$) becomes γ_{21} and the lifetime

$$\tau_{21} = \frac{1}{\gamma_{21}} \tag{1.4}$$

Notice that this last coefficient has dropped the adjective "radiative" to become plainly lifetime, accounting for both, radiative and non-radiative decays.

It is worthy to define the fluorescence quantum efficiency or photoluminescence quantum yield (ϕ_{PL}, PLQY), which is an important parameter for the characterization of active materials, as it provides the proportion of the excited population that contributes to the PL emission. Then, it is defined as the number of fluorescent photons spontaneously emitted on the laser transition ($|2\rangle \rightarrow |1\rangle$) divided by the number of the excited photons in the transition. For the two-level system, it is defined as[27]

$$\phi_{\text{PL}} = \frac{A_{21}}{\gamma_{21}} = \frac{\tau_{21}}{\tau_{\text{rad}}} \tag{1.5}$$

1.1.2 Absorption

As it was previously mentioned, when a radiation field resonant with the electronic transition of the system is present, a photon can be absorbed and its energy transferred to an electron that promotes from state $|1\rangle$ to state $|2\rangle$, see Figure 1.3a. This process is called absorption and, unlike spontaneous emission, it requires external stimulation by the photons field. The rate equation for the absorption process is[26]

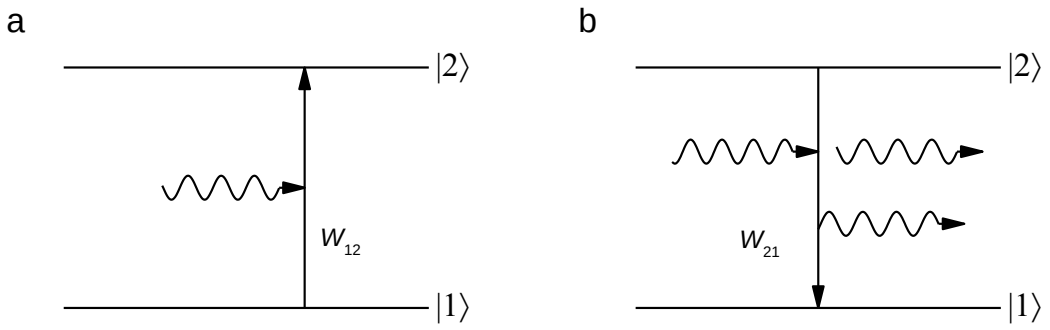

Figure 1.3 Two-level system induced transitions. (a) Absorption and (b) stimulated emission.

$$\frac{dN_1(t)}{dt} = -W_{12}N_1(t) \qquad 1.6$$

where $N_1(t)$ is the population of the ground level at time t of the two-level material and W_{12} is the probability of absorbing a photon per unit time, which depends not only on the particular transition but also on the intensity of the incident beam. It might be useful sometimes to define the absorption rate in terms of the absorption cross-section (σ_{12}) and the photon flux of the incident beam (F)

$$W_{12} = \sigma_{12}F \qquad 1.7$$

In this way, the absorption cross-section depends on the characteristics of the transition, whilst the photon flux contains the information of the incident beam.

1.1.3 Stimulated Emission

Einstein realized that, in addition to spontaneous emission, the system might be induced to decay whenever an external radiation field is present. Thus, he postulated the existence of SE, a process in which the photon field can stimulate downward emission transitions as it does upward in absorption, see Figure 1.3b. In this process a photon can interact with an excited two-level system to induce the emission of an identical copy of itself. The SE rate equation can be written in analogy to that of absorption[26]

$$\frac{dN_2(t)}{dt} = -W_{21}N_2(t) \qquad 1.8$$

where W_{21} is the SE rate, that can be written in terms of the photon flux and the corresponding SE cross-section (σ_{21})

$$W_{21} = \sigma_{21}F \qquad 1.9$$

This process is a coherent quantum mechanical effect, in which the emitted photons are in phase with the photons that stimulate their emission. Thus, as the photons impinging the

system induce the emission of other photons, the number of photons leaving the system is higher than the number of those coming into it.

As it has been presented, the absorption and SE cross-sections (σ_{12} and σ_{21}, respectively) might be different. However, Einstein demonstrated that for a non-degenerated system both rates are always equal

$$W_{12} = W_{21} \quad \text{1.10a}$$

$$\sigma_{12} = \sigma_{21} \quad \text{1.10b}$$

meaning that the probability of absorbing a photon is equal to the probability of stimulating the emission of another, i.e. that both processes are symmetrical.[28]

1.2 Light Amplification by Stimulated Emission

1.2.1 Stimulated Emission for Amplification

In first place, it is illustrated how to use SE to amplify a photon beam as it propagates along the material. Let us suppose a two-level system with initial populations N_1 and N_2 that is illuminated by a beam of light resonant with the transition ($h\nu = E_2 - E_1$), that propagates in the z direction. The photon flux F will experiment a differential change (dF), along the differential length (dz), due to absorption, spontaneous emission and SE, see Figure 1.4. If only the photons propagating along z are considered, the contribution of the spontaneous emission can be neglected because the photons are spontaneously emitted in any direction, hardly contributing to the total flux. If S is the cross-section of the light beam, the change between the impinging photons and those leaving the system is given by SdF, which should be equal to the difference between the absorption and SE events in the volume Sdz, i.e. $(W_{21}N_2 - W_{12}N_1)Sdz$. Then, it is possible to write the following differential equation that models the evolution of the light beam through the two-level material[26]

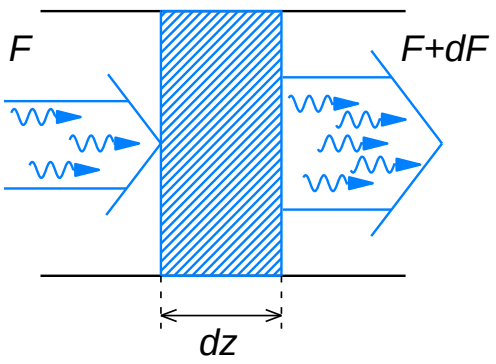

Figure 1.4 Differential change in the photon flux (dF) after traveling a distance dz through the two-level system.

$$dI(z) = (N_2 - N_1)\sigma_{12} I(z) dz \quad 1.11$$

where I is the beam intensity ($I = Fh\nu$). Equation 1.7, 1.9 and 1.10 have been used to derivate this expression, which can be solved to provide

$$I(z) = I_0 e^{(N_2 - N_1)\sigma_{12} z} \quad 1.12$$

with $I_0 = I(z = 0)$, i.e. the intensity impinging the material.

At this point, three particular cases of interest might be considered:[28]

- When $N_1 > N_2$, the material absorbs the impinging light, as there are more atoms in the ground state than in the excited state. Indeed, in the limit $N_2 \to 0$, Equation 1.12 reduces to the Beer-Lambert law for absorption

$$I(z) = I_0 e^{-\alpha z} \quad 1.13$$

  where $\alpha = N_1\sigma_{12}$ is the absorption coefficient.

- When $N_1 = N_2$, the beam intensity keeps constant during propagation. At this point, SE balances absorption. If the spontaneous emission term is taken into account when solving Equation 1.11, a low increase of the number of photons would have been found with z.

- When $N_1 < N_2$, the material amplifies the light propagating through it, as there are more atoms in the excited state than in the ground state. In such a case, the population is said to be inverted. Then, Equation 1.12 can be rewritten

$$I(z) = I_0 e^{g_{\text{net}} z} \quad 1.14$$

  where $g_{\text{net}} = (N_2 - N_1)\sigma_{12}$ is the net gain coefficient

$$g_{\text{net}} = (N_2 - N_1)\sigma_{12} = g - \alpha \quad 1.15$$

  and g the low-signal gain coefficient. This expression predicts an exponential growth of the intensity with z. However, two phenomena limit the growth: the finite population of the excited state and the absorption caused by the atoms in the ground state.

1.2.2 The Two-Level System and the Population Inversion Problem

At this point, it is clear that the SE can be used to amplify an optical signal traveling through a medium, provided its population has been inverted. Therefore, it is worth asking, how is it possible to achieve such population inversion in the medium? In this regard, energy has to be supplied externally to the system, so that ground state electrons are promoted to the excited state, a process known as pumping. Unfortunately, the population of the simple two-level material used in the previous section to illustrate the

basic light-matter interactions cannot be inverted, when its constituents are in thermal equilibrium. Electrons follow the Fermi-Dirac statistic[28]

$$\frac{N_2}{N_1} = \frac{1}{e^{\Delta E/k_B T} + 1} \tag{1.16}$$

where $\Delta E = E_2 - E_1$ is the energy difference between levels $|1\rangle$ and $|2\rangle$. The population ratio also goes to 0 when the temperature $T \to 0$ K, meaning that all the electrons are in the ground state. On the other hand, if $T \to \infty$, the population is equally share between the ground and excited states, becoming impossible the thermal inversion of the two-level system population. Something similar happens when a two-level system with most of the electrons in the ground state ($N_2/N_1 \sim 0$) is illuminated with a beam of photons, optically pumped. At the beginning, absorption predominates over SE in the system and electrons are promoted to the excited state as photons are absorbed. However, as the population of the excited state grows, so it does the SE contribution, thus the electrons return back to the ground state. Eventually, both processes compensate and the system reaches its equilibrium ($N_2/N_1 = 1/2$). Thus, the population inversion of the two-level system by optical pumping is unfeasible. In the following section, the problem is solved by introducing three- and four-level systems.

1.2.3 Three- and Four-Level Systems

Although, the simple two-level system retains its academic interest, most real electronic structures present in nature are constituted of many states. Fortunately, all they can be modelled either as three- or four-level systems, see Figure 1.5. These two models can maintain an inverted population between certain transitions (the laser transitions), being suitable for amplification. Each system has particular requirements for reaching the population inversion, which can be compared.

Let us start by describing the four-level system first, in which a population inversion can be built between levels $|2\rangle$ and $|3\rangle$, see Figure 1.5b. This transition is therefore known as the lasing transition. Initially, electrons in the ground state $|1\rangle$ are excited to state $|4\rangle$ by optical pumping with pump fluence F_{pump}. Notice that, at the same time, the pump stimulates downward transitions between states $|4\rangle$ and $|1\rangle$. The rate equations for the system are written[27]

$$\begin{aligned} \frac{dN_4}{dt} &= W_p(N_1 - N_4) - N_4(\gamma_{41} + \gamma_{42} + \gamma_{43}) \\ &= W_p(N_1 - N_4) - N_4/\tau_4 \end{aligned} \tag{1.17a}$$

$$\begin{aligned} \frac{dN_3}{dt} &= -N_3(\gamma_{31} + \gamma_{32}) + N_4\gamma_{43} \\ &= -N_3/\tau_3 + N_4/\tau_{43} \end{aligned} \tag{1.17b}$$

$$\begin{aligned} \frac{dN_2}{dt} &= -N_2\gamma_{21} + N_3\gamma_{32} + N_4\gamma_{43} \\ &= -N_2/\tau_{21} + N_3/\tau_{32} + N_4/\tau_{43} \end{aligned} \tag{1.17c}$$

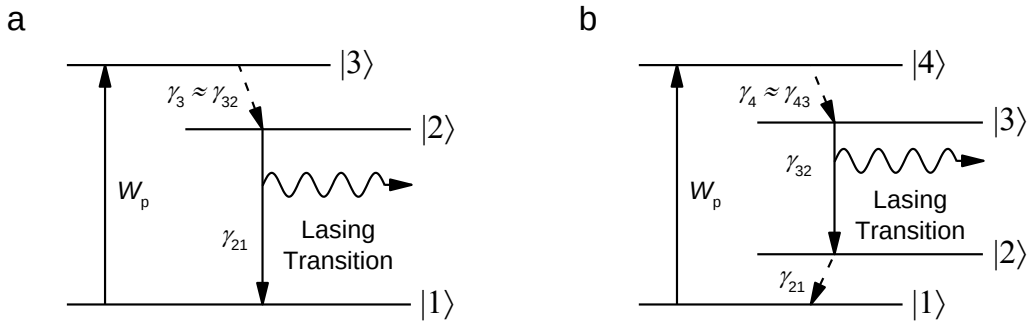

Figure 1.5 Energetic structure of lasing models. (a) Three-level system and (b) four-level system.

where the stimulated pump transition probability $W_p = F_{pump}\sigma_{14}$ and the level lifetimes $\tau_3 = \gamma_3^{-1} = (\gamma_{31}+\gamma_{32})^{-1}$ and $\tau_4 = \gamma_4^{-1} = (\gamma_{41}+\gamma_{42}+\gamma_{43})^{-1}$ have been introduced. In the dynamical steady-state, each state population is conserved over time ($dN_m/dt = 0$). Then, the relative population between levels $|4\rangle$ and $|3\rangle$ can be determined from Equation 1.17b

$$\frac{N_3}{N_4} = \frac{\tau_3}{\tau_{43}} \tag{1.18}$$

which can be inserted in Equation 1.17c to determine the population ratio between the lasing levels $|3\rangle$ and $|2\rangle$

$$\eta_{23} = \frac{N_2}{N_3} = \frac{\tau_{21}}{\tau_{32}} + \frac{\tau_{43}\tau_{21}}{\tau_{42}\tau_3} \tag{1.19}$$

In the good laser material, this parameter is less than unity, resulting in the population inversion between the lasing levels. The condition is satisfied whenever: *i*) the population of level $|4\rangle$ decays mainly through the transition $|4\rangle \rightarrow |3\rangle$, i.e. $\tau_{42} \gg \tau_{43}$; and *ii*) such relaxation is faster than the level $|3\rangle$ spontaneous decay, $\tau_3 \gg \tau_{43}$. Then, the condition for population inversion become

$$\eta_{23} \approx \frac{\tau_{21}}{\tau_{32}} \ll 1 \tag{1.20}$$

Consequently, the optimal laser material might present a short-living lower laser level $|2\rangle$ and stable upper laser level $|3\rangle$ in order to optimize the population inversion.

Additionally, the PLQY is defined as the number of fluorescent photons spontaneously emitted on the laser transition ($|3\rangle \rightarrow |2\rangle$) divided by the number of pumped photons that pass through the upper lasing transition when the system is below threshold[27]

$$\phi_{PL} = \frac{\gamma_{43}}{\gamma_4} \times \frac{A_{32}}{\gamma_3} = \frac{\tau_4}{\tau_{43}} \times \frac{\tau_3}{\tau_{rad}} \tag{1.21}$$

This is an important parameter for the characterization of the laser performance, as it provides the proportion of the excited population that contributes to the laser emission.

Finally, it is possible to find out the difference of population between levels $|3\rangle$ and $|2\rangle$ by using η_{23}, ϕ_{PL} and the conservation of energy ($N = N_1 + N_2 + N_3 + N_4$)[27]

$$\frac{N_3 - N_2}{N} = \frac{(1-\eta_{23})\phi_{\mathrm{PL}} W_p \tau_{rad}}{1 + (1 + \eta_{23} + 2\tau_{43}/\tau_{rad})\phi_{\mathrm{PL}} W_p \tau_{rad}} \qquad 1.22$$

The perfect laser material fulfils two important conditions: *i*) the population excited to level $|4\rangle$ should relax very quickly to state $|3\rangle$, so that $\eta_{23} \rightarrow 0$; and *ii*) the excited population should majorly relax radiatively, so that $\phi_{\mathrm{PL}} \rightarrow 1$. In such limit, the expression for the population inversion becomes

$$\frac{N_3 - N_2}{N} \approx \frac{W_p \tau_{rad}}{1 + W_p \tau_{rad}} \qquad 1.23$$

In the case of the three-level system, it is possible to maintain an inverted population between their states $|2\rangle$ and $|1\rangle$, see Figure 1.5a. The rate equations for the three-level system can be written[27]

$$\frac{dN_3}{dt} = W_{\mathrm{p}}(N_1 - N_3) - N_3(\gamma_{31} + \gamma_{32}) = W_{\mathrm{p}}(N_1 - N_3) - N_3/\tau_3 \qquad 1.24a$$

$$\frac{dN_2}{dt} = -N_2\gamma_{21} + N_3\gamma_{32} = -N_2/\tau_{21} + N_3/\tau_{32} \qquad 1.24b$$

where Equation 1.24b, in the dynamic steady-state, becomes

$$\eta_{32} = \frac{N_3}{N_2} = \frac{\tau_{32}}{\tau_{21}} \qquad 1.25$$

Additionally, the PLQY for the three-level system is defined as[27]

$$\phi_{\mathrm{PL}} = \frac{\gamma_{32}}{\gamma_3} \times \frac{A_{21}}{\gamma_{21}} = \frac{\tau_3}{\tau_{32}} \times \frac{\tau_{21}}{\tau_{\mathrm{rad}}} \qquad 1.26$$

where the radiative transition corresponds to the laser transition ($|2\rangle \rightarrow |1\rangle$). Following the previous analysis, the difference of population between levels $|2\rangle$ and $|1\rangle$ is found in terms of η_{32} and ϕ_{PL}, by using the conservation of energy ($N = N_1 + N_2 + N_3$)[27]

$$\frac{N_2 - N_1}{N} = \frac{(1-\eta_{32})\phi_{\mathrm{PL}} W_p \tau_{rad} - 1}{(1 + 2\eta_{32})\phi_{\mathrm{PL}} W_p \tau_{rad} + 1} \qquad 1.27$$

The optimal three-level system fulfils the conditions $\eta_{32} \rightarrow 0$ and $\phi_{\mathrm{PL}} \rightarrow 1$ and the expression for the population inversion becomes

$$\frac{N_2 - N_1}{N} \approx \frac{W_p \tau_{rad} - 1}{W_p \tau_{rad} + 1} \qquad 1.28$$

Although, an inverted population can be built in both systems, the four-level system is more efficient. Indeed, the expressions for the population inversion found for the optimal cases (Equation 1.23 and 1.28) indicate that, whilst certain pump intensity is needed to bring the three-level system to population inversion, any pump intensity will result in the population inversion of the four-level system. Thus, laser media that can be modelled by a four-level system are preferred upon those based in the three-level system.

1.2.4 Amplified Spontaneous Emission

Once its population has been inverted, the system is prepared for amplifying an incident light beam, as just stated. Interestingly, this amplification process can be triggered by the system spontaneous emission, resulting in its amplification. The phenomenon is known as amplified spontaneous emission (ASE) and can be observed in certain active materials (typically with very large gain coefficients and with one of the dimensions larger than the other) in absence of any laser cavity. Thus the ASE is useful to assess the amplification properties of the medium. The observation of ASE is a clear signature of the existence of gain, thus it is useful to identify and assess the potential of a given material to be used as an active medium for lasing. However, it shows only moderate coherence and directionality and it is not real lasing since there is no laser cavity, and therefore no lasing modes.

For studying these properties, let us consider a cylindrically-shaped active medium of diameter D and length l and let Ω_0 be the solid angle subtended by one facet of the cylinder from the centre of the opposite facet, see Figure 1.6. If the population inversion is large enough, the spontaneous emission coming from the emitters at one extreme of the cylinder into the solid angle Ω_0 would be amplified. Then, the existence of directionality is clearly ascertained by the expression of the solid angle[26]

$$\Omega_0 = \frac{\pi D^2}{4l^2} \qquad 1.29$$

which for a narrow and large cylinder ($D \ll l$) tends to 0.

Additionally, the active material is considered to behave as an ideal four-level system ($N_2 \sim 0$) operating in the low-signal regime (i.e., the inverted population is not saturated by the ASE intensity). Under such assumptions, if $I_{\mathrm{ASE}}(z, \nu)$ is the ASE intensity at coordinate z and the beam propagates in the positive z-direction, the intensity differential (dI_{ASE}) can be written following the same train of thought used for deducing Equation 1.11[26]

$$dI_{\mathrm{ASE}}(z,\nu) = \left[(N_2 - N_1)\sigma_{32} I_{\mathrm{ASE}} + N_2 A_{32} \frac{\Omega(z)}{4\pi}\right] dz \qquad 1.30$$

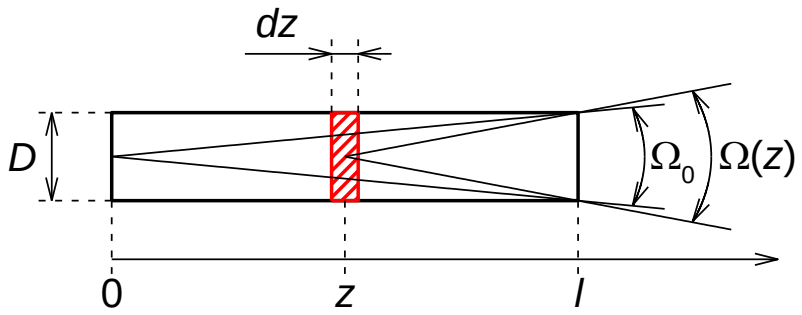

Figure 1.6 Amplified spontaneous emission in an active material. The medium consists of a cylinder of diameter *D* and length *l*. The light travels through the *z*-coordinate, leaving the medium within the solid angle $\Omega(z)$ that depends on the position at which the light was emitted with $\Omega_0 = \Omega(0)$.

where the first and second terms in the right hand side of the equation correspond respectively to the SE and spontaneous emission contributions arising from the element *dz*. Equation 1.30 have to be integrated over the *z*-coordinate to determine $I_{\mathrm{ASE}}(l,\ \nu)$. As much of the ASE originates at $z = 0$, the solid angle Ω can be supposed to be *z*-independent ($\Omega(z) \sim \Omega_0$) and approximately equal to Equation 1.29. Then, Equation 1.30 can be integrated using the boundary condition $I_{\mathrm{ASE}}(0,\nu) = 0$ to obtain[29]

$$I_{\mathrm{ASE}}(l,\nu) = \frac{\Omega_0}{4\pi} A_{32} I_{pump} \frac{(e^{g_{net} l} - 1)}{g_{net}} \qquad 1.31$$

where $I_{\mathrm{pump}} = F_{\mathrm{pump}} h\nu$ is the pump intensity. Additionally, Equation 1.15 has been used to write Equation 1.31 in terms of the g_{net}. Thus, the system exhibits a threshold-like behaviour with the pump intensity, which is implicit in the g_{net}. While the pumping is maintained below the threshold, the gain cannot compensate the system losses and I_{ASE} responds linearly with I_{pump}. However, as soon as I_{pump} is sufficiently large for the gain to overcome the system losses ($g_{\mathrm{net}} > 0$), I_{ASE} grows exponentially. The turning point ($g = \alpha$) is defined as the ASE threshold.

Furthermore, not all the frequencies are amplified in the same proportion. The ones close to the transition frequency ($h\nu = E_3 - E_2$) would be amplified with more probability. Thus, the original spontaneous emission (i.e. the PL spectrum) collapses into a narrow peak centred at the transition frequency, wavelength (λ_{ASE}), that is the ASE peak.

1.3 Organic Molecules as Lasing Media

As stated in the introduction, this thesis deals with the laser properties of organic compounds, which are based on covalently-bonded carbon atoms. The importance of carbon relies in its electronic configuration ($1s^2\ 2s^2\ 2p^2$) with four valence electrons in its

outer shell, capable of forming single, double or triple bonds. Owing to this capability, carbon atoms can be combined to form myriads of different compounds with varying properties. The valence electrons in molecules with double and triple bonds are divided between σ and π orbitals, with orbitals of the first kind being formed also between single bonded carbon atoms. Organic molecules with alternating multiple and single bonds are said to be π-conjugated and the π-electrons in them are spread out in large delocalized π-orbitals, in contrast to the more localized electrons in the σ-orbitals.

1.3.1 Electronic States

Upon the formation of an organic molecule, the electronic orbitals of the individual components are combined to create the molecular orbitals. Each of these orbitals can be thought as an electronic state, which has an associated energy. The electronic structure resulting from the formation of the molecule is occupied in order of increasing energy. Two important levels are the higher occupied molecular orbital (HOMO) and the lowest unoccupied molecular orbital (LUMO), which determine the so-called optical gap of the molecule. In conjugated molecules, the HOMO is a π state because the σ-electrons are very tightly bounded, being filled first. Then, the LUMO corresponds to an excited configuration of the π-orbital, labelled as π^*, and the fundamental transition is of $\pi \rightarrow \pi^*$ nature.[30]

The electrons in the molecule ground state (i.e. the HOMO) are all paired with their spins anti-parallel, i.e. with the spin quantum number $S = 0$. However, the electrons in the excited states do not have to be paired and, accordingly, can have $S = 0$ or $S = 1$. These states are named after their spin multiplicity $(2S+1)$ as singlet and triplet states, respectively. Theoretically, since photons carry no spin, the optical transitions can occur only between states of the same spin and, in consequence, the absorption and PL spectra of conjugated molecules are dominated by the singlet–singlet transitions. However, singlet–triplet transitions can also take place in real systems, although with a lower probability.

1.3.2 Vibronic Coupling

Typically, the electronic states of organic molecules are coupled with their nuclear vibrational modes, leading to vibronic transitions (i.e. vibrational–electronic). The atoms in a molecule can vibrate around their positions of equilibrium, giving an extra energy to the molecule that is added to its electronic energy. According to quantum mechanics, only certain vibrational modes are possible and therefore a discrete number of vibrational levels are associated to each electronic state.

The vibronic spectrum of organic molecules can be understood in more detail by introducing the configuration diagram, see Figure 1.7. In these representations, the electronic energy of the molecule is shown as a function of the relative positions between atoms or configuration coordinates (Q). Initially, the Born-Oppenheimer approximation is used to determine the dependency of the electronic levels upon the variation of Q. Since the nuclear vibrations and electronic motion occurs in a different time scale, their movements

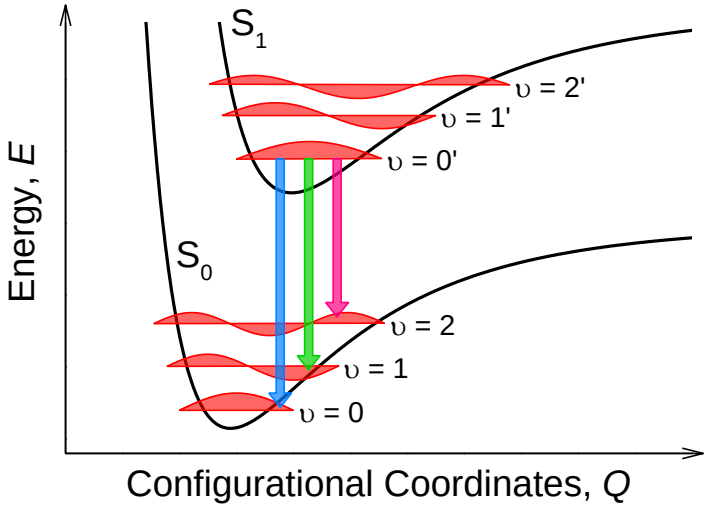

Figure 1.7 Configuration diagram of a diatomic molecule.

can be considered separately, i.e. their wave functions are separable, and the electronic energy can be calculated by fixing Q.[31]

The configuration diagram of a simple diatomic molecule is represented in Figure 1.7 to illustrate the physics behind these representations. Here, the singlet ground state ($|S_0\rangle$) and first excited state ($|S_1\rangle$) are shown. At large interatomic distances ($Q \rightarrow \infty$), the states retrieve the single atom character. On the other hand, when the interatomic distance gets reduced below a certain distance ($Q \rightarrow 0$), a repulsion force appears. Between both limits, the electronic energy presents a minimum that corresponds to the equilibrium distance (Q_0) in the absence of oscillations. Notice that the different electronic configuration of the excited state displaces the equilibrium toward larger distances (Q_0^*).

Once the electronic levels are known, it is possible to calculate the vibrational energies associated to each level. Let us suppose that atoms are released at the position $Q \neq Q_0$. The restoring forces will make the atoms oscillate around their position of equilibrium, generating a set of vibrational states. Thus, the vibronic state will be described by the electronic quantum number (n) and the vibrational quantum number (υ), and its energy will be the sum of both contributions. For small oscillations around Q_0, the electronic level can be approximated by a parabola and the solutions will be those of the harmonic oscillator, i.e. a set of uniformly spaced states. However, in the general solution, the separation between states depends on the shape of the electronic potential and the population of vibrational states becomes denser as υ increases.

1.3.3 Absorption and Emission Spectra

Optical transitions between vibronic states give rise to the absorption and emission spectra of molecules and, therefore, studying the spectral properties of the molecules implies studying its transitions. As it was assumed before, the electronic motion happens in a shorter time scale than the atoms vibration. Under such approximation, the transitions

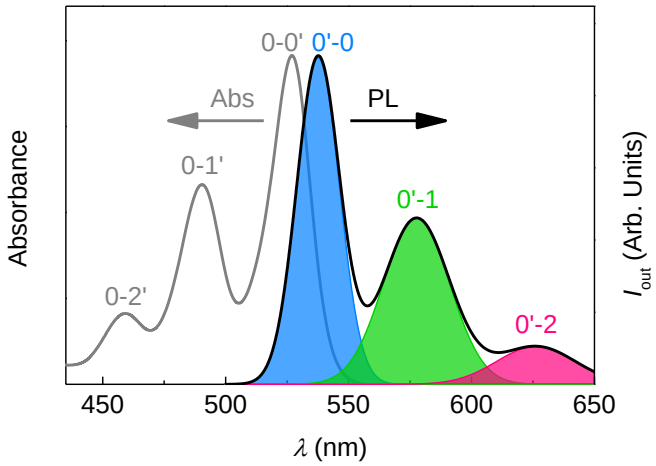

Figure 1.8 Organic molecule spectra. Absorption (grey line, left axis) and spontaneous emission (photoluminescence PL; black line, right axis) spectra. The corresponding vibronic transition is indicated over each peak. The PL spectrum has been decomposed in the corresponding vibronic transitions, which are represented with the same colours in Figure 1.7.

follow the Franck-Condon principle,[26,31] which states that the nuclear separation does not change during vibronic transitions.

Let us suppose a molecule in the first vibronic state of its ground electronic state with average configuration coordinates Q_0. The absorption of a photon will promote an electron to the excited state without changing the configuration coordinates of the system. After the transition, the molecule will be in its excited state and its atoms will be out of their equilibrium position (Q_0^*). Then, the atoms of the molecule will relax quickly to Q_0^* and, eventually, the molecule will decay by emitting a photon, also without changing its configuration coordinates. So, the molecule is left in its ground state but out of equilibrium. Quickly, the molecule's atoms will relax by coming back to Q_0 and the cycle is closed.

Under such a picture, the transition probabilities, and therefore the peaks in the absorption and emission spectra, are proportional to the square of the overlapping integral between vibronic states, the so-called Franck-Condon factors.[31]

Let us start with the interpretation of the absorption spectrum. Thermal energy (0.025 eV) is typically lower than the separation between vibronic levels (~ 0.1 eV), meaning that a molecule in thermal equilibrium will be in the first vibronic level of its ground electronic state. Then, the intensities of the absorption peaks are proportional to the overlapping between first vibronic level of the ground electronic state and the different vibronic levels of the excited state, resulting in the typical vibronic progression shown in Figure 1.8. The peaks are named in the order that appear from higher to lower energies, i.e. first vibronic, second vibronic, etc.

According to Kasha's rule,[31] emission takes place from the first vibronic of the excited state to any vibronic state of the ground electronic state. The reason is that independently of the originally excited vibronic state, the atoms will relax to their new

equilibrium positions right after the excitation by dissipating their vibrational energy into the surrounding medium. This phenomenon is known as internal conversion (IC) and relies in the fact that non-radiative transitions ($\tau_{IC} \sim 0.1–1$ ps) are much faster than radiative ones ($\tau_{rad} \sim 1–10$ ns). The intensities of the emission peaks are therefore proportional to the overlapping between the first vibronic of the excited state and the various vibronic levels of the ground state. The emission spectrum obtained under these conditions is a mirror-like reproduction of the absorption spectrum, see Figure 1.8. Notice the separation between the absorption and emission first vibronics, termed Stokes shift, which is a consequence of the different equilibrium configurations of the ground and excited states. Indeed, rigid molecules present a reduced Stokes shift according to the reduced configurational change between their ground and excited states.[30]

1.3.4 Organic Molecules as Four-Level Systems

Conjugated organic molecules are excellent candidates for lasing applications owing to their energy level structure, which can be modelled as a four-level system. The dynamics of the system can be understood more easily with the introduction of Jablonski diagrams that represent in a more straightforward way the energy structure at the expense of configurational information, see Figure 1.9. To begin with, an active material formed by N isolated molecules at thermal equilibrium is considered, i.e. N molecules in the first vibronic of the ground electronic state ($|S_0,\ v = 0\rangle$). This state performs the role of the four-level system state $|1\rangle$ described in Section 1.2.3. From there, the active molecule can be excited to any vibronic of the excited state ($|S_1,\ v\rangle$) by optical pumping in resonance with the corresponding optical transitions, to immediately decay to the first vibronic of the excited electronic state ($|S_1,\ v = 0\rangle$) by IC. These states correspond, respectively, to the states $|4\rangle$ and $|3\rangle$ of the analogous four-level system. Eventually, the active material can decay radiatively to any vibronic of its ground electronic state ($|S_0,\ v\rangle$) and from there to

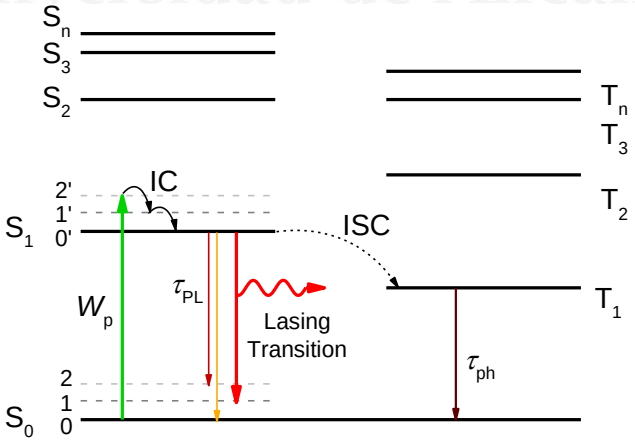

Figure 1.9 Organic molecule Jablonski diagram.

the first vibronic of the ground state ($|S_1,\ v = 0\rangle$), again by IC. If the first vibronic is playing the role of the four-level system ground state, any other vibronic can act as the state $|2\rangle$.

Considering this association of states and the previous discussion on the four-level system (Section 1.2.3), it is possible to demonstrate that organic molecules behave in fact as excellent four-level systems. As stated in Section 1.2.3, for the four-level system to operate under optimal circumstances, two conditions should be fulfilled: *i*) the parameter η_{23} should be negligible, ($\eta_{23} \to 0$); and *ii*) the system should have high PLQY ($\phi_{PL} \to 1$). According to the previous discussion, the lifetimes τ_4, τ_{43} and τ_{21} are of the order of the characteristic times for IC (0.1–1 ps) and τ_3, τ_{32} and τ_{42} are of the order of radiative transitions (1–10 ns). Thus, both operative conditions are corroborated by introducing these lifetimes in Equation 1.19 and 1.21, which demonstrate that conjugated organic molecules can be implemented successfully as four-level systems.

1.3.5 Intersystem Crossing and Pulsed Pump

Still today, organic lasers present an important issue hampering their operation in continuous wave mode. As stated before, despite being spin-forbidden, singlet–triplet transitions can take place in real systems. The radiation-less transition from a singlet excited state ($|S_n\rangle$) into a triplet state ($|T_n\rangle$) can occur assisted by spin-orbit coupling ($|S_n\rangle \to |T_n\rangle + \Delta E$), which is known as intersystem crossing (ISC). The ISC rate in planar organic molecules ($k_{ISC}^{-1} \sim 0.1–100$ µs) is typically much lower than the radiative decay ($\tau_{PL} \sim 1–10$ ns). ISC is therefore very unlikely, compared to radiative decay. Something similar happens with phosphorescence, in which the system passes from the ground triplet state ($|T_1\rangle$) to the ground singlet state ($|S_0\rangle$) by emitting a photon ($|T_n\rangle \to |S_0\rangle + h\nu$). The typical phosphorescence lifetimes are also in the order of ISC rates (µs to s). Hence, an excited electron undergoing ISC kept trapped for quite a long term in the triplet state without contributing to the SE. Indeed, ISC becomes sizable in an organic active material under continuous wave pumping that maintains permanently excited its population, even precluding the light amplification.[26] Furthermore, triplet states can react with molecular oxygen resulting in the deterioration of the organic molecule.

All this detrimental effect can be prevented with the use of pulsed pumping. The ISC can be minimized by exciting the population with a brief light pulse comparable or shorter than the fluorescence lifetime. Thus, the excited electrons are exposed to suffer ISC only during a time equal to the lifetime. The pulses might additionally be spaced a time larger than the phosphorescent lifetime, allowing the reduced number of triplets generated during the previous pulse to decay back to the ground singlet state before the next pulse arrives. In this way, all the electrons are available to be used during each excitation cycle.

1.4 Waveguides Theory

The amplification properties of organic materials can be conveniently analysed by characterizing optical waveguides fabricated with them. As it was stated in Section 1.2.4, ASE can be observed whenever the light being amplified propagates preferentially in a certain direction; for example, if the active material is shaped as a cylinder. Such is the case for light propagating in a waveguide, which consist of optical structures that confine light within their boundaries by total internal reflection. The light confinement allows maintaining high optical densities than can be guided across the waveguide. Particularly, waveguides fabricated out of or containing active materials, called active waveguides, can be used to generate or amplify optical signals that propagate in them. Therefore, the amplification of an active material, e.g. conjugated organic molecules, can be studied by analysing the outcome of an active waveguide containing it. This method optimizes the collection of the generated light, while the high optical density facilitates obtaining ASE. Additionally, active organic molecules can be dispersed in inert waveguides to study their properties in absence of detrimental concentration effects.

Optical waveguides are classified according to their geometry in planar waveguides, channel waveguides and optical fibres. Planar waveguides confine the light only in one direction, letting it propagate in the other two. Channel waveguides and optical fibres confine light in two dimensions allowing the propagation in the remaining one. The difference between them is that optical fibres have cylindrical symmetry in the confinement plane, while channel waveguides present a rectangular section. The waveguides used in this thesis are planar waveguides constituted by films of high refractive index (n_f) surrounded by two homogeneous dielectric media of lower refractive index, cover (n_c) and substrate (n_s), with $n_c < n_s$. Despite being less efficient at confining light, planar waveguides are straightforward to fabricate as stated in Section 3.1.1, and can be easily integrated with a DFB resonator to manufacture a DFB laser, see Section 3.1.2.

1.4.1 Guided Modes

According to ray optics, light propagates in waveguides only for certain angles determined by the conditions of total internal reflection between media, i.e. the critical angle ($\theta_c = \arcsin(n_2/n_1)$, with $n_2 < n_1$), and the interference between light reflected in

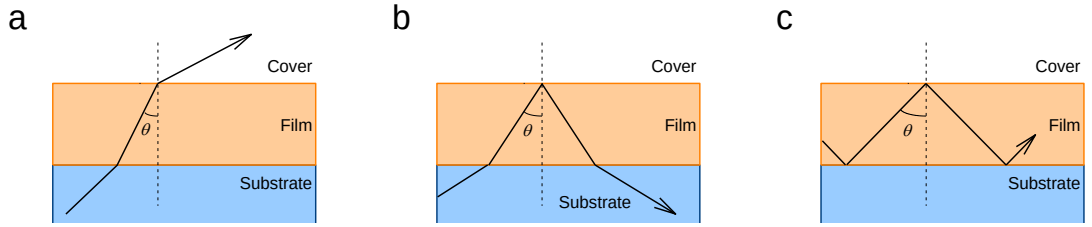

Figure 1.10 Ray path followed by the different modes present in a step-index planar waveguide. (a) Radiation mode, (b) substrate radiation mode and (c) guided mode.

the film-cover and film-substrate interfaces. If light form an angle θ with the normal to the surface, the three cases shown in Figure 1.10 are possible: *i*) when $\theta < \theta_{c,cover}$, light can escape by the substrate and cover interfaces producing a radiation mode; *ii*) when $\theta_{c,cover} < \theta < \theta_{c,substrate}$, light is reflected at the film-cover interface but can be radiated through the substrate ,which is known as a substrate radiation mode; and *iii*) when $\theta_{c,substrate} < \theta < \pi/2$, light kept trapped inside the waveguide producing a guided mode.

The guided modes of a planar waveguide can in turn be divided in two independent sets illustrated in Figure 1.11: *i*) those modes which electric component is exclusively transversal designated as transversal electric modes (TE modes); and *ii*) those modes which electric component is parallel to the propagation direction, their magnetic component is transversal, called transversal magnetic modes (TM modes).

The form and characteristics of guided modes can be understood in more detail by using the electromagnetic theory. Under the assumption of an optically inhomogeneous medium, the wave equation can be derived from Maxwell's equations[32]

$$\nabla^2 \boldsymbol{E} + \nabla\left(\frac{1}{n^2}\nabla n^2 \boldsymbol{E}\right) = \varepsilon_0 \mu_0 n^2 \frac{\partial^2 \boldsymbol{E}}{\partial t^2} \quad 1.32a$$

$$\nabla^2 \boldsymbol{H} + \frac{1}{n^2}\nabla n^2 \times (\nabla \times \boldsymbol{H}) = \varepsilon_0 \mu_0 n^2 \frac{\partial^2 \boldsymbol{H}}{\partial t^2} \quad 1.32b$$

where μ_0 is the free space permeability, ε_0 the free space permittivity, n is the refractive index of the medium, $\boldsymbol{E}$ is the electric field and $\boldsymbol{H}$ is the magnetic field. If the light propagates along z and $n = n(x)$, the solutions for the wave equations (Equation 1.32) are written

$$\boldsymbol{E}(\boldsymbol{r}, t) = \boldsymbol{E}(x) e^{i(\omega t - \beta z)} \quad 1.33a$$

$$\boldsymbol{H}(\boldsymbol{r}, t) = \boldsymbol{H}(x) e^{i(\omega t - \beta z)} \quad 1.33b$$

where ω is the angular frequency and β the propagation constant of the wave. Thus, the problem is reduced to find out the field amplitudes $\boldsymbol{E}(x)$ and $\boldsymbol{H}(x)$ and the propagation constant β. For a given waveguide structure and frequency, there might be several possible solutions of the transversal field distribution or modes, with different β depending on the

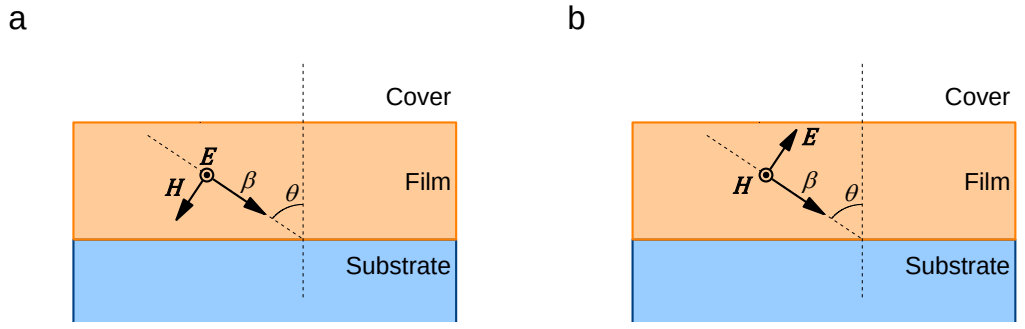

Figure 1.11 Transversal modes propagating in a planar waveguide. (a) Transversal electric (TE) and (b) transversal magnetic (TM) modes. The propagation constant is β.

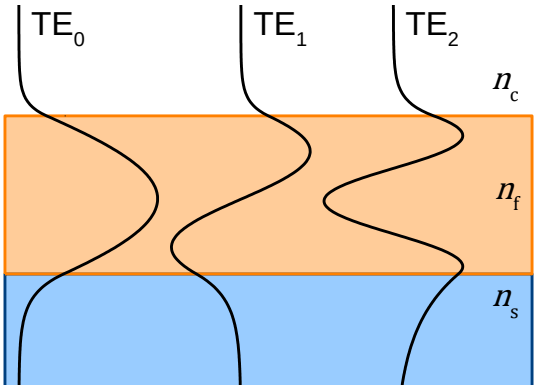

Figure 1.12 Electric field distribution of transversal electric modes in an asymmetric planar waveguide. The refractive indexes of the film (n_f), substrate (n_s) and cover (n_c) fulfil that $n_f > n_s > n_c$.

mode order m. The electric field distribution for the first three TE modes is shown in Figure 1.12. Similar distributions can be found for the magnetic field in the case of TM modes.

In order to understand the meaning of β, it is possible to introduce the effective refractive index (n_{eff}) of the propagating mode that is related with β through

$$\beta = kn_{eff} \qquad 1.34$$

where $k = 2\pi\lambda^{-1}$, λ is the wavelength of light in free space and n_{eff} represent the refractive index experienced by the light in the propagating mode, which is a weighted average of the different indexes of the waveguide attending to the portion of light traveling in each one. Indeed, for a propagating modes the effective refractive index fulfils that $n_f > n_{eff} > n_s$, being physically impossible to find a $n_{eff} > n_f$. On the other hand, $n_{eff} < n_s$ is possible but corresponds to radiation modes.

1.4.2 Cut-off Condition

The cut-off condition is an important characteristic of asymmetric planar waveguides ($n_s > n_c$) that provides, for a certain wavelength $\lambda_{cut\text{-}off}$, the minimum film thickness $h_{cut\text{-}off}$ needed to support a guided mode or vice versa. As stated before, the limit between guided and radiation modes is defined in terms of the refractive index as the point where $n_{eff} = n_s$. It is possible to find a relation between $\lambda_{cut\text{-}off}$ y $h_{cut\text{-}off}$ for each polarization mode (TE and TM), if this limit is applied to their corresponding dispersion relations, yielding[32]

$$\frac{h_{\text{cut-off}}}{\lambda_{\text{cut-off}}} = \frac{\arctan\left(\sqrt{\frac{n_s^2 - n_c^2}{n_f^2 - n_s^2}}\right) + m\pi}{2\pi\sqrt{n_f^2 - n_s^2}} \quad \text{(for TE modes)} \tag{1.35a}$$

$$\frac{h_{\text{cut-off}}}{\lambda_{\text{cut-off}}} = \frac{\arctan\left(\frac{n_f^2}{n_c^2}\sqrt{\frac{n_s^2 - n_c^2}{n_f^2 - n_s^2}}\right) + m\pi}{2\pi\sqrt{n_f^2 - n_s^2}} \quad \text{(for TM modes)} \tag{1.35b}$$

Note that, comparing both equations and taking into account that by construction $n_f > n_s$, if a planar waveguide supports a TM mode of order m, it supports the same order TE mode.

1.4.3 Confinement Factor

Typically, a waveguide gain is concentrated in the film (active film) with passive media as substrate and cover. Therefore, an important factor to quantify the portion of the energy that will undergo amplification is the mode confinement factor (Γ) defined as the fraction of the total energy confined in the active film. The expression used to calculate the mode confinement factor is written[32]

$$\Gamma = \frac{\int_{-h_f}^{0} |E_y(x)|^2 dx}{\int_{-\infty}^{\infty} |E_y(x)|^2 dx} \tag{1.36}$$

Therefore, only the portion Γ of the guided mode participate on the gain generation and Equation 1.15 is rewritten

$$g_{\text{net}} = \Gamma g - \kappa \tag{1.37}$$

where κ is the propagation losses coefficient, that contains the absorption coefficient (α) and other detrimental effects consequence of the light propagation in the waveguide, e.g. light scattering. This definition of the net gain is used together with Equation 1.31 to characterize the ASE emission of the waveguide, i.e. its amplification properties.

1.5 Optical Cavity

As stated at the beginning of this chapter, laser emission is characterized by its high spatial and temporal coherences that are provided by the optical cavity or resonator. The fundamental working principles of an optical cavity can be conveniently presented by

analysing the most elementary cavity formed by two plane mirrors separated a distance L between which a rod of an active material has been placed, see Figure 1.1.

Once the active material has been inverted, a few photons might be spontaneously emitted in the axial direction of the device, being amplified as they propagate through the active material. The propagating light is reflected by the end mirror going through the active material where is amplified again. In this way, light keep trapped bouncing back and forth in the optical cavity being amplified in each round-trip, which is known as the optical feedback. Typically, some losses are introduced by the mirrors, for example to produce the laser output beam, or by scattering of the propagating light. Therefore, the light is amplified in the cavity only if the optical gain in a round-trip is greater than the cavity losses, otherwise the propagating light will be attenuated. Moreover, for a plane wave propagating in the cavity the phase shift accumulated in a round-trip[27] $\varphi = 4\pi\nu Lc^{-1}$ might be conserved, meaning that it should be equal to $2\pi m$, where m is an integer, ν the light frequency and c the speed of light. Thus, the cavity can maintain only certain longitudinal modes of which only those spectrally coincident with optical gain are amplified. For example, 10^5–10^6 modes exist for an optical frequency in a cm-scale cavity, of which only the one or the few ones closer to the laser transition are amplified.

The laser beam is said to be temporally coherent whenever there is a strong correlation between the amplitude and phase of the signal at any two separated times. That is, if the amplitude of the signal is considered at a given point, at times t and $t+\Delta t$, the phase difference between t and $t+\Delta t$ should remain equal for any t. Additionally, the temporal coherence of a laser beam is directly connected with its monochromaticity, i.e. the spectral bandwidth of the laser emission. Indeed, the more monochromatic, the more temporally coherent the beam is; which constitutes an easy way to experimentally test this property.[26,27]

In the case of the spatial coherence, the correlation appears between the instantaneous amplitudes or phase angles of the wave-front at any two points across the laser beam. This means that the phase difference between the electric field at two different points of the wave-front should be zero at $t = 0$. Beam directionality appears as a consequence of spatial coherence. Particularly, a laser beam with perfect spatial coherence is said to be diffraction limited, as its divergence angle (θ_d) is dictated by diffraction being[26]

$$\theta_d = \frac{1.22\lambda}{D} \tag{1.38}$$

where $\lambda = c\nu^{-1}$ is the wavelength of the laser emission and D de size of the laser beam at the surface of the device. Therefore, the directionality of the laser beam can be used as a test for spatial coherence.

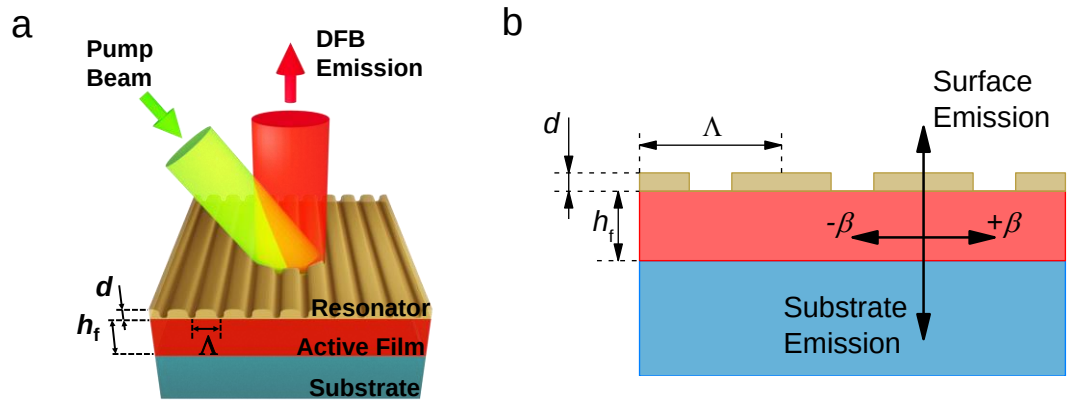

Figure 1.13 Top-layer distributed feedback (DFB) laser. (a) General picture and (b) longitudinal section of the DFB device. The parameters correspond with the active film thickness (h_f), the resonator depth (d) and the grating period (Λ).

1.5.1 Distributed Feedback Resonator

Other than the classical laser cavity presented above, several kinds of resonators such as micro-cavities, micro-rings, micro-disks and micro-spheres have been used to fabricate organic solid-state lasers (OSLs),[33] but the more suitable to be integrated with planar waveguides are the DFB resonators. A DFB resonator consists of a periodic corrugation of the effective refractive index of the waveguide. The most typical one is a 1D relief grating that can be engraved in the substrate, directly on the active film or in a separated layer situated below or on top of the active film. The last geometry with the DFB engraved in a separated top layer is shown in Figure 1.13. The resonator provides the optical feedback and out-couples the propagating light. In an approximated picture, the propagating modes of the waveguide are scattered by the DFB structure. Under certain conditions, the scattered light combines coherently in a counter-propagating Bragg wave that under the interaction with the propagating mode results in a periodic modulation of the electric field in the waveguide. The DFB resonator presents an excellent lasing performance in terms of:[34] *i*) optical feedback, which is distributed across the gain medium enabling a strong interaction between the light and active material; *ii*) tunability of lasing mode, that can be accomplish by modifying the different geometrical parameters of the device to obtain efficient single-mode emission; *iii*) diffraction-limited out-coupling, that is provided by the periodic structure. Moreover, the top-layer configuration used in this thesis provides additional advantages such as constant film thickness of the active film, multi-colour emission on-a-chip and preservation of the active film from the surrounding atmosphere.

Typically, DFB devices are designed to operate in the second diffraction order ($m = 2$) of the Bragg condition[29]

$$m\lambda_{\text{Bragg}} = 2n_{\text{eff}}\Lambda \qquad 1.39$$

where n_{eff} is the effective refractive index of the waveguide propagating mode and Λ the grating period. In second-order DFB resonators, light is out-coupled perpendicularly to the device surface by first-order diffraction at a wavelength λ_{DFB} close to λ_{Bragg}. In the case of the top-layer DFB resonator, i.e. pure index grating in a separated layer, and for a propagating waveguide mode, coupled mode theory predicts the formation of a photonic stop-band centre at λ_{Bragg} with lasing taking place at two close wavelengths, one at each edge of the stop-band.[29,35] Therefore, Λ is tailored to provide that λ_{Bragg} approximately matches the gain maximum of the active material. Even so, single-mode emission is observed at the peak of longer wavelength as the peak at shorter wavelength is hampered by higher reabsorption losses.[36]

Chapter 2
State of the Art

Conjugated organic materials have been thoroughly investigated, proving to be valuable for a wide variety of optoelectronic applications, e.g. solar cells, field-effect transistors and light-emitting diodes, among others. That is also the case of organic lasers, in which organic materials are used as active media. As it is stated in Section 1.3, conjugated organic compounds are intrinsic four-level systems optimal for lasing applications. Moreover, the broad PL spectrum of organic compounds offers the opportunity for tuning the laser emission across it.

Indeed, organic dyes dispersed in liquid solutions were used as active media in dye lasers,[37,38] soon after the first laser was demonstrated by Maiman.[1] Later, organic dyes were dispersed in polymer matrixes shaped as monolithic rods intended to improve the compactness and maintenance of their liquid counterpart.[39,40] However, these OSLs still present the high operational energy requirements of their predecessors and bring additional photostability issues. Then, novel and more efficient laser architectures, used with the active material prepared as a thin film, e.g. DFBs, micro-cavities and plasmonic resonators, were developed to reduce the operational energy, introducing other advantages such as compactness and mechanical flexibility at low-cost of production.[3]

Nevertheless, the larger improvements in the field have been achieved from the point of view of the active material itself. In the last few years, a myriad of organic compounds with varying properties have been synthetized propelled by the development of computational tools and bottom-up synthesis approaches.[4] These techniques provide smart design and control of the optoelectronic properties with outstanding precision and reproducibility.[16] In this regard, TFOLs were demonstrated for the first time in 1996 thanks to the development of semiconducting polymers.[41–44] Since that moment, many organic compounds have been investigated in the seeking for active materials with lower

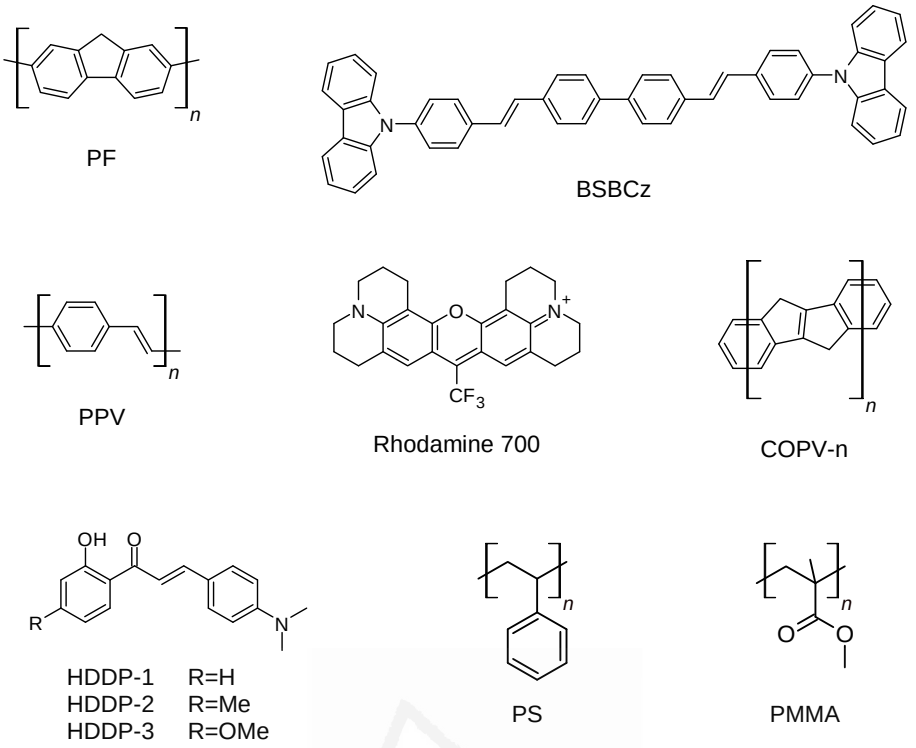

Figure 2.1 Conjugated organic compounds used as active materials and inert matrixes. Polyfluorene (PF) and polyphenylenevinylene (PPV) are conjugated polymers, 2'-hydroxychalcone derivatives (HDDP-*n*, *n* = 1–3) are single crystals, rhodamine 700 is a dye, carbon-bridged oligo(*p*-phenylenevinylene) (COPV-*n*, *n* = 1–6) are ladder-type molecules, 4,4'-bis[(*N*-carbazole)styryl]biphenyl (BSBCz) is a thermally activated delayed fluorescence compound and polystyrene (PS) and poly(methyl methacrylate) (PMMA) are inert thermoplastic polymers.

operational pumping (threshold),[4] reaching the point in which indirect electrical pumping is possible with pulsed LEDs.[45,46]

2.1 Classification of Organic Active Materials

Here we focus on materials for TFOLs. Different possibilities can be considered when classifying conjugated organic compounds. Typically, their optoelectronic properties and morphology are considered to divide then in three categories, i.e. dyes, organic semiconductors and triplet gain media.[4] However, from the point of view of the TFOLs, it seems more convenient to gather them in two groups according to how they are processed, i.e. as net/pure materials or blended with another material.

2.1.1 Organic Compounds Processed as Net Materials

This group includes the conjugated polymers –e.g. polyphenylenevinylenes and polyfluorenes–, oligomers, dendrimers, and small molecules prepared as net materials in the form of single crystals (SCs) or amorphous solids. Some examples are shown in Figure 2.1. Typically, many of these compounds have been developed in the pursuing for electrically-pumped TFOLs, focussing most efforts in lowering the lasing threshold. Such strategy conducted to the development of DFB lasers pumped with compact inorganic diode lasers, even with LEDs.[45,46] Unfortunately, these compounds generally present low photostability and must be encapsulated for practical applications.

2.1.2 Organic Compounds Dispersed in a Matrix

As a rule of thumb, the compounds of this group correspond with small organic molecules, such as dyes (molecules or oligomers), NGs or thermally activated delayed fluorescence (TADF) compounds. Note that in these compounds, intermolecular interactions generally lead to PL quenching. For this reason, they are dispersed in an inert matrix (for example, PS or PMMA) intended to prevent those intermolecular interactions. Moreover, such matrixes are ideal materials to be prepared as high quality waveguides (high transparency and low scattering, thus low propagation losses; and good mechanical properties) which is a key aspect for the manufacture of TFOLs. Some examples of organic compounds appertaining to this category are given in Figure 2.1. They are usually doped in low amounts leading to active materials with large photostability and moderate laser thresholds. Interestingly, a variant of these materials in which a TADF compound (4,4'-bis[(*N*-carbazole)styryl]biphenyl) is dispersed in an electroactive matrix (Cs) has been used to demonstrate for the first time an operative electrically-pumped OSL.[5] Additionally, these materials are attracting a lot of attention due to the emergence of novel compounds such as NGs.[18,47] Despite of their success, there are still plenty of room for improving the performance of these materials.

In the following sections, the focus will be on two families of small molecules dispersed in polymeric inert matrixes. On one hand, we consider the family of PDI compounds, which has been thoroughly studied as active material since the 80's. Despite being one of the most studied active materials, PDI compounds are investigated still today thanks to their versatility for being substituted with peripheral groups that modify their properties.[17] On the other hand, we have focussed on the family of NGs, which have recently burst onto the scene with the promise of being versatile compounds. Indeed, their optoelectronic properties rely on their shape and size that can be tailored at wish by using Organic Chemistry bottom-up synthesis.[48]

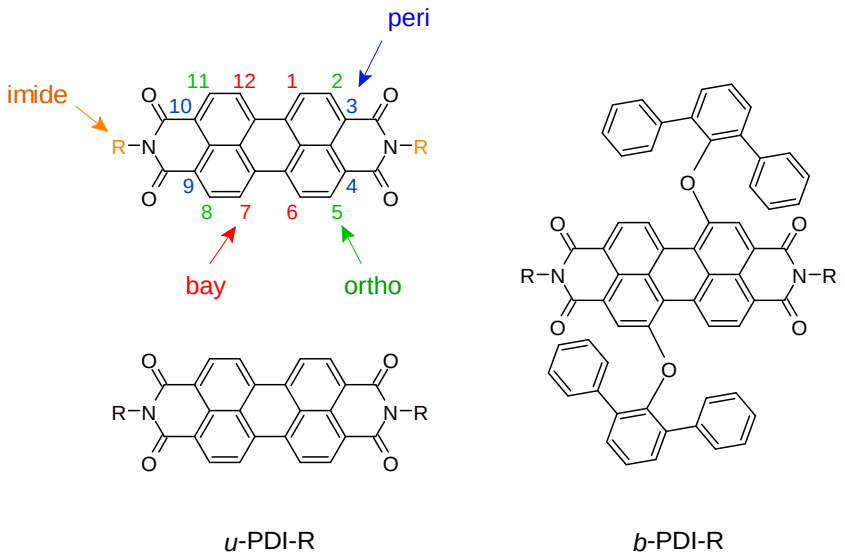

u-PDI-R *b*-PDI-R

Figure 2.2 Chemical structures of PDI compounds. *u*-PDI-R stands for bay/ortho undoped PDI with R substituents at the imida position and *b*-PDI-R for PDI substituted with R substituents at the imida and 2,6-diphenylphenoxy groups at the 1,7-bay positions.

2.2 Perylenediimide Compounds

Since their implementation as active materials for dye lasers[49–51] and OSLs,[52–54] PDI compounds have become one of the most important families of laser dyes, demonstrating excellent optical properties, such as high PLQY, and outstanding stability against photo-, thermal and chemical degradation. More recently, PDI compounds have been used as active materials in DFB lasers,[55,56] self-ensemble microcavities[57] or polariton lasers,[58,59] which opened the door to practical applications. For example, PDI compound-based DFB lasers were used to demonstrate the label-free biosensing of the ErbB2 protein, a clinical indicator used for the diagnosis and treatment of some common cancers.[13] However, important challenges remain still unsolved, precluding the successful commercial implementation of these technologies. Particularly, PDI-based devices optically-pumped with a compact inorganic diode might be feasible, though lower operational energy would be needed for it. Furthermore, PDI compounds emitting at different wavelengths and with improved photostability would be desirable for practical applications.

Undoubtedly, the importance of PDI compounds relies not only in their outstanding optical and laser properties, but also in the incredible development of the synthetic chemistry of this class of dyes, particularly flourishing during the last decade.[17] Indeed, different synthetic strategies have been developed to improve the properties of PDI compounds towards lower energetic requirements for ASE and wavelength tuning of the PDI emission. Initially, the PDI core was substituted only at the imide positions, leaving the bay and ortho positions unsubstituted (i.e., bay/ortho-unsubstituted PDI or *u*-PDI; see

Figure 2.2), in an attempt for improving the PDI solubility and increasing the amount of PDI that could be incorporated into the matrix without getting significant PL quenching.[60,61] Following this approach, the best results in terms of ASE threshold and photostability were obtained for a 2,6-diisopropylphenyl-substituted *u*-PDI (PDI-O) dispersed in PS at 1 wt%, which showed $E_{\text{th-ASE}} = 30$ μJ cm^{-2} and $\tau_{1/2} = 8 \times 10^5$ pump pulses, under excitation with the second harmonic of a pulsed Nd:YAG laser (10 Hz, 10 ns).[62] However, *u*-PDI compounds suffer molecular interaction/aggregation for concentrations above typically ~ 1 wt%, thus leading to concentration quenching.[62,63] This issue evidences the importance of concentration-dependence studies for the optimization of optical and ASE performance. Moreover, the absorption and PL spectra of *u*-PDI remains unchanged with respect to that of unsubstituted PDI core because of the electronic nodal character of the imide nitrogen atoms, which isolate electronically the core from the imide substituent.[17] This constitutes a handicap, since it limits the range of wavelengths available for these PDI compounds. Initial attempts of colour tuning consist in the substitution at the bay positions, yielding PDI compounds with rather low PLQY, as consequence of their distorted core.[64–68] This issue was solved by using phenoxy-like groups at the 1,7-bay positions of the PDI core, which red-shift their absorption and PL spectra ~30–40 nm with respect to *u*-PDI, maintaining high PLQY.[69–71] Particularly, PDI compounds substituted at 1,7-bay positions with 2,6-diphenylphenoxy groups (*b*-PDI, see Figure 2.2) demonstrated to prevent molecular aggregation by steric hindrance. Hence, *b*-PDI compounds could be incorporated into de matrix up to ~30% with moderate concentration quenching.[63,70] Similarly, substitution with phenoxy-like groups at the ortho positions were attempted with similar results,[72] though typically substitutions of this kind present lower PLQY and generate PDI aggregates.[57,73,74] Despite their attractive features, *b*-PDI compounds present lower photostability than state of the art PDI compounds, such as PDI-O. For example, PDI-O ($\tau_{1/2} \sim 23000$ pump pulses)[62] displayed 6–7 fold larger photostability than *b*-PDI-1 ($\tau_{1/2} \sim 3600$ pump pulses)[70] under similar conditions, i.e. same pump energy density ($E_{\text{pump}} = 2.5 \times 10^4$ μJ cm^{-2}) and concentration in the PS matrix (0.5 mol g^{-1}). Thus, the design of *b*-PDI compounds with improved photostability remains as a challenge.

2.3 Nanographenes

Graphene was isolated for the first time by Novoselov et al.,[75] Since then, it has been thoroughly investigated and has demonstrated optimal properties for optoelectronic[76] and spintronic[77] applications. However, its optical properties remained elusive as a consequence of its zero band gap.[78] Initial attempts to open a finite band gap consisted in using graphene oxide,[79] π-stacking a few graphene layers[80] or using bended graphenes.[81] Unfortunately, such strategies proved to be insufficient for gain applications.[82,83] Alternatively, the quantum confinement of the electronic wave function

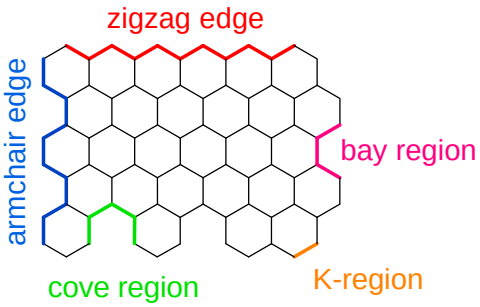

Figure 2.3 Principal edge topologies in nanographenes.

can be used to open a finite band gap in graphene by shaping it into nanostructures (the so-called NGs),[84] which have demonstrated success for gain applications.[85,86] Interestingly, the optical properties of such NGs rely upon their size and structure, particularly on that of their edge (see Figure 2.3): armchair, zigzag, cove, etc.[15,87] This opens the door to design NGs with tailored optoelectronic properties through bottom-up fabrication techniques developed in the frame of Organic Chemistry.[16]

In this regard, there are only a few studies towards understanding the influence of each type of edge or the NG size over its gain performance.[47] For example, it is known that the elongation of the zigzag edge is an efficient way for maximizing the red-shift of the absorption and emission bands in similar systems, such as graphene nanoribbons (GNRs), which results ideal for colour tunability.[88] Moreover, it has been theoretically predicted a sharper decrease of the energy gap in NGs with zigzag edges rather than in those with armchair ones,[89] which might be consistent with the aromatic sextet rule.[15] However, it is still in debate whether zigzag edges are playing an even more fundamental role in the generation of gain.[85,90] Thus, more sophisticated experiments are needed to elucidate the role of the zigzag edge on the gain performance. beyond changing the size and shape of the NG, other routes have been explored for tuning the emission properties of NGs, such as replacing carbon atoms of the molecular structure by heteroatoms[91] or edge functionalization with bathochromic groups.[92] Nevertheless, reports on their effect over the gain properties of the NGs are still missing.

2.4 The Matrix

The matrix is one of the fundamental pieces in the optical and laser performance of the active material. Ideally, the matrix should be inert and provide optimal dispersion of the compound to prevent PL quenching, which deteriorates the emission properties. In addition, it should properly isolate the active compound and efficiently dissipate heat, which are essential properties to reduce photodegradation and extend the operational lifetime of the laser devices.[93] Moreover, the material should be easily processed as a high-quality optical waveguide with low propagation losses. In this regard, many efforts have been devoted to design materials with optimal properties to serve as matrixes for laser

dyes used in OSLs.[94] This includes myriad of organic and inorganic materials, e.g. glasses, polymers, mesostructurated materials, etc, which are typically manufactured as monoliths intended to be used with external laser cavities. Despite their success for such purpose, much of them can hardly be processed as optical waveguides, precluding their implementation in TFOL devices. An exception to this are thermoplastic polymers, which can be processed as high-quality optical waveguides through solution-based methods such as spin-coating, dip-coating, doctor blading or printing over any substrate.[29,95] Furthermore, these polymers are compatible with techniques such as nanoimprint lithography, which is very attractive for the integration of the DFB resonator directly in the active film.[96–99] Among others, PS and PMMA (see Figure 2.1) are two of the more widespread thermoplastic polymers for the manufacture of optical waveguides, given their low cost and excellent processability. However, PMMA is often avoided due to its relatively low refractive index ($n = 1.49$, at $\lambda = 600$ nm), which would restrict the number of available substrates and film thickness to obtain a low-loss optical waveguide.[61,62,96] Indeed, PDI-based TFOLs relying in PMMA waveguides are scarce.[61,62,100] Actually, there are just a few studies on the optimization of the matrix, considering not only the emission properties but also its processability as a high-quality low-loss optical waveguide.[101–103] Hence, a thorough concentration-dependence study of the optical and laser properties comparing systematically different matrixes might be helpful for improving the performance of certain TFOLs.

2.5 Near-Infrared Organic Laser Materials

During the last few years, the interest for organic compounds emitting in the NIR region has been growing[19] propelled by the biomedical and telecommunication applications.[21] In this regard, organic compounds with NIR emission must deal with detrimental issues other than the concentration quenching: *i*) excited-state absorption promoting charge transfer states, triplet states and other photoproducts that destroy the population inversion;[8,25] and *ii*) the fast non-radiative decay following the energy gap law.[22,23] These are the reasons why just a few organic compounds have demonstrated amplification in the NIR region, see Table 2.1.

2.6. Main Actuations

As stated in previous sections, important questions remain still unsolved concerning the photostability and operational energy of the active materials. PDI compounds dispersed in inert matrixes have demonstrated to be proper candidates for the manufacture of TFOLs. However, their operational energy should be reduced by an order of magnitude so that indirect electrical pumping become feasible and with it their practical implementation.

Additionally, novel PDI compounds (e.g. *b*-PDIs) present a reduced photostability in comparison with state of the art PDI compounds such as PDI-O. Understanding the mechanisms responsible for this drawback could be important for the development of more lasting devices.

The fine control over the molecular structure provided by the organic synthesis bottom-up approach and the development of computational calculations enable the design of organic molecules with tailored properties. Therefore, knowing the relationship between structural and chemical characteristics of the molecules and their optoelectronic properties become essential. In this regard, NGs properties rely on their size and shape, particularly, on that of their edge, which represent a unique opportunity to study these effects and applying them to the problem of obtaining compounds with emission in the NIR region suitable for lasing applications.

In this thesis, the previous aspects are investigated using different spectroscopic techniques (for instance; absorption, PL, TRPL and TA) and by characterizing their ASE, gain and losses performance. All the experimental methods used are presented in Chapter 3. The different actuations performed consist in studying:

- The impact of the matrix and dye content over the optical and ASE properties of different PDIs (Section 4.1).
- The effect over the photostability and aggregation of different groups anchored at the imide positions of *b*-PDI compounds (Section 4.2).
- The influence of the wave function delocalization over the optical and gain properties of NGs (Section 5.1).
- The effect of the NG zigzag edge over the delocalization (Section 5.2).
- The possibility of breaking the delocalization over the NG zigzag edge (Section 5.3).
- The effect of cove edge over the NG gain properties (Section 5.4).
- The relevance of the substituents on controlling the formation of CT states (Section 5.5).
- The suitability of NGs for lasing applications by the demonstration of operative DFB lasers (Section 5.6).

Table 2.1 Comparison of near-infrared organic fluorophores amplified spontaneous emission performance in solid state.

Compound[a)]	Material[b)]	Sample	Conc. (matrix) [wt%] [c)]	λ_{pump} (t_p, rr) [nm (ns, Hz)][d)]	λ_{ASE} [nm][e)]	$E_{th\text{-}ASE}$ [μJ cm^{-2}][f)]	$\tau_{1/2}$ [pp] @ E_{pump} [μJ cm^{-2}][g)]	Reference
Rh700	OD	0.8 μm film	1 (4:1 PMMA:SP)	650 (5, 10)	747	200		[104]
LSD798	OD	1.5 μm film	1 (PVP)	565 (0.8, -)	800	12.5		[105]
LSD820	OD	50 μm film	0.5 (PVP)	532 (5 ns, 10)	820	130	$\sim 10^4$ @ 165	[106]
LSD950	OD	9.3 μm film	1 (FPI)	337 (4 ns, 10)	970	220		[107]
NK-125	OD	Unknown h_f	2 (PVP)	740 (5 ns, 10)	830	130		[108]
BDFC-1	TADF	Unknown h_f	2-40 (CBP)	337 (0.8 ns, 8)	801-860	7.5-91		[109]
BDFC-2	TADF	120 nm film	4-60 (CBP)	337 (0.8 ns, 8)	738-798	4.7-37	$\sim 10^5$ @ 25 (6wt%)	[109,110]
HDDP-1	OSC	cm size slab	neat	355 (10, 10)	714	92		[111]
HDDP-3	OSC	cm size slab	neat	355 (10, 10)	746	1000		[111]
DPHP[†)]	OSC	2.4 μm size hemisphere	neat	400 (1.5×10^{-4},10^3)	723	0.78		[112]
DMHP[†)]	OSC	120 nm nanowire	neat	400 (1.5×10^{-4},10^3)	720	1.4		[113]
H_2TPyP	OSC	Rectangular microtubes	neat	410 (2×10^{-4}, 7.6×10^7)	732	3400		[114]

[a)]Different compounds with reported near-infrared (NIR) amplified spontaneous emission (ASE) in solid-state; [b)]The different families of organic compounds compared are nanographenes (NGs), organic dyes (ODs), thermally activated delayed fluorescence dyes (TADF) and organic single crystals (OSCs). [c)]Concentration of the molecule in the matrix (polystyrene, PS; poly(methyl methacrylate), PMMA; spyropyran, SP; poly(vinyl-pyrrolidone), PVP; fluorinated-polyimide, FPI; 4,4'-bis(N-carbazolyl)–1,10-biphenyl, CBP); [d)]Excitation wavelength (pulse width, repetition rate); [e)]ASE wavelength; [f)]ASE threshold expressed as energy density; [g)]Photostability half-live expressed in number of pump pulses(pp) measured at the indicated pump energy density. [†)]The results correspond to lasing rather than ASE.

Chapter 3
Experimental Methods

3.1 Sample Preparation

3.1.1 Polymeric Waveguide Manufacture

The research developed throughout this thesis involves mainly the characterization of planar waveguide samples manufactured with organic materials, which consist of thin films of an inert thermoplastic polymer laying over a quartz substrate. Such polymer film serves as inert matrix to host a certain organic molecule, homogeneously disperse in it, which provides the photoluminescent and lasing properties to the waveguide. The high solubility of these compounds in organic solvents enables them to be processed from solution-based techniques such as drop-casting, doctor blading, dip-coating, etc. Among them, spin-coating is a cost effective and time-saving technique widely used in optoelectronics manufacture, which provides smooth thin films of remarkable uniformity.[95] These characteristics make the spin-coating technique suitable for fabricating high-quality planar waveguides based on organic materials, such as those studied here.

In a first step, a solution with the polymer and the organic molecule is prepared by using an appropriate solvent. The relative proportion between polymer and organic molecule in the solution is adjusted to obtain the desired doping concentration in the final waveguide. The ideal solvent should dissolve completely both compounds to avoid aggregation and guarantee a homogeneous sample. Moreover, it should also be volatile, with a boiling point higher than the glass transition temperature (T_g) of the polymer matrix, to enable solvent extraction once the film is formed. Then, the solution is stirred overnight to achieve a correct dispersion of the polymeric chains, and filtered prior to deposition, to ensure a high homogeneity of the final film.

Next, the solution is spin-coated over the substrate, which has been previously anchored to the substrate holder. This was performed in a LabSpin6 (SUSSMicroTec) apparatus. The filtered solution is dropped gently over the fixed substrate, with the drop covering abundantly the whole area. Then, the sample is accelerated up to a certain spin-speed, which is maintained for a certain time. At the beginning of the spinning, the solution flows out of the substrate driven by the centrifugal force, which expels the solution excess through the sample edge and forms a homogeneous film. The film gets thinner during this process and, at the same time, its viscosity rises due to solvent evaporation. Then, the final film thickness (h_f) is determined from the balance between the centrifugal driving force and the viscous resisting force.[115,116] The centrifugal force depends solely on the spinning-speed and the viscous force on the solution viscosity, both tuneable parameters that can be used for adjusting the film thickness. Here, the spinning parameters (acceleration $= 1000$ rpm s^{-1}, speed $= 3000$ rpm and time $= 30$ s) are fixed to ensure a flat homogeneous film over the whole substrate. On the other hand, the solution viscosity, which depends mainly on the polymer concentration in the solution, is used for tuning h_f. Details on the expected h_f depending on the solvent, polymer and relative concentration are available in Appendix A.

Finally, the film is baked for two hours at a temperature larger than the polymer T_g and slightly below the boiling point of the solvent to remove any remnant of the solvent.[12,117,118] A JP Selecta S-201 oven is used for this purpose. Although, the larger part of the solvent evaporates during the spinning, a certain portion of it remains trapped inside the film.[119–121] The presence of trapped solvent in the film might translate into inhomogeneity, as well as polymeric chains mobility, given the non-equilibrium state of the system.[122,123] Thus, it is important to perform annealing treatments to optimize the film properties. Nevertheless, it should be taken into account that the annealing process might cause damage to certain compounds due to the high temperatures used. Thus, this step is skipped whenever the materials thermal stability is unknown.

3.1.2 Distributed Feedback Resonator Manufacture

Occasionally, second order DFB lasers are manufactured to illustrate the suitability of certain compounds for lasing applications. The device architecture comprises a top-layer resonator deposited over the active waveguide, which consist of a 1D relief grating engraved on water-soluble dichromated gelatine (DCG) by holographic lithography (HL). Processing the resonator from water helps preserve the great optical properties of the active films deposited from organic solutions, contributing to low lasing thresholds. Additionally, the versatility of the HL technique allows tailoring the resonance condition, i.e. tuning of the different resonator parameters (Λ, d, h_f), to match the gain band of the active material and optimize the laser performance. The preparation of such devices is commissioned to V. Bonal, Dr. J. M. Villalvilla and Dr. J. A. Quintana (Organic Photonics and Electronics group, UA), who are expert on the subject.

All the DFB resonators used in this thesis have been manufactured following a method that involves several steps. Firstly, a layer of the negative photoresist DCG is spin-

coated on top of the active film from a hot water solution (40ºC). The concentration of gelatine (Russelot, 200 bloom) in water is adjusted to obtain a 100 nm thick layer and the sensitizer (ammonium dichromate) is added in a proportion of 35 wt% with respect to gelatine. Secondly, a grating pattern is recorded in the DCG layer through exposure to a holographic pattern generated with the light from an Ar laser (λ = 364 nm) in Lloyds configuration (the scheme of the setup can be found elsewhere)[124]. The average exposure is 45 mJ cm^{-2}. The light pattern translates into hardness variations between exposed and unexposed areas in the DCG layer. Finally, the DCG layer is desensitized in a cool-water bath (15ºC) and the latent pattern is extracted by dry development in the oxygen plasma generated in a surface treatment machine (Diener Zepto; 10 min). The result is a relief grating of depth d = 90 nm and rectangular grating profile with 0.75:0.25 duty cycle. These parameters optimize the laser threshold and efficiency.[56,124,125]

3.2 Characterization of Standard Optical Properties

In this thesis, absorption, PL and PLQY are the more elemental properties used to characterize planar waveguides. The analysis of such properties provides the spectral characteristics and optical quality of the sample, which are crucial for the correct interpretation of the gain and lasing performances.

3.2.1 Absorption

As stated in Section 1.1.2, light propagating in an optical medium can be partially absorbed by it; a phenomenon strongly dependent on the light wavelength. Experimentally, light absorption is characterized through the absorbance or optical density (OD), which is defined for a certain sample as the logarithm of the ratio between the impinging and transmitted light intensities. Therefore, the absorbance can be defined in terms of the transmittance (T) of the sample as

$$OD = -\log\left(\frac{I(l)}{I_0}\right) = -\log(T) \qquad 3.1$$

where l is the sample thickness, I_0 is the impinging intensity and $I(l)$ the transmitted intensity (light intensity after traveling a distance l). However, the absorbance presents an implicit dependency in the sample thickness that precludes a direct comparison of samples; particularly, when the comparison is between different materials. In such case, α is used to quantify the sample's absorption. This intrinsic parameter is defined as the fraction of light intensity absorbed by the material per unit of length. The attenuation of light in the sample follows Beer's law (Equation 1.13). Therefore, absorbance and α are related by

$$\alpha = \frac{OD}{l}\ln(10) \qquad 3.2$$

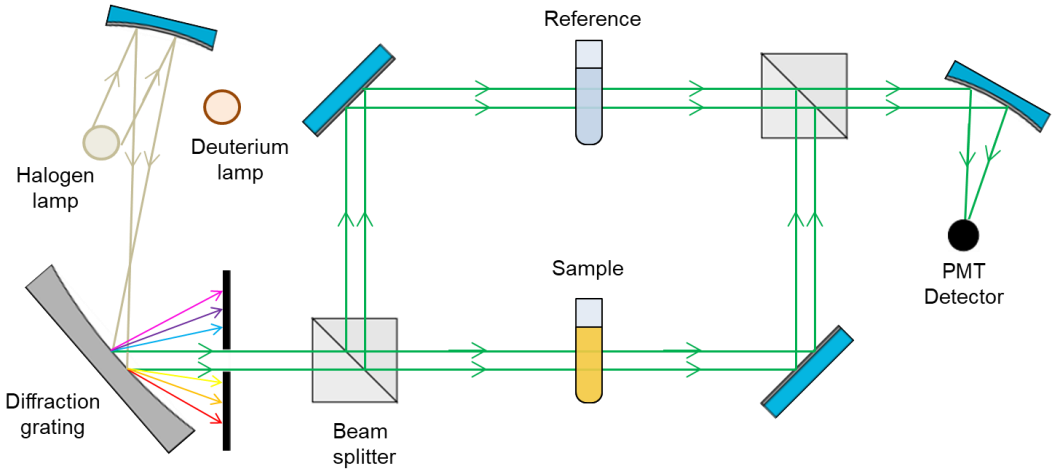

Figure 3.1 Double-beam spectrophotometer scheme.

Additionally, the molar extinction coefficient (ε) is defined for materials consisting in absorbing species dispersed in a passive medium, e.g. a chromophore dispersed in a solvent or a thermoplastic matrix. It takes into account not only the sample thickness but also its molar concentration (C) and can be written

$$\varepsilon = \frac{OD}{l\,C} \tag{3.3}$$

Most absorption measurements in this thesis have been performed with a double-beam spectrophotometer V-650 UV-VIS (Jasco). Figure 3.1 shows the basic scheme for a double-beam spectrophotometer. The V-650 UV-VIS system uses two light sources to cover the spectral range from 190 nm to 900 nm; a deuterium lamp covering from 190 nm to 350 nm and a halogen lamp covering from 330 nm to 900 nm. These light sources fed an automated monochromator that select the light with the desired spectral parameters, i.e. wavelength and bandwidth. The resulting beam is divided in two approximately equal beams with a beam splitter, the reference and sample beams. These beams pass through their corresponding channels, to be finally analysed in the photomultiplier tube detector. Prior to the sample measurement, a blank measurement (with no sample or reference) is taken to calibrate the ratio between the intensities of sample and reference beams. Then, the sample is measured using the appropriate reference and the ratio between both beams is compared with the blank ratio to determine the sample's transmittance. The double-beam configuration present advantages in terms of temporal stability and avoid the effects of light source's fluctuation by comparing equivalent beams, which increases the precision of the measured values. Additionally, the high efficiency of the photomultiplier tube allows the characterization of samples with very low absorbance with high accuracy ($\pm$ 0.002 OD).

Two kinds of samples have been characterized with this system: liquid solutions and thin films deposited over substrates (planar waveguides). The liquid solutions were measured by using UV quartz cuvettes with a 10 mm path-length. In this case, the

reference consisted in a cuvette with the same solvent used to disperse the organic molecule under analysis. For the waveguides, no reference was use as will be discussed in next section.

3.2.2 Film Thickness Determination

Film thickness (h_f) has been determined with a spectrophotometric method,[126] which consists in an extension of the spectrophotometric envelope method originally proposed by Manifacier et al.[127] and developed by Swanepoel.[128–130] Swanepoel's method relies in the analysis of the interference pattern appearing in the transmission spectrum of the sample and can be applied for transparent or weakly absorbing films. In this method, the envelope of the interference maxima and minima are used to estimate the refractive index from the transmittance difference between both envelopes. Then, the separation between maxima and minima is used together with the refractive indexes at such points to estimate h_f. Therefore, at least a few interference maxima and minima are required to operate, what restricts its application to film thicknesses in the range between 5000 nm to 400 nm for materials like the ones studied here.[131,132]

On the other hand, the updated method used in this thesis consists in the comparison of the experimental transmission spectrum at normal incidence with the calculated one, respectively T_{exp} and T_{calc}, see Figure 3.2. This can be done only in the transparent spectral window, where no absorption is present. For the calculation, the refractive indexes of substrate and film (n_s and n_f, respectively) are needed. The calculated transmittance $T_{calc}(\lambda\ n_s,\ n_f,\ h_f)$ is determined with the model proposed by Swanepoel et al.,[128] that is

$$T_{calc} = A/(B - C\cos\varphi + D) \qquad 3.4$$

where $A = 16n_f^2 n_s$, $B = (n_f+1)^3(n_f+n_s^2)$, $C = 2n_f^2(n_f^2-n_s^2)$, $D = (n_f-1)^3(n_f-n_s^2)$ and $\varphi = 4\pi n_f h_f \lambda^{-1}$. Then, several values of T_{calc} are calculated for different values of h_f and compared to T_{exp} by determining the accumulated absolute deviation (R)

$$R(h_f) = \sum_i \left| T_{exp}(\lambda_i) - T_{calc}(\lambda_i, h_f) \right| \qquad 3.5$$

The absolute minimum of R corresponds with the value of h_f.

With this method, h_f values down to 40 nm can be determined, with results comparable to those obtained with other methods, such as profilometry. The typical error in h_f for a single measurement in a single film is around 5 nm. For the application of this method it is necessary to know the refractive index of the material. In this work, the analysed waveguides consist of thermoplastic polymer films doped with organic molecules deposited over quartz substrates. Typically, low concentrations of the dopant are used to avoid PL concentration quenching. In these cases, the refractive index of the composite is assumed to be approximately equal to that of the polymer. The refractive indexes of the thermoplastic polymers and quartz substrate follow the Sellmeier equation

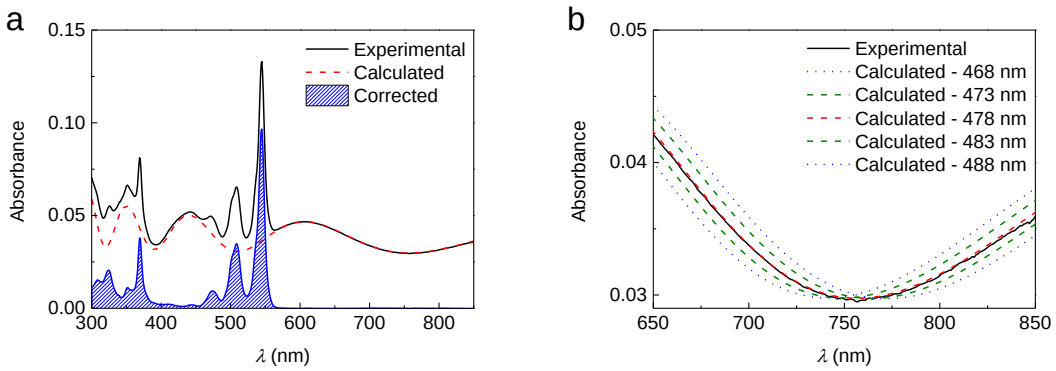

Figure 3.2 Film thickness determination. (a) Absorbance spectrum of a PS film doped with 1wt% FZ2 (black solid line), calculated absorbance spectrum of un-doped PS film (red dashed line) and corrected absorbance spectrum of the FZ2-doped PS film (blue area). (b) Calculated absorbance spectra of films with increasing thickness, compared to the experimental absorbance spectrum in the transparency region used to determine the experimental film thickness of the sample.

$$n^2(\lambda) = 1 + \sum_i \frac{B_i \lambda^2}{\lambda^2 - C_i} \qquad 3.6$$

where λ is the vacuum wavelength that should be used in μm and B_i and C_i are experimental coefficients that are available in an online data base.[133] For the thermoplastic polymers only one term is needed (i.e. $i = 1$): for PS, $B = 1.4435$ and $C = 0.020216$ μm²; and for PMMA, $B = 1.1819$ and $C = 0.011313$ μm². In the case of quartz, three terms are used, $B_1 = 0.6961663$, $B_2 = 0.4079426$, $B_3 = 0.8974794$, $C_1 = 0.0684043$ μm², $C_2 = 0.1162414$ μm² and $C_3 = 9.896161$ μm².

The film homogeneity is another important factor in the precision of the method. The presence of superficial irregularities and thickness variation in the film contribute to reduce the contrast of the interference pattern, hindering the thickness determination. In this case, the comparison between the interference minima envelope and the simulated transmission of the substrate is used as a control test for the sample quality. Then, the transmittance spectra are measured without reference, as was anticipated in the previous section, to ascertain a better thickness determination.

3.2.3 Guided Modes Calculation

For the design and characterization of waveguides, computational calculations are performed with a free software available online.[134] The programme uses the refractive indexes of the different materials, h_f and λ to calculate the number of supported modes, their n_{eff}, the field distribution in the waveguide and the confinement factor (Γ). During the waveguide design and fabrication, it is important to ensure that h_f is larger than the cut-off thickness for the TE_0 to get a waveguide (see Section 1.4.2). Moreover, Γ provides de overlap between the guided mode and the gain medium, therefore, the larger Γ is the better. However, higher modes are typically undesired to maximize the gain in a single mode.

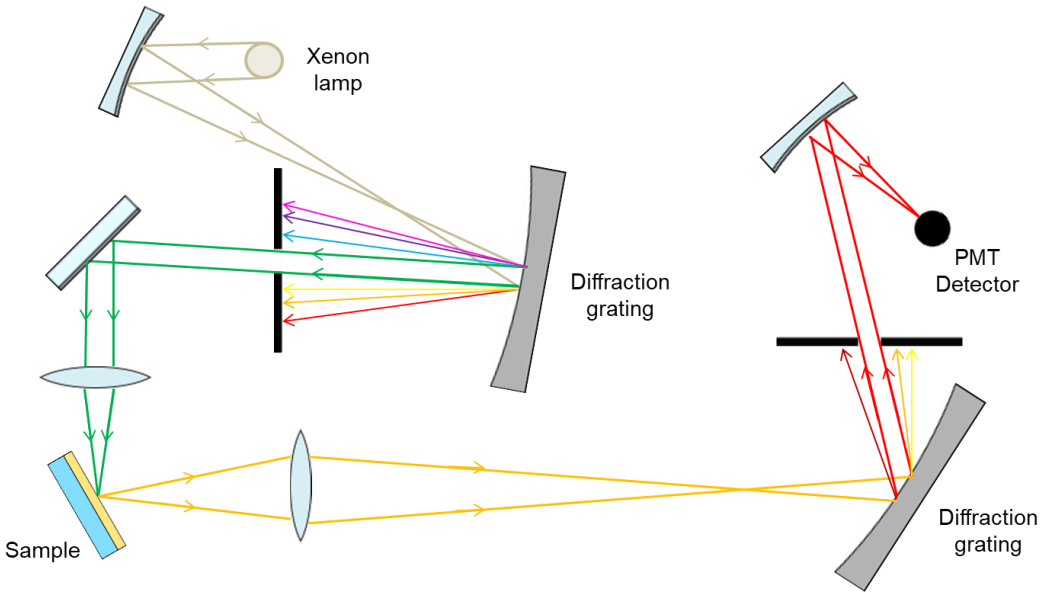

Figure 3.3 Spectrofluorometer scheme.

Additionally, the design of DFB devices implies that n_{eff} should be known with high precision. For this purpose, the film thickness calculated in the previous section is used together with the refractive indexes of the different materials, see previous section.

3.2.4 Photoluminescence

PL measurements are performed in a spectrofluorometer FP-6500 (Jasco) (see its main scheme in Figure 3.3). To generate the pump beam, the system is equipped with a Xenon lamp that is felt into a monochromator to select the desired wavelength and bandwidth. The system allows for tuning the pump wavelength between 220 and 750 nm, which is convenient for optimizing the sample excitation. The pump beam impinges on to the sample, where part of the light is reflected, part absorbed and part transmitted. Then, the PL of the sample is collected at a 90° angle with respect to the pump beam and sent to the detector. For liquid samples, the cuvette walls are placed perpendicularly to the pump beam, with this configuration just the PL is collected avoiding the pump light. On the other hand, thin film samples are placed with their surface forming a 60° angle with the pump beam, 30° with the collection direction, to avoid damages in the detector due to reflected light from the pump. The detector combines a monochromator and a photomultiplier to analyse separately each wavelength, which is beneficial for detecting low intensity signals. Although, the system operational wavelength range extends between 220 and 750 nm, the noise to signal ratio increases beyond 650 nm distorting the measure.

During the stay in the Politecnico di Milano, PL measurements were performed in a NanoLog spectrofluorometer (Horiba Jobin Yvon). Although, the system is basically identical to the FP-6500 (Jasco), it incorporates a more sophisticated photomultiplier that extends the detection range to 800 nm. Moreover, the NanoLog system counts with a secondary photodetector (Liquid nitrogen cooled InGaAs array) with an operational spectral range from 800 to 1700 nm.

3.2.5 Photoluminescence Quantum Yield

The PL efficiency or PLQY (ϕ_{PL}) is, besides the PL spectrum, one of the most important parameters for the PL characterization of a given material. As stated in Section 1.1.1, the ϕ_{PL} is defined as the number of emitted photons relative to the number of absorbed ones. Then, it determines the suitability of a certain compound for PL applications and consequently for gain application. Implicitly, such parameter contains not only the information of radiative processes but also that for non-radiative ones, which might be useful to trace intermolecular interactions, aggregation and other non-radiative processes detrimental for the PL. Here, two methods are used to determine ϕ_{PL} depending on whether the samples are liquid solutions or thin films over substrates.

Liquid Solution Samples

In this case, $\phi_{PL}{}^{sol}$ is determined by a comparative method,[135] which relies on a direct comparison between the absorbed and emitted light of the sample with those of a well-established reference. In first place, the absorption and emission spectra of both sample and reference are collected to determine their absorbance at the pump wavelength (OD_λ) and their integrated PL intensity (E). Then, the sample's $\phi_{PL}{}^{sol}$ is determined by applying

$$\phi_{PL}^{sol} = \phi_{PL}^{ref} \frac{E\ OD_\lambda^{ref}\ I_{pump}^{ref}\ n^2}{E^{ref}\ OD_\lambda\ I_{pump}\ n_{ref}^2} \qquad 3.7$$

where I_{pump} is the pump intensity and n the refractive index. The labelled parameters refer to reference and those unlabelled to sample. This expression contains terms to correct the effect of different solvents or/and variations in pump wavelength (λ_{pump}) between sample and reference. Nonetheless, these are arduous measurements and special attention should be taken to avoid false results. Specially, appropriate references should be used, whose absorption and emission regions should approximately coincide with those of the sample. Thus, mistakes related to variations in the pump intensity are avoided by selecting a common λ_{pump}. Also, the use of at least two references for cross-referencing assures the result. Furthermore, the excitation conditions used for the PL collection should match those used for the absorption characterization. Importantly, the error can be minimized by performing several measurements, i.e. on solutions with different concentrations to determine the ratio between emission and absorption, see Figure 3.4. Hence, the comparison holds between the slopes of the linear fits (m)

$$\phi_{PL}^{sol} = \phi_{PL}^{ref} \frac{m\ I_{pump}^{ref}\ n^2}{m^{ref}\ I_{pump}\ n_{ref}^2} \qquad 3.8$$

More details on these measurements appear in the online guide for PL quantum yield determination by Horiba.[136]

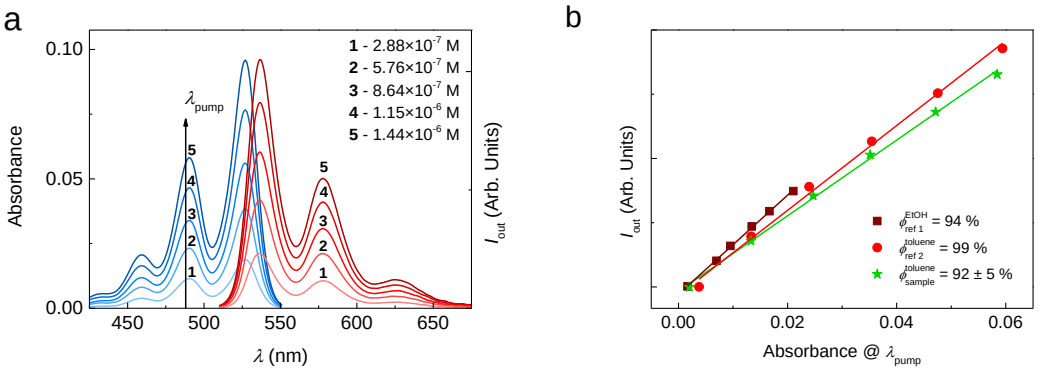

Figure 3.4 Photoluminescence quantum yield determination for solution samples. (a) Absorption (blue lines, left axis) and PL spectra (red lines, right axis) of PDI-O dissolved in toluene at different concentrations (see legend). (b) Integrated PL spectrum versus absorbance at $\lambda_{pump} = 488$ nm for PDI-O and PDI-C6 (reference 2) in toluene and rhodamine 6G (reference 1) in ethanol.

Thin Film Samples

The PL quantum yield of thin film samples (ϕ_{PL}^{film}) was determined with an integrating sphere SF-834 (Jasco) attached to the spectrofluorometer FP-6500, see the scheme in Figure 3.5a. This integrating sphere is designed for measurements in opaque solid or powder samples. However, it can be adapted for quantum yield measurements in planar waveguides by employing a multiplicative correction factor (ξ) accounting for the emitted light that kept trapped in the waveguide and therefore not detected (see Figure 3.5b). For this purpose, it is assumed that the PL emission by the molecules in the waveguide is isotropic, i.e. the light is emitted in all directions forming a sphere of area $\Omega_0 = 4\pi R$. Only part of the emitted light would escape the waveguide. Particularly, with the light forming an angle with respect to the normal to the surface shorter than the critical angle (θ_c)

$$n_f \sin\theta_c = n_c \qquad 3.9$$

where n_f and n_c are the refractive indexes of the film and the cover (air in this case), respectively. Then, the escaping light forms a spherical dome of area Ω that can be calculated using

$$\Omega = 2\pi R h = \pi(a^2 + h^2) \qquad 3.10$$

with R the radius of the emission sphere and h and a the height and radius of the spherical dome formed by the escaped light. Then, the portion of light escaping the waveguide can be expressed as

$$\frac{\Omega}{\Omega_0} = \frac{1}{2}\left(\left(\frac{a}{R}\right)^2 + \left(\frac{h}{R}\right)^2\right) \qquad 3.11$$

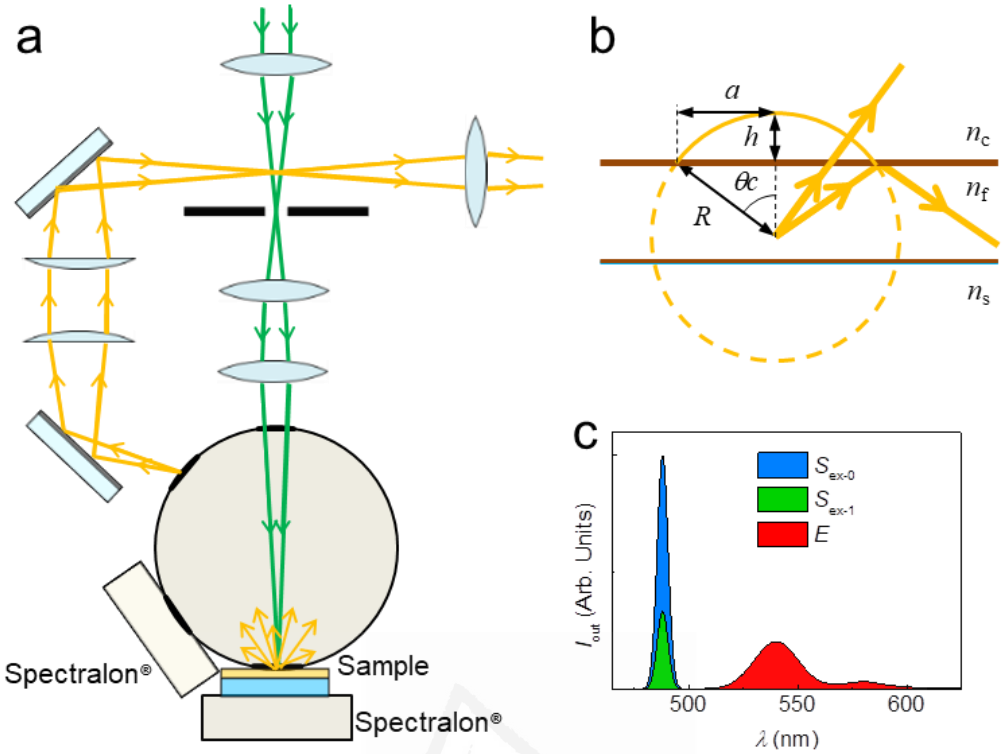

Figure 3.5 Photoluminescence quantum yield determination for planar waveguide samples. (a) Integrating sphere scheme. (b) Emission diagram used to calculate the geometric correction. R is the radius of the emission sphere, h and a the height and radius of the spherical dome, θ_c the critical angle and n_c, n_f and n_s the refractive indexes of the cover, film and substrate, respectively. (c) Reference scattering spectrum (S_{ex-0}, blue peak) and sample scattering (S_{ex-1}, green peak) and emission (E, red peaks) spectra used to calculate ϕ_{PL}^{film}.

By applying the basic trigonometric relationships $\sin(\theta_c) = a/R$, $\cos(\theta_c) = 1\text{-}(h/R)$ and $\cos(\theta_c)^2+\sin(\theta_c)^2 = 1$, it is possible to demonstrate that

$$\frac{a}{R} = \frac{n_c}{n_f} \qquad 3.12a$$

$$\frac{h}{R} = 1 - \sqrt{1 - \left(\frac{n_c}{n_f}\right)^2} \qquad 3.12b$$

Then, the portion of light escaping the waveguide can be expressed in terms of the refractive indexes

$$\frac{\Omega}{\Omega_0} = \frac{1}{2}\left(\left(\frac{n_c}{n_f}\right)^2 + \left(1 - \sqrt{1 - \left(\frac{n_c}{n_f}\right)^2}\right)^2\right) \qquad 3.13$$

This expression accounts for the light escaped to the cover, but even a larger portion of light is also radiated to the substrate, which is reflected backward by a Spectralon® piece attached to the substrate, see Figure 3.5a. Then, the light escaping the system is twice that

calculated in Equation 3.13. Thus, by applying elementary arithmetic, it is possible to demonstrate that the geometric correction factor can be written

$$\xi = \frac{\Omega_0}{\Omega} = \frac{2{n_\mathrm{f}}^2}{1 + \left(n_\mathrm{f} - \sqrt{{n_\mathrm{f}}^2 - 1}\right)^2} \qquad 3.14$$

where an air cover is assumed ($n_\mathrm{c} = 1$). This factor corrects for the emitted light that keep trapped in the waveguide, and then is not detected.

The measurement involves the determination of the reference scattering spectrum and the sample spectrum, see Figure 3.5c. The reference consists in an identical waveguide with the same film thickness and without the active dopant, i.e. the organic molecule. The spectra are determined by placing the reference/sample in the window 1 with a Spectralon® piece behind and a second piece of Spectralon® blocking the window 2, see Figure 3.5a. The integral of the reference scattering spectrum ($S_{\text{ex-0}}$) is proportional to the excitation intensity. The sample spectrum is composed of the scattering spectrum and the emission spectrum. The integral of the scattering component ($S_{\text{ex-1}}$) is proportional to the non-absorbed light and the integral of the emission spectrum (E) is proportional to the emitted light. Then, the uncorrected PL quantum yield ${\delta_\mathrm{PL}}^{\text{film}}$ is calculated by applying

$$\delta_\mathrm{PL}^{\text{film}} = \frac{E}{S_{\text{ex}-0} - S_{\text{ex}-1}} \qquad 3.15$$

Then, to get ${\phi_\mathrm{PL}}^{\text{film}}$ the correction is applied to ${\delta_\mathrm{PL}}^{\text{film}}$

$$\phi_\mathrm{PL}^{\text{film}} = \xi \theta_\mathrm{PL}^{\text{film}} \qquad 3.16$$

The precision in determining the light absorption ($S_{\text{ex-0}}$-$S_{\text{ex-1}}$) is the main source of error of this method. The error can be maintained at its minimum by using as a reference an inert waveguide, as similar as possible to that of the sample, i.e. similar refractive index and thickness. Eventually, several measurements are used to estimate a statistical error.

3.3 Characterization of Transient Photophysical Properties

Important information about the time evolution of the system after excitation can be extracted from the transient photophysical properties, for example the energy transferring between different energy levels, the formation of excimeric species, etc. Here, two techniques are used in order to characterize such transient properties, time-correlated single photon counting (TCSPC) and ultrafast TA spectroscopy. As none of them are available at the UA, the measurements have been performed through two research stays performed during this thesis. Particularly, a brief visit to the Institute of Photonics and Nanotechnology at Vilnius University and a 3 moth stay at the Physics Department of the

Politecnico di Milano. In both institutions, data acquisition was performed in collaboration with experienced colleagues in charge of the experimental setups.

3.3.1 Time-Correlated Single Photon Counting

PL is generated when a molecule in its excited state decays to its ground state by emitting a photon, see Section 1.1.1. Since molecular decay is a stochastic process, the time elapsed between the excitation and the decay is not unique, but rather a distribution of times instead. Indeed, after the sample is excited with a laser pulse and many molecules are in their excited state, the molecular decay produces a continuous waveform. Then, the PL lifetime (τ_{PL}) is defined as the average time needed for the molecule to decay from its electronic excited state to its ground state. As in the case of ϕ_{PL}, τ_{PL} encodes information about both, radiative and non-radiative processes in the system, being a way of quantifying the average time available for the electron to be used for radiative process. However, resolving such waveform in time to determine τ_{PL} is a complicated process because the time scale in which the process occurs is rather small (ns).

In order to solve this issue, the approach of TCSPC consists in adjusting the experimental conditions in order to have only one photon detected per laser pulse. Under such conditions, the time delay (Δt) between the excitation pulse and the detection of the emitted photon is individually determined and added to a histogram. Such histogram is a representation of the sample waveform or transient, which can be eventually fitted with single, double or triple exponential functions, to determine τ_{PL}. For double and triple exponentials, τ_{PL} is calculated as the weighted average of the exponentials time constants using[137]

$$\tau_{PL} = \frac{\sum A_{\mathrm{i}} \tau_{\mathrm{i}}}{\sum A_{\mathrm{i}}} \qquad 3.17$$

where τ_{i} are the time constants of the exponentials and A_{i} their corresponding weights in the fit. The scheme presented in Figure 3.6 illustrates the basic TCSPC setup.

At the Institute of Photonics and Nanotechnology at Vilnius University, a TCSPC system PicoHarp 300 (PicoQuant GmbH) was used. In this setup, a picosecond diode laser (1 MHz, 70 ps, 510 nm), driven by its internal clock, is used as excitation source. First, the excitation beam is projected over the sample via some appropriate optics and neutral density filters are used to maintain a single photon per cycle regime at the detector. Then, the PL generated by the sample is collected and sent into a monochromator, where the desired wavelength is selected and passed to the photomultiplier detector. Finally, theoutput signal of the photomultiplier, together with the laser driver sync signal, is fed to the TCSPC electronics, where both signals are analysed to provide the photons statistics.

The TCSPC system used at the Physics Department in the Politecnico di Milano, is somehow similar to that previously described.[138] Nevertheless, in this second setup, asupercontinuum laser (Fianium) is used as the excitation source. Such laser presents ps

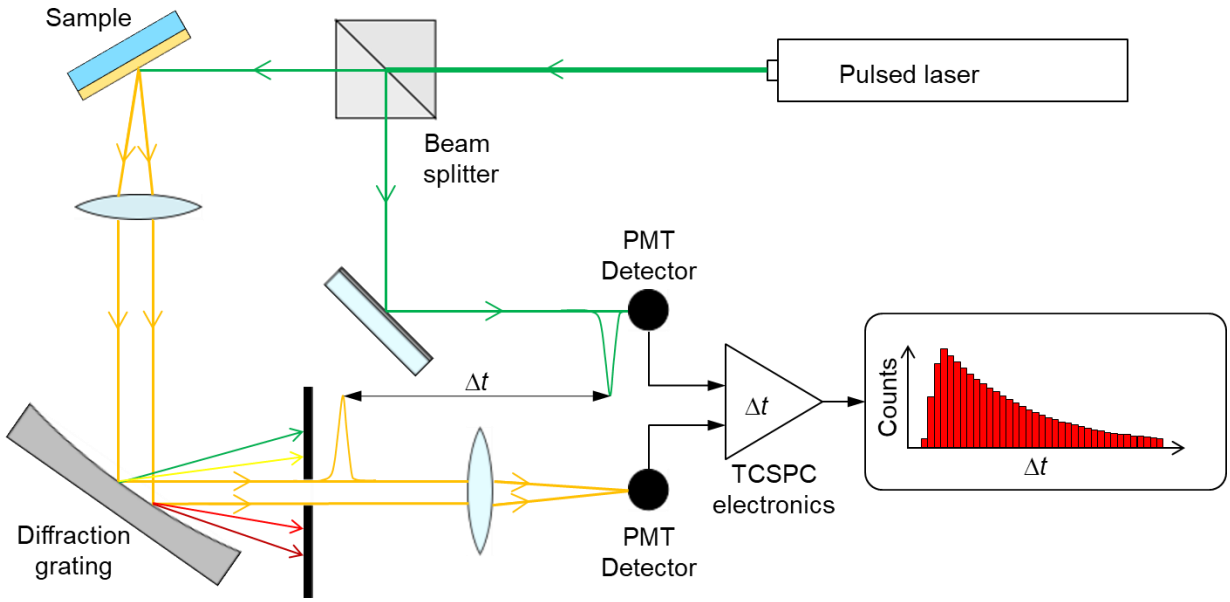

Figure 3.6 Scheme of time-correlated single photon counting basic setup.

emission at 40 MHz rate in the spectral range between 480 nm to 1700 nm and band-pass filters are used to select the excitation wavelength. Then, the emission is collected at 90° with respect to excitation using appropriate optics and the scattered excitation is filtered out with a long-pass filter. Finally, the filtered signal is sent to an imaging spectrometer SP-2150i (Princeton Instruments), where it is spatially dispersed before being imaged with a 16-channel photomultiplier (about 9 nm/channel) coupled to the TCSPC electronics (Becker and Hickl).

3.3.2 Ultrafast Transient Absorption Spectroscopy

The ultrafast TA technique is based in the detection of the spectral changes induced in the absorption spectrum of the sample by a pump pulse, which is accomplished by testing the sample with a probe pulse before and after the excitation. The pump-induced changes can be tracked in time by controlling the time delay between pump and probe, being the temporal resolution limited by the duration of the pump and probe pulses. In the non-degenerate version of this technique, different wavelengths are used for pumping and probing the sample. Typically, a narrow pump pulse is desirable to excite selectively the different transitions. However, a compromise between spectral and temporal resolution exists. The probe should be spectrally broad to test simultaneously many wavelengths. Besides, it should be as short as possible to warrantee an optimal temporal resolution.

Figure 3.7 shows the experimental setup used at the Politecnico di Milano for the TA characterization. Initially, the output of an amplified Ti:Sapphire laser (1 kHz, $\lambda = 800$ nm, pulse width $\sim$ 100 fs) is split in two similar beams destined to generate the pump and probe beams. An optical parametric amplifier (OPA) is used to tune λ_{pump} from 400 to 800 nm. In the OPA, a second-order nonlinear crystal (barium borate, BBO) is used to convert a pump photon of frequency (ν_{p}) into two photons of lower energy called signal

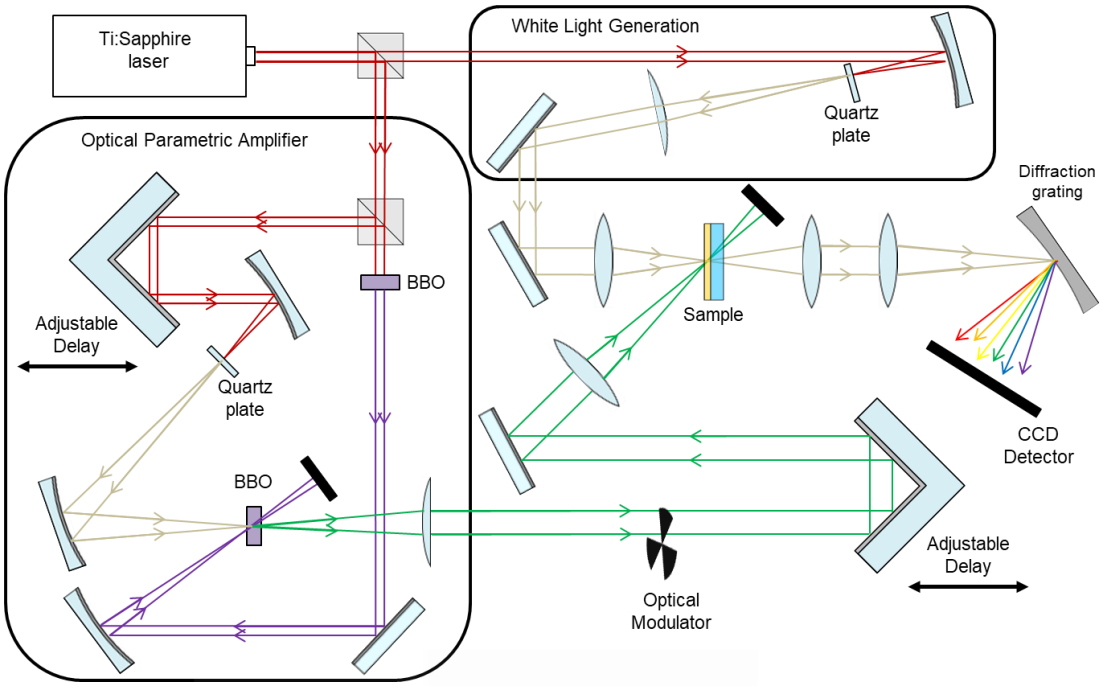

Figure 3.7 Experimental setup for transient absorption characterization.

(ν_s) and idler (ν_i). The process should preserve the energy ($\nu_p = \nu_s + \nu_i$) and momentum ($\Delta k = k_p - k_s - k_i$), which is warranted by the phase matching condition. Additionally, the process is amplified by seeding the crystal with a second photon with the same frequency of the signal. The BBO crystal is pumped with one half of the laser beam, whose frequency is doubled with a second-harmonic generation crystal (BBO). For the seed, the other half of the laser beam is tightly focussed over a quartz plate to generate a white pulse. The spatial dispersion of the white pulse is used to select the seed wavelength by adjusting the overlap between the pump and the seed pulses in the BBO crystal. In this way, the signal pulse generated is used as the pump pulse for the experiment. The pump pulse is modulated and passed through an adjustable delay to control the time delay between the pump and probe beams. On the other hand, the probe beam is generated by focussing tightly the laser beam on a quartz plate to generate a spectrally broad white pulse. Eventually, both pulses, i.e. pump and probe, are focussed on the same spot of the sample and the probe is interrogated within a multichannel detector.

Initially, the pump-induced change in the transmittance (ΔT) is determined by measuring the pump-on (T^*) and pump-off (T) transmittance spectra and normalized to T, providing the amount $\Delta T/T$. In this thesis, third-order nonlinear effects are disregarded attending to the separation between pulses and the use of non-degenerated pump-probe. Then, the interpretation is based in the population dynamics following the Beer's law presented in Equation 1.13. The absorption coefficient (α_{ij}) for an electronic transition between two levels, $|i\rangle$ and $|j\rangle$, with electronic populations N_i and N_j can be expressed in terms of its cross-section (σ_{ij}) as $\alpha_{ij}(\lambda) = \sigma_{ij}(\lambda)\ (N_i - N_j)$. Here, $\alpha_{ij} > 0$ corresponds to absorption and $\alpha_{ij} < 0$ to gain. Then, considering several transitions the absorption coefficient of the system can be expressed according to

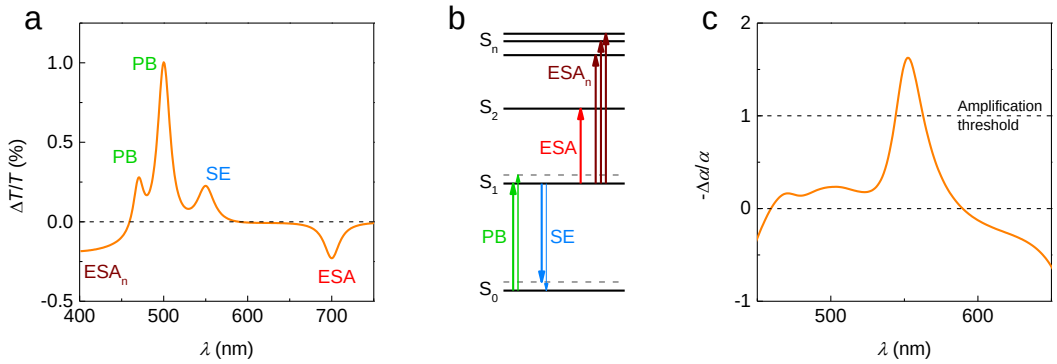

Figure 3.8 Transient Absorption spectroscopy. (a) Typical transient absorption spectra of organic compound. (b) Jablonski diagram of such organic compound. (c) Pump-induced absorption coefficient normalized to the steady-state absorption coefficient.

$$\alpha = \sum_{\mathrm{i,j}} \sigma_{\mathrm{ij}}(\omega)\left(N_{\mathrm{i}} - N_{\mathrm{j}}\right) \qquad 3.18$$

In the experiment, the pump pulse promotes a change in the level occupation, which pass from N to $N + \Delta N$. It is possible to demonstrate that in the small-signal approximation the following expression is derived from Beer's law (Equation 1.13)

$$\frac{\Delta T}{T} = -\sum_{\mathrm{i,j}} \sigma_{\mathrm{ij}}(\omega)\Delta N_{\mathrm{j}} l \qquad 3.19$$

with l is the sample thickness. The time evolution of the system is implicit in the population term ($\Delta N_{\mathrm{j}}(\Delta t)$) where Δt is the time delay between pump and probe. Three principal effects can be found in the TA spectra, as illustrated in Figure 3.8a and 3.8b for the typical organic compound. Whenever the probe is resonant with the ground state absorption, i.e. an electronic transition between levels $|0\rangle$ and $|\mathrm{j}\rangle$, an increment is observed in the probe transmission after excitation. This phenomenon is a consequence of the ground-state depletion upon excitation, termed photobleaching (PB). Another possibility is the promotion of an electron from an excited level $|\mathrm{i} \neq 0\rangle$ to another state laying at higher energy $|\mathrm{j}\rangle$, which results in a negative signal in the TA spectrum. This phenomenon is known as excited-state absorption (ESA). Finally, decay of electrons from the lowest excited state $|1\rangle$ stimulated by the probe pulse, results in an enhancement of the transmission ($\Delta T/T > 0$). This phenomenon is known as stimulated emission (SE).

Important information about the gain of the system can be extracted from the pump-induced change in the absorption coefficient relative to the steady-state absorption coefficient ($-\Delta\alpha/\alpha$), where three main spectral regions can be observed (see Figure 3.8c): *i*) negative values ($-\Delta\alpha/\alpha < 0$), which correspond to pump-induced losses; *ii*) positive values below the amplification threshold ($0 < -\Delta\alpha/\alpha < 1$), that correspond to pump-induced gain, which is not sufficient to compensate the system losses; and *iii*) positive values above the amplification threshold ($-\Delta\alpha/\alpha > 1$), which correspond to pump-induced gain, which is sufficient to overtake losses, thus amplification is observed.

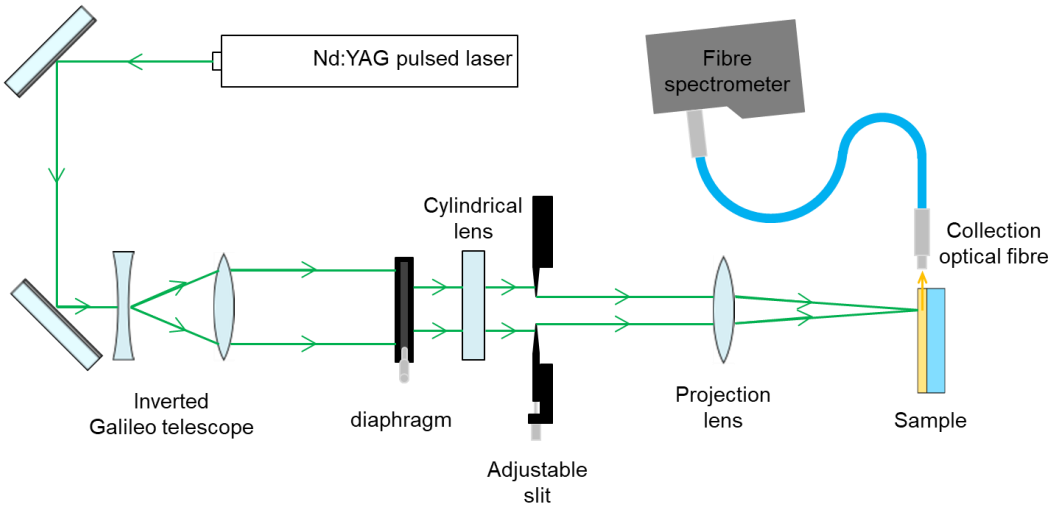

Figure 3.9 Amplified spontaneous emission setup.

3.4 Lasing Studies

The suitability of photoluminescent materials for gain applications is tested by exposing them to intense photoexcitation sufficient to generate a population inversion. In this sense, the presence of ASE in the active waveguide is an indication of gain and amplification that convert the material in a good candidate for lasing applications, as described in Section 1.2. In this section, the methods used to quantify the ASE performance are described, which include the determination of the ASE threshold, the gain coefficient and the propagation losses. Additionally, the characterization of DFB lasers is explained.

3.4.1 Experimental Setup for Amplified Spontaneous Emission Characterization, Including Gain and Losses

The ASE properties, gain and losses have been characterized in a common setup represented in Figure 3.9, which consists of a pumping source, as well as excitation and collection optical systems. Such elements are described separately below.

Two different models of Nd:YAG lasers have been used as excitation sources: *i*) a NG:YAG laser Quanta-Ray INDI (Spectra-Physics) operating in Q-switch mode with 10 Hz repetition rate and 5.7 ns pulse width, which can provide emission at three different wavelengths, 1064 nm, 532 nm and 355 nm, corresponding to the fundamental emission and its second and third harmonics, respectively; *ii*) a Nd:YAG laser LS-2137U (LOTIS TII), operating in Q-switch mode with 10 Hz repetition rate, whose output is coupled to a built-in optical parametric oscillator (OPO) LT-2214OPO (LOTIS TII). An OPO uses a second-order nonlinear crystal (BBO here) to convert the impinging laser pulse of wavelength λ_p into two pulses of longer wavelengths, termed as signal (λ_s) and idler (λ_i).

The process must preserve energy ($\nu_p = \nu_s + \nu_i$) and momentum ($\Delta k = k_p - k_s - k_i$), which is achieved by phase matching. In this way, the OPO provides conversion of the Nd:YAG third harmonic (355 nm) to the desired wavelength in the range from 420 to 690 nm, for the signal, and from 720 to 2300 nm, for the idler.

The excitation optics allows shaping and finely controlling the laser beam generated by the excitation source. Initially, the laser beam is expanded and collimated with an inverted Galileo telescope and its external part is filtered out with a diaphragm to ensure a homogeneous beam profile. The inverted Galileo telescope is composed by combination of a divergent lens (focal length, $f_{g1} = -5$ cm) and a convergent lens ($f_{g2} = +10$ cm), with a distance between them of $f_{g1} + f_{g2}$. Next, a cylindrical lens ($f_c = +15$ cm) and an adjustable slit are used to shape the laser beam into a narrow strip of 3.5 mm by 0.5 mm, which finally is projected over the sample's (with one end of the stripe reaching the edge sample) with a spherical lens ($f_p = +10$ cm). This avoids the slit diffraction and ensures the intensity beam homogeneity.[139] The strip length is controlled with an adjustable slit aperture and its thickness with the distance between the cylindrical lens and the slit. The distance between the slit and the projection lens and between the projection lens and the sample is $2f_p$, so that the dimensions of the projected image coincide with those of the slit. Eventually, the pump energy density (E_{pump}) impinging over the sample is measured with a power meter 843-R (Newport) and controlled with a set of neutral density filters (E_{pump} error $\sim 20\%$).

After excitation, a fibre optics (600 μm diameter) is used to collect the guided PL generated by the sample from its edge. Then, the collected emission is sent to a fibre spectrometer USB2000+ UV-VIS (Ocean Optics), operative in the range 340-1026 nm with a 1.3 nm optical resolution, attached to a computer. Additionally, a fibre optics attenuator can be introduced to attenuate the collected signal when needed. Finally, the collected spectra are analysed to determine the different ASE parameters.

3.4.1.1 Basic Amplified Spontaneous Emission Parameters: Linewidth, Threshold and Operational Lifetime

Typically, the presence of ASE in a certain material is detected by two pump-dependent evidences. In first place, the PL spectrum collapses into a narrow peak centred at λ_{ASE}, usually known as the ASE peak, above a certain value of the pump energy density termed ASE threshold ($E_{th\text{-}ASE}$), see Figure 3.10a. The linewidth of the ASE peak well above threshold (referred as the ASE linewidth) is typically of a few nm. Particularly, the spectral narrowing occurs at one of the PL transitions of the material and is a direct consequence of the amplification of this transition above the others. Secondly, the output intensity (I_{out}) as a function of pump energy density (E_{pump}) shows two regimes (see Figure 3.10b): a linear regime is observed for $E_{pump} < E_{th\text{-}ASE}$, where only spontaneous emission contributes to the PL spectrum; and an exponential regime for $E_{pump} > E_{th\text{-}ASE}$, in which stimulated emission dominates over the spontaneous one. Thus, $E_{th\text{-}ASE}$ is an important parameter to be determined, as it represents the minimum energy needed for the system to start providing light amplification. Among the several ways reported in literature for

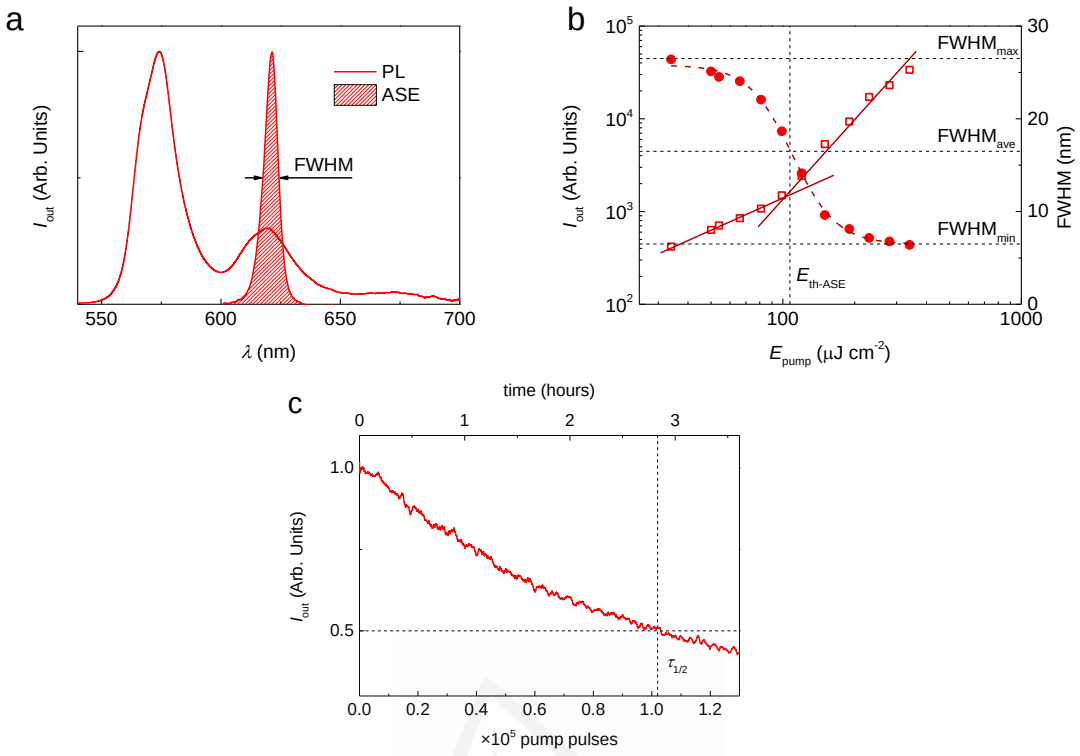

Figure 3.10 Amplified spontaneous emission basic characterization. (a) Guided PL (red solid line) and ASE (red-dashed area) spectra collected from the edge of the sample upon optical excitation. (b) Output intensity (I_{out}; open squares, left axis) and emission linewidth, defined as the full width at half maximum (FWHM; solid circles, right axis), as a function of pump energy density (E_{pump}). (c) I_{out} normalized to its initial value as a function of time or the number of pump pulses (bottom and top axis, respectively).

determining $E_{th\text{-}ASE}$,[140] in this work it is obtained as the fluence at which the emission linewidth (defined as the full width at half maximum, FWHM) reaches the average value between the ones observed at low and high excitation densities. Such $E_{th\text{-}ASE}$ value is approximately coincident with that at which a drastic slope change is observed in the in I_{out} versus E_{pump} representation see Figure 3.10b.

The resistance to photodegradation during ASE operation is another important characteristic of the active materials. Here, the ASE photostability is characterized by analysing the temporal evolution of the ASE emission under uninterrupted pump at permanent energy, in a fixed position of the sample and under ambient conditions, see Figure 3.10c. The ASE peak evolution is used to determine the ASE photostability half-life ($\tau_{1/2}$), which is defined as the time or number of pump pulses needed for the ASE intensity to reach half of its initial value.

3.4.1.2 Gain and Losses Determination

Through this thesis, two different methods have been used to determine the net gain coefficient (g_{net}) and propagation losses (κ) in the waveguides.

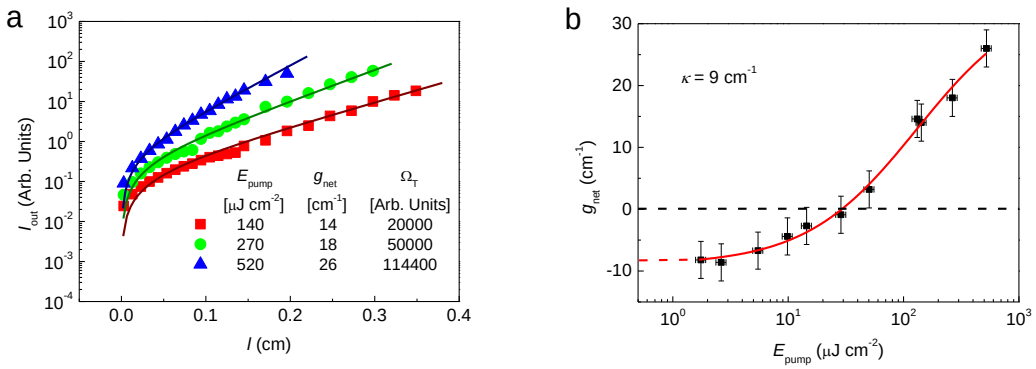

Figure 3.11 Variable stripe length method for gain and losses retrieval. (a) Output intensity (I_{out}) as a function of excitation stripe length (l) under different pump fluences (E_{pump}). Solid lines are fits to data with Equation 1.31, to determine the net gain parameter (g_{net}). (b) Evolution of g_{net} with E_{pump}. The red solid line is a guide to the eye and the red dashed line corresponds to the extrapolation of the experimental data to determine the propagation losses coefficient (κ).

Variable Stripe Length Method

The variable stripe length (VSL) method is the best established procedure in the literature for determining g_{net} and κ.[29,141] In practice, the ASE intensity (I_{out}) is measured as a function of the excitation stripe length (l) at a fixed E_{pump}. As stated in Section 1.2.4, in the small-signal regime, in which saturation can be neglected, I_{out} follows Equation 1.31. Despite the fact that there are more complex models that take into account the effects of saturation,[142–144] the one presented in Section 1.2.4 is the more frequently used model. Under the experimental conditions, it is possible to combine the geometrical parameter ($\Omega_0(4\pi)^{-1}$), the spontaneous emission rate (A) and the pump intensity (I_{pump}) into a single constant parameter (Ω_T) to simplify the expression into

$$I_{ASE}(l) = \Omega_T \frac{(e^{g_{net}l} - 1)}{g_{net}} \qquad 3.20$$

Therefore, the model has two free parameters only and can be easily fitted to the experimental data to retrieve g_{net} and Ω_T for a given λ and E_{pump}, see Figure 3.11a. Additionally, g_{net} is the result of subtracting losses κ from gain Γg, as expressed in Equation 1.37. Interestingly, g_{net} and g are pump-dependent, whilst κ is not, which implies the limit

$$\lim_{E_{pump}\to 0} g_{net} = -\kappa \qquad 3.20$$

Thus, κ can be estimated from plot of g_{net} versus E_{pump} by extrapolating g_{net} to $E_{pump} = 0$, see Figure 3.11b.[63,145]

Variable Pump Intensity Method

Alternatively to the VSL method, Dr. L. Cerdán recently proposed another method to determine the gain and losses, based in the standard ASE measurement or variable pump intensity (VPI) method.[146,147] Although the VSL method can be implemented quite simply, it presents some drawbacks such as dealing with detection coupling artefacts, photostability issues of the material, etc. At this respect, the VPI method, in which E_{pump} varies for a fixed l, is more robust against misleading results and less time-consuming. By assuming a homogeneous gain distribution, the expression describing the evolution of ASE as a function of λ, E_{pump} and l can be written

$$I_0\left(\lambda, E_{\mathrm{pump}}, l\right) = \frac{\Omega(\lambda)\eta\left(E_{\mathrm{pump}}\right)}{\gamma(\lambda)\Delta n\left(E_{\mathrm{pump}}\right) - \kappa(\lambda)}\left(e^{\left(\gamma(\lambda)\Delta n\left(E_{\mathrm{pump}}\right) - \kappa(\lambda)\right)l} - 1\right) \qquad 3.21a$$

$$\Delta n\left(E_{\mathrm{pump}}\right) = \Delta n_0 \frac{\frac{E_{\mathrm{pump}}}{E_1^s} + \left(\frac{E_{\mathrm{pump}}}{E_2^s}\right)^m}{1 + \frac{E_{\mathrm{pump}}}{E_1^s} + \left(\frac{E_{\mathrm{pump}}}{E_2^s}\right)^n} \qquad 3.21b$$

where η and Δn are different measures of the temporally integrated spatially averaged excited state population, Δn_0 is a proportionality factor, $I_1{}^s$ and $I_2{}^s$ are a sort of saturation intensities, m and n (with $m > n$) are exponents that determine how fast or slow the population inversion grows and saturates, and the fluorescence parameter $\Omega(\lambda)$ is proportional to the fluorescence spectrum. Fitting the experimental data with this model represents by itself a challenge. For this reason, Dr. Luis Cerdán has developed a graphical user interface (GUI) to do it.[148] Initially, the GUI uses the PL spectrum as a constraint to calculate the system losses (κ) by comparison with the ASE spectrum well-below the threshold, which implies a high sensitivity to initial conditions. Therefore, extreme attention should be paid to collect ASE spectra well-below the threshold. Additionally, it is recommended to measure the PL spectrum with the same spectrophotometer used to collect the ASE spectra, rather than with a fluorimeter, to avoid systematic errors. Subsequently, the GUI fits the rest of the ASE spectra to determine g_{net} and the other parameters.

3.4.2 Distributed Feedback Laser Characterization

Despite of certain modifications included to deal with the particular geometry of second order DFB lasers emission, the setup used for laser characterization is essentially the same used for ASE, see Figure 3.12. Here, the laser beam is expanded, collimated and filtered with the particular combination of inverted Galileo telescope and diaphragm previously described, see Section 3.4.1. Then, the pump beam is focused on the DFB device by means of a spherical lens ($f = +10$ cm), forming an impinging angle of $\sim 30°$ with respect to the normal of the device surface. Therefore, the pump beam is shaped into an ellipse of 1.1 mm short axis over the device's surface. Again, E_{pump} is determined with a power meter and controlled with a set of neutral density filters. For second order DFB

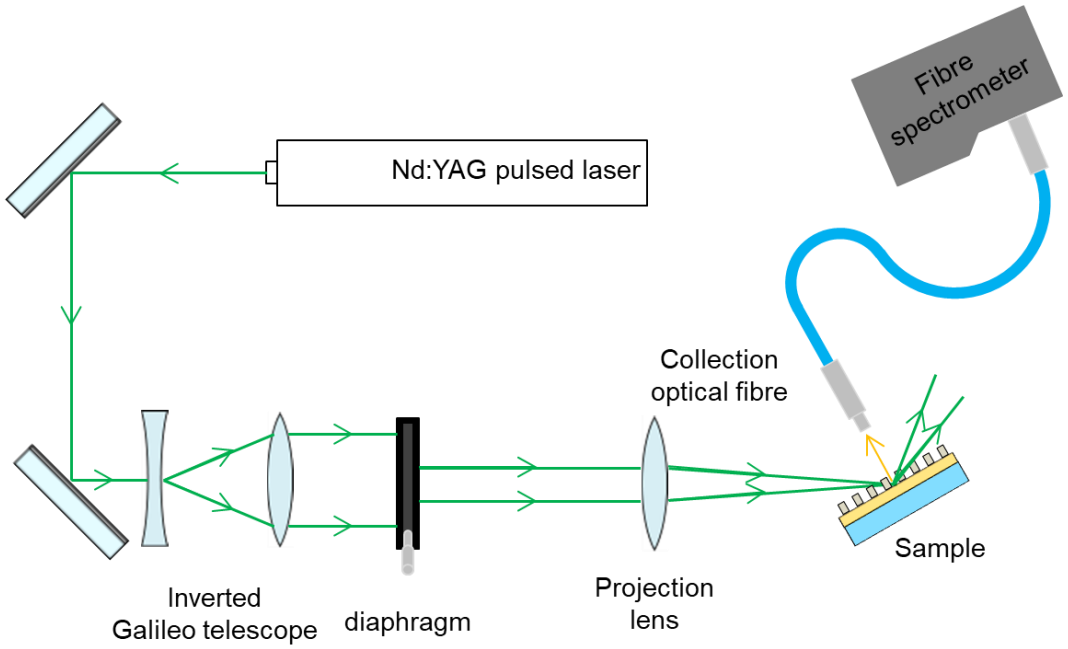

Figure 3.12 Setup for distributed feedback characterization.

devices, light emission comes majorly in a direction perpendicular to their surface (which corresponds to first order diffraction for the light extraction). Thus, the same collection optics previously described in Section 3.4.1 is placed in front of the sample to collect its normal emission.

As established in Section 1.5, DFB emission spectrum consists of narrow peaks (laser modes), each one associated with a propagating mode of the waveguide. Interestingly, the waveguide mode polarization is reflected in the laser mode. The laser emission polarized parallel to the grating lines is associated with TE modes of the waveguide, whereas laser emission with polarization perpendicular to the grating lines comes from TM modes.

Three important parameters are characterized to ascertain that the device emission is laser light: the laser threshold ($E_{\text{th-DFB}}$), the linewidth (FWHM) of the emission and the divergence of the laser beam. In first place, the collected light is analysed and $E_{\text{th-DFB}}$ is determined from plots of I_{out} and FWHM versus E_{pump}, see Figure 3.13a. This is an important parameter as it determines the energetic efficiency of the device. Secondly, the FWHM and the divergence angle (θ_{d}) are determined to characterize the temporal and spatial coherence of the laser emission. Complementary to the USB2000+, a second fibre spectrometer MAYA2000 (Ocean Optics) with a shorter operative range 550.2 – 613.7 nm, but with higher optical resolution 0.13 nm, is used here to characterize with more precision the spectral linewidth (see Figure 3.13b). which is related with its temporal coherence as stated in Section 1.5. Additionally, the laser divergence in the direction perpendicular to the grating lines is determined with an OrcaSpark CCD (Hamamatsu) by capturing the beam size at different distances from the device. Figure 3.13c shows the far-field pattern of the laser beam.

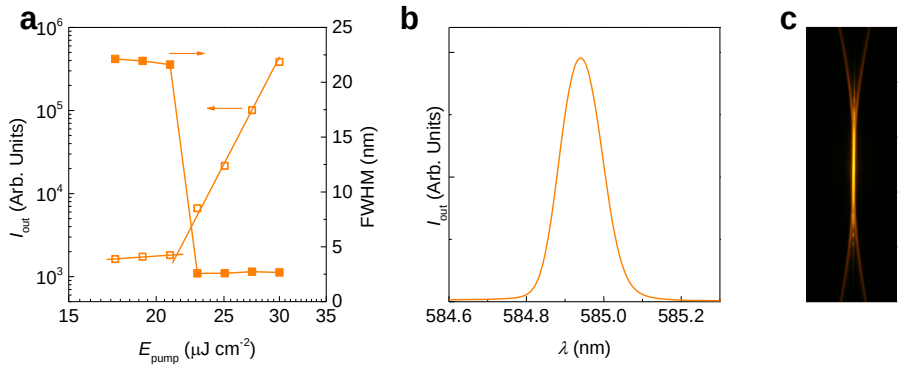

Figure 3.13 Distributed feedback (DFB) laser characterization. (a) Output intensity (I_{out}; open squares, left axis) and emission linewidth, defined as the full width at half maximum (FWHM; solid circles, right axis), as a function of pump energy density (E_{pump}). (b) High resolution spectrum of the laser emission for an E_{pump} well-above the laser threshold. (c) Image of the DFB laser emission.

Chapter 4
Perylenediimide Compounds

4.1 Influence of Blending Ratio and Polymer Matrix on the Lasing Properties of Perylenediimide Compounds

As it was stated in Section 2.4, the optimal laser performance of a certain organic compound dispersed in an inert matrix relies in several parameters, such as the compound concentration and type of matrix. In this regard, the main objective of this section is to determine which matrix (PS or PMMA) and PDI-concentration are the best for the manufacture of PDI-based TFOSL devices. With this in mind, the optical and ASE properties of PDI-doped films are analysed for a range of dye-concentrations, paying attention to the net gain and losses coefficients, which determine the material potential for a waveguide-base laser. The analysis is conducted with two entirely different PDI compounds, PDI-O and the brand new derivative *b*-PDI-A, see Figure 4.1. A distinct feature among both systems is the existence or not of substituents at the bay positions (particularly on the 1 and 7). As discussed in Section 2.2, the particular substituents anchored at the bay positions allow to incorporate the compound into the matrix in a larger concentration without significantly affecting its PL efficiency. At the same time, the substituents produce a displacement of the optical properties towards longer wavelengths.

4.1.1 PDI-O Dispersed in Polystyrene and Poly(Methyl Methacrylate) Films

Although, the optical and ASE properties of PDI-O-doped PS and PMMA films were previously reported, it was for a limited range of concentration (0.5–5 wt% for PS and 0.5–1 wt% for PMMA) and no PLQY, gain or losses data were provided.[62] Here, a more exhaustive and broad study (1–8 wt%, limited by PDI-O solubility in

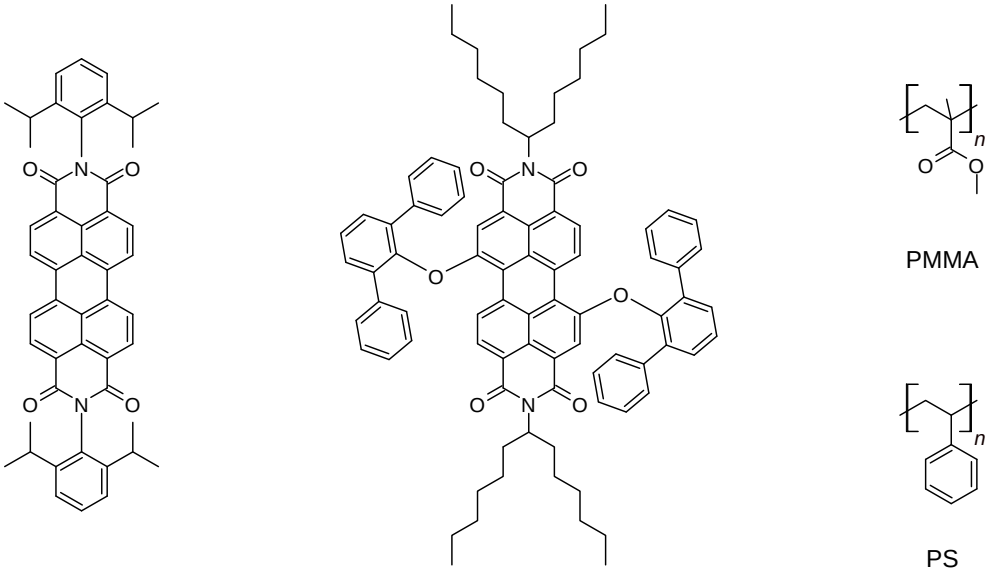

Figure 4.1 Chemical structures of PDI compounds (PDI-O and *b*-PDI-A) and thermoplastic matrixes (PS and PMMA).

tetrahydrofurane; THF) is performed to understand the effect of the matrix, either PS or PMMA, over the optical and ASE properties of PDI-O-doped films. The full set of parameters discussed in this section has been collected in Table 4.1 to facilitate the discussion. Additionally, it aids to both, support previously reported results and to fill in the gaps in the literature.

For both matrixes, the effect of aggregation and excimer formation becomes apparent as the PDI-concentration increases, see Figure 4.2. For the lowest concentration studied (1 wt%), both polymers present molecule-like character PL spectra with clear vibronic progressions and with PLQY values close to 1, indicative of isolated chromophores. However, as the concentration increases, a disruption of the $|S_1,\ 0\rangle \rightarrow |S_0,\ 0\rangle$ vibronic peak appears, accompanied of a severe drop of the PLQY. Both characteristics are consistent with H-aggregation and excimer formation, given the linear response of the absorption spectra.[149–152] Remarkably, the changes in the spectral shape appear at concentrations around 2.5 wt% for PMMA films, whereas this happens at 5 wt% for PS films, suggesting that the onset of aggregation occurs first in PMMA. Accordingly, higher PLQY values are found in PS than in PMMA at each concentration analysed.

The effects of aggregation and excimer formation have an impact on the ASE properties of the analysed films. As it usually occurs in PDI derivatives, the ASE emission consists in a narrow peak matching the first vibronic of the PL spectrum ($\sim$ 580 nm), see Table 4.1 and Figure 4.3a. The exact position of the ASE peak slightly shifts towards longer wavelengths with the concentration increase. For PS-based films, when the ASE thresholds ($E_{\text{th-ASE}}$) are represented as a function of PDI concentration in the matrix, a minimum is found at 1–3 wt% (30 μJ cm^{-2}), see Figure 4.3b. In the case of PMMA, the lowest threshold ($E_{\text{th-ASE}} = 120$ μJ cm^{-2}) is found at the lowest concentration (1 wt%), which is followed by a monotonous increase at larger concentrations. These results are

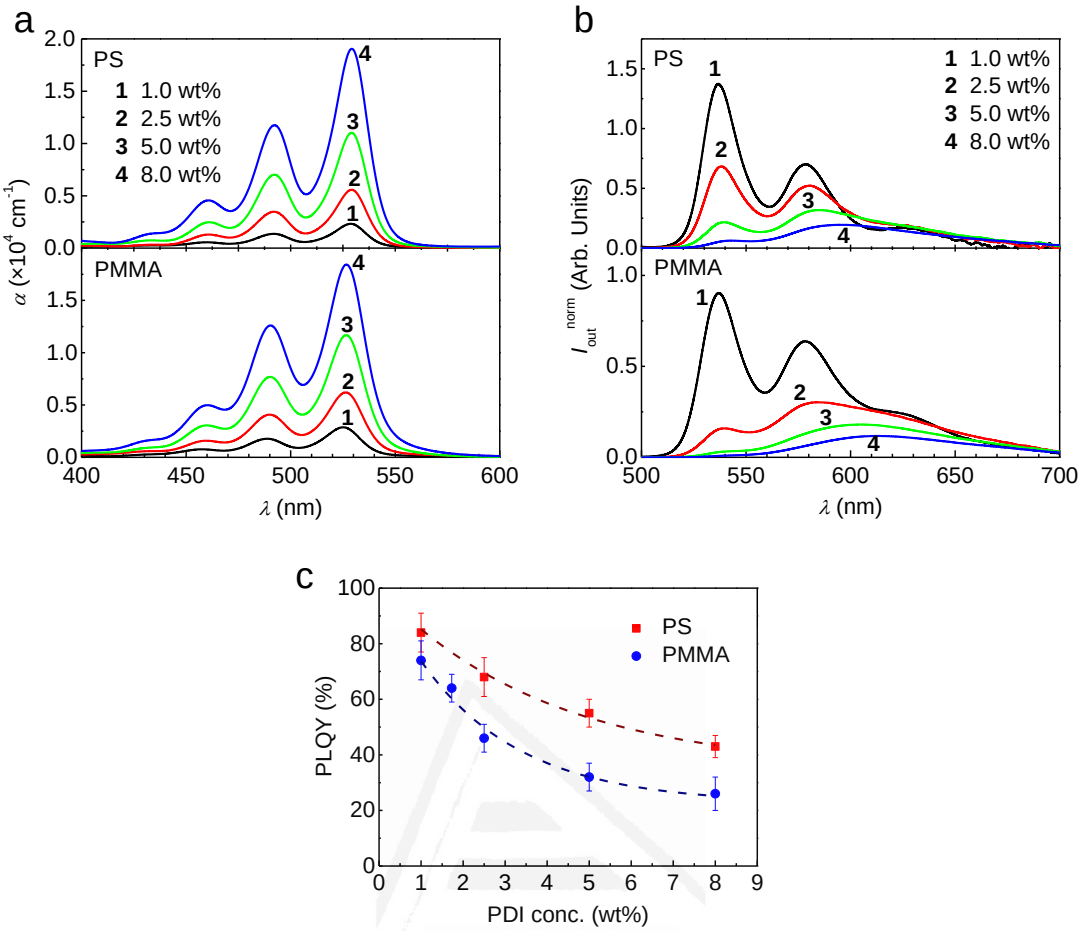

Figure 4.2 Absorption and PL properties of PDI-O dispersed in PS and PMMA films. (a) Absorption coefficient (α); and (b) PL intensity normalized to absorbance at the excitation wavelength (I_{out}^{norm}) versus wavelength (λ) for PDI-O dispersed at various doping rates in PS and PMMA films (top and bottom panels, respectively). The corresponding PDI concentrations are indicated in the legend. (c) PLQY as a function of PDI concentration for PDI-O dispersed in either PS (red squares) or PMMA (blue circles). Dashed lines are guides to the eye.

consistent with those previously reported.[62] According to the previous description of the optical properties, the threshold increase might be attributed to the formation of aggregates/excimers. Interestingly, for a given PDI concentration, the $E_{th\text{-}ASE}$ values found for PS-based films are in all cases lower than for those based in PMMA, being the difference more pronounced at higher concentrations. This suggests that other phenomena contribute detrimentally to it, as it is evidenced below with the losses characterization.

The ASE photostability of PDI-O dispersed in PS and PMMA at concentrations of 1 wt% and below were previously reported.[62] For these concentrations, the samples present high ASE half-lives ($\tau_{1/2} \sim 10^5$ pump pulses, under $E_{pump} = 2\ E_{th\text{-}ASE}$) with similar results for both polymers, PS and PMMA. Here, higher concentrations are explored revealing a reduction of $\tau_{1/2}$ with the concentration increase, see Table 4.1. Note that in order to make meaningful comparisons, values recorded at the same pump intensity

Table 4.1 Optical and ASE parameters for PS and PMMA films hosting PDI-O or *b*-PDI-A at different concentrations.

Dye	Matrix	Conc. [$\times 10^{-5}$ mol g^{-1} (wt%)][a)]	λ_{abs} [nm][c)]	α_{pump} [$\times 10^{4}$ cm^{-1}][d)]	λ_{PL} [nm][e)]	PLQY [%][f)]	λ_{ASE} [nm][g)]	$E_{th\text{-}ASE}$ [μJ cm^{-2}][i)]	$\tau_{1/2}$ (E_{pump}) [$\times 10^{3}$ pulses (mJ cm^{-2})][j)]	κ [cm^{-1}][k)]
PDI-O	PS	1.4 (1.0)	529/492/461	0.21	537/578	84	579.6	30	7 (26)[†] 500 (0.09)[†]	6
		3.6 (2.5)	529/492/461	0.52	539/581	68	580.1	43	6 (28)	
		7.4 (5.0)	529/492/461	1.02	540/585	55	581.5	130		8
		12.3 (8.0)	529/492/461	1.79	543/598	43	582.5	460	2 (26)	
	PMMA	1.4 (1.0)	526/490/459	0.20	537/578	74	579.0	120	10 (27)[†]	15
		3.6 (2.5)	526/490/459	0.50	538/583	46	579.5	210	5 (27)	
		7.5 (5.0)	526/490/459	0.96	541/603	32	580.7	1200		25
		12.2 (8.0)	526/490/459	1.54	541/610	26	580.2	8600		
b-PDI-A	PS	5.0 (5.9)	558/518/485	0.27	576/618	80	622.2	290	2.0 (3.4)	
		10.0 (11.0)	559/518/485	0.47	578/619	67	624.4	100	11 (0.6)	8
		40.0 (33.2)	559/519/485	1.53	582/620	29	626.3	150	1.7 (0.6)	
		70.0 (46.9)	560/519/486	2.12	584/622	21	627.6	660	2.6 (1.8)	
	PMMA	5.0 (5.9)	555/516/483	0.33	577/617	65	615.8	1200	1.4 (4.0)	
		10.0 (11.0)	556/516/484	0.75	580/618	31	620.9	320	1.8 (0.6)	
		40.0 (33.3)	558/518/485	1.54	581/620	10	626.0	550	0.4 (0.6)	
		70.0 (46.9)	559/518/486	2.26	584/623	15				

[a)]Dye concentration in matrix (error $\sim 0.1 \times 10^{-5}$ mol g^{-1} and ~ 0.1 wt%); [b)]Film thickness (error $\sim 5\%$); [c)]Peak absorption wavelengths (error ~ 1 nm); [d)]Absorption coefficient at $\lambda_{pump} = 532$ nm; [e)]Peak photoluminescence wavelengths (error ~ 1 nm); [f)]PLQY: photoluminescence quantum yield (error in Fig. 4.2c and Fig. 4.5c); [g)]Amplified spontaneous emission (ASE) wavelength (error is ± 0.7 nm); [h)]ASE line width, defined as the full width at half of the maximum (error is ± 1.4 nm); [i)]ASE threshold expressed as energy density ($E_{th\text{-}ASE}$; error $\sim 20\%$, estimated statistically as the standard deviation form measurements on several nominally identical samples); [j)]ASE photostability half-life under indicated E_{pump} at 10 Hz pump (error $\sim 20\%$, estimated as above); [k)]Losses determined from g_{net} as a function of E_{pump} (Fig. 4.4 and Fig. 4.7, for PDI-O and *b*-PDI-A, respectively). [†]Results taken from references [55,62].

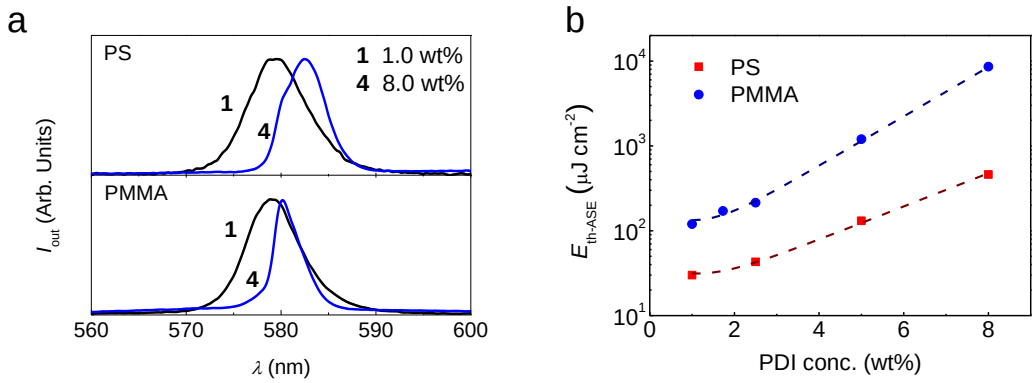

Figure 4.3 ASE properties of PDI-O dispersed in PS and PMMA films. (a) ASE spectra normalized to its maximum value for PS and PMMA films (top and bottom panels, respectively) doped with PDI-O at concentrations of 1 and 8 wt% (labels 1 and 4, respectively); (b) ASE threshold energy density ($E_{\text{th-ASE}}$) as a function of PDI concentration for PS (red squares) and PMMA (blue circles) films doped with PDI-O. Dashed lines are guides to the eye.

(independently on the threshold) have been considered. The observed reduction of threshold upon the concentration increase might be attributed to the absorption increase and subsequent larger rate of photobleaching, in accordance with observations with other types of organic molecules dispersed in thermoplastic matrixes.[70,153]

Net gain (g_{net}) and propagation losses (κ) are determined by the VLS method (Section 3.4.1.2) for the films doped with the 1 and 5 wt%, see Figure 4.4. Remarkably, PS films doped with 1 wt% of PDI-O display larger gain values ($g_{\text{net}} = 39$ cm^{-1} for $E_{\text{pump}} = 150$ μJ cm^{-2}) than those reported with other PDI derivatives ($g_{\text{net}} = 2$ cm^{-1}, at $E_{\text{pump}} = 260$ μJ cm^{-2})[60] and comparable values to state of the art dye-doped polymers such as carbon-bridged oligo(*p*-phenylenevinylene) derivatives dispersed in PS ($g_{\text{net}} = 60$ and 6 cm^{-1}, at $E_{\text{pump}} = 433$ and 115 μJ cm^{-2} respectively).[153] On the other hand, PMMA films doped with 1 wt% of PDI-O also show large gain ($g_{\text{net}} = 27$ cm^{-1} for $E_{\text{pump}} = 200$ μJ cm^{-2}), but lower than those of PS films. For higher concentrations, the differences between PS and PMMA become even more important.

The waveguide propagation losses at λ_{ASE} are estimated by extrapolating g_{net} to $I_{\text{pump}} = 0$, see Figure 4.4. For low concentrations (1 wt%), PS films present low losses ($\kappa = 6 \pm 1$ cm^{-1}), around half the value found for PMMA films ($\kappa = 15 \pm 2$ cm^{-1}). This might also contribute to the higher ASE threshold of the latter. For higher concentrations (5 wt%), PS films maintain similar losses ($\kappa = 8 \pm 1$ cm^{-1}), whereas PMMA losses duplicate ($\kappa = 25 \pm 3$ cm^{-1}) respect to low concentration films. The similar losses found for both, low and high concentration, of PDI-O in PS indicate that films have similar optical quality, meaning a good dispersion of the PDI-O in the polymer. Thus, the scarce increment in the film losses cannot explain by itself the increase observed in $E_{\text{th-ASE}}$ and the decrease observed in g_{net}, which might mainly be a consequence of the concentration PL quenching. Notice that, in the PS films, it starts becoming important for concentrations of 5 wt% and above. It is possible to assume that the aggregated species in the case of PDI-O are excimers as it has been reported.[152] On the other hand, for PMMA, the formation of

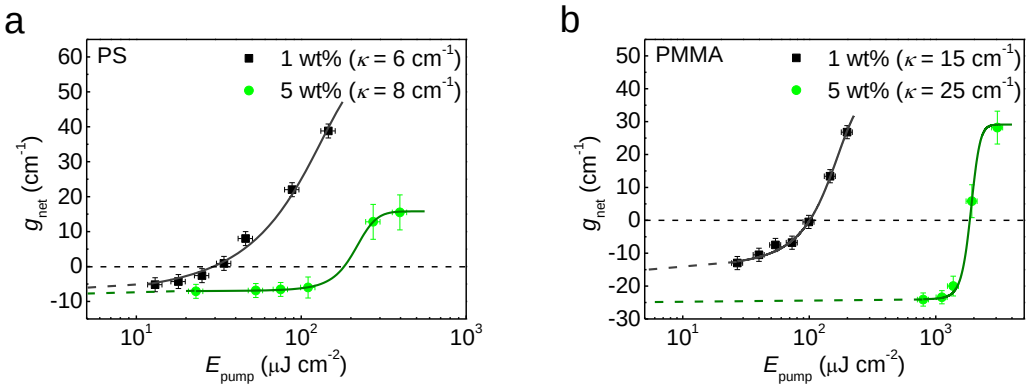

Figure 4.4 Net gain and losses coefficients of PDI-O dispersed in PS and PMMA films. (a, b) Net gain coefficient (g_{net}) as a function of pump energy density (E_{pump}) for PDI-O dispersed in PS and PMMA films (a and b, respectively) for dye concentrations of 1 and 5 wt% (black squares and green circles, respectively). Full lines are guides to the eye and their intersection with the *y* axis correspond to the losses coefficient (κ, values in the legend).

excimer species affects not only the PLQY, but also the film optical quality. Thus, $E_{th\text{-}ASE}$ and g_{net} might be affected by the PL quenching and by the enhanced losses of the waveguide, which is consistent with the more pronounced increase of the ASE threshold observed in PMMA.

4.1.2 *b*-PDI-A Dispersed in Polystyrene and Poly(Methyl Methacrylate) Films

In this section, PS and PMMA waveguides doped with a novel *b*-PDI compound (*b*-PDI-A; see Figure 4.1) are studied in a similar way to PDI-O in the previous section. All the relevant parameters are listed in Table 4.1 to facilitate the discussion. The novel compound incorporates aliphatic-like substituents at the imida positions that provide an improved solubility, which allows it to be incorporated into the matrix up to 50 wt% by using dichloromethane (DCM) as solvent. This represents an improvement with respect to PDI-O (see previous section) and a previously reported *b*-PDI with sorter aliphatic substituents at the imide positions that was incorporated only up to 27 wt% in PS using DCM.[70] The compound was synthetized by Dr. Nathalie Zink-Lorre under the supervision of Prof. Ángela Sastre-Santos and Prof. Fernando Fernández-Lázaro (Molecular Design and Synthesis Group, Miguel Hernández University), who kindly provided it for the present study.[63]

From the analysis of the optical properties (Figure 4.5), two relevant phenomena should be highlighted: *i)* the 29 nm red-shift of the absorption and PL spectra with respect to those of PDI compounds with no substituents at bay positions (*u*-PDI, accounting for bay-unsubstituted PDIs); *ii)* the absence of aggregates/excimers in both matrixes even for the higher dye-concentration studied (50 wt%). In the first case, the bathochromic shift of the absorption and PL spectra is a consequence of the terphenyl-like groups substituted at the 1,7-bay positions, which are anchored to the PDI core through an oxygen atom that provides a certain electron-donor character to the substituent.[69,71] Thus, the main

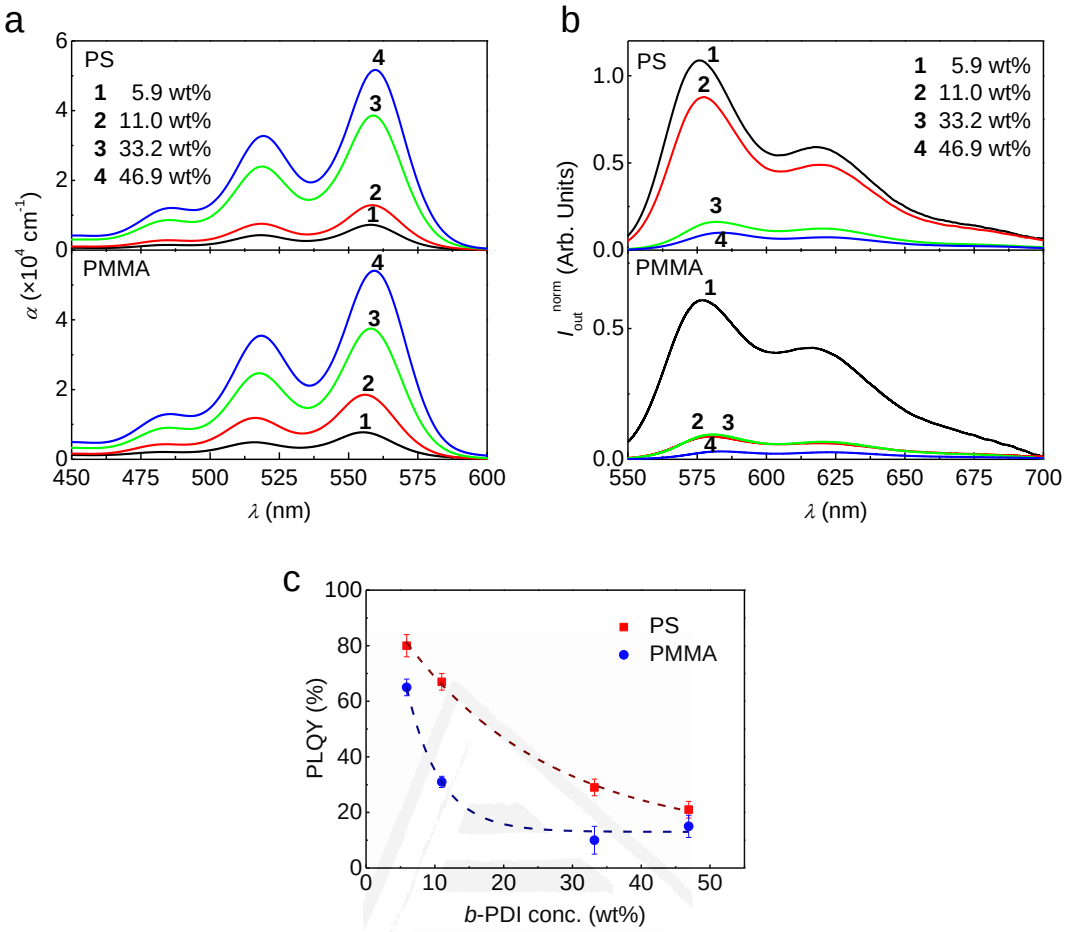

Figure 4.5 Absorption and PL properties of *b*-PDI-A dispersed in PS and PMMA films. (a) Absorption coefficient (α) and (b) PL intensity normalized to absorbance at the excitation wavelength (I_{out}^{norm}) versus wavelength (λ) for *b*-PDI-A dispersed at various doping rates in PS and PMMA films (top and bottom panels, respectively). The corresponding dye concentrations are indicated in the legend. (c) PLQY as a function of *b*-PDI-concentration in either PS (red squares) or PMMA (blue circles). Dashed lines are guides to the eye.

absorption/PL peaks shift from 529/537 nm in *u*-PDI compounds (such as PDI-O) towards 558/576 nm in *b*-PDI compounds. In the second case, the shapes of absorption and PL spectra are maintained across the full range of analysed concentrations (see Figure 4.5), which means that no signs of aggregation are present. The diphenylphenoxy groups attached to the 1,7-bay positions significantly disrupt molecular aggregation by steric hindrance. Note that PL quenching still appears when the *b*-PDI-concentration grows. Indeed, the PLQY drops with the concentration increase of *b*-PDI-A as shown in Figure 4.5c. Comparing both matrixes, *b*-PDI-A doped PS films present always higher PLQY than those of PMMA. Moreover, the PL quenching becomes significant (PLQY drops below the 50 %) at concentrations higher than 18 wt% in PS, whilst the same occurs at 7 wt% in PMMA. In general, all the results point to a better dispersion of *b*-PDI-A in the PS matrix than in its PMMA counterpart, as it occurs for PDI-O.

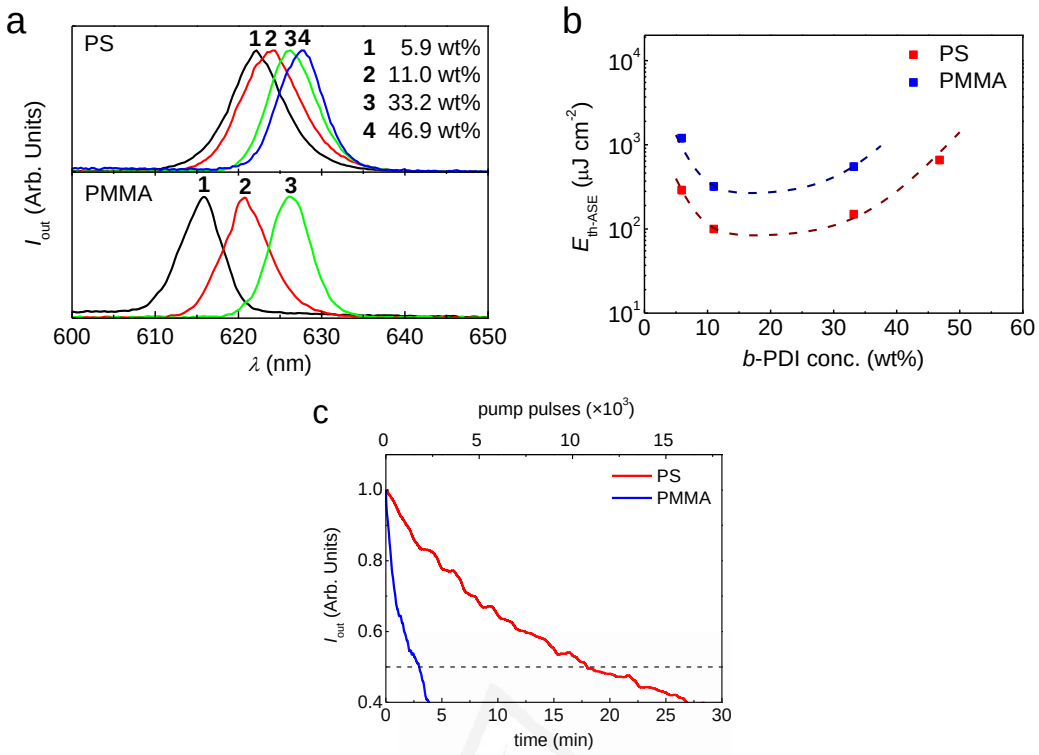

Figure 4.6 ASE properties of *b*-PDI-A dispersed in PS and PMMA films. (a) ASE spectra normalized to its maximum value for PS and PMMA films (top and bottom panels, respectively) doped with *b*-PDI-A at concentrations of 5.9, 11, 33.2 and 46.9 wt%, equivalent to 5×10^{-5}, 10^{-4}, 4×10^{-4} and 7×10^{-4} mol g^{-1} (labels 1 to 4, respectively); (b) ASE threshold ($E_{th\text{-}ASE}$) as a function of *b*-PDI-concentration for PS (red squares) and PMMA (blue circles) films doped with *b*-PDI-A. Dashed lines are guides to the eye; (c) ASE intensity at the peak wavelength normalized to its initial value (I_{out}) as a function of the irradiation time (bottom axis) and the number of pump pulses (top axis) for films of 11 wt% *b*-PDI-A dispersed in PS (red line) and PMMA (blue lines) excited at 60 μJ cm^{-2} (four and two times above their thresholds, respectively).

The films doped with *b*-PDI-A present ASE emission at the first PL vibronic peak, whose exact position changes with the *b*-PDI-A content in the film, see Figure 4.6a. Then, the ASE can be tuned in the wavelength range 615–628 nm by adjusting the *b*-PDI-concentration. Such dependence of the wavelength with the concentration is mainly a consequence of the refractive index increase with the *b*-PDI-A content in the film, although reabsorption might also be playing a role.

The ASE thresholds follow similar trends for both matrixes, although lower values are found for PS than for PMMA at any given *b*-PDI-concentration, see Figure 4.6b. At low concentrations, the threshold decreases with the concentration up to a certain minimum ($E_{th\text{-}ASE}$ = 100 and 320 μJ cm^{-2} for PS and PMMA, respectively) just to rise if the concentration is increased beyond that point. Remarkably, $E_{th\text{-}ASE}$ = 100 μJ cm^{-2} is the lowest threshold reported to date for a *b*-PDI derivative. Additionally, these results are comparable to those obtained for PDI-O (30 and 120 μJ cm^{-2} for PS and PMMA, respectively), if the pump is optimized. Notice that PDI-O-based films are pumped in resonance with their main transition, whilst *b*-PDI-A is pumped at a minimum between two

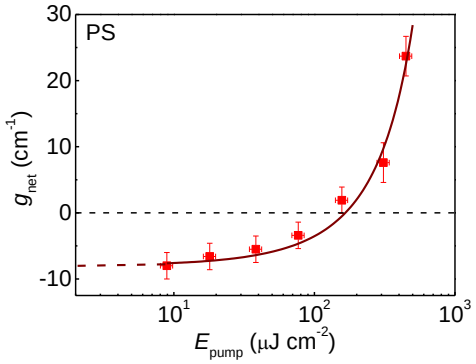

Figure 4.7 Net gain and losses coefficients of *b*-PDI-A dispersed in PS films. Net gain coefficient (g_{net}) as a function of pump energy density (E_{pump}) for a PS film doped with 11 wt% *b*-PDI-A. The full line is a guide to the eye and its intersection with the *y* axis corresponds to the negative value of the loss coefficient ($\kappa = 8 \pm 1$ cm^{-1}).

absorption peaks. Nonetheless, this minimum value is reached for a higher concentration in *b*-PDI-A (10–30 wt%) than in PDI-O (1–3 wt%), which will be understood with the transient absorption experiments performed in Section 4.2.2.

Additionally, the photostability of *b*-PDI-A-doped films with the lowest $E_{th\text{-}ASE}$ (11 wt%) is investigated, see Figure 4.6c. Both films were pumped at the same energy density ($E_{pump} = 600$ μJ cm^{-2}), which correspond to 6 and 2 times the $E_{th\text{-}ASE}$ of PS and PMMA films, respectively. Under such conditions, PS-based films last approximately five times more than PMMA-based ones. Notice that PS films present a lower threshold; therefore, if the films were pumped under moderate conditions, i.e. $E_{pump} = 2\ E_{th\text{-}ASE}$, the difference between them would increase. Besides, *b*-PDI-A-based films present shorter ASE half-lives than those of PDI-O-based films, similarly to what was reported for a similar *b*-PDI in PS.[70] This issue is discussed in more detail in the next Section 4.2.

Eventually, the gain and propagation losses are determined for the PS film doped with 11 wt% *b*-PDI-A through the VSL method, see Figure 4.7. On the other hand, it was not possible to obtain reliable data for doped PMMA films given their rather poor photostability. Nevertheless, taking into account the higher thresholds of PMMA films, such values are expected to be worse than those found for PS films. The g_{net} values for the PS films doped with *b*-PDI-A at 11 wt% and similar that those obtained when doped with PDI-O at 1 wt% if the absorption is taken into account. Moreover, the films doped with *b*-PDI-A present the same value of propagation losses than those of films doped with PDI-O ($\kappa = 8 \pm 1$ cm^{-1}). This indicates that the propagation losses of these films are determined by the PS matrix and not by the dopant.

4.1.3 Discussion about the Different Performance of Polystyrene and Poly(Methyl Methacrylate) Films

From the results previously discussed, it is concluded that PS is clearly a better matrix than PMMA for both, PDI-O and *b*-PDI-A. However, the different properties

characterized show eminent sings of PL quenching and aggregation in both matrixes. Confocal microscopy experiments aimed to directly observe aggregates were performed.[102] Unfortunately, the preliminary results lead to no conclusion: even samples with very different concentrations show uniform PL across the film without any hint of aggregation or phase separation. Further work with more sophisticated techniques, e.g. small-angle x-ray scattering or confocal Raman spectroscopy, would be needed to directly observe aggregation.

Additionally, the ultimate mechanism responsible for the PL quenching remains still unknown. However, the dye concentration above which it become significant is lower in PMMA than in PS. A possible explanation could lie on conformational effects or electronic interactions between dye and polymer, which depend on the electron-donor character of the substituents. Both studied PDI compounds display a quite hydrophobic character, whereas the two polymers present certain polarity. Particularly, PMMA (monomeric dipole moment of 1.67 D) shows a higher polarity than PS (0.123 D) as a consequence of the higher electron-donor character of its functional groups (–COO–) compared to those of PS (phenyl-type).[154] Such change in the electron-donor character was invoked in previous works to account for differences between the photostability performance of PS and PMMA doped with PDI-O.[62,155] According to those studies, PDI photodegradation can proceed through two mechanisms: *i*) type II photooxidation, predominant under aerobic conditions; and *ii*) partially reversible photoreduction, which would prevail under anaerobic conditions. While the first mechanism relies in the oxygen permeability of the matrix, the type and strength of the PDI-polymer interactions would play a role in the second. Then, the lower electron-donor character of PS would imply less photoreduction of PDI-O in PS than in PMMA. Conversely, PMMA present lower oxygen permeability than PS, which means less photooxidation in the former. Following the same train of thoughts used to understand the photostability performance, it is reasonable to think that different molecular conformations would be possible in each matrix. In the literature, the importance of the electronic interactions between dye and matrix was investigated by observing the aggregation effects of the polar molecule azo-dye Red 1 dispersed in several polymers with different polarities.[156] According to the eminent differences found, the authors concluded that it was possible to control the amount of aggregation present in the film through the polarity of the constituents, i.e. dye and polymer, which clearly influences the film optical properties.

4.2 Effect of Substituents at Imide Positions on the Laser Performance of 1,7-Bay-Substituted Perylenediimide Compounds

Hitherto, all the *b*-PDI compounds reported present high PLQY and excellent ASE thresholds even at high concentrations, *b*-PDI-A might be an example of it.[63,69,70] However, all they present a lower ASE photostability than state of the art *u*-PDI compounds, such as PDI-O, as it was discussed in the previous Section 4.1.2. Interestingly,

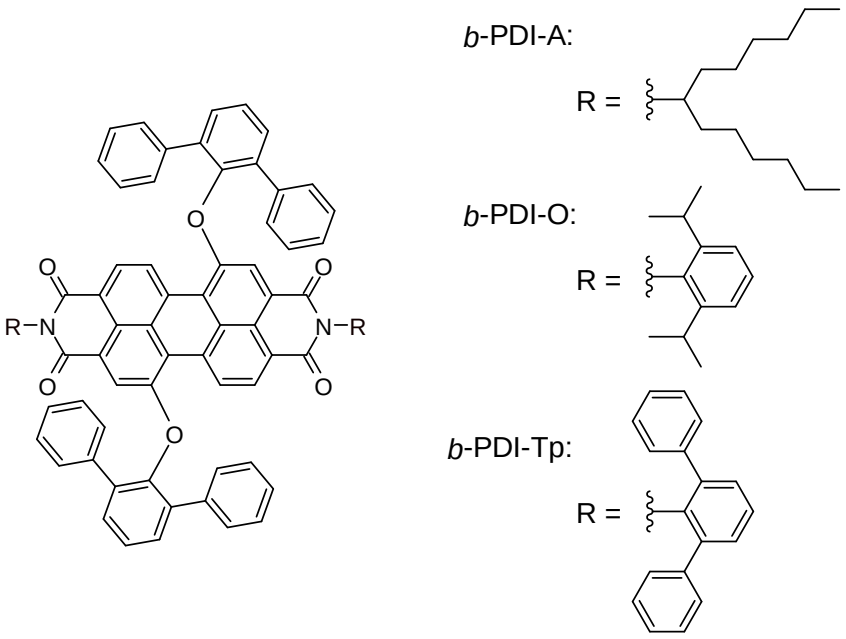

Figure 4.8 Chemical structures of *b*-PDI derivatives investigated: *b*-PDI-O, *b*-PDI-Tp and *b*-PDI-A.

those *b*-PDI compounds bear aliphatic-like substituents at the imide position, which demonstrated to yield less photostable *u*-PDI compounds than phenyl-like substituents.[62] Then, two new *b*-PDI compounds with phenyl-like imide substituents named *b*-PDI-O and *b*-PDI-Tp (see Figure 4.8) are proposed with the aim of improving the photostability of *b*-PDIs. Remarkably, the thorough study of their optical and ASE properties evidences the photostability improvement, but also their mayor propensity for aggregation. The study is conducted first with PS films doped with a low concentration of the *b*-PDI and liquid solutions of the *b*-PDI compounds to determine their properties as isolated molecules. In second place, PS films doped with higher concentrations of the *b*-PDI are characterized to study the dependence of the intermolecular interactions/aggregation with the concentration in the matrix.

4.2.1 Highly Diluted b-PDI-Doped Films

In first place, the optical properties of PS films doped with a low concentration of *b*-PDI (0.8×10^{-5} mol g^{-1} for *b*-PDI-O and 1×10^{-5} mol g^{-1}, for *b*-PDI-Tp and *b*-PDI-A) are analysed and compared with the *b*-PDI performance in toluene solution (1×10^{-6} M) to determine the extent of molecular interaction/aggregation present in the films. These *b*-PDI compounds were synthetized by Dr. Nathalie Zink-Lorre under the supervision of Prof. Ángela Sastre-Santos and Prof. Fernando Fernández-Lázaro (Molecular Design and Synthesis Group, Miguel Hernandez University).[157] All the relevant parameters determined during this study are listed in Table 4.2 to facilitate the discussion.

Table 4.2 Photophysical parameters for *b*-PDIs in toluene solution and in PS-doped films.

b-PDI	Sample	*b*-PDI conc. [$\times 10^{-5}$ mol g^{-1} (wt%)][a]	λ_{ABS} [nm][b]	λ_{PL} [nm][c]	ϕ_{PL} [%][d]	τ_{PL} [ns][e]	α_{pump} [$\times 10^4$ cm^{-1}][f]	λ_{ASE} [nm][g]	$E_{th\text{-}ASE}$ [μJ cm^{-2}][h]	$\tau_{1/2}$ [$\times 10^3$ pulses (min)][i]
b-PDI-O	Solution	†	485/518/<u>558</u>	<u>576</u>/618	89 ± 5	4.9				
	Film	0.8 (1.0)	487/520/<u>560</u>	<u>575</u>/617	87 ± 6	5.1	0.05	620.3	600	14 (23)
	Film	5.0 (5.7)	487/520/<u>560</u>	<u>579</u>/619	42 ± 3	3.0	0.29	623.5	500	4.8 (8)
	Film	10.0 (10.7)	487/520/<u>560</u>	<u>580</u>/620	21 ± 3	1.4	0.54	624.5	550	0.6 (1)
b-PDI-Tp	Solution	†	487/519/<u>558</u>	<u>574</u>/616	78 ± 5	5.1				
	Film	1.0 (1.3)	487/519/<u>559</u>	<u>570</u>/616	61 ± 5	4.2	0.06	617.8	2300	16 (27)
	Film	5.0 (6.7)	487/519/<u>559</u>	575/<u>620</u>/670	12 ± 5	0.5	0.29	620.6	4300	
	Film	10.0 (11.7)	487/519/<u>559</u>	579/<u>623</u>/670	2 ± 5	0.3	0.55			
b-PDI-A	Solution	†	484/517/<u>556</u>	<u>573</u>/617	92 ± 5	5.1				
	Film	1.0 (1.2)	485/518/<u>558</u>	<u>572</u>/617	89 ± 5	5.6	0.06	617.7	400	5.4 (9)
	Film	5.0 (5.9)	485/518/<u>558</u>	<u>575</u>/618	83 ± 3	6.3	0.26	621.2	85	1.2 (2)
	Film	10.0 (11.1)	485/518/<u>558</u>	<u>577</u>/619	78 ± 3	6.0	0.50	623.1	75	1.8 (3)

[a] Dye concentration in matrix (error $\sim 0.1 \times 10^{-5}$ mol g^{-1} and ~ 0.1 wt%); † *b*-PDI concentration in toluene solutions is 1×10^{-6} M. [b] Peak absorption wavelengths (error $= \pm 1$ nm, maximum absorption peak is underlined). [c] Peak photoluminescence wavelengths (error $= \pm 1$ nm, maximum emission peak is underlined). [d] Photoluminescence quantum yield. [e] Average fluorescence lifetime (error ≈ 5 %). [f] Absorption coefficient at λ_{pump} (error $= \pm 100$ cm^{-1}). [g] Amplified spontaneous emission (ASE) wavelength (error is ± 0.7 nm). [h] ASE threshold (error ≈ 20 %). $\lambda_{pump} = 532$ nm from Nd:YAG second harmonic (10 Hz and 10 ns). [i] Photostability half-life measured under permanent pulsed pump at 532 nm (10 Hz, 10 nm) with 25 mJ·cm^{-2} in the same spot and under ambient conditions (error ≈ 20 %).

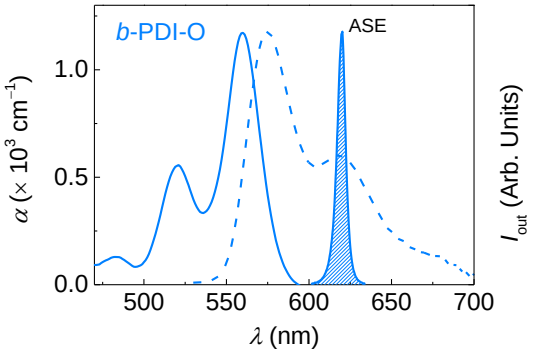

Figure 4.9 Optical properties of PS films doped with *b*-PDI-O. Absorption coefficient (α, solid line, left axis), photoluminescence (PL, dashed line, right axis) and amplified spontaneous emission (ASE, filled area, right axis) as a function of wavelength (λ). The concentration of *b*-PDI-O in the film is 0.8×10^{-5} mol g^{-1}.

The optical properties of the highly diluted films show that molecular interaction/aggregation effects are negligible for the films doped with *b*-PDI-O and *b*-PDI-A, but noticeable for those doped with *b*-PDI-Tp. The absorption and PL spectra of the films preserve the typical mirror-like vibronic progression of isolated molecules observed in solution, which is illustrated in Figure 4.9 for the films doped with *b*-PDI-O. These *b*-PDI compounds present their absorption/PL spectra $\sim$ 30 nm red-shifted in comparison with *u*-PDI derivatives. As discussed in Section 4.1.2, the red-shift is a consequence of the electron donor character of the bay substituent.[69,71] Concerning the PLQY, the values measured for PS films doped with *b*-PDI-A and *b*-PDI-O (89 and 87%, respectively) are comparable to those measured in toluene solutions (92 and 89%, respectively). However, the PLQY determined for *b*-PDI-Tp films (61%) is lower than its value in liquid solution (78%). Moreover, the three *b*-PDI compounds display similar PL lifetimes in solution with single exponential character ($\tau_{PL}^{sol} \sim 5$ ns), whilst some differences emerge between the values obtained for their diluted films. PS doped with *b*-PDI-A maintain the single exponential decay with a slightly larger value ($\tau_{PL}^{film} = 5.6$ ns). Conversely, *b*-PDI-O and *b*-PDI-Tp show PL transients following a double exponential decay, with $\tau_{PL}^{film} = 5.1$ and 4.2 ns, respectively. The value determined for *b*-PDI-O is quite similar to that obtained in liquid solution, meanwhile the value for the *b*-PDI-Tp film is shorter than the one in liquid solution. The double exponential character and time shortening observed for these two *b*-PDI compounds evidence a certain degree of molecular interaction/aggregation, even for the very low concentrations used here.

The imide substituent reveals to be particularly significant for the ASE performance of the *b*-PDI compounds, in special for the photostability. In all three *b*-PDI compounds, ASE appears at a wavelength coincident with the first PL vibronic transition ($\sim$ 620 nm; see Figure 4.9).In terms of the ASE threshold, quite similar values are found for PS films doped with *b*-PDI-A and *b*-PDI-O ($E_{th\text{-}ASE} = 400$ and 600 μJ cm^{-2}, respectively), whereas a

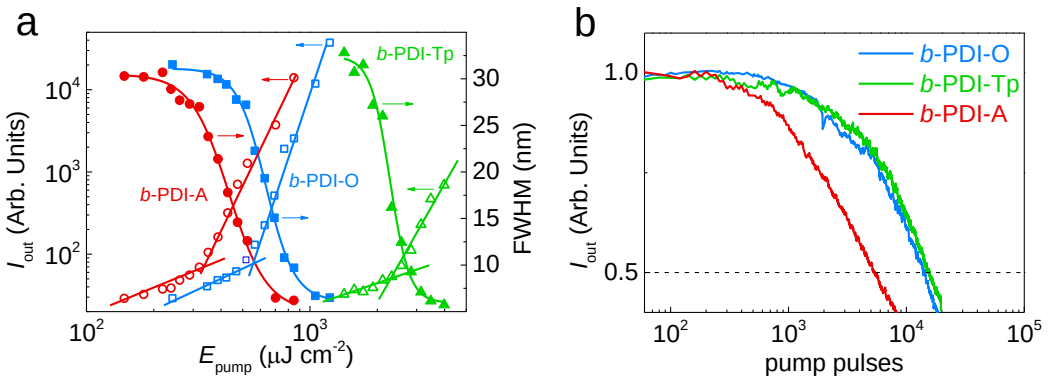

Figure 4.10 ASE properties of PS films doped with a low concentration of *b*-PDI. The films are doped with *b*-PDI-O (blue lines and squares; 0.8 × 10^{-5} mol g^{-1}), *b*-PDI-Tp (green lines and triangles; 1 × 10^{-5} mol g^{-1}) or *b*-PDI-A (red lines and circles; 1 × 10^{-5} mol g^{-1}). (a) Output intensity at λ_{ASE} (I_{out}; open symbols, left axis) and linewidth (FWHM; full symbols, right axis) as a function of pump energy density (E_{pump}). Lines are guides to the eye. (b) Normalized output intensity (I_{out}) at its initial value as a function of time (pump pulses) under uninterrupted pulsed excitation at 25 mJ cm^{-2} (532 nm, 10 ns, 10 Hz).

rather large value is found for *b*-PDI-Tp ($E_{th\text{-}ASE}$ = 2300 μJ cm^{-2}), see Figure 4.10a. These results are in agreement with the differences found between their PLQY values and the incipient molecular aggregation/interaction in *b*-PDI-Tp as it can be endorsed by its PL lifetime.

Remarkably, PS films doped with either *b*-PDI-O or *b*-PDI-Tp display improved photostability with respect to *b*-PDI-A-doped films, as shown in Figure 4.10b. The experiment was conducted under extreme pump conditions (E_{pump} = 25 mJ cm^{-2}). Such E_{pump} value is well above the ASE threshold of the three compounds, which guarantees a comparison under similar conditions for all of them, given their similar absorption at λ_{pump}. Specifically, the ASE half-lives measured for PS films doped with *b*-PDI-O and *b*-PDI-Tp ($\tau_{1/2}$ = 23 and 27 min, respectively) are similar between them and around three times larger than that found for *b*-PDI-A-doped films ($\tau_{1/2}$ = 9 min).

As a matter of fact, finding out the physical mechanism behind the dye photodegradation is an ambitious task. Several mechanisms have been proposed in literature for different dyes,[93,158] yet little has been said in connection with the chemical structure.[159] Concerning to PDI compounds, a few studies exist on *u*-PDI compounds, which invoke mainly two photodegradation mechanisms: type II pho-oxidation under aerobic conditions,[155,160] and photo-reduction under anaerobic conditions;[155] neglecting thermal photodegradation.[61] In systems different than PDIs, other mechanisms have been proposed; e.g., photoionization from excited electronic states, which is typical in polar media; direct bond fission under high excitation power;[93] or photo-oxidation proceeding through radical formation and subsequent chain reaction in polymers.[161]

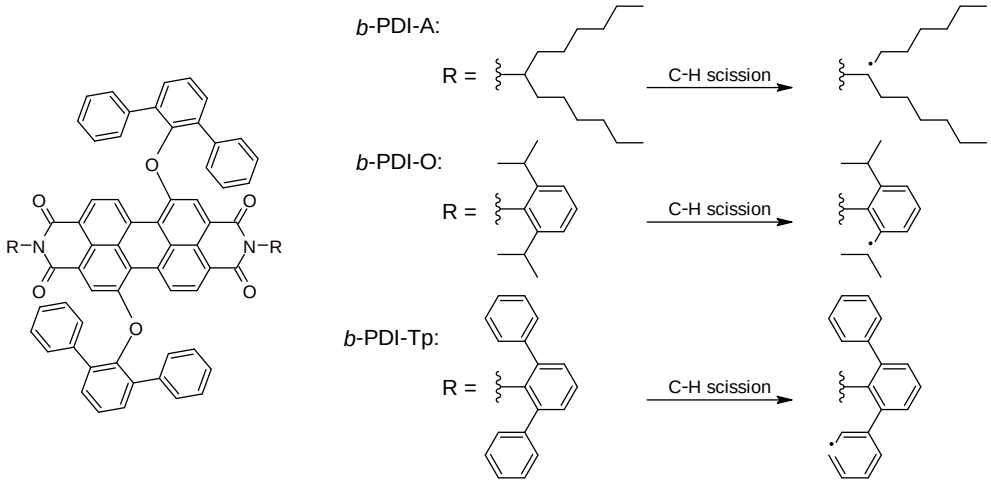

Figure 4.11 Proposed C–H scission reactions in *b*-PDI compounds.

Certainly, the larger photostability found for PS films doped with *b*-PDI-O and *b*-PDI-Tp compounds, relative to that of *b*-PDI-A, might be attributed to the type of substituent attached to their imide positions, since this is the only difference among the three *b*-PDI compounds. Actually, the nodal character of the imide nitrogen atoms uncouples electronically the *b*-PDI core from the imide substituent, which precludes the explanation of the differences in photostability in terms of mechanisms involving ISC, triplets or any other difference between the energy level structure of the compounds. A possible hypothesis might proceed through a radical reaction at the imide substituent after a C–H scission, as illustrated in Figure 4.11. The latter would occur via photo-oxidation reaction, assuming that, despite the nodal character, the excited core is capable of transferring part of its energy to the imide substituent. The formation of this carbon centred radical would lead preferentially to the decomposition of the substituent, and then to a nitrogen-based PDI radical. This would continue reacting and, eventually, might lead to the chromophore decomposition. In this case, the ease of the reaction would be related to the stability of the alkyl/aryl radicals generated, which is inversely proportional to the bond dissociation energy (*D*). Initially, *b*-PDI-A would yield the most stable radical, after losing the hydrogen atom located in the alpha position to the nitrogen, which is a tertiary radical (*D* for a Me_3C–H bond is 95.8 kcal mol^{-1}).[162] In the case of *b*-PDI-O, a tertiary radical could be generated on the isopropyl group, but chain breaking in this case is less feasible, because it will lead to the formation of a phenyl radical, which is less stable (*D* for Ph–H bond is 111 kcal mol^{-1}).[162] Finally, *b*-PDI-Tp would lead directly to a phenyl radical that is the least stable, thus assuring a better photostability for this *b*-PDI compound. This mechanism would explain similar differences reported previously for *u*-PDI compounds.[62]

To corroborate this mechanism, we collaborated with Prof. Fernando Fernández-Lázaro (Molecular Design and Synthesis Group, Miguel Hernández University), who performed MALDY-ToF mass spectroscopy over the photodegradated samples. The mass spectrum of PS films doped with *b*-PDI-A presents signals that can be related with PDI-residue after losing the aliphatic chains or even the aliphatic chain and partially the imida. In the case of *b*-PDI-O-doped films, several signals appear that can be associated with the

PDI-residue after losing the isopropyl at the imida substituent. Finally, in samples doped with *b*-PDI-Tp, no signal for the loss of phenyl or therphenyl-N groups are found, and only a peak attributed to the PDI-residue after losing a terphenyl group is hardly visible.[157]

4.2.2 *b*-PDI-Concentration Dependence

Some important differences have been pointed out between *b*-PDI compounds after studying their optical and ASE properties in highly diluted films. However, the molecular interaction/aggregation effects over these properties become more evident with the increase of the *b*-PDI content in the film, which in turn will intensify the differences among the three *b*-PDI compounds. In this section, PS films doped with concentrations of 1×10^{-5} (0.8×10^{-5} for *b*-PDI-O), 5×10^{-5} and 10×10^{-5} mol g^{-1} are studied seeking for the effect of molecular interaction/aggregation over their optical and ASE properties.

In this regard, it might be important to get some theoretical insides into the potential self-assemblies that might appear in the concentrated films, for which a collaboration was established with Dr. Juan Aragó and Prof. Enrique Ortí (Molecular Materials Theoretical Chemistry Group, University of Valencia) who performed density functional theory (DFT) calculations at the semiempirical GFN2-xTB level. Three important conclusions can be extracted from the theoretical analysis: *i*) the optimized structures show a slightly distorted core (~ 25º between the two naphthaleneimides) and a geometrical arrangement that in principle might hinder molecular aggregation; *ii*) the diphenylphenoxy groups at the bay positions can interact between them (C─H···π interactions) and with the PDI core (π─π interactions), which might be a source of non-radiative decay; and *iii*) despite the fact that the PDI core is protected by the bulky diphenylphenoxy substituents, molecular aggregation can take place via π─π interactions between the bulky diphenylphenoxy and terphenyl substituents. According to this picture, *b*-PDI-Tp, with the larger number of benzene rings in its substituents, is the more prone to form aggregates, followed by *b*-PDI-O and *b*-PDI-A in this order.[157]

Indeed, the effect of the concentration increase over the PL properties is prominent, being affected each *b*-PDI in a different extent, see Figure 4.12. As a general tendency, the PLQY decreases upon the increase of PDI concentration, being this process more pronounced for PS films doped with *b*-PDI-O and *b*-PDI-Tp. The drop of the PLQY is indicative of molecular aggregation/interaction, which seems to be more significant in the *b*-PDI compounds with phenyl-like imide substituent rather than aliphatic-like one.

Notably, the lifetimes follow similar tendencies to PLQY. The PL transients of *b*-PDI-A-doped films preserve the single exponential decay observed in liquid solutions and highly diluted films, although the lifetimes seems to be slightly larger, $\tau_{PL} \approx 6$ ns. However, the PL transients of PS films doped with *b*-PDI-O and *b*-PDI-Tp follow double or even triple decays and show a severe drop of the lifetime when the concentration increases, with an onset al lower concentrations for *b*-PDI-Tp. Again, the multi-exponential character of the PL transient and the lifetime shortening are clear indicative of molecular aggregation/interaction.

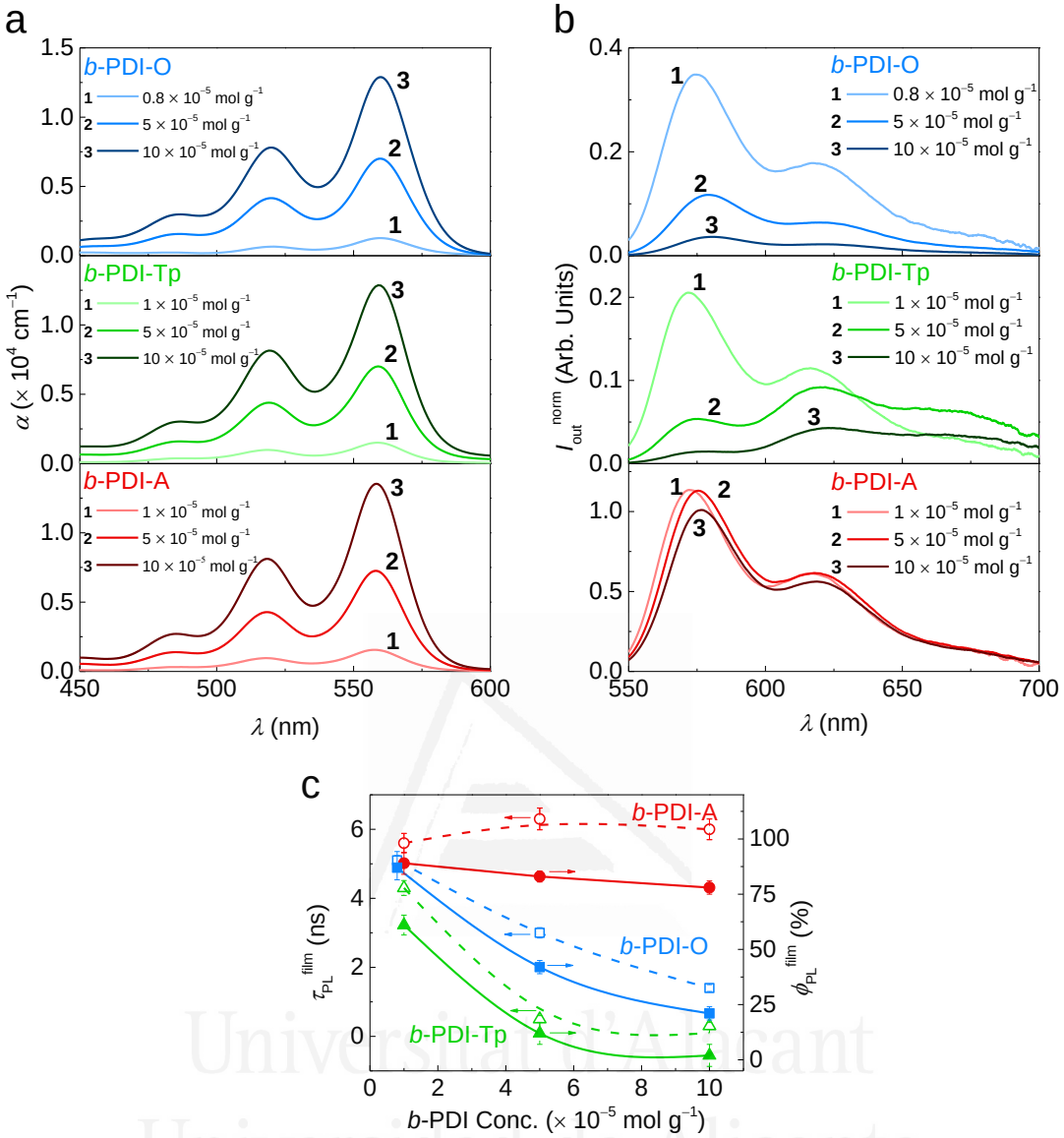

Figure 4.12 Optical properties of PS films doped with *b*-PDI compounds. (a) Absorption coefficient (α) and (b) output intensity normalized to the film absorption at λ_{pump} (I_{out}^{norm}) for PS films doped with *b*-PDIs. Top, middle, and bottom panels correspond respectively to *b*-PDI-O, *b*-PDI-Tp, and *b*-PDI-A doped films. In each panel three concentrations are reflected: (1) 1×10^{-5} (0.8×10^{-5} for *b*-PDI-O) mol g^{-1}, (2) 5×10^{-5} mol g^{-1}, and (3) 10×10^{-5} mol g^{-1}. (c) Photoluminescence efficiency (ϕ_{PL}^{film}, full symbols) and average photoluminescence lifetime (τ_{PL}^{film}, open symbols) in terms of the *b*-PDI-concentration for PS films doped with *b*-PDI-O (blue squares), *b*-PDI-Tp (green triangles), and *b*-PDI-A (red circles). Solid and dashed lines are guides to the eye.

The PL spectra normalized to the film absorption at λ_{pump} reflect perfectly the changes in the PLQY and lifetime, showing quenching upon the concentration increase, which is less pronounced for *b*-PDI-A than for the other two compounds. Furthermore, the PL spectral shape of PS films doped with *b*-PDI-A and *b*-PDI-O suffers minimal variations

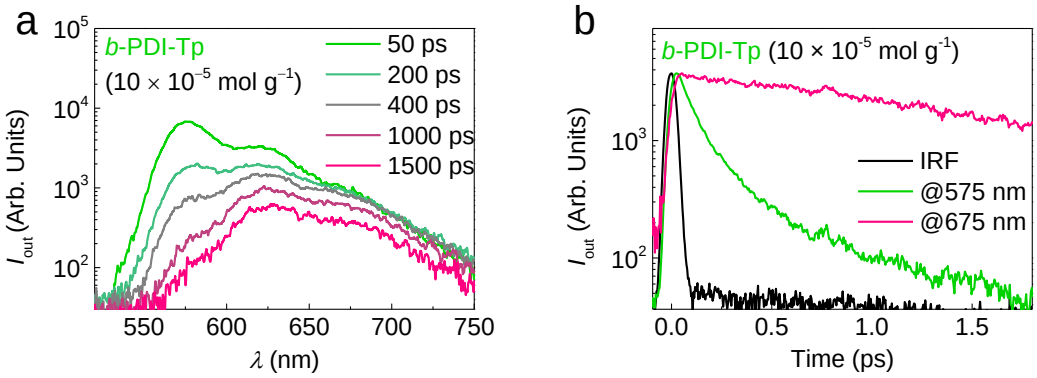

Figure 4.13 PL spectra evolution with time for PS film doped with 10×10^{-5} mol g^{-1} of *b*-PDI-Tp. (a) PL spectra for different times after excitation. (b) PL intensity at 575 nm (green line) and 675 nm (red line) as function of time. Grey line corresponds to the instrument response function. The decay times as obtained from exponential fits of the data appear in the figure.

with the concentration, whereas important variations are observed for those doped with *b*-PDI-Tp. Particularly, the disruption of the main PL peak and the rise of a third peak on the red side of the spectrum (~ 670 nm), together with the lack of changes in the absorption band, points to the formation of excimer species, as it occurs in *u*-PDI compounds.[62,63]

To confirm the formation of excimer species in PS films doped with *b*-PDI-Tp, Dr. Paulius Baronas and Džiugas Litvinas directed by Prof. Saulius Juršėnas (Organic Optoelectronic Research Group, Vilnius University) performed TRPL measurement with a streak camera. The PL spectra of PS films doped with *b*-PDI-Tp (10×10^{-5} mol g^{-1}) captured at different times after excitation are shown in Figure 4.13a. In this way, it is possible to observe how the initial single-molecule spectrum (50 ps) quickly fades, leaving just the more lasting aggregate component that peaks at 625 nm (1500 ps). Then, the single-molecule PL transient (measured at 575 nm) follows a double exponential decay with 0.14 ns lifetime, whereas the aggregate (measured at 675 nm) exhibits a single exponential decay with 2.2 ns lifetime, as shown in Figure 4.13b. By comparing both PL spectra, it is possible to estimate the association energy for the aggregate species (< 20 meV). So far, the evidences accumulated, small energy of association and pronounced spectral changes, suggest the formation of H-aggregate dimers in the films doped with *b*-PDI-Tp.[163] In a sense, it cannot be disregarded the possibility of the formation of the same type of aggregates in *b*-PDI-O-doped films, despite the lack of spectral changes. As the onset of PL quenching occurs at a lower concentration in *b*-PDI-Tp, those effects might appear equally for *b*-PDI-O but at higher concentrations.

The differences observed among the optical properties of these *b*-PDIs are reflected in their ASE performance, see Figure 4.14. Indeed, the only similarity between compounds consists of the red-shift of the ASE spectra upon the concentration increase. The major difference among them occurs for the concentration dependence of their ASE thresholds. The case of PS films doped with *b*-PDI-A were discussed previously in Section 4.1.2, where it was stated that the ASE threshold decreases with the concentration in the range of interest, reaching the lower value ($E_{\text{th-ASE}} = 75$ μJ cm^{-2}) for the higher concentration

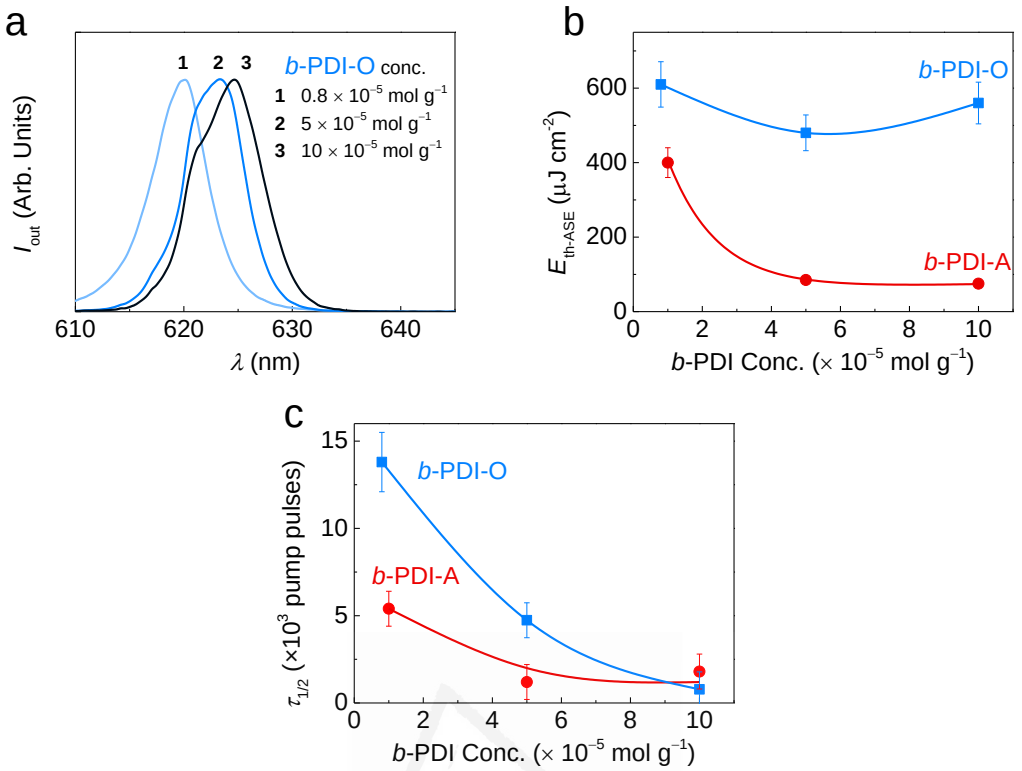

Figure 4.14 ASE properties characterization of *b*-PDI-doped PS films. (a) Normalized ASE spectra for PS films doped with *b*-PDI-O at concentrations of 0.8 × 10^{-5}, 5 × 10^{-5}, and 10 × 10^{-5} mol g^{-1}. (b) ASE threshold ($E_{th\text{-}ASE}$) as a function of dye concentration for PS films doped with *b*-PDI-O (blue squares) and *b*-PDI-A (red circles). (c) ASE half-life ($\tau_{1/2}$) versus dye concentration for PS films doped with *b*-PDI-O (blue squares) and *b*-PDI-A (red circles) under uninterrupted excitation at 25 mJ cm^{-2}. Lines are guides to the eye.

analysed here. For *b*-PDI-O, the $E_{th\text{-}ASE}$ shows a mild decline followed by a slow increase. In this case, the minimum value ($E_{th\text{-}ASE}$ = 500 μJ cm^{-2}) is found for 5 × 10^{-5} mol g^{-1}. Finally, the thresholds of *b*-PDI-Tp increase with the concentration. Then, the lower value ($E_{th\text{-}ASE}$ = 2300 μJ cm^{-2}) is found for the lower concentration analysed and no ASE was found for the largest concentration of *b*-PDI-Tp. These results are in agreement with the rates of molecular aggregation/interaction observed in the PL properties.

Additionally, the concentration dependence of the ASE photostability is analysed for PS films doped with *b*-PDI-O and *b*-PDI-A, see Figure 4.14c. Their half-lives were determined under uninterrupted pump with a fluence of 25 mJ cm^{-2}, as in the previous Section 4.2.1. For both *b*-PDI, a severe drop is found with the increase of concentration, showing those films doped with *b*-PDI-O a steeper slope. As previously discussed, *b*-PDI-O is approximately three times more photostable than *b*-PDI-A in highly diluted films. However, such difference gets reduced upon the concentration increase, becoming comparable the results obtained for the larger concentration. The photostability deterioration with the concentration is attributed mainly to the absorption increase inherent to the concentration increase. However, other factors such as molecular

interaction/aggregation cannot be discarded as the distance between *b*-PDI-O and *b*-PDI-A get reduced while the molecular aggregation/interaction rises.

Finally, the TA spectra of the films are analysed to determine the existence of photophysical processes competing with the stimulated emission (SE). As the TRPL experiments, the TA characterization was conducted by Dr. Paulius Baronas and Dziugas Litvinas under the supervision of Prof. Julius Jursenas (Organic Optoelectronic Research Group, Vilnius University) with whom a collaboration was stablised. All three compounds present the same features in their TA spectra, which are independent of the concentration, see Figure 4.15. The positive peaks at 520 and 560 nm can be associated with PB from the ground-state absorption. The one at 615 nm is attributed to SE. Additionally, the negative band extending from approximately 640 to 950 nm, probably further, corresponds to ESA. Such band reflects the absorption of initially created population leading to losses. Unfortunately, the ESA band overlaps partially with the SE peak, which represents a limiting factor for the ASE performance of these PDI derivatives. As observed in Section 4.1.2, by optimizing pump, a similar ASE threshold can be obtained for PDI-O and *b*-PDI-A, although this occurs for a lower concentration for PDI-O (1–3 wt%) than for *b*-PDI-A (11 wt%). In the case of PDI-O, a severe PL quenching is observed upon the concentration increase. On the other hand, this happens much more mildly in the case of *b*-PDI-A, which can be incorporated into the matrix in larger concentrations while a considerable PLQY is maintained. Then, a lower ASE threshold might be expected for *b*-PDI-A, what is not observed. The cause might be related with the presence of the ESA band that represents an additional source of losses, particularly under the intense pump needed to generate the population inversion and ASE.

4.3 Summary

In this chapter, different PDI derivatives dispersed in inert matrixes have been studied, attending particularly to the influence of the matrix and the different substituents over the optical and ASE properties. For each compound and matrix, concentration dependence studies have been performed that provide valuable information about the different quenching rates exhibited by each of these materials. Additionally, some photophysical studies have been conducted to properly characterize the concentration quenching mechanism and ASE performance in the novel *b*-PDI compounds. The main conclusions after such characterization are resumed in the following paragraphs.

In first place, PS and PMMA have been compared as matrixes for hosting PDI compounds, concluding the major suitability of PS for such purpose (Section 4.1). The same conclusion has been extracted from the analysis of two different PDI derivatives, the commercial PDI-O and the novel derivative *b*-PDI-A. Although, the ASE performance of PDI-O is among that of the state of the art dyes dispersed in a matrix, it shows excimeric emission when the concentration is increased above a certain limit (5 wt% in PS). On the other hand, *b*-PDI-A presents an improved solubility that allows its dispersion in the matrix

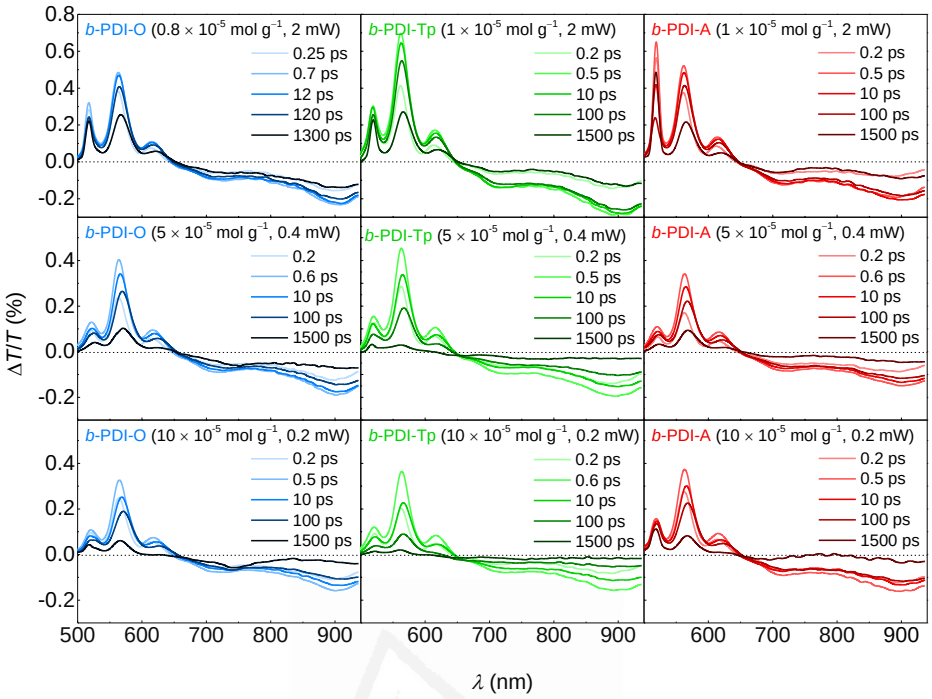

Figure 4.15 Transient absorption spectra for PS films doped with *b*-PDI. Left, centre, and right panels correspond respectively to *b*-PDI-O (blue lines), *b*-PDI-Tp (green lines), and *b*-PDI-A (red lines) doped films with a concentration of 1×10^{-5} (0.8×10^{-5} for *b*-PDI-O) mol g^{-1} (top panels), 5×10^{-5} mol g^{-1} (middle panels), and 10×10^{-5} mol g^{-1} (bottom panels). The pump wavelength was fixed at 520 nm and the power used in each case appears in the respective panel.

up to the 50 wt% with moderate concentration quenching and no hint of aggregation or excimer formation. In particular, at any given concentration, the values of PLQY, ASE thresholds and photostability found for the samples based on PS are systematically better than those found for PMMA samples. Additionally, PS films present the onset of PL quenching at higher concentrations than PMMA films, resulting in an even more pronounced difference between the optimal results of both matrixes. The analysis of the gain and losses points in the same direction, with the higher gain values and lower propagation losses found for the films based on PS. Moreover, similar propagation losses are found for PS films doped with low and high concentrations of PDI-O (1 and 5 wt%), whilst for the same concentrations in PMMA propagation losses duplicate from one concentration to the other. Thus, the major rate of aggregation observed in PMMA is affecting, not just the emission properties of the compound, but also the optical quality of the waveguide. Unfortunately, the lower photostability of *b*-PDI-A precludes the extraction of reliable gain and loss data from PMMA samples doped with it to fully extend the comparison between matrixes.

The second part of this chapter (Section 4.2) is devoted to investigate the optical and ASE properties of three *b*-PDI compounds with different substituents at their imide positions. Three compounds have been compared, *b*-PDI-A with aliphatic-like substituents

and *b*-PDI-O and *b*-PDI-Tp, with phenyl-like substituents. In a sense, the compounds with phenyl-like substituents at the imide positions are more photostable than those with aliphatic chains on them, as concluded from the analysis of films doped with low dye concentrations. However, the compounds with phenyl-like substituents are also the more prone to suffer PL quenching upon the increase of the dye concentration in the film, with the associated negative consequences in terms of ASE thresholds and photostability. Particularly, PS films doped with high concentrations of *b*-PDI-Tp present clear signals of H-aggregates formation with excimeric emission, as endorsed with TRPL. Despite the lack of spectral changes, some similar phenomenon cannot be disregarded in films doped with *b*-PDI-O, given the dramatic PL quenching observed in them. Finally, the TA spectra of the films doped with *b*-PDI compounds show an ESA band close to the SE peak, which might be detrimental for the generation of the population inversion. This phenomenon might be the reason behind the higher thresholds observed in the *b*-PDI compounds in comparison with other state of the art PDI, such as PDI-O.

Chapter 5
Nanographenes

5.1 2D π-Conjugation Extension in Peri-Acenoacenes, FZ Series

Throughout this section, the optical and ASE properties of three four-zigzag edged NGs with increasing size (designated as FZ1, FZ2 and FZ3, see Figure 5.1) are characterized. These NGs belong to the [*n*,*m*]*peri*-acenoacene family, which consists of a number *m* of [*n*]acenes fused into a rhombic nanoflake. In particular, these three NGs have the same *n* (*n* = 3) and increasing *m* (*m* = 2, 3, 4, for FZ1, FZ2 and FZ3, respectively). The zigzag edge of the NG is elongated with the size increase, which has been described as an optimal way for red-shifting the absorption and emission bands in similar systems.[88,89] Although extended zigzag edge can support mid-gap states with paramagnetic character (edge states) detrimental for light emission,[164] FZ compounds present a reduced size, insufficient to form such edge state. Hence, these NGs represent an excellent choice for colour tunability of emission as it is illustrated here.

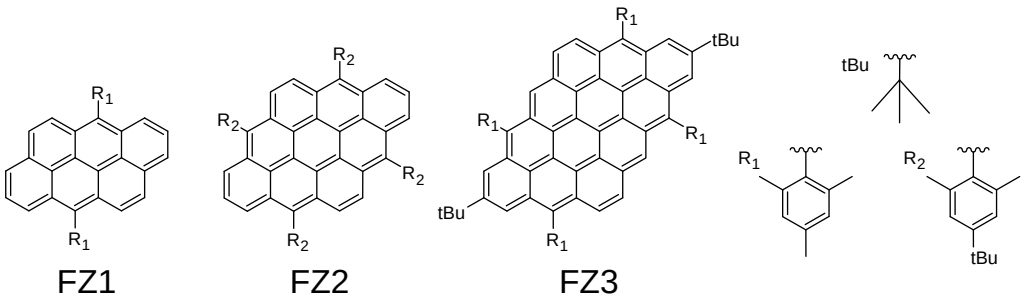

Figure 5.1 Chemical structure of FZ NGs.

Table 5.1 Optical and ASE parameter of FZ-doped PS films

NG (Conc.)[a)]	h_f [nm][b)]	λ_{abs} [nm][c)]	λ_{PL} [nm][d)]	PLQY [%][e)]	τ_{PL} [nm][f)]	λ_{pump} [nm][g)]	α_{pump} [$\times 10^3$ cm^{-1}][h)]	t_{pump} [ns][i)]	λ_{ASE} [nm][j)]	FWHM [nm][k)]	$E_{th\text{-}ASE}$ [μJ cm^{-2}][l)]
FZ1 (1 wt%)	400	402/426/452	456/485/519	82	1.6 ± 0.2	452	4.40	3.9	486	4	45
						426	1.95	3.8	486	4	60
FZ2 (1 wt%)	480	474/509/545	547/588	73	2.1 ± 0.1	545	4.40	4.4	591	4	30
						509	1.55	4.2	591	4	70
FZ2 (3 wt%)	500	474/509/545	548/589	31		545	14.3	4.4	592	5	200
FZ3 (1 wt%)	600	613/668	676/740		3.1 ± 0.3	613	0.56	4.5	685	3	6×10^4
									739	6	4.4×10^3

[a)]The sample consist of a PS film doped with the corresponding NG on top of a quartz substrate, the concentration in the film is indicated in brackets (error $\sim$ 0.1 wt%); [b)]Film thickness (error $\sim$ 2 %); [c)]Wavelengths of the main absorption lines, the underlined value corresponds with the fundamental transition; [d)]Wavelengths of the main photoluminescence (PL) lines, the underlined value indicates the more intense peak; [e)]PL quantum yield (error $\sim$ 10 %); [f)]PL lifetime; [g)]Pump wavelength; [h)]Absorption coefficient at λ_{pump} (error $\sim$ 2 %); [i)]Pump pulse width at λ_{pump}; [j)]Amplified spontaneous emission (ASE) wavelength (error $\pm$ 0.7 nm); [k)]ASE linewidth, defined as the full width at half maximum (FWHM), well above the threshold (error $\pm$ 1.3 nm); [l)]ASE threshold (error $\sim$ 20 %).

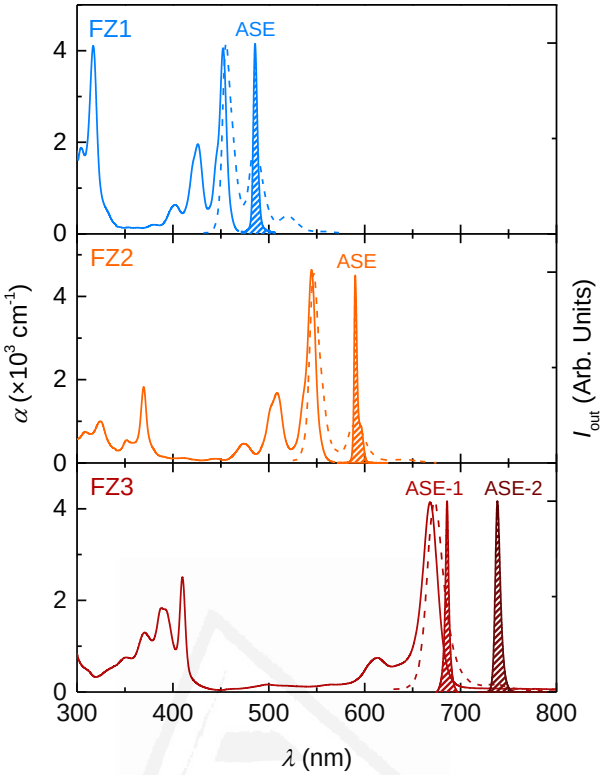

Figure 5.2 Optical properties of FZ-doped PS films. Absorption coefficient (α; solid lines, left axis), photoluminescence (dashed lines, right axis) and amplified spontaneous emission (ASE; shaded areas, right axis) spectra of PS films doped with 1 wt% of FZ1 (top panel, blue), FZ2 (middle panel, orange) and FZ3 (bottom panel, garnet).

5.1.1 Absorption and Photoluminescence Properties

The samples analysed through this section consist of PS thin films with the corresponding FZ NG dispersed in them at 1 wt% and deposited over quartz substrates, using toluene as solvent. The novel NGs were synthetized for the first time by Dr. Yanwei Gu and Prof. Jishan Wu (Department of Chemistry, National University of Singapore), who kindly provided them for this study.[165]

The absorption and PL spectra of the FZ-doped films cover a broad part of the visible spectrum, slightly entering into the NIR, as shown in Figure 5.2. These spectra are mirror-like between them with a small Stokes shift. Moreover, PLQY values as high as 82% are found (see Table 5.1), indicative that these NGs have a planar scaffold. Specifically, the main absorption/PL peaks appear at 452 nm/456 nm in FZ1, at 545 nm/547 nm in FZ2, and at 668 nm/676 nm in FZ3. All three NGs exhibit a second PL peak at 486 nm, 588 nm, and 740 nm in FZ1, FZ2 and FZ3, respectively, the last one in the NIR region. Additionally, the effect of the molecular extension is reflected in the PL lifetimes, which became larger as the NG size increases, see Table 5.1.

In order to understand the origin of the PL transitions, our collaborator Prof. Juan Casado (Physical Chemistry Department, University of Malaga) performed PL measurements at low temperature (80 K) in methyl THF solution and Raman characterization in solid state.[86] It was found that each PL peak resolve in subpeaks delineating two main vibronic progressions spaced by ~ 1300 cm^{-1} (1324 cm^{-1} in FZ1, 1326 cm^{-1} in FZ2 and 1329 cm^{-1} in FZ3) and ~ 300 cm^{-1} (333 cm^{-1} in FZ1, 268 cm^{-1} in FZ2 and 236 cm^{-1} in FZ3). These vibronic progressions correspond approximately to main Raman peaks at 1321 cm^{-1} (342 cm^{-1}) in FZ1, 1279 cm^{-1} (301 cm^{-1}) in FZ2 and 1298 cm^{-1} (243 cm^{-1}) in FZ3. The two series of Raman bands can be associated to in-plane CC stretching modes, ~ 1300 cm^{-1} band, and CCC bending modes spreading over the whole molecule, ~ 300 cm^{-1} band.[166]

5.1.2 Amplified Spontaneous Emission Characterization

Remarkably, these NGs with different sizes show ASE at different spectral regions, from the blue to the NIR, probing the efficiency of the zigzag edge elongation strategy for colour tunability. As shown in Figure 5.2, the films doped with FZ1 and FZ2 display efficient ASE at 486 nm and 591 nm, respectively. Besides, those films doped with FZ3 show ASE simultaneously at two wavelengths, 685 nm and 739 nm, a phenomenon known as dual-ASE. It would be worth comparing the ASE performance of FZ NGs to that previously reported for COPV*n* (with *n* = 1 to 6) dispersed also in PS films.[153] In that case, ASE emission was swept from 385 nm in COPV1 to 583 nm in COPV6, a wavelength segment of 200 nm for which six compounds were needed. Here, a larger part of the spectrum is covered (up to 250 nm), from 486 nm to 739 nm, with only three compounds. Interestingly, the same increment of eight π-electrons takes place in both series, FZ1-3 or COPV1-6, when passing from one element to the following. However, the influence over the wavelength shift is clearly different for each series, probably because the mechanisms underlying π-conjugation is different in COPV1-6 and FZ1-3. An important feature pointing towards this direction is the lifetime difference with the molecular size. In the COPV1-6 series the lifetime decreases as the molecular size increases (3.15–1.37 ns),[167] meanwhile lifetime of NGs increases with the size (1.6–3.1 ns, see Table 5.1).

A possible hypothesis about the mechanisms underneath the development of ASE in each NG is the following: The ASE peaks of FZ1 and FZ2 and the second ASE peak of FZ3 (739 nm) approximately match the corresponding Raman bands at ~ 1300 cm^{-1} in each NG, the second vibronic $|S_1,\ 0\rangle \rightarrow |S_0,\ 2\rangle$, which can be related with in-plane CC stretching modes. On the other hand, the first ASE peak of FZ3 can be related with the low frequency Raman band at 243 cm^{-1}, first vibronic $|S_1,\ 0\rangle \rightarrow |S_0,\ 1\rangle$, associated to CCC spreading modes. Typically, ASE is observed at the second vibronic as the first one suffers larger reabsorption. The reason why ASE is observed at the first vibronic in FZ3 will be clarified with the help of TA spectroscopy in Section 5.1.3.

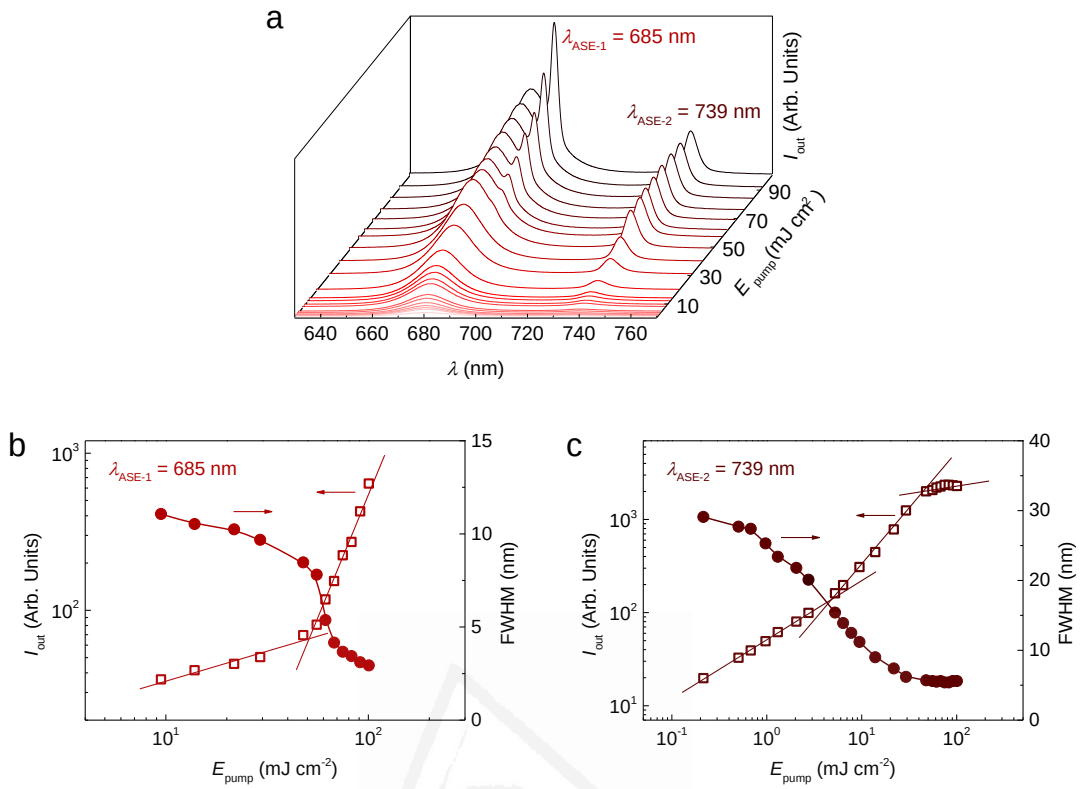

Figure 5.3 Amplified spontaneous emission (ASE) of FZ3-doped PS films (1 wt%). (a) Emission spectra at different pump energy densities (E_{pump}) with ASE peaks appearing at $\lambda_{ASE\text{-}1} = 685$ nm and $\lambda_{ASE\text{-}2} = 739$ nm. Output intensity (I_{out}; open squares, left axis) and linewidth, defined as the full width at half maximum (FWHM; full circles, right axis), as a function of E_{pump} for (b) ASE-1 and (c) ASE-2 peaks. Solid lines are guides to the eye.

The performance of these FZ-doped films in terms of ASE threshold is exceptional for FZ1 and FZ2, showing values as low as 45 μJ cm^{-2} and 30 μJ cm^{-2}, respectively. These values are lower than those previously reported for other NGs (60 μJ cm^{-2})[85] and comparable to that of state of the art dyes dispersed in PS, such as PDI derivatives[63] or COPV*n*.[153] However, larger threshold values are obtained for both ASE peaks of FZ3, as shown in Figure 5.3. At first, ASE emerge at the second vibronic (ASE-2) when the pump energy density increases ($E_{th\text{-}ASE} = 4.4$ mJ cm^{-2}). Then, as the pump is further increased, another ASE peak appears at the first vibronic (ASE-1, $E_{th\text{-}ASE} = 60$ mJ cm^{-2}). Certainly, the larger $E_{th\text{-}ASE}$ of the last peak is a consequence of the larger reabsorption. Although, both peaks are present for pump energy densities above the $E_{th\text{-}ASE}$ of ASE-1 peak, the output intensity of ASE-2 peak stagnates, see Figure 5.3c.

The possible optimization (lowering) of the threshold by increasing the NG doping rate into the film was investigated. Thus, PS films doped with 3 wt% FZ2 were prepared and studied, see results in Table 5.1. However, the PLQY of these films dropped and their threshold grew, as a consequence of molecular aggregation/interaction.

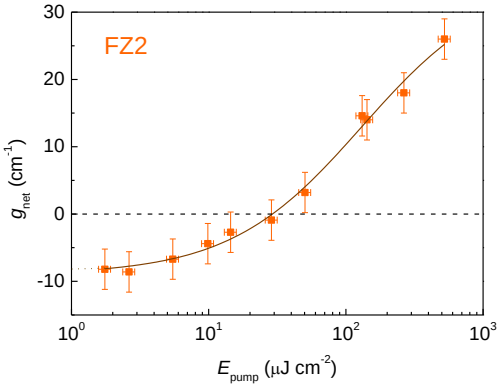

Figure 5.4 Net gain (g_{net}) versus pump energy density (E_{pump}) for FZ2-doped PS films (1 wt%). The values were obtained by applying the VSL method. The full line is a guide to the eye and its intersection with the *y*-axis corresponds to the loss coefficient ($\kappa = 9 \pm 1$ cm^{-1}).

The net gain (g_{net}) was determined for FZ2-doped films (1 wt%) by the VSL method (Section 3.4.1.2) for different values of E_{pump}, see Figure 5.4. The general performance is only slightly inferior to that of state of the art dyes dispersed in PS, though these dyes present better PLQY.[63,153] Additionally, the waveguide propagation losses were determined from the extrapolation of g_{net} to $E_{pump} = 0$. The value ($\kappa = 9 \pm 1$ cm^{-1}) is comparable to that found for similar systems, such as PDI dyes dispersed in PS films,[63] which indicates that this value is govern by the PS.

With regard to photostability, FZ-doped films present a $\tau_{1/2} \sim 10^5$ pump pulses under uninterrupted optical pump at several times above the threshold. The high photostability of these NGs might be attributed to their chemical structures, in which the highly reactive zigzag edges have been deactivated by substitutions with bulky aryl groups. Furthermore, their rigid and planar scaffolds preclude non-radiative processes.

5.1.3 Transient Absorption Spectroscopy

The transient absorption (TA) of the NG-doped films provides a better understanding of the ongoing processes after excitation, which can be useful for the correct interpretation of the ASE results. Particularly, the origin of the dual-ASE performance of FZ3 can be identified from the confrontation of FZ3 with FZ1 and FZ2. As shown in Figure 5.5, the TA spectra of the NG-doped PS films can be deconvoluted into their different contributions (see the insets of Figure 5.5a, 5.5b and 5.5c). Some common features can be appreciated in the three NGs: *i*) they all show a main positive peak and left-side positive replicas matching ground-state absorption that correspond to photobleaching (PB); *ii*) their positive peak matching the $|S_1,\ 0\rangle \rightarrow |S_0,\ 2\rangle$ PL vibronic (482, 593 and 737 nm for FZ1, FZ2 and FZ3, respectively) is associated to stimulated emission (SE); *iii*) Finally, they display a negative broad band convoluted with the other features that can be attributed to photoinduced excited-state absorption (ESA). Notice that such negative band is particularly important in FZ3, as it extends over the whole TA spectrum and cancels the

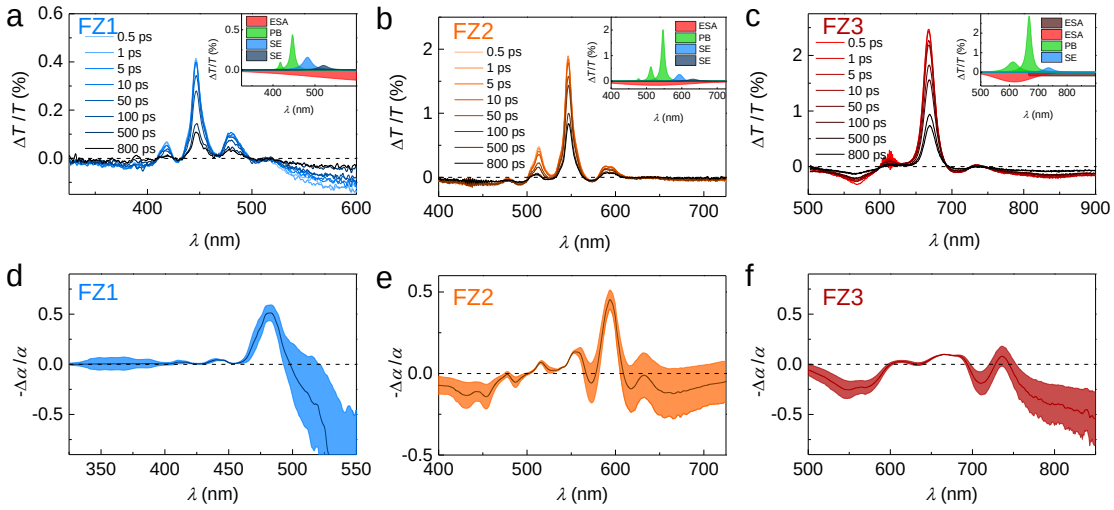

Figure 5.5 Transient absorption spectroscopy of FZ-doped PS films. Transient absorption spectra captured at different delays between pump and probe for PS films doped with 1 wt% (a) FZ1, (b) FZ2 and (c) FZ3. Inset shows the deconvolution of the 10 ps pump-probe delay curve. Pump-induced absorption coefficient normalized to steady-state absorption coefficient for the same (d) FZ1, (e) FZ2 and (f) FZ3 films. The shaded areas correspond to the estimated error.

SE band. Moreover, comparable transient dynamics are found for the three compounds, which follow a double exponential decay with a dominant component of $\tau \sim 1$ ns, see Table 5.2.

An interesting parameter for the interpretation of ASE is the pump-induced change in the absorption coefficient, relative to the steady-state absorption coefficient ($-\Delta\alpha/\alpha$), which carry the gain information of the system. The positive and negative features of these spectra correspond with gain and losses bands, respectively. The differences between NGs become more evident when their $-\Delta\alpha/\alpha$ are compared, see Figure 5.5. Here, the positive bands approximately match the PL bands of the three NGs. Particularly, FZ1 and FZ2 show dominant gain bands at 482 and 594 nm, respectively, which lead to the ASE emission in these NGs. Similarly, the $-\Delta\alpha/\alpha$ spectrum of FZ3 displays two gain bands of quite similar intensity at 680 and 737 nm. Certainly, the presence of these two gain bands with equilibrated intensity make possible the dual-ASE performance of FZ3. Indeed, although secondary gain bands can also be found in FZ1 and FZ2, the large difference of intensity between both gain bands prevents the observation of the second ASE peak. The modification of the gain pattern in FZ3 can be associated with the cancellation of the SE band by the more intense ESA band in this NG, whose effect can also be noticed in the ASE threshold. All three NGs have similar SE cross-sections (σ_{SE}). However, FZ3 presents an ASE threshold at least ten times larger than those of FZ1 and FZ2, due to the larger effect of the ESA band.

Table 5.2 Transient absorption parameters of FZ-doped PS films

NG (Conc.)[a)]	h_f [nm][b)]	λ_{pump} [nm][c)]	A_{pump} [$\times 10^{-4}$ cm^2][d)]	E_{pump} [μJ cm^{-2}][e)]	α_{pump} [$\times 10^3$ cm^{-1}][f)]	σ_{SE} [$\times 10^{-16}$ cm^2][g)]	τ_{TA} [ns][h)]
FZ1 (1 wt%)	410	390	5.3	240	0.37	~2	1.0, 0.1
FZ2 (1 wt%)	480	507	11	16	1.7	8	1.5, 0.06
		546	8.6	21	4.44	9	0.9, 0.07
FZ3 (1 wt%)	600	618	15	30	0.69	6	1.0, 0.05
		667	23	26	4.10	4	1.0, 0.08

[a)]The sample consist of a PS film doped with the corresponding NG on top of a quartz substrate (conc. error ~ 0.1 wt%); [b)]Film thickness (error ~ 2 %); [c)]Pump wavelength for the TA experiments; [d)]Pumped area for the TA experiments (error ~ 10 %); [e)]Pump fluence (error ~ 20 %); [f)]Absorption coefficient at λ_{pump} (error ~ 2 %); [g)]Stimulated emission cross-section (error ~ 20 %); [h)]TA lifetime (error ~ 20 %), the first value correspond to the dominant component.

5.2 1D π-Conjugation Extension in Peri-Acenoacenes, TT-Ar and PP-Ar

In the previous Section 5.1, the electronic conjugation of FZ1 ([3,2]*peri*-acenoacene) has been extended by expanding the NG towards a square-like scaffold (i.e., in 2D), resulting in a red-shift of the spectral properties. In this section, the optical and ASE properties of two NGs (denoted as TT-Ar and PP-Ar), appertaining to the same [*n*,*m*]*peri*-acenoacene family, and generated by extending FZ1 in 1D, are examined. In particular, these two NGs are generated by maintaining $m = 2$ while n is increased from 3 to 5, elements of the series termed as FZ1, TT-Ar and PP-Ar, respectively, see Figure 5.6. Remarkably, a larger red-shift is achieved by increasing n than m, which can be attributed to a more efficient delocalization of the electronic wave function over the zigzag edge in this new series of NGs.

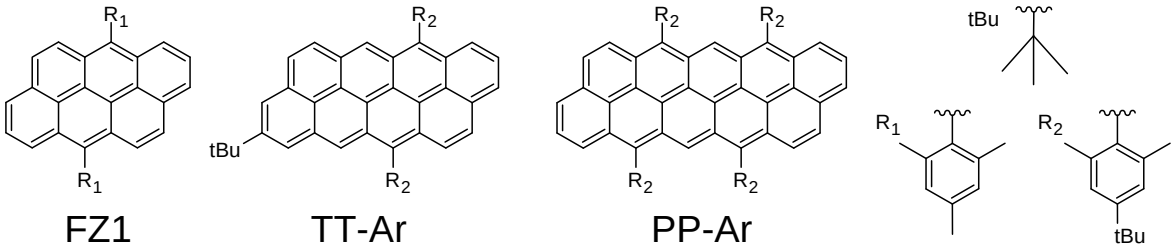

Figure 5.6 Chemical structure of TT-Ar and PP-Ar.

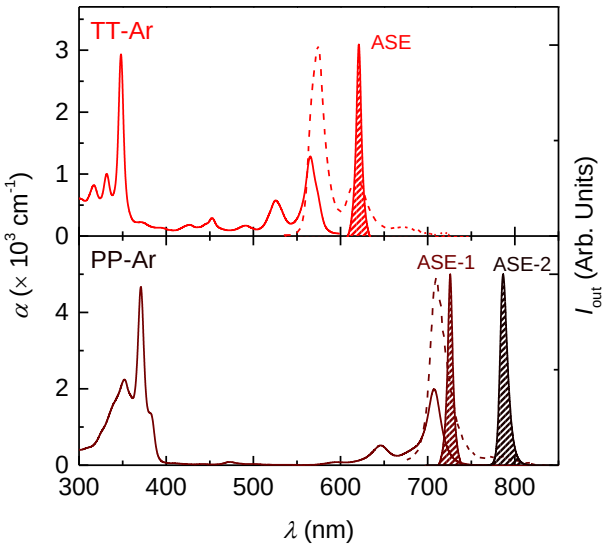

Figure 5.7 Optical properties of PS films doped with TT-Ar and PP-Ar. Absorption coefficient (α; solid lines, left axis), photoluminescence (dashed lines, right axis) and amplified spontaneous emission (ASE; shaded areas, right axis) spectra of PS films doped with 1 wt% of TT-Ar (top panel, red) and PP-Ar (bottom panel, brown).

5.2.1 Absorption and Photoluminescence Properties

The study developed in this section is hold with PS thin films doped with 1 wt% of either TT-Ar or PP-Ar, which have been deposited over quartz substrates by using toluene as solvent. These NGs were provided by Dr. Yanwei Gu and Prof. Jishan Wu (Department of Chemistry, National University of Singapore), who synthetized them.[168]

The absorption and PL spectra of films containing TT-Ar and PP-Ar cover the red part of the visible spectrum and enter into the NIR region, as shown in Figure 5.7 and Table 5.3. These TT-Ar and PP-Ar films exhibit their main absorption/PL peaks at 565/574 nm and 707/710 nm, featuring second PL peaks at 619 and 785 nm, respectively. Remarkably, the spectra of these two NGs are clearly red-shifted compare to those of their FZ counterparts. So, the absorption/PL spectrum of TT-Ar appears 20/27 nm shifted to the red with respect to FZ2. Particularly interesting is the red-shift for PP-Ar, whose absorption/PL spectrum appears at 39/34 nm from those of FZ3. Therefore, the PL spectrum of FZ3 presents just its 10% in the NIR region, whilst that of PP-Ar is fully placed beyond the 700 nm. Moreover, these NGs present similar PLQY values to those previously presented for their FZ counterparts, see Table 5.1 and 5.3. Again, the PL lifetimes became larger as the NG size increase, being this effect more exaggerated in the current series (FZ1, TT-Ar and PP-Ar), see Table 5.3.

PL measurements at low temperature (80 K) in methyl THF solution and Raman characterization in solid state were performed by our collaborator Prof. Juan Casado (Physical Chemistry Department, University of Malaga) with the aim of understanding the

Table 5.3 Optical and ASE parameter of PS films doped with TT-Ar and PP-Ar

NG[a]	h_f [nm][b]	λ_{abs} [nm][c]	λ_{PL} [nm][d]	PLQY [%][e]	ϕ_{PL} [nm][f]	λ_{pump} [nm][g]	α_{pump} [$\times 10^3$ cm^{-1}][h]	t_{pump} [ns][i]	λ_{ASE} [nm][j]	FWHM [nm][k]	$E_{th\text{-}ASE}$ [μJ cm^{-2}][l]	$\tau_{1/2}$ (E_{pump}) [$\times 10^5$ pp (mJ cm^{-2})][m]
TT-Ar	670	491/526/<u>565</u>	<u>574</u>/619	72	4.0 ± 0.5	565	0	4.4	621	7	100	5.0 (0.40)
PP-Ar	590	646/<u>707</u>	<u>710</u>/785		4.7 ± 0.5	646	0.52	4.6	726	6	6×10^4	0.4 (80)
									787	9	1.5×10^3	10 (6.0)

[a]The sample consist of a PS film doped with the corresponding NG on top of a quartz substrate, the concentration in the film is 1.0 ± 0.1 wt%; [b]Film thickness (error $\sim$ 2 %); [c]Wavelengths of the main absorption lines, the underlined value corresponds with the fundamental transition; [d]Wavelengths of the main photoluminescence (PL) lines, the underlined value indicates the more intense peak; [e]PL quantum yield (error $\sim$ 10 %); [f]PL lifetime; [g]Pump wavelength; [h]Absorption coefficient at λ_{pump} (error $\sim$ 2 %); [i]Pump pulse width at λ_{pump}; [j]Amplified spontaneous emission (ASE) wavelength (error $\pm$ 0.7 nm); [k]ASE linewidth, defined as the full width at half maximum (FWHM), well above the threshold (error $\pm$ 1.3 nm); [l]ASE threshold (error $\sim$ 20 %); [m]Photostability half-life parameter expressed in pump pulses (error $\sim$ 20 %). The experimental pump fluence is indicated in brackets.

origin of the different transitions present in these spectra.[166] As it happened for the FZ series, the low temperature PL spectra show that each PL peak is composed of various sub-peaks outlining two vibrational progressions ($|S_1, 0\rangle \rightarrow |S_0, 1\rangle$ and $|S_1, 0\rangle \rightarrow |S_0, 2\rangle$) spaced by $247/1332$ cm^{-1} in TT-Ar and $177/1352$ cm^{-1} in PP-Ar from the fundamental ($|S_1, 0\rangle \rightarrow |S_0, 0\rangle$). The Raman spectra show bands at $222/1352$ cm^{-1} in TT-Ar and (-)/1340 cm^{-1} in PP-Ar that match well these vibrational progressions. Interestingly, if all five NGs are considered, it is possible to observe that the evolution of the two vibronic progressions with the NG size is rather different. The high wavenumber progression is almost constant in the five NGs, whereas the low wavenumber progression decreases as the NG size increases. Indeed, this change in the low wavenumber progression is more pronounced in the FZ1/TT-Ar/PP-Ar series. To determine the origin of these two progressions, Prof. Juan Casado performed quantum chemical calculations to reproduce the Raman spectrum of PP-Ar, founding two vibrational normal modes at 1381 and 248 cm^{-1} that can be associated to the experimental Raman bands. The high wavenumber mode corresponds to in-plane CC stretching modes, which are independent of the molecular size. On the other hand, the low wavenumber modes correspond to in-plane CCC deformation modes (bending modes), which spread over the whole molecule, becoming sensitive to molecular size. More details can be found elsewhere.[166]

5.2.2 Amplified Spontaneous Emission Characterization

Notably, the significant red-shift observed in the spectral properties of TT-Ar and PP-Ar compared to those of FZ2 and FZ3, transfers to their ASE emission. Particularly, TT-Ar displays ASE emission at 621 nm, which represent a 30 nm red-shift with respect to FZ2 ($\lambda_{ASE} = 591$ nm). Besides, PP-Ar displays dual-ASE at 726 and 787 nm, both bands in the NIR region. These ASE bands are more than 40 nm red-shifted than those of FZ3, which shows dual-ASE at 685 and 739 nm. These results are particularly meaningful given the lower increment of π-electrons taken place in [*m*,*n*]*peri*-acenoacenes when passing from the element *n* to *n*+1, while *m* is maintained constant (+6 π-electrons; in the FZ1/TT-Ar/PP-Ar series), rather than to element *m*+1, while *n* is maintained (+8 π-electrons; in the FZ1/FZ2/FZ3 series). The improvement in the red-shift despite the lower increment of π-electrons points towards the more efficient delocalization of the electronic wave function in the NGs with larger edges, rather than with larger number of benzene rings or π-electrons. Indeed, the improved electron delocalization in the FZ1/TT-Ar/PP-Ar series with respect to the FZ1/FZ2/FZ3 series is evident, not only in their more red-shifted spectral properties, but also in their longer PL lifetimes, see Table 5.1 and 5.3. In this regard, the capability of the zigzag edge for maintaining a delocalized state seems to be playing a role. To corroborate this hypothesis, a collaboration was established with Prof. Juan Carlos Sancho (Physcical-Chemistry Department, University of Alicante), who calculated the Harmonic Oscillator Model or Aromaticity (HOMA) index from the PBEh-3c optimized structures of the compounds. The values determined along the larger edge of

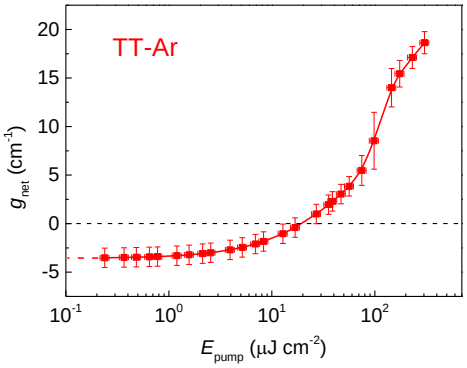

Figure 5.8 Net gain (g_{net}) versus pump energy density (E_{pump}) for TT-Ar-doped PS films (1 wt%). The values were obtained by applying the VPI method. The full line is a guide to the eye and its intersection with the *y*-axis corresponds to the loss coefficient ($\kappa = 3.5 \pm 1.0$ cm^{-1}).

the compound were 0.56 and 0.72 for FZ3 and PP-Ar, respectively, which points to a more marked delocalization of the electronic wave function on the NG edge for PP-Ar.[166]

Clearly, ASE associated to the $|S_1,\ 0\rangle \rightarrow |S_0,\ 2\rangle$ vibronic transition appears in TT-Ar and PP-Ar, with reabsorption acting detrimentally over the $|S_1,\ 0\rangle \rightarrow |S_0,\ 0\rangle$ and $|S_1,\ 0\rangle \rightarrow |S_0,\ 1\rangle$ vibronic transitions. Besides, in PP-Ar a second ASE peak appears, associated to the $|S_1,\ 0\rangle \rightarrow |S_0,\ 1\rangle$ vibronic transition. The mechanism behind this performance is discussed in Section 5.2.3.

Regarding the ASE thresholds of this NG series, a similar performance to that of the FZ1-3 one is found, see Table 5.3. Particularly, TT-Ar presents a slightly larger threshold ($E_{th\text{-}ASE} = 100$ μJ cm^{-2}) than FZ2 ($E_{th\text{-}ASE} = 30$ μJ cm^{-2}), which can be attributed to the lower absorption coefficient at λ_{pump} of TT-Ar (around three times). Actually, threshold values of 60 and 1.5 mJ cm^{-2} are found for PP-Ar ASE-1 and ASE-2 peaks, respectively, which are similar values to those obtained for FZ3, having both NGs similar absorption coefficient at λ_{pump}.

The propagation losses and net gain of the PS films doped with TT-Ar have been determined through the VPI method developed by Dr. Luis Cerdán, see Section 3.4.1.2. Figure 5.8 shows the results as a function of the pump energy density. Particularly, low propagation losses are found for TT-Ar-doped films ($\kappa = 3.5 \pm 1.0$ cm^{-1}), which are similar to those found for other NGs, indicating that the losses of the system are governed by those of the PS. In terms of net gain, a similar performance to that of FZ2-doped PS films at the same concentration can be observed. This means, only slightly lower values than state of the art dyes dispersed in PS, presenting those a better PLQY.[63]

Remarkably, TT-Ar and PP-Ar demonstrate an excellent ASE photostability, comparable to that of FZ NGs, see Table 5.3. The quantification of the ASE photostability has been performed by determining their corresponding ASE half-life ($\tau_{1/2}$) under an excitation four times above its threshold. Very large values have been determined for PP-Ar (ASE-2 peak), i.e. $\tau_{1/2} \sim 10^6$ pump pulses, and for TT-Ar ($\tau_{1/2} = 5 \times 10^5$ pump pulses) and a somehow lower value for PP-Ar (ASE-1 peak) ($\tau_{1/2} = 3.5 \times 10^4$ pump pulses) accordingly to the larger pump energy required (higher ASE thresholds).

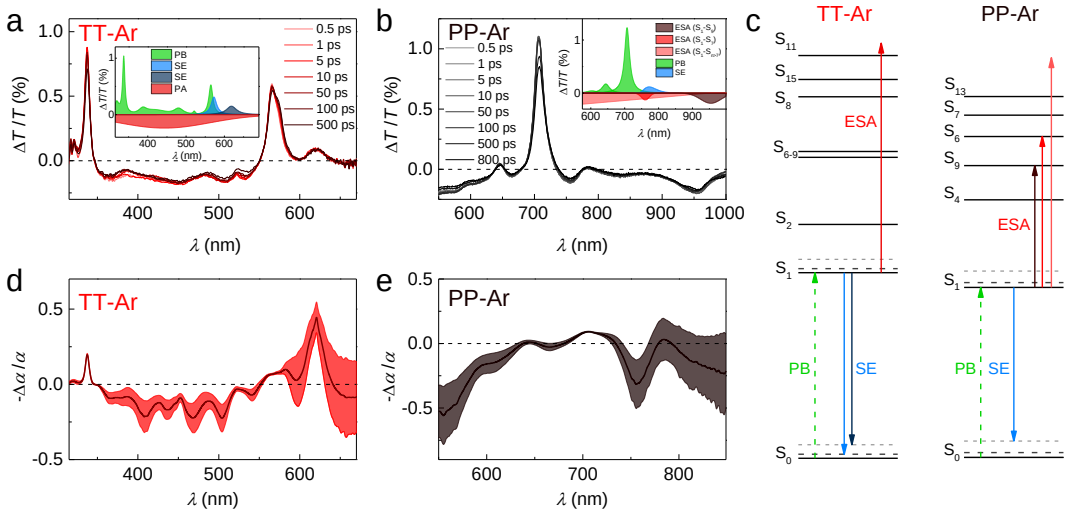

Figure 5.9 Transient absorption spectroscopy of PS films doped with TT-Ar and PP-Ar. Transient absorption spectra captured at different delays between pump and probe for PS films doped with 1 wt% (a) TT-Ar and (b) PP-Ar. Inset shows the deconvolution of the 10 ps pump-probe delay curve. Pump-induced absorption coefficient normalized to steady-state absorption coefficient for (d) TT-Ar and (e) PP-Ar. The shaded areas correspond to the estimated error. (c) Excited-state energy levels of TT-Ar and PP-Ar (left and right, respectively) obtained via NEVPT2/def2-SVP calculations. The principal deconvoluted components of the TA spectrum are indicated with arrows.

5.2.3 Transient Absorption Spectroscopy

Similarly to the FZ1-3 series, the TA spectroscopy of TT-Ar and PP-Ar allows to understand the photophysical processes taking place after excitation. The TA spectra for these NGs after excitation in resonance with the fundamental transition ($|S_0\rangle \rightarrow |S_1\rangle$) are shown in Figure 5.9. Initially, the TA spectra are deconvoluted to separate their different contributions, insets Figure 5.9a and 5.9b. Some analogous features appear in both NGs, which are also shared with the previous FZ1-3. For example, both NGs present a main positive peak and shorter positive peaks at shorter wavelengths that can be related to PB from the ground state absorption. Particularly, TT-Ar presents a differential feature as its main transition is composed of two separated peaks, attributed to PB (565 nm) and SE (573 nm). Furthermore, both NGs present positive peaks spectrally coinciding with their $|S_1,\ 0\rangle \rightarrow |S_0,\ 2\rangle$ vibronic transition that correspond to SE and broad negative bands superimposed with all the PB features which is attributed to ESA from electronic states lying at higher energies. Besides, PP-Ar presents two negative peaks at wavelengths shorter than $|S_0\rangle \rightarrow |S_1\rangle$, which partially cancel the SE band. These two peaks are associated to ESA, specifically, with the transitions $|S_0\rangle \rightarrow |S_7\rangle$ (761 nm) and $|S_0\rangle \rightarrow |S_9\rangle$ (950 nm), as illustrated in Figure 5.9c. The energy levels shown in the Jablonski diagram have been determined by our collaborator Prof. Juan Carlos Sancho (Physical-Chemistry Department, University of Alicante) using NEVPT2/def2-SVP calculations.[166]

The differences between both compounds become even more noticeable when their $-\Delta\alpha/\alpha$ spectra are determined, Figure 5.9d and 5.9e. In the case of TT-Ar, the $-\Delta\alpha/\alpha$

Table 5.4 Transient absorption parameters of PS films doped with TT-Ar and PP-Ar

NG (Conc.)[a)]	h_f [nm][b)]	λ_{pump} [nm][c)]	A_{pump} [$\times 10^{-4}$ cm^2][d)]	E_{pump} [μJ cm^{-2}][e)]	α_{pump} [$\times 10^3$ cm^{-1}][f)]	σ_{SE} [$\times 10^{-16}$ cm^2][g)]
TT-Ar (1 wt%)	670	565	4.5	44	1.29	5
PP-Ar (1 wt%)	590	707	26	12	2.00	3

[a)]The sample consist of a PS film doped with the corresponding NG on top of a quartz substrate (conc. error ~ 0.1 wt%); [b)]Film thickness (error ~ 2 %); [c)]Pump wavelength for the TA experiments; [d)]Pumped area for the TA experiments (error ~ 10 %); [e)]Pump fluence (error ~ 20%); [f)]Absorption coefficient at λ_{pump} (error ~ 2%); [g)]Stimulated emission cross-section (error ~ 20%).

spectrum displays two positive bands, approximately coinciding with the PL peaks. Particularly, ASE emission is happening from the dominant band at 621 nm. Equivalently, PP-Ar spectrum presents two positive peaks of similar intensity spectrally coincident with the PL peaks. The balance between both peaks is a direct consequence of the partial cancelation of the SE band by the overlapping with the ESA peaks. The similar values of these two pump-induced gain bands makes possible the observation of the dual-ASE in PP-Ar, with an ASE peak appearing from each pump-induced gain band. Thus, the losses induced by the ESA peaks appear to be the ultimate cause of the dual-ASE emission.

5.3 Nanographene Optical Properties Modulation via BO Hetero-Substitution

As it has been explored in previous sections, the spectral properties of NGs can be successfully tuned via extension of the molecular size, i.e. by extending the molecular conjugation. However, alternative routes for such purpose might be contemplated, for example carbon atoms can be substituted by boron heteroatoms, while the NG structure remains approximately constant. This results in a decrease of the electronic density in the substituted sites and an increase of the electronic density in the neighbouring carbon sites. As a result, some groups have reported p-type behaviour in B-doped NGs.[91] In this section, the optical and laser properties of a NG doped with boron and oxygen heteroatoms, termed BOTT (see Figure 5.10), is studied. Particularly, this NG consists of a TT-Ar core, in which four carbon atoms have been replaced by two boron atoms and two oxygen atoms. Interestingly, this particular combination of heteroatoms significantly blue-

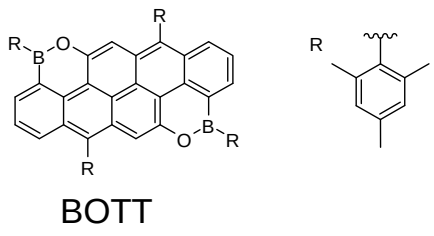

BOTT

Figure 5.10 Chemical structure of BOTT.

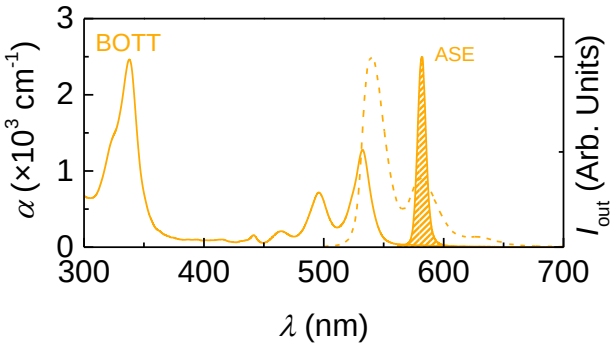

Figure 5.11 Optical properties of BOTT-doped PS films. Absorption coefficient (α; solid lines, left axis), photoluminescence (dashed lines, right axis) and amplified spontaneous emission (ASE; shaded areas, right axis) spectra of PS films doped with 0.9 wt% of BOTT.

shifts the spectral properties of BOTT with respect to those of the undoped TT-Ar, while maintains the good ASE performance of the latter.

5.3.1 Absorption and Photoluminescence Properties

The samples analysed in this section consists of PS thin films doped with BOTT at different concentrations (See Table 5.5), deposited over quartz substrates. The NG was provided by Dr. Yanwei Gu and Prof. Jishan Wu (Department of Chemistry, National University of Singapore), who synthetized them.[169] During the film manufacture, BOTT demonstrated insufficient solubility on toluene, so DCM was used instead. Even so, concentrations of BOTT in DCM larger than 0.5 wt% dissolve only partially and the final concentration of BOTT in the PS films was calculated by assuming a linear increase of the absorption spectrum with the NG concentration.

Remarkably, the absorption and PL spectra of BOTT are blue-shifted in comparison to those of TT-Ar. As shown in Figure 5.11 and Table 5.5, BOTT, doped into PS films, presents its fundamental absorption transition at 532 nm and main/secondary PL peaks at 540/580 nm. These transitions are blue-shifted, on average, by 35 nm with respect to the corresponding transitions of TT-Ar. Moreover, high PLQY values, reaching up to 80% have been found for BOTT-doped films, which are similar to the ones of previously discussed NGs.

5.3.3 Amplified Spontaneous Emission Characterization

Consistently, the blue-shift of the BOTT emission spectrum replicates on its ASE emission. Although, the position of the ASE peak depends slightly on the NG concentration in the film (see Table 5.5), $\lambda_{ASE} = 582$ nm is found for the concentration with the best performance in terms of threshold ($E_{th\text{-}ASE} = 66$ μJ cm^{-2}; 0.9 wt%). Such ASE peak appears 39 nm blue-shifted with respect to the ASE peak of TT-Ar. This blue-shift

Table 5.5 Optical and ASE parameter of BOTT-doped PS films

Conc. [wt%][a)]	h_f [nm][b)]	λ_{abs} [nm][c)]	λ_{PL} [nm][d)]	PLQY [%][e)]	α_{pump} [$\times 10^3$ cm^{-1}][f)]	λ_{ASE} [nm][g)]	$E_{th\text{-}ASE}$ [μJ cm^{-2}][h)]	$\tau_{1/2}$ (E_{pump}) [$\times 10^5$ pp (μJ cm^{-2})][i)]
0.1	460	464/496/<u>532</u>	<u>537</u>/579		0.21	578.8	1300	
0.21	520	464/496/<u>532</u>	<u>537</u>/579		0.40	578.9	440	
0.35	480	464/496/<u>532</u>	<u>537</u>/579		0.58	579.4	230	
0.6	490	464/496/<u>532</u>	<u>538</u>/581	80	0.93	580.3	120	
0.9	490	464/496/<u>532</u>	<u>540</u>/582	80	1.30	581.8	66	1.0 (320)

[a)]The sample consist of a PS film doped with BOTT on top of a quartz substrate (error $\sim$ 0.1 wt%); [b)]Film thickness (error $\sim$ 2 %); [c)]Wavelengths of the main absorption lines, the underlined value corresponds with the fundamental transition; [d)]Wavelengths of the main photoluminescence (PL) lines, the underlined value indicates the more intense peak; [e)]PL quantum yield (error $\sim$ 10 %); [f)]Absorption coefficient at pump wavelength (532 nm; error $\sim$ 10 %). [g)]Amplified spontaneous emission (ASE) wavelength (error $\pm$ 0.7 nm). The ASE linewidth, defined as the full width at half maximum (FWHM), for well above the threshold is 6 $\pm$ 1 nm; [h)]ASE threshold (error $\sim$ 20 %); [i)]Photostability half-life parameter expressed in pump pulses (error $\sim$ 20 %). The experimental pump fluence is indicated in brackets.

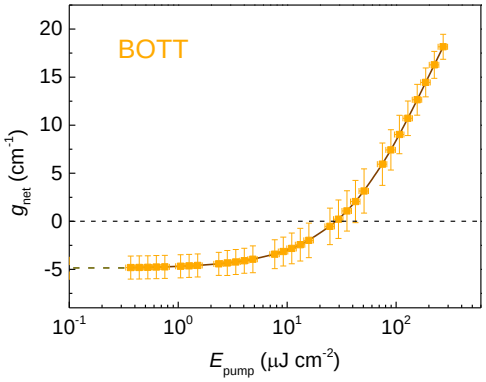

Figure 5.12 Net gain (g_{net}) versus pump energy density (E_{pump}) for BOTT-doped PS films (0.9 wt%). The values were obtained by applying the VPI method. The full line is a guide to the eye and its intersection with the *y*-axis corresponds to the loss coefficient ($\kappa = 5 \pm 1$ cm^{-1}).

can be attributed to the reduction of the total number of π-electrons, as a consequence of the carbon replacement with boron and oxygen heteroatoms, which pass from 28 π-electrons in TT-Ar to 24 π-electrons in BOTT. Indeed, boron/oxygen heteroatoms were used to open a finite electronic band-gap in graphene, which can be extended by increasing the boron content.[79,170] Additionally, NGs with boron heteroatoms, or boron combined with oxygen, demonstrated a larger band gap than their unsubstituted versions.[171–173] Moreover, the position of such heteroatoms in the NG core also plays a role in the formation of the electronic band-gap,[174,175] as it was predicted also for GNRs.[176] Thus, the ultimate cause of the blue-shift appears to be a combination of both, the number of heteroatoms and their position in the NG scaffold. A computational study of the electronic properties can help to get insights on these aspects.

In the referent to the value of the ASE threshold, it decreases with the concentration of BOTT in the PS films, reaching an $E_{th\text{-}ASE}$ as low as 66 μJ cm^{-2} for the 0.9 wt% concentration (see Table 5.5). Unfortunately, the concentration cannot be further increased, aiming to decrease the threshold due to solubility problems. The net gain and propagation losses have also been determined by using the VPI method (see Section 3.4.1.2) for the films doped with this concentration, see Figure 5.12. The gain performance mimics that of previously described NGs FZ2 and TT-Ar, which is only slightly inferior to state of the art dyes dispersed in PS. Moreover, the low loss coefficient found ($\kappa = 5 \pm 1$ cm^{-1}) is a clear indicative of the good optical properties of this films, being the propagation losses governed by those of the PS film.

Regarding to the photostability performance, the experiment was carried out only for the concentration with the best threshold (0.9 wt%) obtaining a reasonably large ASE half-life parameter ($\tau_{1/2} = 1.0 \times 10^5$ pump pulses) for a pump fluence around 4-5 times above its $E_{th\text{-}ASE}$. This $\tau_{1/2}$ value is five times lower than that obtained for TT-Ar, which can be attributed to the presence of the oxygen heteroatoms that are usually more reactive and prone to photodegrade.

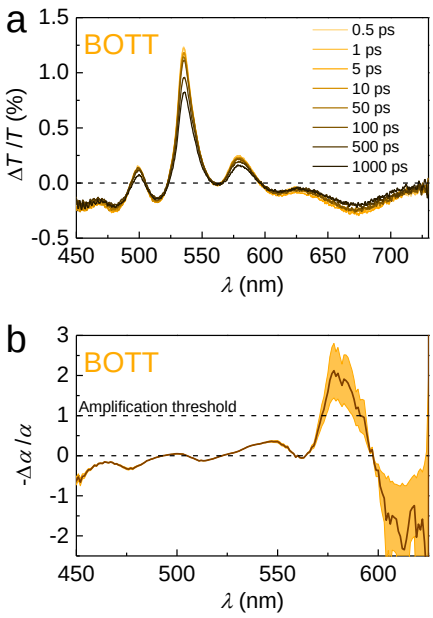

Figure 5.13 Transient absorption spectroscopy of BOTT-doped PS films. (a) Transient absorption spectra captured at different delays between pump and probe for PS films doped with 1 wt% BOTT. (b) Pump-induced absorption coefficient normalized to steady-state absorption coefficient ($-\Delta\alpha/\alpha$). The shaded areas correspond to the estimated error.

5.3.2 Transient Absorption Spectroscopy

In order to dismiss any detrimental phenomenon for the SE, the photophysical processes taking place in the BOTT-doped films under excitation have been investigated using TA spectroscopy. The TA spectra for different time delays between the pump and the probe beams appear in Figure 5.13a. The excitation was tuned to match the main absorption peak ($|S_0\rangle \rightarrow |S_1\rangle$). The different features in the TA spectrum can be attributed to the typical phenomenon previously discussed for other NGs, i.e.: *i*) the main positive peak and the secondary peak at shorter wavelengths can be associated to PB from the ground state absorption, notice that SE can also be contributing to the main positive peak though in a reduced way; *ii*) the positive peak at longer wavelengths, which spectrally coincides with the secondary peak of the PL, is attributed to SE; *iii*) a negative band superimposed with the PB features can be intuited, which might correspond to ESA to electronic states lying at higher energies. In addition to this features, a negative peak appears, which can be associated to ESA related to the particular transition from $|S_1\rangle$ to the singlet state observed in the absorption spectrum at 338 nm (see Figure 5.11). Fortunately, both ESA features are quite separated from the SE peak, corroborating the good ASE performance of this NG. The $-\Delta\alpha/\alpha$ spectrum shown in Figure 5.13b displays two positive bands that correspond to pump-induced gain. The ASE in this compound emerges from the dominant band, which for a pump above the ASE threshold, verifies the amplification condition ($-\Delta\alpha/\alpha > 1$), as shown in Figure 5.13b.

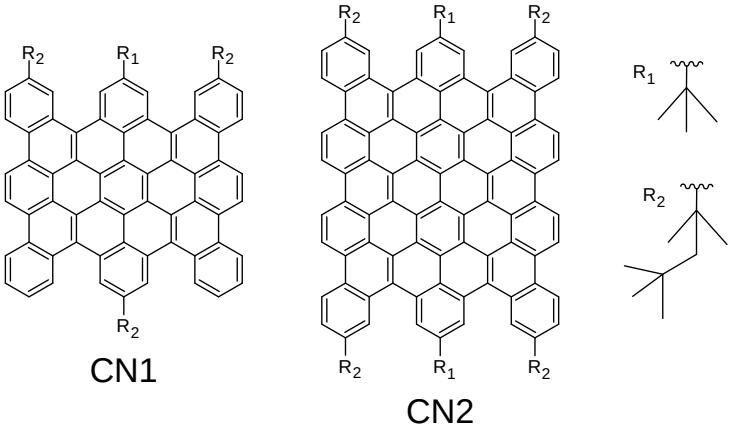

Figure 5.14 Chemical structure of CN NGs.

5.4 Cove Edged Nanographenes

An alternative way of tuning the optical and laser properties of NGs is by modifying their edge structures. For example, it is well-known that fully benzenoid NGs, which are formed almost exclusively by armchair edges, are more stable and present larger energy gaps than zigzag edged NGs of similar size.[15] In this sense, some works exist reporting the spectral properties of cove edged NGs,[171,177–179] but none of them reports ASE or lasing action on these NGs. In this section, two squared NGs of increasing size termed CN1 and CN2 are investigated, each one with two cove edges and two armchair edges (see Figure 5.14). Although these two NGs do not show ASE, important conclusions regarding molecular design for lasing can be extracted from their analysis.

5.4.1 Results and Discussion

The samples analysed here consist of PS films doped with 1 wt% of CN1/CN2, that were prepared by spin-coating a toluene/THF solution over quartz substrates. Both NGs were synthetized by Dr. Yanwei Gu and Prof. Jishan Wu (Department of Chemistry, National University of Singapore), who provided them for this study.[179] Despite the fact that these NGs are substituted unsymmetrically with *tert*-butyl groups, these molecules still suffer strong interactions, attributed to their big size that reduce their solubility. Such issue hinders the preparation of the CN-doped PS films, particularly those based on CN2. Finally, the films were prepared by skipping the overnight stirring of the solution, which was spin-coated over the quartz substrates two hours after its preparation. By doing so, the polymer was only partially swallowed and more solvent was still available for the NG. Certainly, part of the compounds remained in the filter used during the deposition, remaining the exact concentration of the NG in the film unknown. Then, the given concentration corresponds with the initial concentration in the solution.

These compounds present their principal absorption and emission bands in the reddish part of the spectrum as shown in Figure 5.15. Particularly, CN1 display the main

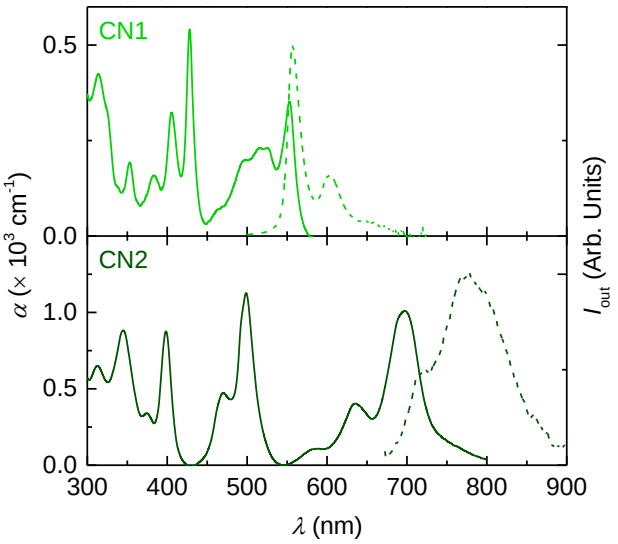

Figure 5.15 Optical properties of CN-doped PS films. Absorption coefficient (α; solid lines, left axis) and photoluminescence (dashed lines, right axis) spectra of PS films doped with 1 wt% of CN1 (light green, top panel) and CN2 (dark green, bottom panel).

absorption peak at 553 nm and PL peaks at 557 and 604 nm. In the case of CN2, attending to the broad absorption peak at 698 nm, the presence of a shoulder at longer wavelengths (~ 750 nm) and the solubility problems, it is possible to hypostasize the presence of aggregated species in the film. Moreover, emission peaks appear at 720 and 778 nm, but the spectral shape might indicate the presence of either a strong reabsorption or aggregation. For these NGs, the absorption and emission appear at much longer wavelengths compared to fully benzenoid NGs of the similar size,[180] but at much shorter wavelengths if they are compared with zigzag edged NGs (see previous sections). According to the Clar's sextet rule,[181] this can be explained by the conjugative effect of the olefinic C=C double bonds. Moreover, the spectral properties red-shifts with the size increase of the NG. Particularly, an increase of 22 π-electrons produces a red-shift of ~ 145 nm, which is a similar result to that observed when passing from TT-Ar to PP-Ar, though with an increase of only 6 π-electrons between both NGs (see Section 5.2.1). Additionally, both CN NGs present distorted cores, owing to the steric repulsion between C–H bonds at their cove positions, which seems to be a common characteristic for cove edged NGs.[171,177–179] This feature might be responsible for the moderate PLQY determined in solution (35 % for CN1 and 50 % for CN2).[179]

For NGs CN1 and CN2, ASE measurements were performed under ns excitation without success. Despite pumping in resonance with the different features of their absorption spectra and using all the energy available in the system, no signs of ASE were observed in the films prepared with these NGs.

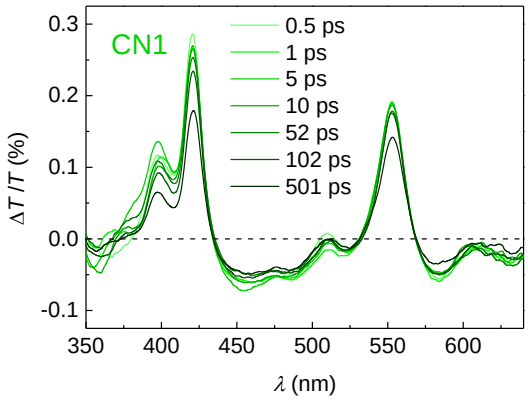

Figure 5.16 Transient absorption spectroscopy of CN1-doped PS films. Transient absorption spectra captured at different delays between pump and probe for PS films doped with 1 wt% CN1.

TA spectroscopy was performed on the CN1-doped PS samples to investigate the photophysical processes taking place after excitation. The TA spectra captured for different time delays between the pump ($\lambda_{\text{pump}} = 546$ nm) and probe pulses are shown in Figure 5.16, where it is possible to differentiate the following features: *i*) the positive peaks at 420 and 553 nm and their smaller replica at shorter wavelengths can be attributed to PB from the ground state absorption; *ii*) the peak at approximately 610 nm correspond to SE; and *iii*) the broad negative band superimposed with all the features that tentatively will be assigned to ESA to higher energy lying electronic states, though its exact origin remains still unknown. Precisely, this last negative feature overtakes the possible optical gain from the SE peak, which maximum appears clearly bellow $\Delta T/T = 0$, precluding amplification in the system.

To elucidate the actual origin of the broad negative band, numerous TA experiments involving different concentration of the NG in the PS film and in solution would be needed. However, a speculative cause might consist in a simple reabsorption process (ESA) to electronic states lying at higher energy, which is probable given the proximity between the different absorption bands of the molecule. Such reabsorption might be followed by ISC to a charge separated state and exciton migration, if aggregation is present in the system.[25] Alternatively, ISC to triplet states might be a more likely possibility, given the contorted skeleton of these NGs.[178,179]

5.5 Excited State Engineering through Bulky Edge Substitution

The results discussed in previous sections of this chapter demonstrate the suitability of molecular extension for wavelength tuning towards the NIR. However, several fundamental issues limit this route, such as fast IC of electrons back to their ground state and intra-gap absorption of triplets and CT states. In the first case, the energy gap law for radiationless transitions establish that non-radiative IC in the system is proportional to the

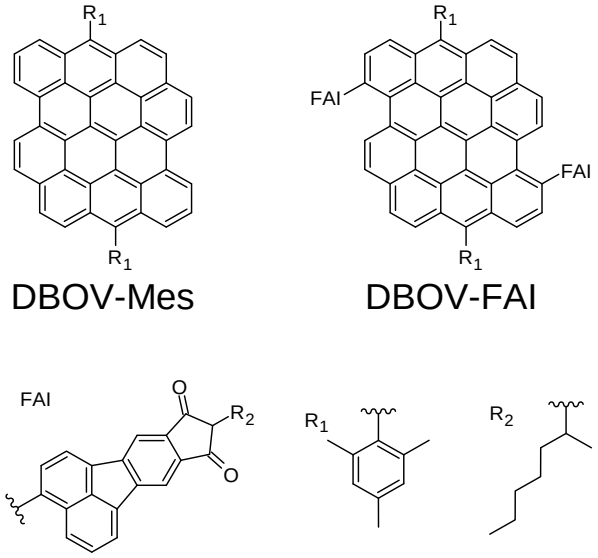

Figure 5.17 Chemical structure of DBOV NGs.

overlap between the wave functions of the electronic excited state and the vibronic levels associated to the electronic ground state.[23,182] Moreover, the number of vibronic modes increases with the molecular size, making the situation worse. In the second case, CT and triplet states could result in gain losses whenever they overlap with the SE of the system.[8] However, these mechanisms are very different in nature. Indeed, triplet states are an intramolecular phenomenon, being generated via ISC from singlet excited states, whilst, CT states are generated in supramolecular aggregates. Sometimes both can occur simultaneously, as is the case for DBOV-Mes (see Figure 5.17), which presents a CT state and triplet absorption bands superimposed with its SE band.[25,183] To cope with this issue, a new version of this NG incorporating two bulky FAI substituents anchored to their armchair edges, termed DBOV-FAI, has been considered, see Figure 5.17. In this section, the optical and ASE properties of DBOV-Mes and DBOV-FAI are studied, demonstrating that efficient NIR ASE is possible through intelligent design of the molecular structure.[183]

5.5.1 Absorption and Photoluminescence Properties

The samples analysed through this section consists of PS thin films doped with either DBOV-Mes or DBOV-FAI at 1 wt%. The compounds were dispersed in a toluene solution that was spin-coated over quartz substrates. Both NGs were provided by Dr. Qiang Chen, Dr. Akimitsu Narita and Prof. Klaus Müllen (Max Planck Institute for Polymer Research), who synthetized them.[183,184] All the parameters characterized can be found in Table 5.6.

By looking at their absorption and PL spectra, shown in Figure 5.18, several differences can be noticed between DBOV-Mes and DBOV-FAI. In first place, both spectra suffer a considerable red-shift after the incorporation of FAI substituents. The absorption and PL maximum of DBOV-Mes appear at 613 nm and 615 nm, respectively, displaying a really small Stokes shift and mirror-like vibronic progressions distinctive of

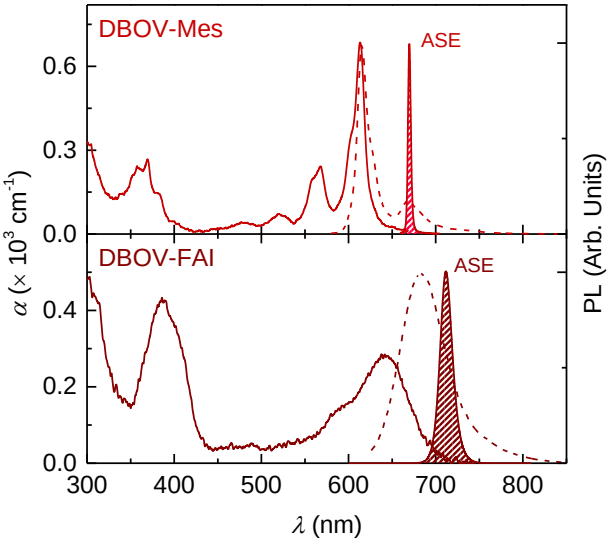

Figure 5.18 Optical properties of DBOV-doped PS films. Absorption coefficient (α; solid lines, left axis), photoluminescence (dashed lines, right axis) and amplified spontaneous emission (ASE; shaded areas, right axis) spectra of PS films doped with 1 wt% of DBOV-Mes (top panel, red) and DBOV-FAI (bottom panel, brown).

its extraordinarily planar and rigid skeleton.[85] Indeed, its sharp spectral shape allows distinguishing two vibronic progressions of low and high frequencies, shoulders at ~ 600 nm and 668 nm, respectively. On the other hand, absorption and PL spectra of DBOV-FAI present less features, only one vibronic progression is hardly distinguishable in them due to spectral broadening. To elucidate the origin of the spectral broadening, our collaborator Dr. Francesco Scotognella (Physics Department, Politecnico di Milano) performed DFT calculations. The results show that the fundamental state wave function is localized in the DBOV core, while the excited state wave function spreads over the whole molecular structure, entering into the FAI substituents. Indeed, for some excited states, the electronic wave function is completely localized in the FAI substituents. Such delocalization is controlled through the angle between the core and the substituent, which introduces a broad distribution of conformers that accounts for the inhomogeneous spectral broadening of DBOV-FAI. Now, absorption and PL maxima of DBOV-FAI appear at 644 nm and 684 nm, respectively, showing a wider Stokes shift and red-shifted spectra (by 31 and 69 nm the absorption and PL spectra, respectively) compared to DBOV-Mes. Also, the absorption band placed at 369 nm in DBOV-Mes red-shifts to 388 nm when the NG is substituted with the side FAI molecules, increasing its intensity relative to the main transition. Additionally, both compounds presented high PLQY in solution, up to 79 %[184] DBOV-Mes and 75 % DBOV-FAI.

Table 5.6 Optical and ASE parameter of DBOV-doped PS films

NG[a)]	h_f [nm][b)]	λ_{abs} [nm][c)]	λ_{PL} [nm][d)]	λ_{pump} [nm][e)]	α_{pump} [$\times 10^3$ cm^{-1}][f)]	t_{pump} [ns][g)]	λ_{ASE} [nm][h)]	FWHM [nm][i)]	$E_{th\text{-}ASE}$ [μJ cm^{-2}][j)]	$\tau_{1/2}$ [$\times 10^5$ pp][k)]
DBOV-Mes	570	369/568/<u>613</u>	<u>615</u>/668	568	0.24	4.5	670	4	420	6.6
				613	0.69	4.5	670	4	150	
DBOV-FAI	610	388/590/<u>644</u>	<u>684</u>	415	0.23	3.7	712	15	310	1.3
				644	0.28	4.6	714	15	270	3.5

[a)]The sample consist of a PS film doped with the corresponding NG on top of a quartz substrate, the concentration in the film is 1.0 ± 0.1 wt%; [b)]Film thickness (error $\sim$ 2 %); [c)]Wavelengths of the main absorption lines, the underlined value corresponds with the fundamental transition; [d)]Wavelengths of the main photoluminescence (PL) lines, the underlined value indicates the more intense peak; [e)]Pump wavelength; [f)]Absorption coefficient at λ_{pump} (error $\sim$ 2 %); [g)]Pump pulse width at λ_{pump}; [h)]Amplified spontaneous emission (ASE) wavelength (error $\pm$ 0.7 nm); [i)]ASE linewidth, defined as the full width at half maximum (FWHM), well above the threshold (error $\pm$ 1.3 nm); [j)]ASE threshold (error $\sim$ 20 %); [k)]Photostability half-life parameter expressed in pump pulses (error $\sim$ 20 %). The experimental pump fluence was set around four times $E_{th\text{-}ASE}$.

To study the photophysics arising after excitation, Dr. Giuseppe Paternò (Italian Institute of Technology in Milano) performed ultrafast TA spectroscopy in the 0.3–1 ns range.[183] The reversal dynamics between the SE and PB observed at short times for DBOV-FAI is absent in DBOV-Mes. This phenomenon can be related with the conformational rearrangement that produces the inhomogeneous broadening of DBOV-FAI spectra. Moreover, the CT state competing with the SE reported for DBOV-Mes[25] was absent in the TA spectra of DBOV-FAI, which is an important consequence of the substitution with bulky groups that prevent the π—π aggregation and, therefore, the formation of CT states. Additional experiments in the ns-ms regime were conducted to investigate the presence of long-living states. Interestingly, two peaks are observed in DBOV-Mes (530 nm and 680 nm) that can be associated to the absorption of triplet states generated via ISC. Notice that one of them is overlapped with the SE band, being highly detrimental for the operation of this material under continuous wave pump. On the other hand, no triplet absorption was observed in DBOV-FAI. It is possible to argue that the delocalization of the electronic wave-function affect mainly to the electronic structure of singlet states, leaving approximately unaltered the position of triplet states. Consequently, two hypotheses might me invoked to explain the phenomenon: *i*) the new electronic configuration hamper the ISC mechanisms, hence no triplet became available; and *ii*) the reverse ISC mechanism become more efficient as occurs with TADF compounds used for organic LEDs. Further theoretical calculations will be needed to elucidate the actual mechanism.

5.5.2 Amplified Spontaneous Emission Characterization

Next, the ASE properties of the PS films doped with DBOV compounds are characterized to demonstrate their suitability for gain applications. For DBOV-Mes, a narrow ASE peak (FWHM = 4 nm) was found by pumping in resonance with the main transition and its second vibronic ($E_{\text{th-ASE}}$ = 150 and 420 μJ cm^{-2}, respectively), but not with its absorption band at 369 nm. By pumping with higher energy, the system is excited to electronic states with CT character, precluding the amplification.[25] On the other hand, DBOV-FAI displayed ASE by pumping at 644 nm (λ_{ASE} = 714 nm, $E_{\text{th-ASE}}$ = 270 μJ cm^{-2}) and 415 nm (λ_{ASE} = 712 nm, $E_{\text{th-ASE}}$ = 310 μJ cm^{-2}), which is possible because the CT state is absent, owning to the new electronic structure. The ASE peak shows a linewidth of 15 nm, which is attributed to the spectral broadening as in the case of the PL spectrum. This feature could be used for the manufacture of tuneable laser devices in a wide spectral range. Remarkably, the thresholds obtained for DBOV-FAI are more than one order of magnitude lower than those obtained for other NGs emitting in the NIR, such as FZ3 (4400 μJ cm^{-2}, λ_{ASE} = 739 nm) or PP-Ar (1500 μJ cm^{-2}, λ_{ASE} = 787 nm), proving the success of this strategy for ASE tuning toward NIR.

The VPI method recently proposed by Dr. Luis Cerdán (see Section 3.4.1.2) has been used to determine the propagation losses and net gain parameters of these DBOV-doped PS films. As shown in Figure 5.19, DBOV-FAI presents approximately twice more propagation losses than DBOV-Mes (κ = 5.3 ± 1.0 and 2.5 ± 1.0 cm^{-1}, respectively). In

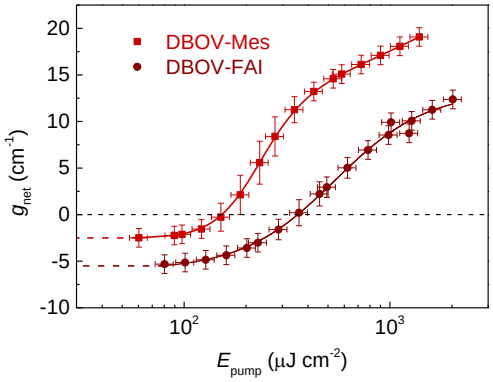

Figure 5.19 Net gain (g_{net}) versus pump energy density (E_{pump}) for DBOV-doped PS films. The values were obtained by applying the VPI method. Full lines are a guide to the eye and its intersection with the *y*-axis corresponds to the propagation loss coefficient (κ = 2.5 ± 1.0 and 5.3 ± 1.0 cm^{-1} for DBOV-Mes and DBOV-FAI, respectively).

the case of DBOV-Mes, the losses are governed by those of the PS film. However, the spectral broadening observed in the PL spectrum of DBOV-FAI introduces larger reabsorption losses, as the larger Stokes shift corroborates. Additionally, larger values of net gain are found for DBOV-Mes at any given pump energy density, which is a consequence of the lower molar content in the films. The same 1 wt% of compound in the film corresponds to twice more molecules of DBOV-Mes (1.4×10^{-5} mol g^{-1}) than DBOV-FAI (0.7×10^{-5} mol g^{-1}). Therefore, both higher propagation losses and lower molar concentration contribute to the larger ASE threshold of films doped with DBOV-FAI compared to those doped with DBOV-Mes.

The photostability of both DBOV compounds was tested by pumping the films uninterruptedly at $4 \times E_{th\text{-}ASE}$, demonstrating both NGs an excellent performance. The ASE half-life parameter determined for DBOV-FAI, under excitation at either 644 or 415 nm, were $\tau_{1/2} = 3.5 \times 10^5$ and 1.3×10^5 pump pulses, respectively. Similarly, DBOV-Mes shows $\tau_{1/2} = 6.6 \times 10^5$ pump pulses under excitation at 613 nm. These values are in accordance with those reported for other zigzag edged NGs, see previous sections.

5.6 Nanographene-Based Distributed Feedback Lasers

In order to demonstrate the convenience of all these NGs for practical applications, DFB lasers based in the NG-doped films analysed through the present chapter were manufactured in collaboration with other members of my research team (Víctor Bonal, Dr. José M. Villalvilla and Dr. José A. Quintana). The details about the fabrication and characterization of such devices would be one of the topics covered by the doctoral thesis

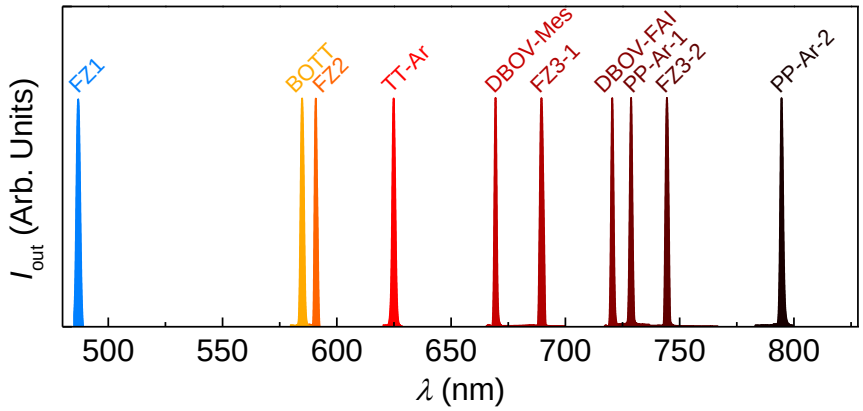

Figure 5.20 Nanographenes based distributed feedback (DFB) lasers. Each peak corresponds to the TE_0 mode of a different DFB device, the nanographene used as active material is indicated on top. The device's parameter can be found in Table 5.7.

Table 5.7 Parameters of NG-based DFB lasers

NG[a)]	h_f [nm][b)]	Λ [nm][c)]	λ_{pump} [nm][d)]	t_{pump} [ns][e)]	λ_{DFB} [nm][f)]	$E_{th\text{-}DFB}$ [μJ cm^{-2}][g)]	reference
FZ1	400	311	452	3.9	487.1	50	[86]
FZ2	480	382	545	4.4	590.5	11	[86]
FZ3-1	600	446	613	4.5	689.5	9500	[86,185]
FZ3-2	600	481	613	4.5	744.5	1300	[185]
FZ3-3	600	442/482	613	4.5	687.5/741.1	8700/7200	[185]
TT-Ar	520	403.2	565	4.4	624.9	25	[166]
PP-Ar-1	500	471.6	646	4.6	728.8	3100	[166]
PP-Ar-2	500	517.7	646	4.6	794.6	600	[166]
BOTT	490	377.0	532	4.3	584.9	22	[169]
DBOV-Mes	570	432.8	613	4.5	669.1	50	[183]
DBOV-FAI	610	467.4	415	3.7	720.3	60	[183]
			644	4.6	720.7	25	[183]

[a)]The device consist of a PS film doped with the corresponding NG at 1 wt% over a quartz substrate and covered with a relief grating of ~ 90 nm depth; [b)]Film thickness (error ~ 2 %); [c)]Grating period (error ~ 0.5 %); [d)]Pump wavelength; [e)]Pump pulse width at λ_{pump}; [f)]DFB emission wavelength (error ± 0.1 nm); [g)]DFB laser threshold (error ~ 20 %).

of Víctor Bonal, but a brief description of the manufacturing process can be found in Section 3.1.2. These DFBs consist of a top layer DCG resonator (i.e. a relief grating) deposited over the NG-doped PS film, which in turn is placed over a quartz substrate. The grating period is adjusted in each case so that the device emission matches the gain maximum of the material, see Table 5.7.

Remarkably, it is possible to manufacture operative lasers covering a broad part of the visible spectrum and entering into the NIR, as shown in Figure 5.20. Each of these narrow peaks (linewidth < 0.13 nm, limited by the instrumental spectral resolution) corresponds with the TE_0 laser mode emitted by a different device. The divergence of the laser beam was used to characterize the spatial coherence, getting a value of $\theta_d = (0.9 \pm$

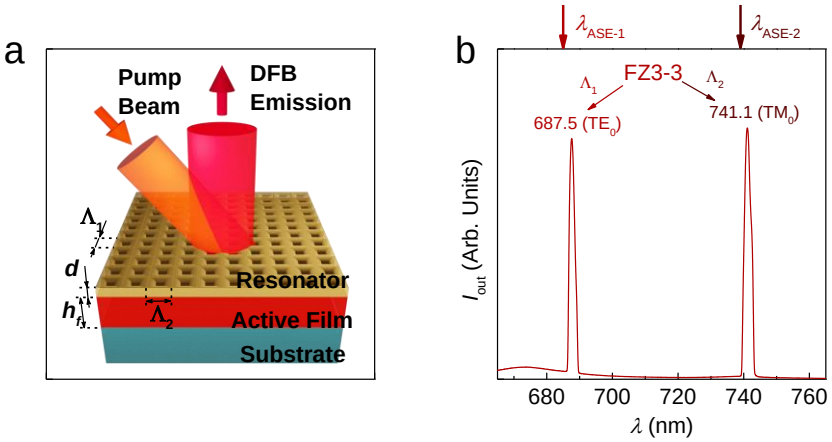

Figure 5.21 FZ3 based two dimensional distributed feedback (2D-DFB) laser. (a) 2D-DFB device scheme with a 2D top-layer resonator of periods Λ_1 and Λ_2 and depth d, disposed over an active film of thickness h_f. (b) Laser emission of the device, each peak correspond with the emission associated to a different period of the resonator. Their wavelengths and polarization respect to the grating lines are indicated close to each peak. The arrows on top of the figure indicate the position of FZ3 amplified spontaneous emission maxima in the spectrum. The device's parameter can be found in Table 5.7.

0.1) mrad. Respect to the laser thresholds, all these NGs present low values, in accordance to those of state of the art COPV*n* and PDI dyes dispersed in polymer matrixes,[4,62,153] with the exception of FZ3 and PP-Ar, whose thresholds are higher, in accordance with their ASE thresholds.

As a probe of concept, a two dimensional DFB (2D-DFB) device, based on a FZ3-doped PS film as active layer which shows dual ASE, was manufactured to demonstrate that functional lasing can be obtained simultaneously from both gain bands. Again the manufacture of such devices was performed by Víctor Bonal, Dr. José M. Villalvilla and Dr. José A. Quintana. As illustrated in Figure 5.21a, the resonator consists of two crossed gratings (90º) of different periods (Λ_1 and Λ_2) engraved by performing a double exposition of the photoresist before the desensitization process, see Section 3.1.2. The device was successfully operated showing two laser peaks, each one associated with a different grating period, as illustrated in Figure 5.21b. This device presents similar characteristics (linewidth and threshold) to those of DFBs with one-dimensional gratings based on FZ3. These results indicate that the dual-ASE observed in FZ3 and PP-Ar can be exploited for gain applications such as lasing.

5.7 Summary

Throughout this chapter, several NGs dispersed in PS films have been studied as active materials for laser applications, with a mayor focus on their optical and photophysical properties. Particularly, such characterization includes their steady-state

absorption and PL, PLQY, PL lifetime, ASE threshold and photostability, net gain, propagation losses and ultrafast TA. Moreover, low-temperature PL measurements, Raman spectroscopy and quantum chemical calculations were performed for some of them too. Important conclusions can be extracted from such an extensive characterization, which are summarized in the following lines.

From the studies with [*n,m*]*peri*-acenoacenes (Section 5.1 and 5.2), it is concluded that the elongation of the zigzag edge is an efficient way for red-shifting the absorption and emission spectra of NGs. Particularly, the more the electronic wave function is delocalized in a zigzag edge, the more the spectral properties red-shift. Additionally, the gain performance of FZ2 and TT-Ar is at the level of state of the art dyes dispersed in polymer matrixes, presenting a reduced value for their propagation losses, which are dominated by those of the PS matrix. Such picture can explain by itself the excellent ASE performance found for this family of NGs. The larger NGs FZ3 and PP-Ar, present rather larger ASE thresholds as consequence of ESA to electronic states laying at higher energy. Such process depletes the SE and increases the ASE threshold. Moreover, all this NGs present two gain bands associated to different vibronic progressions, being the one at shorter wavelengths strongly hampered by reabsorption. For FZ3 and PP-Ar, the ESA band equilibrates both gain bands, and them, dual-ASE is observed. Given the reactivity of zigzag edges, rather poor ASE photostability might be expected in the [*n,m*]*peri*-acenoacenes. However, the substitution with aryl groups at such positions protects the molecular structure, providing really lasting materials ($\sim 10^5$ pump pulses under ns excitation).

In Section 5.3, BOTT has been studied, which corresponds with a BO-doped version of TT-Ar. The results show that the replacement of the carbon atoms of the NG core by BO heteroatoms preserves the NG scaffold and modify its conjugation. Consequently, the spectral properties are blue-shifted, whilst an excellent performance is maintained in terms of PLQY, ASE threshold, net gain and propagation losses. Only the ASE photostability has been detrimentally affected, which might be related to the mayor reactivity of oxygen atoms.

Although the cove-edged NGs studied in Section 5.4 did not show ASE, an important conclusion can be extracted from their analysis. Typically, cove edged NGs present a distorted scaffold, as a consequence of the steric repulsion between the faced C-H bonds in the terminal positions. Such distortion has been related with a larger ICS rate to triplet states, which is highly detrimental for the gain performance. Indeed, TA spectra of CN1 show a negative broad feature that depletes the SE band and precludes gain.

The effect of incorporating bulky edge substituents over the optical and ASE properties of the NG has been investigated in Section 5.5. For it, the optical and ASE performance of DBOV-Mes has been compared to that of its substituted version DBOV-FAI, to which a couple of FAI molecules have been anchored. Such groups have a bathochromic effect over the original NG, inducing a red-shift over its absorption and PL spectra. Moreover, a large number of conformers with slightly different energetic distribution exist, which correspond to different dihedral angle between the core and the FAI substituents. Such phenomenon is evidenced in the inhomogeneous spectral

broadening of the absorption, PL and ASE spectra. Additionally, the propagation losses increase with the substitution given the larger value of the ground state reabsorption. However, the net gain is maintained and both NGs present a formidable ASE performance. Regarding the ASE photostability, the substitution with such a bulky group seems to be detrimental, which might be related to the stability of the FAI group.

DFB lasers have been manufactured and characterized to prove the suitability of these NGs for lasing applications.

General Conclusions and Future Research

The progress in the organic semiconductor field relies in three interacting actors, the synthetic chemistry, photophysical characterization and quantum chemical modelling. It is on the coordinated work of these fields that the smart design of organic materials with tailored properties becomes possible. Indeed, new compounds are continuously generated by organic chemists, whose properties are characterized by different spectroscopic techniques. Such studies provide precious knowledge for the development of more precise computational models, which in turn provide the basis for the creation of new compounds. The feedback between the three agents is therefore a self-propelled closed cycle that is at the centre of the field rapid expansion.

In this context, this thesis has dealt with the understanding of the optical and gain performance of organic molecules dispersed in inert matrixes. Particularly, novel organic compounds have been evaluated with an especial interest in the effect of their structural features over their photophysical properties. Such daunting task has been accomplished through the characterization of several photophysical properties (i.e. absorption, PL, PLQY, ASE threshold and photostability, net gain and propagation losses), but it would not have been possible without the collaboration with other leading research groups for the synthesis of the organic compounds (Molecular Design and Synthesis Group, Miguel Hernández University; Department of Chemistry, National University of Singapore; and Max Planck Institute for Polymer Research), the characterization of transient photophysical properties (Physics Department, Politecnico di Milano; Organic Optoelectronic Research Group, Vilnius University), low-temperature PL and Raman spectroscopy (Physical Chemistry Department, University of Málaga) and the performance of quantum chemical calculations (Physical Chemistry Department, University of Alicante; and Molecular Materials Theoretical Chemistry Group, University of Valencia).

The more relevant conclusions from this investigation are summarized below:

1) **The election of an appropriate matrix is fundamental for the efficiency of the active material. In this regard, the compatibility between the host polymer and the guest organic molecule can make the difference even between two a priori inert polymers**. The results obtained in the first part of chapter 4 points in this direction. There, the influence of the matrix is investigated through concentration dependence studies of two different PDI derivatives (PDI-O and *b*-PDI-A)

dispersed in two inert matrixes, PS and PMMA. These polymers are among the most widely used in optoelectronics. The major suitability of PS for hosting PDI derivatives is proven by the lower rates of intermolecular interaction/aggregation observed in PS with respect to PMMA. Consequently, a lower rate of PL quenching and better ASE thresholds and photostability are observed in PS rather than in PMMA. Moreover, the high rate of aggregation observed in PMMA affects adversely, not only the emission properties of the PDI derivatives, but also the optical quality of the waveguides which is better in PS. Therefore, an intelligent election of the matrix is crucial for the design of efficient active materials.

2) **The substitution of organic molecules with lateral groups has a direct impact on their photostability**. Typically, side groups are used to provide solubility to the molecule or even to prevent molecular aggregation, but other fundamental aspects might be modified as well, e.g. the photostability. The experiments performed in the second part of chapter 4 with PS films doped with three different *b*-PDI derivatives attest to this. The difference between these derivatives lies in their substituents at the imide positions that are aliphatic chains (*b*-PDI-A), diisopropylphenyl groups (*b*-PDI-O) or terphenyl moieties (*b*-PDI-Tp). The analysis of PS films doped with low concentrations of the molecules shows that *b*-PDI compounds with phenyl-like substituents at the imide positions are three times more lasting than that with the aliphatic chains. Unfortunately, the concentration dependence study demonstrates that the compounds with phenyl-like moieties are also more prone to aggregate and suffer PL quenching, which is detrimental for the ASE performance, including the photostability. Indeed, *b*-PDI-A can be incorporated into the matrix up to the 50 wt% with moderate concentration quenching and no hint of aggregation, whilst for *b*-PDI-Tp, H-aggregation is observed at concentrations of 6 wt% and above.

3) **The optoelectronic properties of NGs depend on their structure, i.e. their size and edge. Hence, knowing how the two are related become a key piece for the development of new organic compounds with tailored properties**. In this regard, studies performed with [*n,m*]*peri*-acenoacenes have made it possible to understand that the presence of zigzag edges red-shifts the spectral properties. The intensity of the shift depends on the portion of the wave function delocalized over the zigzag edge. Additionally, full-zigzag edged NGs have demonstrated to be efficient lasing materials at the level of other state-of -the-art organic molecules. The substitution with aryl groups at the more reactive positions proved valuable for preventing the photodegradation of the compounds, yielding lasting materials ($\sim 10^5$ pump pulses under ns excitation) with optimal solubility. Interestingly, the larger NGs FZ3 and PP-Ar present dual-ASE emission, which is consequence of the overlapping between their SE and ESA bands, a phenomenon that depletes the SE and increases the ASE threshold.

4) **Another important way for modulating the optoelectronic properties is the substitution of carbon atoms of the NG backbone for heteroatoms, for example nitrogen or boron atoms**. Indeed, such substitution modifies the wave function delocalization and, therefore, the optoelectronic properties. Here, two pairs of carbon atoms from the backbone of one previously studied [*n,m*]*peri*-acenoacene have been substituted by two pairs of boron-oxygen atoms, preserving its scaffold. Remarkably, the spectral properties blue-shifted by 35 nm, whilst other photophysical parameters, such as the PLQY or the ASE threshold have been maintained. Only the operational lifetime has been barely affected.

5) **The optoelectronic properties of the NGs can be modified via substitution with bulky edge groups**. In the particular case of the NG called DBOV-Mes, substitution with FAI molecules (DBOV-FAI), produced a red-shift of the spectral properties. The exact position of the electronic levels depends on the dihedral angle between the DBOV core and the FAI substituent, resulting in the inhomogeneous spectral broadening of the absorption, PS and ASE spectra. Consequently, a larger portion of the absorption spectrum overlaps with the ASE peak, resulting in an increase of the propagation losses. Besides this, the net gain is maintained and both NGs present a formidable ASE performance. Actually, the inclusion of the bulky groups presents other two advantages that might be related with the excellent ASE performance of DBOV-FAI despite the increase of reabsorption losses: *i*) the bulky substituents prevent molecular aggregation, thus inhibiting the formation of detrimental CT states present in DBOV-Mes; *ii*) the induced modification of the electronic structure cancel out the triplet states (present in DBOV-Mes), which are detrimental because which they overlap with the SE.

6) **The suitability of all these strategies for laser applications has been proved with the manufacture of operative DFB lasers.** Particularly, three of the compounds present laser emission in the relevant NIR region, where a shortage of organic emitters exists.

Prospects for future works

For the development of practical applications, particular interest exists in the possibility of electrically-pumped devices.[5] Accordingly, inert matrixes should be replaced by electroactive ones. For example, 4,4'-bis(N-carbazikyl)-1,1'-biphenyl has been used in the literature for LEDs and in some cases for electrically-pumped organic lasers.[5,110] Additionally, new strategies for increasing the amount of organic compound dispersed in the matrix without suffering self-quenching might contribute to the reduction of the operational energy and the use of compact optical pumping sources.[45] For such purpose, the dispersion of the active molecule in a covalent organic framework or other similar macrostructure that isolate the chromophores might be important.[186] Other possibility is the use of massive substituents to isolate the molecules, and prevent interactions among them, as very recently was demonstrated with bay substituted PDI

compounds.[187] Furthermore, the concept of TADF molecule, in which the electronic states are engineered to retrieve all the generated triplet states towards singlet states, might be useful for the development of continuous wave organic lasers.[188] Additionally, the effect of different types of edges, different heteroatoms and their position, the molecular twist and other structural features over the gain properties of NGs are interesting aspects that need to be clarified.[18]

Resumen y Conclusiones

Esta sección recoge un resumen y unas conclusiones en castellano. La sección ha sido incluida tal y como está establecido en normativa de la Escuela de Doctorado de la Universidad de Alicante. Sin embargo esta sección ha sido elaborada a partir de la traducción de las secciones principales de la tesis, por lo que se recomienda la lectura del texto principal para tener una idea más clara de los conceptos tratados.

1 Introducción

Desde la primera demostración experimental de emisión láser realizada por Theodore H. Maiman en 1960,[1] esta tecnología ha experimentado una expansión sin precedentes, convirtiéndose en parte de nuestra vida diaria. De hecho, el término láser (del inglés, luz amplificada por emisión estimulada de radiación) se ha convertido en una palabra cotidiana con el paso del tiempo y los láseres se utilizan en una amplia gama de áreas, incluidas las telecomunicaciones, la fabricación industrial, la cirugía láser o la instrumentación de alta precisión, entre otras. El estudio del láser y sus aplicaciones es un campo multidisciplinario, que se basó originalmente en la física, la química y la ciencia de los materiales; pero hoy en día también forma parte de la fotónica, la nanotecnología, la ingeniería biomédica y mucho más. Después de tantos años, la investigación en láser sigue siendo hoy un campo de investigación floreciente con más de sesenta mil artículos de investigación publicados durante el año 2020. Su relevancia es tal que el láser ha sido galardonado, entre nominaciones directas e indirectas, al menos treinta y ocho veces con el Premio Nobel, aunque, paradójicamente, T. H. Maiman nunca recibió uno.[2]

Los láseres basados en medios activos orgánicos han atraído gran atención durante muchos años, principalmente porque permiten la sintonización de la longitud de onda de emisión en todo el espectro visible, pero recientemente además porque ofrecen una alta compacidad, flexibilidad mecánica y producción a bajo costo.[3,4] En particular, muchos esfuerzos se han centrado en láseres orgánicos de película delgada (TFOL), llegando al punto en que estos dispositivos pueden ser bombeados con fuentes ópticas de baja potencia, muy recientemente incluso eléctricamente.[5] Con respecto a las aplicaciones, los láseres orgánicos ya han demostrado su potencial en varias áreas. Por ejemplo, como fuentes sintonizables para espectroscopia,[6,7] amplificadores para comunicaciones

ópticas,[8] sensores químicos para vapor de explosivos[9] y sensores altamente sensibles y específicos no intrusivos para la trazabilidad de fármacos, investigación biológica, pruebas diagnósticas, seguridad alimentaria, etc.[10–14] De hecho, los TFOL presentan un gran potencial en el área de la biomedicina, para la detección o seguimiento de una amplia gama de enfermedades. La identificación temprana de proteínas biomarcadoras de enfermedades es fundamental para tener un buen diagnóstico y mejorar el éxito del tratamiento.

El desarrollo de estas aplicaciones está impulsado por los avances en la ciencia de los materiales, particularmente por el desarrollo de nuevos compuestos orgánicos. Curiosamente, las propiedades de las moléculas orgánicas dependen no solo de su composición, sino también de cómo están dispuestos sus átomos (es decir, del tamaño y la forma de la molécula).[15] Por lo tanto, el diseño inteligente de materiales con propiedades optoelectrónicas personalizadas es posible a través de técnicas de síntesis ascendente utilizadas en química orgánica, que proporcionan los medios para obtener los compuestos con una precisión y reproducibilidad excepcionales.[16,17] Además, estudios fotofísicos y modelos computacionales son necesarios para comprender la relación real entre las diferentes características moleculares y las propiedades optoelectrónicas. En este sentido, la conexión entre muchas de las características físicas moleculares (por ejemplo, el borde y la forma de la molécula o la torsión del núcleo) y las propiedades de ganancia óptica siguen siendo desconocidas,[18] lo que limita el desarrollo futuro de aplicaciones prácticas. De hecho, todavía hay aspectos importantes desde el punto de vista de los materiales orgánicos que deben evaluarse para llevar las aplicaciones TFOL a un nivel de comercialización.

A primera vista, el material deseable debería ser simultáneamente procesable a bajo costo mediante métodos basados en disoluciones, fotoestables y energéticamente eficientes, al menos para permitir el bombeo con fuentes compactas. En este sentido, los compuestos orgánicos dispersos en matrices termoplásticas, preparados como películas delgadas que constituyen guías de ondas, se encuentran entre los materiales más fotoestables utilizados para este fin y han demostrado ser materiales eficientes. Sin embargo, todavía hay mucho espacio para mejorar los requisitos energéticos optimizando el rendimiento de la guía de ondas. Además, la comprensión de los mecanismos de fotodegradación podría conducir a una mejora de la ya alta estabilidad.

Además, existe un interés creciente en los materiales que operan en la región del infrarrojo cercano (NIR)[19] impulsado por el desarrollo de aplicaciones biomédicas[20] y de telecomunicaciones.[21] Hasta la fecha, solo se han demostrado unos pocos láseres orgánicos cuya emisión se produce más allá de los 700 nm,[4,19] principalmente como consecuencia del efecto perjudicial de la desintegración rápida no radiativa que se produce siguiendo la ley del gap de energía,[22,23] de mecanismos de quenching que aparecen con la concentración[24] y de la presencia intra-gap de estados de transferencia de carga (CT) y estados triplete.[8,25] Por lo tanto, una comprensión adecuada de tales mecanismos y cómo prevenirlos podría conducir a una nueva generación de emisores orgánicos en el NIR. En este sentido, existen materiales emergentes que son una gran promesa para los dispositivos emisores de luz y la integración con otras tecnologías, cuyo conocimiento se encuentra en una etapa muy temprana. Ese es el caso de los nanografenos (NGs).

El objetivo principal de esta tesis es estudiar las propiedades fotofísicas de moléculas orgánicas dispersas en matrices inertes con el objetivo de mejorar su desempeño como materiales láser. En este sentido, se han realizado varias actuaciones: *i*) investigación sistemática de dos polímeros termoplásticos comerciales (poliestireno, PS; y polimetilmetacrilato, PMMA) como matrices inertes para dispersar compuestos de perilenodiimida (PDI) con un mayor enfoque en optimizar las propiedades de la guía de ondas para la reducción de las necesidades energéticas operativas de los dispositivos; *ii*) conocer los mecanismos de quenching con la concentración y la fotodegradación de los compuestos de PDI dispersos en películas de PS con el objetivo de obtener dispositivos más duraderos y eficientes; y *iii*) estudiar las propiedades fotofísicas de nuevos compuestos NG dispersos en matrices inertes con el fin de dilucidar la relación existente entre su estructura (borde, heteroátomos, sustituyentes) y su ganancia óptica.

Esta disertación de tesis se organiza en torno a tres bloques principales más algunas observaciones finales:

Primero, una introducción dividida en dos capítulos. Los principios de fotofísica fundamentales para la amplificación de luz en moléculas orgánicas se presentan en el capítulo 1, incluidos también los principios de funcionamiento operativo de los dispositivos utilizados para la caracterización de los materiales, es decir, guías de ondas planas y láseres de retroalimentación distribuida (DFB). El segundo capítulo proporciona un compendio bibliográfico actualizado de los compuestos orgánicos utilizados como medios de ganancia, para establecer el marco para fijar la motivación y los objetivos de esta tesis.

A continuación, los procedimientos adoptados para la fabricación y caracterización de las muestras se explican en detalle en el capítulo 3. Prácticamente, todas las muestras analizadas en el desarrollo de esta tesis son guías de ondas planas utilizadas para la caracterización de los materiales, aunque también existen algunos láseres DFB utilizados para demostrar la conveniencia de estos materiales para aplicaciones prácticas. Las técnicas de caracterización se han dividido en tres categorías, a saber, propiedades ópticas de estado estacionario, propiedades fotofísicas transitorias y estudios láser. La caracterización óptica estándar y los experimentos de emisión espontánea amplificada (ASE) y láser se realizaron en la Universidad de Alicante (UA), mientras que los experimentos de absorción transitoria (TA) y fotoluminiscencia resuelta en el tiempo (TRPL) se realizaron durante una estancia de tres meses en el Politécnico de Milán o en colaboración con la Universidad de Vilnius.

En tercer lugar, los resultados se presentan en dos partes separadas según los materiales orgánicos analizados en ellas. El capítulo 4 recoge todos los estudios realizados con compuestos PDI, mientras que los realizados con NG se resumen en el capítulo 5.

Finalmente, la disertación de tesis concluye con un resumen de los principales resultados y una prospectiva para el desarrollo posterior de los temas tratados.

2 Estudios con Derivados de la Perilenodiimida

2.1 Influencia de la Proporción de PDI en la Mezcla y la Matriz Polimérica en las Propiedades Laser de los Compuestos de Perilenodiimida

Como se describe en la Sección 2.4, el rendimiento óptimo del láser de un determinado compuesto orgánico disperso en una matriz inerte depende de varios parámetros, como la concentración del compuesto y el tipo de matriz. En este sentido, el objetivo principal desarrollado en la Sección 4.1 de la tesis consiste en determinar qué matriz (PS o PMMA) y concentración de PDI son las mejores para la fabricación de dispositivos TFOL basados en PDI. Teniendo esto en cuenta, las propiedades ópticas y ASE de las películas dopadas con PDI se analizan para una variedad de concentraciones de colorante, prestando atención a los coeficientes de ganancia y pérdida neta, que determinan el potencial del material para un láser con base de guía de ondas. El análisis se realiza con dos derivados de la PDI completamente diferentes, PDI-O y el nuevo derivado *b*-PDI-A, pueden verse en la Figura 4.1. Una característica distintiva entre ambos sistemas es la existencia o no de sustituyentes en las posiciones de la bahía (particularmente en las posiciones 1 y 7). Como se discute en la Sección 2.2, los sustituyentes elegidos para las posiciones de las bahías permiten incorporar el compuesto en la matriz en una concentración mayor sin que esto afecte significativamente la eficiencia de su PL. Al mismo tiempo, los sustituyentes producen un desplazamiento de las propiedades ópticas hacia longitudes de onda más largas.

2.2 Efecto de los Sustituyentes en las Posiciones de Imida sobre las Propiedades Láser de Compuestos de Perilendiimida Sustituidos en las Posiciones 1 y 7 de la Bahía

Hasta ahora, todos los compuestos de *b*-PDI reportados presentan altos niveles de eficiencia cuántica (PLQY) y excelentes umbrales ASE incluso a altas concentraciones, *b*-PDI-A podría ser un ejemplo de ello.[63,69,70] Sin embargo, todos ellos presentan una fotoestabilidad de ASE más baja que derivados de la PDI no sustituidos en la bahía de (*u*-PDI) de última generación, como PDI-O. Curiosamente, esos compuestos *b*-PDI llevan sustituyentes de tipo alifático en la posición imida, lo que demostró producir *u*-PDI menos fotoestables que los sustituyentes de tipo fenilo.[62] Por tanto, se han propuesto dos nuevos derivados de tipo *b*-PDI con sustituyentes en las imidas de tipo fenilo denominados *b*-PDI-O y *b*-PDI-Tp (representados en la Figura 4.8) con el objetivo de mejorar la fotoestabilidad de los *b*-PDI. Sorprendentemente, el estudio minucioso de sus propiedades ópticas y ASE evidencia la mejora de la fotoestabilidad, pero también su mayor propensión a la agregación. El estudio se ha realizado primero con películas de PS dopadas con una baja concentración de *b*-PDI y soluciones líquidas de los derivados de *b*-PDI para determinar sus propiedades como moléculas aisladas. En segundo lugar, las películas de PS dopadas con concentraciones más altas de *b*-PDI han sido caracterizadas para estudiar la dependencia de las interacciones/agregaciones moleculares con la concentración en la matriz.

2.3 Resultados de los Estudios con Perilenodiimidas

En esta Sección se han estudiado diferentes derivados de la PDI dispersos en matrices inertes, prestando especial atención a la influencia de la matriz y los diferentes sustituyentes sobre las propiedades ópticas y ASE. Para cada compuesto y matriz, se han realizado estudios de dependencia de la concentración que proporcionan información valiosa sobre los diferentes ratios de quenching exhibidos por cada uno de estos materiales. Además, se han realizado algunos estudios fotofísicos para caracterizar adecuadamente el mecanismo de quenching con la concentración y las propiedades ASE en los nuevos compuestos de *b*-PDI. Las principales conclusiones tras dicha caracterización se resumen en los siguientes párrafos.

En primer lugar, se han comparado PS y PMMA como matrices para albergar compuestos PDI, concluyendo la mayor idoneidad del PS para tal fin (véase la Sección 4.1 de la tesis). La misma conclusión se ha extraído del análisis de dos derivados de PDI diferentes, un compuesto comercial PDI-O y un derivado novedoso *b*-PDI-A. Aunque las propiedades ASE del compuesto PDI-O se encuentran entre las mejores de las reportadas para moléculas orgánicas pequeñas dispersas en una matriz, el compuesto PDI-O muestra emisión excimérica cuando la concentración aumenta por encima de un cierto límite (5% en peso en PS). Por otro lado, *b*-PDI-A presenta una solubilidad mejorada que permite su dispersión en la matriz hasta el 50% en peso con presencia moderada de quenching y sin indicios de agregación o formación de excímeros. En particular, a cualquier concentración dada, los valores de PLQY, los umbrales de ASE y la fotoestabilidad encontrados para las muestras basadas en PS son sistemáticamente mejores que los encontrados para las muestras de PMMA. Además, las películas de PS presentan indicios de quenching de la PL a concentraciones más altas que las películas de PMMA, lo que resulta en una diferencia aún más pronunciada entre los resultados óptimos de ambas matrices. El análisis de las ganancias y pérdidas apunta en la misma dirección, encontrándose los valores de ganancia más altos y las pérdidas de propagación más bajas para las películas basadas en PS. Además, se encuentran pérdidas de propagación similares para películas de PS dopadas con concentraciones bajas y altas de PDI-O (1 y 5% en peso), mientras que para las mismas concentraciones en PMMA las pérdidas de propagación se duplican de una concentración a otra. Por lo tanto, la mayor tasa de agregación observada en PMMA está afectando no solo las propiedades de emisión del compuesto, sino también la calidad óptica de la guía de ondas. Desafortunadamente, la menor fotoestabilidad de *b*-PDI-A impide la extracción de datos fiables de ganancia y pérdida de muestras de PMMA dopadas con él para extender completamente la comparación entre matrices.

La segunda parte de los estudios con perilenodiimidas (véase la Sección 4.2 de la tesis) está dedicada a investigar las propiedades ópticas y ASE de tres derivados de *b*-PDI con diferentes sustituyentes en sus posiciones imidas. Se han comparado tres compuestos, *b*-PDI-A con sustituyentes de tipo alifático y *b*-PDI-O y *b*-PDI-Tp, con sustituyentes de tipo fenilo. En cierto sentido, los compuestos con sustituyentes de tipo fenilo en las posiciones de las imidas son más fotoestables que los que tienen cadenas alifáticas, como se concluye del análisis de películas dopadas con bajas concentraciones de colorante. Sin

embargo, los compuestos con sustituyentes de tipo fenilo también son los más propensos a sufrir quenching de la PL tras el aumento de la concentración de *b*-PDI en la película, con las consecuencias negativas asociadas en términos de umbrales ASE y fotoestabilidad. Particularmente, las películas de PS dopadas con altas concentraciones de *b*-PDI-Tp presentan señales claras de formación de agregados tipo H con emisión excimérica, como lo avalan los experimentos de TRPL. A pesar de la falta de cambios espectrales, no se puede ignorar algún fenómeno similar en películas dopadas con *b*-PDI-O, dado el dramático quenching de la PL observado en ellas. Finalmente, los espectros TA de las películas dopadas con compuestos *b*-PDI muestran una banda de absorción de especies excitadas (ESA) cercana al pico de emisión estimulada (SE), lo que podría ser perjudicial para la generación de la inversión de población. Este fenómeno podría ser la razón detrás de los umbrales más altos observados en los compuestos de *b*-PDI en comparación con otros PDI punteros, como es el caso del PDI-O.

3 Estudios con Nanografenos

3.1 Extensión 2D de la Conjugación en Periacenoacenos, Serie FZ

A lo largo de la Sección 5.1, se caracterizan las propiedades ópticas y ASE de tres NG con cuatro bordes en zigzag de tamaño creciente (designados como FZ1, FZ2 y FZ3, véase la Figura 5.1). Estos NGs pertenecen a la familia de los [*n*, *m*]periacenoacenos, que consisten en un número *m* de [*n*]acenos fusionados en una nanoestructura rómbica. En particular, estos tres NG tienen el mismo *n* (*n* = 3) y *m* creciente (*m* = 2, 3, 4, para FZ1, FZ2 y FZ3, respectivamente). El borde en zigzag del NG se alarga con el aumento de tamaño, lo que se ha descrito como una forma óptima para desplazar al rojo las bandas de absorción y emisión en sistemas similares.[88,89] Aunque el borde en zigzag extendido puede soportar estados de mitad de gap con carácter paramagnético (estados de borde) perjudiciales para la emisión de luz,[164] los compuestos FZ presentan un tamaño reducido, insuficiente para formar tal estado de borde. Por lo tanto, estos NG representan una excelente opción para la sintonización del color de la emisión.

3.2 1D Extensión 1D de la Conjugación en Periacenoacenos, TT-Ar y PP-Ar

En la Sección anterior, la conjugación electrónica de FZ1 ([3,2]periacenoaceno) se ha ampliado al expandir el NG hacia una estructura más ancha (es decir, en 2D), lo que resulta en un desplazamiento al rojo de las propiedades espectrales. En la Sección 5.2, se examinan las propiedades ópticas y ASE de dos NG (llamados TT-Ar y PP-Ar), pertenecientes a la misma familia de [*n*, *m*]periacenoacenos, y generadas al extender FZ1 en 1D. En particular, estos dos NG se generan manteniendo *m* = 2 mientras que *n* se incrementa de 3 a 5, elementos de la serie denominados FZ1, TT-Ar y PP-Ar, respectivamente, véase la Figura 5.6. Sorprendentemente, se logra un desplazamiento hacia el rojo más grande aumentando *n* que *m*, lo que puede atribuirse a una deslocalización más

eficiente de la función de onda electrónica sobre el borde en zigzag en esta nueva serie de NGs.

3.3 Modulación de las Propiedades Ópticas del Nanografeno a través de la Hetero-Sustitución con BO

Como se plantea en secciones anteriores, las propiedades espectrales de los NG se pueden ajustar con éxito mediante la extensión del tamaño molecular, es decir, extendiendo la conjugación molecular. Sin embargo, se podrían contemplar rutas alternativas para tal propósito. Por ejemplo, los átomos de carbono pueden ser sustituidos por heteroátomos de boro, mientras que la estructura del NG permanece aproximadamente constante. Esto da como resultado una disminución de la densidad electrónica en los sitios sustituidos y un aumento de la densidad electrónica en los sitios de carbono vecinos. Como resultado, algunos grupos han reportado un comportamiento de tipo p en NG dopados con boro.[91] En la Sección 5.3, se estudian las propiedades ópticas y láser de un NG dopado con heteroátomos de boro y oxígeno, denominado BOTT (véase la Figura 5.10). En particular, este NG consiste en un núcleo TT-Ar, en el que cuatro átomos de carbono han sido reemplazados por dos átomos de boro y dos átomos de oxígeno. Curiosamente, esta combinación particular de heteroátomos desplaza significativamente al azul las propiedades espectrales del nuevo compuesto (BOTT) con respecto a las del compuesto sin dopar (TT-Ar), mientras mantiene las buenas propiedades ASE de este último.

3.4 Nanografenos con Bordes tipo Cove

Una forma alternativa de ajustar las propiedades ópticas y láser de los NG es modificando sus estructuras de borde. Por ejemplo, es bien sabido que los NG completamente benzenoides, que están formados casi exclusivamente por los bordes de tipo armchair, son más estables y presentan gaps de energía más grandes que los NG con bordes en zigzag de tamaño similar.[15] En este sentido, existen algunos trabajos sobre las propiedades espectrales de los NG con bordes tipo cove,[171,177–179] pero ninguno de ellos reporta ASE o emisión láser. En la Sección 5.4, se investigan dos NG cuadrados de tamaño creciente denominados CN1 y CN2, cada uno con dos bordes de tipo cove y dos bordes de tipo armchair (véase la Figura 5.14). Aunque estos dos NG no muestran ASE, de su análisis se pueden extraer conclusiones importantes con respecto al diseño molecular para láseres.

3.5 Ingeniería del Estado Excitado a través del Uso de Sustituyentes Voluminosos

Los estudios anteriores de esta sección pretenden demostrar la idoneidad de la extensión molecular para el ajuste de la longitud de onda hacia el NIR. Sin embargo, varios problemas fundamentales limitan esta ruta, como la rápida conversión interna de los electrones que regresan a su estado fundamental y la absorción intragap de tripletes y estados de CT. En el primer caso, la ley del gap de energía para transiciones no radiativas

establece que la conversión interna no radiativa en el sistema es proporcional a la superposición entre las funciones de onda del estado electrónico excitado y los niveles vibrónicos asociados al estado fundamental electrónico.[23,182] Además, el número de modos vibrónicos aumenta con el tamaño molecular, empeorando la situación. En el segundo caso, los estados CT y triplete podrían resultar en pérdidas de ganancia siempre que se superpongan con el SE del sistema.[8] Sin embargo, estos mecanismos son de naturaleza muy diferente. De hecho, los estados de triplete son un fenómeno intramolecular, que se genera a través de la conversión de estados singlete excitados, mientras que los estados de CT se generan en agregados supramoleculares. A veces, ambos pueden ocurrir simultáneamente, como es el caso de DBOV-Mes (véase la Figura 5.17), que presenta un estado CT y bandas de absorción de estados triplete superpuestas con su banda SE.[25,183] Para hacer frente a este problema, una nueva versión de este NG se ha considerado, la cual incorpora dos sustituyentes voluminosos (FAI) anclados a sus bordes armchair, el compuesto es denominado DBOV-FAI, véase la Figura 5.17. En la Sección 5.5, se estudian las propiedades ópticas y ASE de DBOV-Mes y DBOV-FAI, demostrando que es posible obtener ASE eficiente en el NIR mediante el diseño inteligente de la estructura molecular.[183]

3.6 Resultados de los Estudios con Nanografenos

En esta sección, se han estudiado varios NG dispersos en películas de PS como materiales activos para aplicaciones láser, con especial atención a sus propiedades ópticas y fotofísicas. En particular, dicha caracterización incluye su absorción y emisión en estado estacionario, PLQY, tiempo de fluorescencia, umbral y fotoestabilidad ASE, ganancia neta, pérdidas de propagación y TA ultrarrápida. Además, para algunos de ellos también se realizaron mediciones de PL a baja temperatura, espectroscopía Raman y cálculos químico-cuánticos. Se pueden extraer conclusiones importantes de una caracterización tan extensa, que se resumen en las siguientes líneas.

De los estudios con [*n, m*]periacenoacenos (Sección 5.1 y 5.2), se concluye que el alargamiento del borde en zigzag es una forma eficiente de desplazar al rojo los espectros de absorción y emisión de NG. En particular, cuanto más se deslocaliza la función de onda electrónica en un borde en zigzag, más se desplazan al rojo las propiedades espectrales. Adicionalmente, la ganancia de FZ2 y TT-Ar están al nivel de las mejores moléculas orgánicos dispersas en matrices poliméricas, presentando un valor reducido para sus pérdidas de propagación, las cuales están dominadas por las de la matriz PS. Tal imagen puede explicar por sí misma las excelentes propiedades ASE encontradas para esta familia de NG. Los NG más grandes, FZ3 y PP-Ar, presentan umbrales ASE bastante más grandes como consecuencia de la presencia de ESA por parte de estados electrónicos que se encuentran en una energía más alta. Tal proceso deteriora la SE y aumenta el umbral ASE. Además, todos estos NG presentan dos bandas de ganancia asociadas a diferentes progresiones vibrónicas, siendo la de menor longitud de onda fuertemente cancelada por la reabsorción. Para FZ3 y PP-Ar, la banda ESA equilibra ambas bandas de ganancia, y en ellas, se observa ASE dual. Dada la reactividad de los bordes en zigzag, podría esperarse

una fotoestabilidad ASE bastante pobre en los compuestos de la familia de los [*n*, *m*]periacenoacenos. Sin embargo, la sustitución con grupos arilo en tales posiciones protege la estructura molecular, proporcionando materiales realmente duraderos (~ 10^5 pulsos de bombeo bajo excitación en ns).

En la Sección 5.3, se ha estudiado BOTT, que se corresponde con una versión de TT-Ar dopada con BO. Los resultados muestran que al reemplazar los átomos de carbono del núcleo del NG por heteroátomos de BO la estructura es preservada y su conjugación modificada. En consecuencia, las propiedades espectrales se desplazan al azul, mientras que se mantiene un rendimiento excelente en términos de PLQY, umbral ASE, ganancia neta y pérdidas de propagación. Solo la fotoestabilidad ASE se ha visto afectada negativamente, lo que podría estar relacionado con la mayor reactividad de los átomos de oxígeno.

Aunque los NG con borde tipo cove estudiados en la Sección 5.4 no mostraron ASE, se puede extraer una conclusión importante de su análisis. Típicamente, los NG con bordes tipo cove presentan un nucleo distorsionado, como consecuencia de la repulsión estérica entre los enlaces C-H enfrentados en las posiciones terminales. Dicha distorsión se ha relacionado con una mayor tasa de conversión de estados singlete excitados a estados triplete, lo que es muy perjudicial para la ganancia. De hecho, los espectros de TA de CN1 muestran una amplia banda negativa que cancela la banda de SE y previene la ganancia.

El efecto de incorporar sustituyentes de borde voluminosos sobre las propiedades ópticas y ASE del NG se ha investigado en la Sección 5.5. Para ello, se han comparado las propiedades ópticas y ASE de DBOV-Mes con las de su versión sustituida DBOV-FAI, a la que se han anclado un par de moléculas FAI. Dichos grupos tienen un efecto bathocrómico sobre el NG original, induciendo un desplazamiento hacia el rojo sobre los espectros de absorción y emisión. Además, existe un gran número de confórmeros con distribuciones energéticas ligeramente diferentes, que corresponden a diferentes ángulos diedros entre el núcleo y los sustituyentes FAI. Tal fenómeno se evidencia en el ensanchamiento espectral no homogéneo de los espectros de absorción, emisión y ASE. Además, las pérdidas de propagación aumentan con la sustitución dado el mayor valor de la reabsorción del estado fundamental. Sin embargo, la ganancia neta se mantiene y ambos NG presentan un rendimiento ASE formidable. En cuanto a la fotoestabilidad ASE, la sustitución por un grupo tan voluminoso parece ser perjudicial, lo que podría estar relacionado con la estabilidad del grupo FAI.

Finalmente se han fabricado y caracterizado láseres DFB para demostrar la idoneidad de estos NG para aplicaciones láser.

Conclusiones Generales e Investigaciones Futuras

El progreso en el campo de los semiconductores orgánicos se basa en tres actores que interactúan, la química sintética, la caracterización fotofísica y el modelado químico-cuántico. Es gracias al trabajo coordinado de estos campos que es posible el diseño inteligente de materiales orgánicos con propiedades personalizadas. De hecho, los

químicos orgánicos generan continuamente nuevos compuestos, cuyas propiedades se caracterizan por diferentes técnicas espectroscópicas. Estos estudios proporcionan un conocimiento valioso para el desarrollo de modelos computacionales más precisos, que a su vez proporcionan la base para la creación de nuevos compuestos. La retroalimentación entre los tres agentes es, por tanto, un ciclo cerrado autopropulsado que está en rápida expansión.

En este contexto, esta tesis se ha ocupado de la comprensión de las propiedades ópticas y de ganancia de moléculas orgánicas dispersas en matrices inertes. En particular, se han evaluado nuevos compuestos orgánicos con especial interés en el efecto de sus características estructurales sobre sus propiedades fotofísicas. Esta tarea abrumadora se ha logrado mediante la caracterización de varias propiedades fotofísicas (es decir, absorción, emisión, PLQY, umbral y fotoestabilidad ASE, ganancia neta y pérdidas por propagación), pero no hubiera sido posible sin la colaboración con otros grupos de investigación líderes para el síntesis de los compuestos orgánicos (Grupo de Síntesis y Diseño Molecular, Universidad Miguel Hernández; Departamento de Química, Universidad Nacional de Singapur; e Instituto Max Planck para la Investigación de Polímeros), la caracterización de propiedades fotofísicas transitorias (Departamento de Física, Politécnico de Milán; Grupo de Investigación en optoelectrónica orgánica, Universidad de Vilnius), emisión a baja temperatura y espectroscopia Raman (Departamento de Química Física, Universidad de Málaga) y la realización de cálculos químicos-cuánticos (Departamento de Química Física, Universidad de Alicante; y Grupo de Química Teórica de Materiales Moleculares, Universidad de Valencia).

Las conclusiones más relevantes de esta investigación se resumen a continuación:

1) La elección de una matriz adecuada es fundamental para la eficiencia del material activo. A este respecto, la compatibilidad entre el polímero huésped y la molécula orgánica huésped puede marcar la diferencia incluso entre dos polímeros inertes a priori. Los resultados obtenidos en la primera parte del capítulo 4 apuntan en esta dirección. Allí, se investiga la influencia de la matriz mediante estudios de dependencia de la concentración de dos derivados de PDI diferentes (PDI-O y *b*-PDI-A) dispersos en dos matrices inertes, PS y PMMA. Estos polímeros se encuentran entre los más utilizados en optoelectrónica. La mayor idoneidad de PS para albergar derivados de PDI se demuestra por las tasas más bajas de interacción/agregación molecular observadas en PS con respecto a PMMA. En consecuencia, se observa una tasa más baja de quenching de la emission y mejores umbrales de ASE y fotoestabilidad en PS en lugar de en PMMA. Además, la alta tasa de agregación observada en PMMA afecta negativamente, no solo a las propiedades de emisión de los derivados de PDI, sino también a la calidad óptica de las guías de ondas, que es mejor en PS. Por tanto, una elección inteligente de la matriz es crucial para el diseño de materiales activos eficientes.

2) La sustitución de moléculas orgánicas con grupos laterales tiene un impacto directo en su fotoestabilidad. Normalmente, los grupos laterales se utilizan para

proporcionar solubilidad a la molécula o incluso para prevenir la agregación molecular, pero también podrían modificarse otros aspectos fundamentales, por ejemplo, la fotoestabilidad. Los experimentos realizados en la segunda parte del capítulo 4 con películas de PS dopadas con tres derivados diferentes de *b*-PDI dan fe de ello. La diferencia entre estos derivados radica en sus sustituyentes en las posiciones de imida que son cadenas alifáticas (*b*-PDI-A), grupos diisopropilfenilo (*b*-PDI-O) o terfenilos (*b*-PDI-Tp). El análisis de películas de PS dopadas con bajas concentraciones de las moléculas muestra que los compuestos de *b*-PDI con sustituyentes de tipo fenilo en las posiciones imidas son tres veces más duraderos que los de las cadenas alifáticas. Desafortunadamente, el estudio de dependencia de la concentración demuestra que los compuestos con sustituyentes de tipo fenilo también son más propensos a agregarse y sufrir quenching de la emisión, lo que es perjudicial para el rendimiento ASE, incluida la fotoestabilidad. De hecho, *b*-PDI-A se puede incorporar a la matriz hasta el 50% en peso con un quenching moderado y sin indicios de agregación, mientras que para *b*-PDI-Tp, se observa agregación de tipo H a concentraciones del 6% en peso o superiores.

3) Las propiedades optoelectrónicas de los NG dependen de su estructura, es decir, su tamaño y borde. De ahí que saber cómo se relacionan se convierte en una pieza clave para el desarrollo de nuevos compuestos orgánicos con propiedades a medida. En este sentido, estudios realizados con [*n*, *m*]periacenoacenos han permitido comprender que la presencia de bordes en zigzag desplaza al rojo las propiedades espectrales. La intensidad del cambio depende de la parte de la función de onda deslocalizada sobre el borde en zigzag. Además, los NG con bordes en zigzag completo han demostrado ser materiales láser eficientes al nivel de otras moléculas orgánicas de última generación. La sustitución con grupos arilo en las posiciones más reactivas resultó valiosa para prevenir la fotodegradación de los compuestos, produciendo materiales duraderos (~ 10^5 pulsos de bombeo bajo excitación de ns) con una solubilidad óptima. Curiosamente, los NG más grandes FZ3 y PP-Ar presentan emisión ASE dual, que es consecuencia de la superposición entre sus bandas SE y ESA, un fenómeno que limita la SE y aumenta el umbral de ASE.

4) Otra forma importante de modular las propiedades optoelectrónicas es la sustitución de átomos de carbono del esqueleto del NG por heteroátomos, por ejemplo átomos de nitrógeno o boro. De hecho, dicha sustitución modifica la deslocalización de la función de onda y, por tanto, las propiedades optoelectrónicas. Aquí, dos pares de átomos de carbono de un [*n*, *m*]periacenoaceno previamente estudiado han sido sustituidos por dos pares de átomos de boro-oxígeno, preservando su estructura. Sorprendentemente, las propiedades espectrales se desplazaron al azul en 35 nm, mientras que otros parámetros fotofísicos, como el PLQY o el umbral ASE se han mantenido. Solo la vida útil operativa se ha visto afectada negativamente.

5) Las propiedades optoelectrónicas de los NG se pueden modificar mediante la sustitución con grupos de bordes voluminosos. En el caso particular del NG llamado DBOV-Mes, la sustitución con moléculas FAI (DBOV-FAI), produjo un corrimiento al rojo de las propiedades espectrales. La posición exacta de los niveles electrónicos depende del ángulo diedro entre el núcleo DBOV y el sustituyente FAI, lo que da como resultado un ensanchamiento espectral no homogéneo de los espectros de absorción, PL y ASE. En consecuencia, una porción más grande del espectro de absorción se superpone con el pico ASE, lo que resulta en un aumento de las pérdidas por propagación. Además de esto, la ganancia neta se mantiene y ambos NG presentan unas propiedades ASE formidables. En realidad, la inclusión de los grupos voluminosos presenta otras dos ventajas que podrían estar relacionadas con el excelente desempeño ASE de DBOV-FAI a pesar del aumento de las pérdidas por reabsorción: *i*) los sustituyentes voluminosos previenen la agregación molecular, inhibiendo así la formación de los estados de CT perjudiciales presentes en DBOV-Mes; *ii*) la modificación inducida de la estructura electrónica anula los estados triplete (presentes en DBOV-Mes), que son perjudiciales porque se superponen con la SE.

6) La idoneidad de todas estas estrategias para aplicaciones láser se ha demostrado con la fabricación de láseres DFB operativos. En particular, tres de los compuestos presentan emisión láser en la región NIR, donde existe escasez de emisores orgánicos.

Perspectivas para Futuras Investigaciones

Para el desarrollo de aplicaciones prácticas, existe un interés particular en la posibilidad de dispositivos de bombeo eléctrico.[5] En consecuencia, las matrices inertes deben reemplazarse por electroactivas. Por ejemplo, 4,4'-bis(N-carbazikyl)-1,1'-bifenilo se ha utilizado en la literatura para LEDs y en algunos casos para láseres orgánicos bombeados eléctricamente.[5,110] Además, nuevas estrategias para aumentar la cantidad de compuesto orgánico disperso en la matriz evitando el quenching podría contribuir a la reducción de la energía operativa y al uso de fuentes de bombeo ópticas compactas.[45] Para tal fin, la dispersión de la molécula activa en un marco orgánico covalente u otra macroestructura similar que aísle los cromóforos podría ser importante.[186] Otra posibilidad es el uso de sustituyentes masivos para aislar las moléculas y prevenir interacciones entre ellas, como se demostró muy recientemente con compuestos PDI sustituidos en la bahía.[187] Por otro lado, el concepto de molécula TADF, en el que los estados electrónicos están diseñados para recuperar todos los estados tripletes generados y convertirlos de nuevo en estados singlete, podría ser útil para el desarrollo de láseres orgánicos de onda continua.[188] Además, el efecto de diferentes tipos de bordes, diferentes heteroátomos y su posición, la torsión molecular y otras características estructurales sobre las propiedades de ganancia de los NG son aspectos interesantes que deben aclararse.[18]

Appendix A. Film Thickness vs Polymer Concentration in Solution

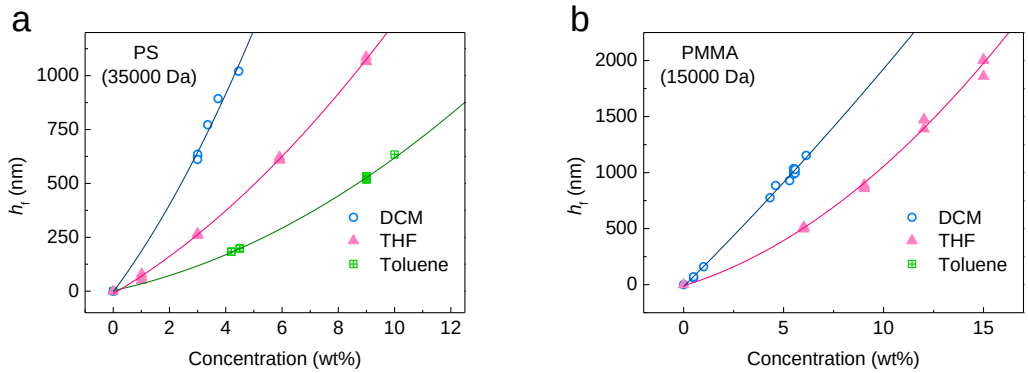

Figure A.1 Film thickness as a function of the polymer concentration in the solution. (a) Polystyrene (PS) and (b) poly(methyl methacrylate) (PMMA). The solvents studied are dichloromethane (DCM, blue open circles), tetrahydrofurane (THF, pink full triangles) and toluene (green crossed squares). Lines correspond with quadratic fits to the experimental data, see below the equations. The spiner parameters are 1000 rpm s^{-1}, 3000 rpm and 30 s.

Table A.1 Empirical expression for the expected thin films[†].

Polymer[a)]	Mw [Da][b)]	Solvent[c)]	B_2 [nm (wt%)$^{-2}$][d)]	B_1 [nm (wt%)$^{-1}$]	B_0 [nm]	R^2
PS	35000	DCM	13.7	175	-3.1	0.985
	35000	THF	4.91	76.7	-12	0.999
	35000	Toluene	3.32	28.4	2.3	0.999
PMMA	15000	DCM	1.69	177	-16	0.997
	15000	THF	5.17	54.9	-9.4	0.993

[†]The spiner parameters are 1000 rpm s^{-1}, 3000 rpm and 30 s; [a)]Polymer used for the fabrication of the thin film, polystyrene (PS) and poly(methyl methacrylate)(PMMA); [b)]Molecular weight of the polymer; [c)]Solvent used to prepare the solution; [d)]The experimental film thicknesses (h_f) in nm have been fitted to a parabola, i.e. $h_f = B_0 + B_1C + B_2C^2$ with C the polymer concentration expressed in wt%.

Appendix B. Publications and Conference Contributions

B.1 Publications on the Scope of the Thesis

[1] R. Muñoz-Mármol, N. Zink-Lorre, J. M. Villalvilla, P. G. Boj, J. A. Quintana, C. Vázquez, A. Anderson, M. J. Gordon, A. Sastre-Santos, F. Fernández-Lázaro, M. A. Díaz-García, "Influence of Blending Ratio and Polymer Matrix on the Lasing Properties of Perylenediimide Dyes", *J. Phys. Chem. C* **2018**, *122*, 24896–24906

[2] V. Bonal, R. Muñoz-Mármol, F. Gordillo Gámez, M. Morales-Vidal, J. M. Villalvilla, P. G. Boj, J. A. Quintana, Y. Gu, J. Wu, J. Casado, M. A. Díaz-García, "Solution-Processed Nanographene Distributed Feedback Lasers", *Nat. Coummun.* **2019**, *10*, 3327

[3] Y. Gu, R. Muñoz-Mármol, S. Wu, Y. Han, Y. Ni, M. A. Díaz-García, J. Casado, J. Wu, "Cove-Edged Nanographenes with Localized Double Bonds", *Angew. Chem., Int. Ed.* **2020**, *59*, 8113–8117

[4] R. Muñoz-Mármol, V. Bonal, G. M. Paternò, A. M. Ross, P. G. Boj, J. M. Villalvilla, J. A. Quintana, F. Scotognella, C. D'Andrea, S. Sardar, G. Lanzani, Y. Gu, J. Wu, and M. A. Díaz-García, "Dual Amplified Spontaneous Emission and Lasing from Nanographene Films", *Nanomaterials* **2020**, *10*, 1525

[5] R. Muñoz-Mármol, P. G. Boj, J. M. Villalvilla, J. A. Quintana, N. Zink-Lorre, Á. Sastre-Santos, J. Aragó, E. Ortí, P. Baronas, D. Litvinas, S. Juršėnas, F. Fernández-Lázaro, M. A. Díaz-García, "Effect of Substituents at Imide Positions on the Laser Performance of 1,7-Bay-Substituted Perylenediimide Dyes", *J. Phys. Chem. C* **2021**, *125*, 12277–12288

[6] R. Muñoz-Mármol, F. Gordillo, V. Bonal, J. M. Villalvilla, P. G. Boj, J. A. Quintana, A. M. Ross, G. M. Paternò, F. Scotognella, G. Lanzani, A. Derradji, J. C. Sancho-García, Y. Gu, J. Wu, J. Casado, M. A. Díaz-García, "Near- Infrared Lasing in Four-Zigzag Edged Nanographenes by 1D versus 2D Electronic π-Conjugation", *Adv. Funct. Mater.* **2021**, 2105073

[7] G. M. Paternò, Q. Chen, R. Muñoz-Mármol, M. Guizzardi, V. Bonal, R. Kabe, P. G. Boj, S. Chatterjee, Y. Ie, J. M. Villalvilla, J. A. Quintana, F. Scotognella, K. Müllen, M. A. Díaz-García, A. Narita, G. Lanzani, "Excited States Engineering Enables Efficient Near-Infrared Lasing in Nanographenes", *Mater. Horiz.* **2021**, Accepted

[8] Y. Gu, R. Muñoz-Mármol et al. "Electronic Structure Modulation by Breaking Nanographene Edge π-Conjugation with 1,2-Oxaborine Hetero-Substitution" (tentative title). Manuscript in preparation

B.2 Other Publications

[1] I. Suárez, R. Muñoz, V. Chirvony, J. P. Martínez-Pastor, M. Artemyev, A. Prudnikau, A. Antanovich, A. Mikhailov, "Multilayers of CdSe/CdS/ZnCdS Core/Wings/Shell Nanoplatelets Integrated in a Polymer Waveguide", *IEEE J. Sel. Top. Quantum Electron.* **2017**, *23*, 4400408

[2] V. Bonal, J. A. Quintana, R. Muñoz-Mármol, J. M. Villalvilla, P. G. Boj, M. A. Díaz-García, "Sub-400 nm Film Thickness Determination from Transmission Spectra in Organic Distributed Feedback Lasers Fabrication", *Thin Solid Films* **2019**, *692*, 137580

[3] V. Bonal, J. A. Quintana, J. M. Villalvilla, R. Muñoz-Mármol, J. C. Mira-Martínez, P. G. Boj, M. E. Cruz, Y. Castro, M. A. Díaz-García, "Simultaneous Determination of Refractive Index and Thickness of Submicron Optical Polymer Films from Transmission Spectra" *Polymers*, **2021**, *13*, 2545

B.3 Conference Contributions

[1] "Matrix Effect on the Optical and Laser Properties of Perylene Dyes Dispersed in Thermoplastic Polymer Films" (Oral Communication). R. Muñoz-Mármol, J. M. Villalvilla, P. G. Boj, J. A. Quintana, C. Vázquez, M. A. Díaz-García. 14th International Conference on Electronic and Related Properties of Organic Solids, 9th-13th July 2017, St Andrews, Scotland.

[2] "Last Advances on Thin Film Organic Lasers" (Invited Oral Communication). M. A. Díaz-García, R. Muñoz-Mármol, M. Morales-Vidal, J. M. Villalvilla, P. G. Boj, J. A. Quintana. XXXVI Reunión Bienal de la Real Sociedad Española de Física, 17th-21th July 2017, Santiago de Compostela, Spain.

[3] "Latest Advances on Solution-processed Thin Film Organic Lasers" (Invited Oral Communication). M. A. Díaz-García, R. Muñoz-Mármol, V. Bonal, M. Morales-Vidal, J. M. Villalvilla, E. M. Calzado, C. Vázquez, P. G. Boj, J. A. Quintana. 2018 Advanced Photonics Congress, 2nd-5th July 2018, Zurich, Switzerland.

[4] "Propiedades Ópticas y Láser de Guías de Onda de Polímeros Termoplásticos Dopados con Perilenodiimidas" (Poster). R. Muñoz-Mármol, P. G. Boj, J. M. Villalvilla, J. A. Quintana, C. Vázquez, M. A. Díaz-García. XII Reunión Nacional de Óptica, 3rd-6th July 2018, Castellón, Spain.

[5] "Solution-Processed Organic Lasers with Top-Layer Nanostructured Resonators" (Oral Communication). M. A. Díaz-García, V. Bonal, R. Muñoz-Mármol, M. Morales-Vidal, J. M. Villalvilla, P. G. Boj y J. A. Quintana. NanoSpain 2019 Conference, 28th-31th May 2019, Barcelona, Spain.

[6] "Novel Organic Compounds for Solution-Processed Thin Film Organic Lasers" (Oral Communication). M. A. Díaz-García, V. Bonal, R. Muñoz-Mármol, M. Morales-Vidal, J. M. Villalvilla, M. Martínez-Marco, E. M. Calzado, C. Vázquez, P. G. Boj, J. A. Quintana. 14th International Symposium on Functional π-Electron Systems, 2nd-7th July 2019, Berlin, Germany.

Bibliography

[1] T. H. Maiman, *Nature* **1960**, *187*, 493.

[2] J. M. Dudley, *Adv. Photonics* **2020**, *2*, 050501.

[3] A. J. C. Kuehne, M. C. Gather, *Chem. Rev.* **2016**, *116*, 12823.

[4] Y. Jiang, Y. Y. Liu, X. Liu, H. Lin, K. Gao, W. Y. Lai, W. Huang, *Chem. Soc. Rev.* **2020**, *49*, 5885.

[5] A. S. D. Sandanayaka, T. Matsushima, F. Bencheikh, S. Terakawa, W. J. Potscavage, C. Qin, T. Fujihara, K. Goushi, J.-C. Ribierre, C. Adachi, *Appl. Phys. Express* **2019**, *12*, 061010.

[6] B. Wang, P. Stefanou, T. Woggon, T. Mappes, U. Lemmer, X. Liu, *Opt. Express* **2013**, *21*, 28941.

[7] S. Schauer, X. Liu, M. Worgull, U. Lemmer, H. Hölscher, *Opt. Mater. Express* **2015**, *5*, 576.

[8] J. Clark, G. Lanzani, *Nat. Photonics* **2010**, *4*, 438.

[9] Y. Wang, P. O. Morawska, A. L. Kanibolotsky, P. J. Skabara, G. A. Turnbull, I. D. W. Samuel, *Laser Photon. Rev.* **2013**, *7*, L71.

[10] E. Heydari, J. Buller, E. Wischerhoff, A. Laschewsky, S. Döring, J. Stumpe, *Adv. Opt. Mater.* **2014**, *2*, 137.

[11] M. Morales-Vidal, P. G. Boj, J. A. Quintana, J. M. Villalvilla, A. Retolaza, S. Merino, M. A. Díaz-García, *Sens. Actuators, B* **2015**, *220*, 1368.

[12] P. G. Boj, M. Morales-Vidal, J. M. Villalvilla, J. A. Quintana, A. Marcilla, M. A. Díaz-García, *Sens. Actuators, B* **2016**, *232*, 605.

[13] A. Retolaza, J. Martinez-Perdiguero, S. Merino, M. Morales-Vidal, P. G. Boj, J. A. Quintana, J. M. Villalvilla, M. A. Díaz-García, *Sens. Actuators, B* **2016**, *223*, 261.

[14] Y.-C. Chen, X. Fan, *Adv. Opt. Mater.* **2019**, *7*, 1900377.

[15] R. Rieger, K. Müllen, *J. Phys. Org. Chem.* **2010**, *23*, 315.

[16] L. Chen, Y. Hernandez, X. Feng, K. Müllen, *Angew. Chem., Int. Ed.* **2012**, *51*, 7640.

[17] A. Nowak-Król, F. Würthner, *Org. Chem. Front.* **2019**, *6*, 1272.

[18] G. M. Paternò, Goudappagouda, Q. Chen, G. Lanzani, F. Scotognella, A. Narita, *Adv. Opt. Mater.* **2021**, 2100508.

[19] J. J. Wu, X. D. Wang, L. S. Liao, *ACS Photonics* **2019**, *6*, 2590.

[20] G. Hong, A. L. Antaris, H. Dai, *Nat. Biomed. Eng.* **2017**, *1*, 0010.

[21] G. Qian, Z. Y. Wang, *Chem. - Asian J.* **2010**, *5*, 1006.

[22] S. H. Lis, *J. Chem. Phys.* **1970**, *53*, 3766.

[23] J. V. Caspar, E. M. Kober, B. Patrick Sullivan, T. J. Meyer, *J. Am. Chem. Soc.* **1982**, *104*, 630.

[24] C. Grivas, *Prog. Quantum Electron.* **2016**, *45–46*, 3.

[25] G. M. Paternò, L. Moretti, A. J. Barker, Q. Chen, K. Müllen, A. Narita, G. Cerullo, F. Scotognella, G. Lanzani, *Adv. Funct. Mater.* **2018**, *29*, 1805249.

[26] O. Svelto, *Principles of Lasers*, Springer, New York, NY, **2010**.

[27] A. E. Siegman, *Lasers*, University Science Books, Mill Valley, CA, **1986**.

[28] C. Rullière, *Fentosecond Laser Pulses*, Springer, New York, NY, **2005**.

[29] M. Anni, S. Lattante, *Organic Lasers: Fundamentals, Developements, and Applications*, Pan Stanford Publishing, Singapore, **2018**.

[30] M. Fox, *Optical Properties of Solids*, Oxford University Press, Oxford, United Kingdom, **2010**.

[31] G. Lanzani, *The Photophysics behind Photovoltaics and Photonics*, WILEY-VCH, Weinheim, Germany, **2012**.

[32] G. Lifante, *Integrated Photonics*, Wiley, Chichester, England, **2003**.

[33] S. Chénais, S. Forget, *Polym. Int.* **2012**, *61*, 390.

[34] W. Huang, S. Shen, D. Pu, G. Wei, Y. Ye, C. Peng, L. Chen, *J. Phys. D: Appl. Phys.* **2015**, *48*, 495105.

[35] H. Kogelnik, C. V. Shank, *J. Appl. Phys.* **1972**, *43*, 2327.

[36] R. Kazarinov, C. Henry, *IEEE J. Quantum Electron.* **1985**, *21*, 144.

[37] F. P. Schäfer, W. Schmidt, J. Volze, *Appl. Phys. Lett.* **1966**, *9*, 306.

[38] P. P. Sorokin, J. R. Lankard, *IBM J. Res. Dev.* **1966**, *10*, 162.

[39] B. H. Soffer, B. B. McFarland, *Appl. Phys. Lett.* **1967**, *10*, 266.

[40] O. G. Peterson, B. B. Snavely, *Appl. Phys. Lett.* **1968**, *12*, 238.

[41] F. Hide, M. A. Díaz-García, B. J. Schwartz, M. R. Andersson, Q. Pei, A. J. Heeger, *Science* **1996**, *273*, 1833.

[42] N. Tessler, G. J. Denton, R. H. Friend, *Nature* **1996**, *382*, 695.

[43] S. V. Frolov, M. Ozaki, W. Gellermann, Z. V. Vardeny, K. Yoshino, *Jpn. J. Appl. Phys.* **1996**, *35*, L1371.

[44] W. Holzer, A. Penzkofer, S.-H. Gong, A. Bleyer, D. D. C. Bradley, *Adv. Mater.* **1996**, *8*, 974.

[45] Y. Yang, G. A. Turnbull, I. D. W. Samuel, *Appl. Phys. Lett.* **2008**, *92*, 163306.

[46] G. Tsiminis, Y. Wang, A. L. Kanibolotsky, A. R. Inigo, P. J. Skabara, I. D. W. Samuel, G. A. Turnbull, *Adv. Mater.* **2013**, *25*, 2826.

[47] M. C. Drummer, V. Singh, N. Gupta, J. L. Gesiorski, R. B. Weerasooriya, K. D. Glusac, *Photosynth. Res.* **2021**

[48] X.-Y. Wang, A. Narita, K. Müllen, *Nat. Rev. Chem.* **2017**, *2*, 0100.

[49] M. Sadrai, G. R. Bird, *Opt. Commun.* **1984**, *51*, 62.

[50] E.-Z. M. Ebeid, S. A. El-Daly, *J. Phys. Chem.* **1988**, *92*, 4565.

[51] H.-G. Löhmannsröben, H. Langhals, *Appl. Phys. B: Photophys. Laser Chem.* **1989**, *48*, 449.

[52] R. Reisfeld, D. Brusilovsky, M. Eyal, E. Miron, Z. Burshtein, J. Ivri, in *French-Israeli Workshop on Solid State Lasers* (Eds.: G. Boulon, C.K. Jorgensen, R. Reisfeld), SPIE, **1989**, p. 230.

[53] M. Fukuda, K. Kodama, K. Mito, *Jpn. J. Appl. Phys.* **2001**, *40*, L440.

[54] I. García-Moreno, A. Costela, M. Pintado-Sierra, V. Martín, R. Sastre, *Opt. Express* **2009**, *17*, 12777.

[55] V. Navarro-Fuster, E. M. Calzado, P. G. Boj, J. A. Quintana, J. M. Villalvilla, M. A. Díaz-García, V. Trabadelo, A. Juarros, A. Retolaza, S. Merino, *Appl. Phys. Lett.* **2010**, *97*, 171104.

[56] V. Bonal, J. A. Quintana, J. M. Villalvilla, P. G. Boj, M. A. Díaz-García, *Sci. Rep.* **2019**, *9*, 11159.

[57] Z. Yu, Y. Wu, Q. Liao, H. Zhang, S. Bai, H. Li, Z. Xu, C. Sun, X. Wang, J. Yao, H. Fu, *J. Am. Chem. Soc.* **2015**, *137*, 15105.

[58] S. Betzold, S. Herbst, A. A. P. Trichet, J. M. Smith, F. Würthner, S. Höfling, C. P. Dietrich, *ACS Photonics* **2017**, *5*, 90.

[59] R. P. Sabatini, F. Maasoumi, S. K. K. Prasad, B. Zhang, C. Clark, T. W. Schmidt, W. W. H. Wong, G. Lakhwani, *Appl. Phys. Lett.* **2020**, *117*, 041103.

[60] E. M. Calzado, J. M. Villalvilla, P. G. Boj, J. A. Quintana, R. Gómez, J. L. Segura, M. A. Díaz García, *Appl. Opt.* **2007**, *46*, 3836.

[61] L. Cerdán, A. Costela, G. Durán-Sampedro, I. García-Moreno, M. Calle, M. Juan-y-

Seva, J. de Abajo, G. A. Turnbull, *J. Mater. Chem.* **2012**, *22*, 8938.

[62] M. G. Ramírez, M. Morales-Vidal, V. Navarro-Fuster, P. G. Boj, J. A. Quintana, J. M. Villalvilla, A. Retolaza, S. Merino, M. A. Díaz-García, *J. Mater. Chem. C* **2013**, *1*, 1182.

[63] R. Muñoz-Mármol, N. Zink-Lorre, J. M. Villalvilla, P. G. Boj, J. A. Quintana, C. Vázquez, A. Anderson, M. J. Gordon, A. Sastre-Santos, F. Fernández-Lázaro, M. A. Díaz-García, *J. Phys. Chem. C* **2018**, *122*, 24896.

[64] E. M. Calzado, J. M. Villalvilla, P. G. Boj, J. A. Quintana, R. Gómez, J. L. Segura, M. A. Díaz-García, *J. Phys. Chem. C* **2007**, *111*, 13595.

[65] M. A. Díaz-García, E. M. Calzado, J. M. Villalvilla, P. G. Boj, J. A. Quintana, F. J. Céspedes-Guirao, F. Fernández-Lázaro, Á. Sastre-Santos, *Synth. Met.* **2009**, *159*, 2293.

[66] V. Sivamurugan, K. Kazlauskas, S. Juršėnas, A. Gruodis, J. Simokaitiene, J. V. Grazulevicius, S. Valiyaveettil, *J. Phys. Chem. B* **2010**, *114*, 1782.

[67] A. Miasojedovas, K. Kazlauskas, G. Armonaite, V. Sivamurugan, S. Valiyaveettil, J. V. Grazulevicius, S. Juršėnas, *Dyes Pigm.* **2012**, *92*, 1285.

[68] J. He, S. Li, H. Zeng, *J. Heterocycl. Chem.* **2017**, *54*, 2800.

[69] M.-J. Lin, Á. J. Jiménez, C. Burschka, F. Würthner, *Chem. Commun.* **2012**, *48*, 12050.

[70] M. G. Ramírez, S. Pla, P. G. Boj, J. M. Villalvilla, J. A. Quintana, M. A. Díaz-García, F. Fernández-Lázaro, Á. Sastre-Santos, *Adv. Opt. Mater.* **2013**, *1*, 933.

[71] Á. J. Jiménez, M. J. Lin, C. Burschka, J. Becker, V. Settels, B. Engels, F. Würthner, *Chem. Sci.* **2014**, *5*, 608.

[72] M. Signoretto, N. Zink-Lorre, I. Suarez, E. Font-Sanchis, Á. Sastre-Santos, V. S. Chirvony, F. Fernandez-La zaro, J. P. Martínez-Pastor, *ACS Photonics* **2017**, *4*, 114.

[73] F. Würthner, C. R. Saha-Möller, B. Fimmel, S. Ogi, P. Leowanawat, D. Schmidt, *Chem. Rev.* **2016**, *116*, 962.

[74] B. Zhang, I. Lyskov, L. J. Wilson, R. P. Sabatini, A. Manian, H. Soleimaninejad, J. M. White, T. A. Smith, G. Lakhwani, D. J. Jones, K. P. Ghiggino, S. P. Russo, W. W. H. Wong, *J. Mater. Chem. C* **2020**, *8*, 8953.

[75] K. S. Novoselov, A. K. Geim, S. V. Morozov, D. Jiang, Y. Zhang, S. V. Dubonos, I. V. Grigorieva, A. A. Firsov, *Science* **2004**, *306*, 666.

[76] F. Bonaccorso, Z. Sun, T. Hasan, A. C. Ferrari, *Nat. Photonics* **2010**, *4*, 611.

[77] W. Han, R. K. Kawakami, M. Gmitra, J. Fabian, *Nat. Nanotechnol.* **2014**, *9*, 794.

[78] A. K. Geim, A. H. MacDonald, *Phys. Today* **2007**, *60*, 35.

[79] K. P. Loh, Q. Bao, G. Eda, M. Chhowalla, *Nat. Chem.* **2010**, *2*, 1015.

[80] T. Ohta, A. Bostwick, T. Seyller, K. Horn, E. Rotenberg, *Science* **2006**, *313*, 951.

[81] Q. Chen, C. Zhang, F. Xue, Y. Zhou, W. Li, Y. Wang, W. Tu, Z. Zou, X. Wang, M. Xiao, *Sci. Rep.* **2013**, *3*, 2315.

[82] P. Das, R. Maiti, P. K. Barman, S. K. Ray, B. B. N. Shivakiran, *Nanotechnology* **2016**, *27*, 055201.

[83] D. Yadav, G. Tamamushi, T. Watanabe, J. Mitsushio, Y. Tobah, K. Sugawara, A. A. Dubinov, A. Satou, M. Ryzhii, V. Ryzhii, T. Otsuji, *Nanophotonics* **2018**, *7*, 741.

[84] L. Li, X. Yan, *J. Phys. Chem. Lett.* **2010**, *1*, 2572.

[85] G. M. Paternò, Q. Chen, X. Y. Wang, J. Liu, S. G. Motti, A. Petrozza, X. Feng, G. Lanzani, K. Müllen, A. Narita, F. Scotognella, *Angew. Chem., Int. Ed.* **2017**, *56*, 6753.

[86] V. Bonal, R. Muñoz-Mármol, F. Gordillo Gámez, M. Morales-Vidal, J. M. Villalvilla, P. G. Boj, J. A. Quintana, Y. Gu, J. Wu, J. Casado, M. A. Díaz-García, *Nat. Commun.* **2019**, *10*, 3327.

[87] K. A. Ritter, J. W. Lyding, *Nat. Mater.* **2009**, *8*, 235.

[88] T. Enoki, T. Ando, *Physics and Chemistry of Graphene: Graphene to Nanographene*, Pan Stanford Publishing, Singapore, **2013**.

[89] Z. Z. Zhang, K. Chang, F. M. Peeters, *Phys. Rev. B* **2008**, *77*, 235411.

[90] T. Dumslaff, Y. Gu, G. M. Paternò, Z. Qiu, A. Maghsoumi, M. Tommasini, X. Feng, F. Scotognella, A. Narita, K. Müllen, *Chem. Sci.* **2020**, *11*, 12816.

[91] N. Chen, X. Huang, L. Qu, *Phys. Chem. Chem. Phys.* **2015**, *17*, 32077.

[92] M. Stępień, E. Gońka, M. Żyła, N. Sprutta, *Chem. Rev.* **2017**, *117*, 3479.

[93] A. P. Demchenko, *Methods Appl. Fluoresc.* **2020**, *8*, 022001.

[94] O. García, L. Garrido, R. Sastre, A. Costela, I. García-Moreno, *Adv. Funct. Mater.* **2008**, *18*, 2017.

[95] S. R. Forrest, *Nature* **2004**, *428*, 911.

[96] Y. Chen, Z. Li, Z. Zhang, D. Psaltis, A. Scherer, *Appl. Phys. Lett.* **2007**, *91*, 051109.

[97] K. Yamashita, M. Arimatsu, M. Takayama, K. Oe, H. Yanagi, *Appl. Phys. Lett.* **2008**, *92*, 243306.

[98] M. G. Ramírez, P. G. Boj, V. Navarro-Fuster, I. Vragovic, J. M. Villalvilla, I. Alonso, V. Trabadelo, S. Merino, M. A. Díaz-García, *Opt. Express* **2011**, *19*, 22443.

[99] E. M. Calzado, A. Retolaza, S. Merino, M. Morales-Vidal, P. G. Boj, J. A. Quintana, J. M. Villalvilla, M. A. Díaz-García, *Opt. Mater. Express* **2017**, *7*, 1295.

[100] A. K. Sheridan, A. R. Buckley, A. M. Fox, A. D. Bacher, D. D. C. Bradley, I. D. W. Samuel, *J. Appl. Phys.* **2002**, *92*, 6367.

[101] E. M. Calzado, M. G. Ramírez, P. G. Boj, M. A. D. García, *Appl. Opt.* **2012**, *51*, 3287.

[102] M. Anni, S. Lattante, *J. Phys. Chem. C* **2015**, *119*, 21620.

[103] M. G. Ramírez, J. P. Jahnke, M. J. N. Junk, J. M. Villalvilla, P. G. Boj, J. A. Quintana, E. M. Calzado, B. F. Chmelka, M. A. Díaz-García, *Adv. Opt. Mater.* **2015**, *3*, 1454.

[104] B. H. Wallikewitz, G. O. Nikiforov, H. Sirringhaus, R. H. Friend, *Appl. Phys. Lett.* **2012**, *100*, 173301.

[105] K. Yamashita, T. Kuro, K. Oe, H. Yanagi, *Appl. Phys. Lett.* **2006**, *88*, 241110.

[106] T. Kobayashi, J.-B. Savatier, G. Jordan, W. J. Blau, Y. Suzuki, T. Kaino, *Appl. Phys. Lett.* **2004**, *85*, 185.

[107] S. Yuyama, T. Nakajima, K. Yamashita, K. Oe, *Appl. Phys. Lett.* **2008**, *93*, 023306.

[108] S. Fujimoto, I. Sakata, H. Yanagi, K. Yamashita, K. Oe, *Jpn. J. Appl. Phys.* **2006**, *45*, L355.

[109] H. Ye, D. H. Kim, X. Chen, A. S. D. Sandanayaka, J. U. Kim, E. Zaborova, G. Canard, Y. Tsuchiya, E. Y. Choi, J. W. Wu, F. Fages, J.-L. Bredas, A. D'Aléo, J.-C. Ribierre, C. Adachi, *Chem. Mater.* **2018**, *30*, 6702.

[110] D.-H. Kim, A. D'Aléo, X.-K. Chen, A. D. S. Sandanayaka, D. Yao, L. Zhao, T. Komino, E. Zaborova, G. Canard, Y. Tsuchiya, E. Choi, J. W. Wu, F. Fages, J.-L. Brédas, J.-C. Ribierre, C. Adachi, *Nat. Photonics* **2018**, *12*, 98.

[111] X. Cheng, K. Wang, S. Huang, H. Zhang, H. Zhang, Y. Wang, *Angew. Chem.* **2015**, *127*, 8489.

[112] X. Wang, Q. Liao, H. Li, S. Bai, Y. Wu, X. Lu, H. Hu, Q. Shi, H. Fu, *J. Am. Chem. Soc.* **2015**, *137*, 9289.

[113] X. Wang, Z.-Z. Li, M.-P. Zhuo, Y. Wu, S. Chen, J. Yao, H. Fu, *Adv. Funct. Mater.* **2017**, *27*, 1703470.

[114] S. M. Yoon, J. Lee, J. H. Je, H. C. Choi, M. Yoon, *ACS Nano* **2011**, *5*, 2923.

[115] D. E. Bornside, C. W. Macosko, L. E. Scriven, *J. Appl. Phys.* **1989**, *66*, 5193.

[116] D. B. Hall, P. Underhill, J. M. Torkelson, *Polym. Eng. Sci.* **1998**, *38*, 2039.

[117] J. García-Turiel, B. Jérôme, *Colloid Polym. Sci. 2007 28514* **2007**, *285*, 1617.

[118] J. Perlich, V. Körstgens, E. Metwalli, L. Schulz, R. Georgii, P. Müller-Buschbaum, *Macromolecules* **2009**, *42*, 337.

[119] C. W. Frank, V. Rao, M. M. Despotopoulou, R. F. W. Please, W. D. Hinberg, R. D. Miller, J. F. Rabolt, *Science* **1996**, *273*, 912.

[120] I. H. Romdhane, P. E. Price, C. A. Miller, P. T. Benson, S. Wang, *Ind. Eng. Chem.*

Res. **2001**, *40*, 3065.

[121] H. Richardson, M. Sferrazza, J. L. Keddie, *Eur. Phys. J. E: Soft Matter Biol. Phys.* **2003**, *12*, 87.

[122] A. Brûlet, F. Boué, A. Menelle, J. P. Cotton, *Macromolecules* **2000**, *33*, 997.

[123] M. K. Mundra, C. J. Ellison, R. E. Behling, J. M. Torkelson, *Polymer* **2006**, *47*, 7747.

[124] V. Bonal, J. M. Villalvilla, J. A. Quintana, P. G. Boj, N. Lin, S. Watanabe, K. Kazlauskas, O. Adomeniene, S. Juršėnas, H. Tsuji, E. Nakamura, M. A. Díaz-García, *Adv. Opt. Mater.* **2020**, *8*, 2001153.

[125] J. A. Quintana, J. M. Villalvilla, M. Morales-Vidal, P. G. Boj, X. Zhu, N. Ruangsupapichat, H. Tsuji, E. Nakamura, M. A. Díaz-García, *Adv. Opt. Mater.* **2017**, *5*, 1700238.

[126] V. Bonal, J. A. Quintana, R. Muñoz-Mármol, J. M. Villalvilla, P. G. Boj, M. A. Díaz-García, *Thin Solid Films* **2019**, *692*, 137580.

[127] J. C. Manifacier, J. Gasiot, J. P. Fillard, *J. Phys. E: Sci. Instrum.* **1976**, *9*, 1002.

[128] R. Swanepoel, *J. Phys. E: Sci. Instrum.* **1983**, *16*, 1214.

[129] R. Swanepoel, *J. Phys. E: Sci. Instrum.* **1984**, *17*, 896.

[130] R. Swanepoel, *J. Opt. Soc. Am. A* **1985**, *2*, 1339.

[131] D. Poelman, P. F. Smet, *J. Phys. D: Appl. Phys.* **2003**, *36*, 1850.

[132] D. A. Minkov, G. M. Gavrilov, G. V. Angelov, J. M. D. Moreno, C. G. Vazquez, S. M. F. Ruano, E. Marquez, *Thin Solid Films* **2018**, *645*, 370.

[133] M. N. Polyanskiy, Refractive index database, https://refractiveindex.info/, accessed: Apr., 2020.

[134] M. Hammer, 1-D mode solver for dielectric multilayer slab waveguides., https://www.computational-photonics.eu/oms.html, accessed: May, 2020.

[135] A. T. Rhys Williams, S. A. Winfield, J. N. Miller, *Analyst* **1983**, *108*, 1067.

[136] Recording Fluorescence Quantum Yields - HORIBA, https://www.horiba.com/en_en/applications/materials/material-research/quantum-dots/recording-fluorescence-quantum-yields/, accessed: Sep., 2021.

[137] J. R. Lakowicz, *Principles of Fluorescence Spectroscopy*, Springer, New York, NY, **2006**.

[138] C. D'Andrea, D. Pezzoli, C. Malloggi, A. Candeo, G. Capelli, A. Bassi, A. Volonterio, P. Taroni, G. Candiani, *Photochem. Photobiol. Sci.* **2014**, *13*, 1680.

[139] H. Rabbani-Haghighi, Ś. Forget, Ś. Cḥnais, A. Siove, M. C. Castex, E. Ishow, *Appl. Phys. Lett.* **2009**, *95*, 033305.

[140] S. Milanese, M. L. De Giorgi, M. Anni, *Molecules* **2020**, *25*, 2992.

[141] K. L. Shaklee, R. F. Leheny, *Appl. Phys. Lett.* **1971**, *18*, 475.

[142] M. Vehse, J. Meinertz, O. Lange, P. Michler, J. Gutowski, S. Bader, A. Lell, V. Härle, *Phys. status solidi* **2002**, *0*, 43.

[143] A. Costela, O. García, L. Cerdán, I. García-Moreno, R. Sastre, *Opt. Express* **2008**, *16*, 7023.

[144] F. Vogelbacher, J. Huang, K. Unterrainer, K.-J. Jiang, M. Li, R. Hainberger, X. Zhou, Y. Song, *Opt. Mater. Express* **2019**, *9*, 1208.

[145] L. Cerdán, A. Costela, G. Durán-Sampedro, I. García-Moreno, *Appl. Phys. B* **2012**, *108*, 839.

[146] L. Cerdán, *Opt. Laser Technol.* **2020**, *121*, 105814.

[147] L. Cerdán, M. Anni, M. L. De Giorgi, P. G. Boj, M. A. Díaz-García, *Opt. Laser Technol.* **2021**, *136*, 106766.

[148] L. Cerdán, GUI available under appropriate request, lcerdanphd@gmail.com.

[149] M. Schlosser, S. Lochbrunner, *J. Phys. Chem. B* **2006**, *110*, 6001.

[150] R. O. Al-Kaysi, T. Sang Ahn, A. M. Müller, C. J. Bardeen, *Phys. Chem. Chem. Phys.* **2006**, *8*, 3453.

[151] F. C. Spano, *Acc. Chem. Res.* **2010**, *43*, 429.

[152] J. A. Ferreira, G. Porter, *J. Chem. Soc. Faraday Trans. 2* **1977**, *73*, 340.

[153] M. Morales-Vidal, P. G. Boj, J. M. Villalvilla, J. A. Quintana, Q. Yan, N.-T. Lin, X. Zhu, N. Ruangsupapichat, J. Casado, H. Tsuji, E. Nakamura, M. A. Díaz-García, *Nat. Commun.* **2015**, *6*, 8458.

[154] D. R. Lide, *CRC Handbook of Chemistry and Physics*, CRC Press, Boca Raton, FL, **2005**.

[155] N. Tanaka, N. Barashkov, J. Heath, W. N. Sisk, *Appl. Opt.* **2006**, *45*, 3846.

[156] A. Priimagi, S. Cattaneo, R. H. A. Ras, S. Valkama, O. Ikkala, M. Kauranen, *Chem. Mater.* **2005**, *17*, 5798.

[157] R. Muñoz-Mármol, P. G. Boj, J. M. Villalvilla, J. A. Quintana, N. Zink-Lorre, Á. Sastre-Santos, J. Aragó, E. Ortí, P. Baronas, D. Litvinas, S. Juršėnas, F. Fenández-Lázaro, M. A. Díaz-García, *J. Phys. Chem. C* **2021**, *125*, 12277.

[158] A. K. Ray, S. Kumar, N. V. Mayekar, S. Sinha, S. Kundu, S. Chattopadhyay, K. Dasgupta, *Appl. Opt.* **2005**, *44*, 7814.

[159] Y. Oyama, M. Mamada, A. Shukla, E. G. Moore, S. C. Lo, E. B. Namdas, C. Adachi, *ACS Mater. Lett.* **2020**, *2*, 161.

[160] G. Seybold, G. Wagenblast, *Dyes Pigm.* **1989**, *11*, 303.

[161] E. Yousif, R. Haddad, *Springerplus* **2013**, *2*, 398.

[162] M. B. Smith, J. March, *March's Advanced Organic Chemistry: Reactions, Mechanisms, and Structure*, Wiley-VCH, Weinheim, Germany, **2000**.

[163] N. J. Hestand, F. C. Spano, *Chem. Rev.* **2018**, *118*, 7069.

[164] K. Nakada, M. Fujita, G. Dresselhaus, M. S. Dresselhaus, *Phys. Rev. B* **1996**, *54*, 17954.

[165] Y. Gu, X. Wu, T. Y. Gopalakrishna, H. Phan, J. Wu, *Angew. Chem.* **2018**, *130*, 6651.

[166] R. Muñoz-Mármol, F. Gordillo, V. Bonal, J. M. Villalvilla, P. G. Boj, J. A. Quintana, A. M. Ross, G. M. Paternò, F. Scotognella, G. Lanzani, A. Derradji, J. C. Sancho-García, Y. Gu, J. Wu, J. Casado, M. A. Díaz-García, *Adv. Funct. Mater.* **2021**, 2105073.

[167] X. Zhu, H. Tsuji, J. T. L. Navarrete, J. Casado, E. Nakamura, *J. Am. Chem. Soc.* **2012**, *134*, 19254.

[168] Y. Gu, Y. Gopalakrishna Tullimilli, J. Feng, H. Phan, W. Zeng, J. Wu, *Chem. Commun.* **2019**, *55*, 5567.

[169] Y. Gu, R. Muñoz-Mármol, V. Bonal, J. M. Villalvilla, J. A. Quintana, P. G. Boj, M. A. Díaz-García, J. Wu, *Prep.* **n.d.**

[170] Y.-B. Tang, L.-C. Yin, Y. Yang, X.-H. Bo, Y.-L. Cao, H.-E. Wang, W.-J. Zhang, I. Bello, S.-T. Lee, H.-M. Cheng, C.-S. Lee, *ACS Nano* **2012**, *6*, 1970.

[171] C. Dou, S. Saito, K. Matsuo, I. Hisaki, S. Yamaguchi, *Angew. Chem.* **2012**, *124*, 12372.

[172] X.-Y. Wang, A. Narita, W. Zhang, X. Feng, K. Müllen, *J. Am. Chem. Soc.* **2016**, *138*, 9021.

[173] T. Kaehler, M. Bolte, H.-W. Lerner, M. Wagner, *Angew. Chem.* **2019**, *131*, 11501.

[174] K.-A. Tsai, P.-Y. Hsieh, T.-H. Lai, C.-W. Tsao, H. Pan, Y.-G. Lin, Y.-J. Hsu, *ACS Appl. Energy Mater.* **2020**, *3*, 5322.

[175] J. Sanz-Rodrigo, G. Ricci, Y. Olivier, J. C. Sancho-García, *J. Phys. Chem. A* **2021**, *125*, 513.

[176] B. Biel, X. Blase, F. Triozon, S. Roche, *Phys. Rev. Lett.* **2009**, *102*, 096803.

[177] S. Xiao, M. Myers, Q. Miao, S. Sanaur, K. Pang, M. L. Steigerwald, C. Nuckolls, *Angew. Chem., Int. Ed.* **2005**, *44*, 7390.

[178] K. Nagarajan, A. R. Mallia, K. Muraleedharan, M. Hariharan, *Chem. Sci.* **2017**, *8*, 1776.

[179] Y. Gu, R. Muñoz-Mármol, S. Wu, Y. Han, Y. Ni, M. A. Díaz-García, J. Casado, J. Wu, *Angew. Chem., Int. Ed.* **2020**, *59*, 8113.

[180] J. Wu, W. Pisula, K. Müllen, *Chem. Rev.* **2007**, *107*, 718.

[181] Clark, *The Aromatic Sextet*, Wiley, London, England, **1972**.

[182] R. Englman, J. Jortner, *Mol. Phys.* **1970**, *18*, 145.

[183] G. M. Paternò, Q. Chen, R. Muñoz-Mármol, M. Guizzardi, V. Bonal, R. Kabe, A. Barker, P. G. Boj, S. Chatterjee, Y. Ie, J. M. Villalvilla, J. A. Quintana, F. Scotognella, K. Müllen, M. A. Díaz-García, A. Narita, G. Lanzani, *Mater. Horizons* **2021**.

[184] D. M. Coles, Q. Chen, L. C. Flatten, J. M. Smith, K. Müllen, A. Narita, D. G. Lidzey, *Nano Lett.* **2017**, *17*, 5521.

[185] R. Muñoz-Mármol, V. Bonal, G. M. Paternò, A. M. Ross, P. G. Boj, J. M. Villalvilla, J. A. Quintana, F. Scotognella, C. D'Andrea, S. Sardar, G. Lanzani, Y. Gu, J. Wu, M. A. Díaz-García, *Nanomaterials* **2020**, *10*, 1525.

[186] K. Geng, T. He, R. Liu, S. Dalapati, K. T. Tan, Z. Li, S. Tao, Y. Gong, Q. Jiang, D. Jiang, *Chem. Rev.* **2020**, *120*, 8814.

[187] M. Stolte, T. Schembri, J. Süß, D. Schmidt, A.-M. Krause, M. O. Vysotsky, F. Würthner, *Chem. Mater.* **2020**, *32*, 6222.

[188] H. Nakanotani, Y. Tsuchiya, C. Adachi, *Chem. Lett.* **2021**, *50*, 938.